CLEMENTE IBARRA CASTANEDO

QUANTITATIVE SUBSURFACE DEFECT EVALUATION BY PULSED PHASE THERMOGRAPHY: DEPTH RETRIEVAL WITH THE PHASE

Thèse présentée
à la Faculté des études supérieures de l'Université Laval
dans le cadre du programme de doctorat en génie électrique
pour l'obtention du grade de Philosophiae Doctor (Ph.D.)

FACULTÉ DES SCIENCES ET DE GÉNIE
UNIVERSITÉ LAVAL
QUÉBEC

OCTOBRE 2005

Résumé

La Thermographie de Phase Pulsée (TPP) est une technique d'Évaluation Non-Destructive basée sur la Transformée de Fourier pouvant être considérée comme étant le lien entre la Thermographie Pulsée, pour laquelle l'acquisition de données est rapide, et la Thermographie Modulée, pour laquelle l'extraction de la profondeur est directe. Une nouvelle technique d'inversion de la profondeur reposant sur l'équation de la longueur de diffusion thermique : $\mu=(\alpha/\pi f)^{1/2}$, est proposée. Le problème se résume alors à la détermination de la fréquence de borne f_b, c à d, la fréquence à laquelle un défaut à une profondeur particulière présente un contraste de phase suffisant pour être détecté dans le spectre des fréquences. Cependant, les profils de température servant d'entrée en TPP, sont des signaux non-périodiques et non-limités en fréquence pour lesquels, des paramètres d'échantillonnage Δt, et de troncature $w(t)$, doivent être soigneusement choisis lors du processus de discrétisation du signal. Une méthodologie à quatre étapes, basée sur la Dualité Temps-Fréquence de la Transformée de Fourier discrète, est proposée pour la détermination interactive de Δt et $w(t)$, en fonction de la profondeur du défaut. Ainsi, pourvu que l'information thermique utilisée pour alimenter l'algorithme de TPP soit correctement échantillonnée et tronquée, une solution de la forme : $z=C_1\mu$, peut être envisagée, où les valeurs expérimentales de C_1 se situent typiquement entre 1.5 et 2. Bien que la détermination de f_b ne soit pas possible dans le cas de données thermiques incorrectement échantillonnées, les profils de phase exhibent quoi qu'il en soit un comportement caractéristique qui peut être utilisé pour l'extraction de la profondeur. La fréquence de borne apparente f'_b, peut être définie comme la fréquence de borne évaluée à un seuil de phase donné ϕ_d, et peut être utilisée en combinaison avec la définition de la phase pour une onde thermique : $\phi=z/\mu$, et le diamètre normalisé $D_n=D/z$, pour arriver à une expression alternative. L'extraction de la profondeur dans ce cas nécessite d'une étape additionnelle pour récupérer la taille du défaut. ▣

Abstract

Pulsed Phase Thermography (PPT) is a NonDestructive Testing and Evaluation (NDT&E) technique based on the Fourier Transform that can be thought as being the link between Pulsed Thermography, for which data acquisition is fast and simple; and Lock-In thermography, for which depth retrieval is straightforward. A new depth inversion technique using the phase obtained by PPT is proposed. The technique relies on the thermal diffusion length equation, *i.e.* $\mu=(\alpha/\pi f)^{1/2}$, in a similar manner as in Lock-In Thermography. The inversion problem reduces to the estimation of the blind frequency, *i.e.* the limiting frequency at which a defect at a particular depth presents enough phase contrast to be detected on the frequency spectra. However, an additional problem arises in PPT when trying to adequately establish the temporal parameters that will produce the desired frequency response. The decaying thermal profiles such as the ones serving as input in PPT, are non-periodic, non-band-limited functions for which, adequate sampling Δt, and truncation *w(t)*, parameters should be selected during the signal discretization process. These parameters are both function of the depth of the defect and of the thermal properties of the specimen/defect system. A four-step methodology based on the Time-Frequency Duality of the discrete Fourier Transform is proposed to interactively determine Δt and *w(t)*. Hence, provided that thermal data used to feed the PPT algorithm is correctly sampled and truncated, the inversion solution using the phase takes the form: $z=C_1\mu$, for which typical experimental C_1 values are between 1.5 and 2. Although determination of f_b is not possible when working with badly sampled data, phase profiles still present a distinctive behavior that can be used for depth retrieval purposes. An apparent blind frequency f'_b, can be defined as the blind frequency at a given phase threshold ϕ_d, and be used in combination with the phase delay definition for a thermal wave: $\phi=z/\mu$, and the normalized diameter, $D_n=D/z$, to derive an alternative expression. Depth extraction in this case requires an additional step to recover the size of the defect. ▣

Resumen

La Termografía de Fase Pulsada (TFP) es una técnica de Evaluación No-Destructiva basada en la Transformada de Fourier y que puede ser vista como el vínculo entre la Termografía Pulsada, en la cual la adquisición de datos se efectúa de manera rápida y sencilla, y la Termografía Modulada, en la que la extracción de la profundidad es directa. Un nuevo método de inversión de la profundidad por TFP es propuesto a partir de la ecuación de la longitud de difusión térmica: $\mu=(\alpha/\pi f)^{1/2}$. El problema de inversion se reduce entonces a la determinación de la frecuencia límite f_b (frecuencia a la cual un defecto de profundidad determinada presenta un contraste de fase suficiente para ser detectado en el espectro de frecuencias). Sin embargo, las curvas de temperatura utilizadas como entrada en TFP, son señales no-periódicas y no limitadas en frecuencia para las cuales, los parámetros de muestreo Δt, y de truncamiento $w(t)$, deben ser cuidadosamente seleccionados durante el proceso de discretización de la señal. Una metodología de cuatro etapas, basada en la Dualidad Tiempo-Frecuencia de la Transformada de Fourier discreta, ha sido desarrollada para la determinación interactiva de Δt y $w(t)$, en función de la profundidad del defecto. Así, a condición que la información de temperatura sea correctamente muestreada y truncada, el problema de inversión de la profundidad por la fase toma la forma : $z=C_1\mu$, donde los valores experimentales de C_1 se sitúan típicamente entre 1.5 y 2. Si bien la determinación de f_b no es posible en el caso de datos térmicos incorrectamente muestreados, los perfiles de fase exhiben de cualquier manera un comportamiento característico que puede ser utilizado para la extracción de la profundidad. La frecuencia límite aparente f'_b, puede ser definida como la frecuencia límite evaluada en un umbral de fase dado ϕ_d, y puede utilizarse en combinación con la definición de la fase para una onda térmica: $\phi=z/\mu$, y el diámetro normalizado D_n, para derivar una expresión alternativa. La determinación de la profundidad en este caso, requiere de una etapa adicional para recuperar el tamaño del defecto. ▣

Acknowledgements

Many people supported me during the completion of this work. I am extremely grateful to all of them. First, I wish to express my deep sense of gratitude to my supervisor Prof. Xavier Maldague for his sympathy, guidance and support during all the stages of my investigation. I appreciate the opportunity to work in such a professional (but friendly) environment. I am also indebted to Dr. Nicolas Avdelidis, who kindly accepted to review this thesis as a pre-lecturer. I also value the time we spend together (in the laboratory and through emails) preparing the material for the papers we wrote together, and some others that are still in preparation! I extend my thanks to the other two members of my thesis committee, Denis Laurendeau and Hakim Bendada, who provided me with very useful inputs to complete the final version of this thesis.

I wish to express my appreciation to Daniel González, with whom I spent so many constructive hours discussing each other's projects, which finally culminated on several joint investigations and a long lasting friendship.

I want to thank all the members of the Computer Vision and Systems Laboratory at the Université Laval. I am particularly thankful to the Thermography team: François Galmiche, Hélène Torresan, Adel Ziadi, Lilia Najjar, Amar El Maadi, Chen Liu, Lukasz Czuban, Mathieu Klein, Christoph Mohr (visiting from Stuttgart University) and Hernan Benitez (visiting from Universidad del Valle de Colombia), they all provided me with useful inputs that enriched my understanding and enthusiasm on the field. I also acknowledge the invaluable help of the skilled technical and professional staff in the laboratory, Denis Ouellet, Sylvain Comtois, François Lemay, Marco Béland and Martin Gagnon; they all have always showed a great capacity to solve any problem, small or…huge!

I would like to express my sincere gratitude to my family in law, Beba, Diego, and Pablo, for their kindness and support when things were not going that well at the beginning of my Ph. D. studies, and also at the end, by providing me with the

material and some peaceful moments to be able to sit down and write while we were in Bolivia.

Special thanks go to my family in Mexico: my parents Mélida and Clemente, my two sisters Laura and Gabriela (and their families: Emilio, Laurita, Mangüe and Manuel), and my brother Ricardo. I thank them ALL for being a role model for me, as persons, as parents and as professionals and for giving me their unconditional support since the beginning of our journey in Quebec and all through our studies with their constant love and encouragement, from near and from far.

Lastly, this work would not be possible without the help of my *little* family. Sandra, I am grateful for all your patience and understanding, your love and your support, and for being able to give birth and raise our Paulo while you were working on a thesis of your own. ⧈

To Paulo
who radiates energy in all directions

Table of Contents

List of Figures

List of Tables

Nomenclature

Symbols	Quantity	Units
A	surface	m^2
M	number of vertical elements on a matrix	-
N	number of horizontal (or vertical) elements on a matrix	-
n	number of frequency component	-
c_P	heat capacity	J / kg K
C	thermal contrast	-
D	diameter	m
e	thermal effusivity	W $s^{½}$ / m^2·K
E	total emissive power	W / m^2
E	Radiated energy by a photon0	W / m^2
G	total irradiation	W / m^2
J	total radiosity	W / m^2
f_n	n^{th} frequency component	Hz
f_s	sampling rate	Hz
f_c	critical (Nyquist) frequency	Hz
f_b	blind frequency	Hz
L	thickness	m
h	convection heat transfer coefficient, Planck's constant (see below)	W / m^2 K
k	thermal conductivity	W / m K
p	momentum	
Q	energy absorption per unit area	J / m^2
$\dot{Q}$	rate of energy generation per unit volume	W / m^3
q	heat	W
q''	heat density	W / m^2
R	thermal resistance	m^2 K / W
T	temperature	K, ^oC
$w(t)$	truncation window	K, ^oC
t	time	s
t_{acq}	acquisition (or observation) duration time	s
t_m	time of maximum temperature excess	s
v	wave propagation speed	m / s
z	depth	m

Greek Symbols	Quantity	Unités
α	thermal diffusivity	m^2 / s
ε	emissivity	
ϕ	phase delay	
λ	wavelength	m
σ	variance of a Gaussian filter, Stefan-Boltzman constant (see below)	-
μ	diffusion length	m
ρ	density	kg / m^3
ω	angular frequency ($2\pi f$)	rad / s
Δ	gradient (temperature or phase)	^{o} or rad

Subindex

a	absolute
acq	acquisition
b	blackbody, blind
d	defect
max	maximum
n	normalized
r	running
0	initial
Sa	sound area
S	surface
s	sampling

Constants

h	universal (or Planck's) constant, $h = 6.6256 \times 10^{-34}$ Js
c	speed of light, $c = 2.9979 \times 10^8$ m/s
C_1	first radiation constant , $C_1 = 3.742 \times 10^8$ W μm^4 / m^2
C_2	second radiation constant , $C_2 = 1.1389 \times 10^4$ μm K
C_3	third radiation constant , $C_3 = 2897.8$ μm K
σ	Stefan-Boltzman constant, $\sigma = 5.6697 \times 10^{-8}$ W / m^2 K^4

Acronyms

CFT: Continuous Fourier Transform
CFRP: Carbon Fiber Reinforced Plastic
CCD: Charge Coupled Device
CMB: Cosmic Microwave Background
CMOS: Complementary Metal Oxide Semiconductor
DFT: Discrete Fourier Transform
EM: Electromagnetic
ERT: Early Recorder Thermogram
FPA: Focal Plane Array
FPN: Fixed Pattern Noise
FFT: Fast Fourier Transform
FT: Fourier Transform
GFRP: Glass Fiber Reinforced Plastic
IR: Infrared
IT: Infrared Thermography
LRT: Last Recorded Thermogram
LT: Lock-In Thermography
LWIR: Large Wave Infrared
MCT: Mercury Cadmium Tellurium
MWIR: Middle Wave Infrared
NDT&E: NonDestructive Testing and Evaluation
NIR: Near Infrared
PPT: Pulsed Phase Thermography
PT: Pulsed Thermography
SH: Step Heating
SfH: Shape from Heating
SNR: Signal-to-Noise Ratio
SWIR: Short Wave Infrared
TSR: Thermographic Signal Reconstruction
UV: Ultraviolet
VLWIR: Very Large Wave Infrared
VT: VibroThermography

Introduction

BACKGROUND

In numerous applications; from the production lines, where an acceptance/rejection criterion helps to speed-up the fabrication process *in situ*, to the characterization under more controlled environments of cultural heritage items such as frescoes and other antique art treasures; there is an increasing demand for *safety*, *i.e.* the insurance of production quality and maintenance [1]. Although destructive procedures are undoubtedly useful during the design stages, NonDestructive Testing and Evaluation techniques (NDT&E) are an invaluable inspection tool, since they allow to *…examine materials or components in ways that do not impair future usefulness…* [2]. NDT&E methods though, are required to be reliable, economical, sensitive, user friendly and fast. Moreover, the materials and processes are constantly evolving, hence the inspection technique should be adaptable as well [3].

Among the different NDT&E techniques that are in use nowadays, Infrared Thermography (IT) stands as an attractive tool for non-contact inspections whenever a thermal contrast between the scene (specimen) and the object of interest (subsurface defects) exists (assuming emissivity variations, reflections from the environment and atmosphere attenuations are negligible). If the scene and the object are in thermal equilibrium, an external stimulation source may serve to induce a difference in temperature; this is known as the active approach in IT. Pulsed Phase Thermography (PPT) [4] is a recent addition to the active field that combines interesting capabilities of two older approaches [5]: Pulsed Thermography (PT) and Lock-In Thermography (LT). In PT, acquisition (performed in stationary regime) is fast and 'simple' (when compared to LT) but defect characterization or *inversion* (*i.e.* the determination of the depth, thermal properties and/or defect size) is complex [6], [7]. On the contrary, inversion by LT is straightforward [8], but it requires a large number of tests at different modular frequencies (one for every inspected depth). For instance, the thermal diffusion length expressed by: $\mu=(2\alpha/\omega_b)^{1/2}$, can be used for depth retrieval by knowing the

thermal diffusivity α, and the modulation frequency at which the defect becomes visible ω_b, while diffusivity can be determined by knowing the sample thickness considering the frequency where the thermal wave reaches the opposite side of the sample [3].

The principal attraction of LT is the availability of amplitude and phase delay images or *phasegrams*. It is well-known [9] that phasegrams are less affected by reflections from the environment, emissivity variations and non-uniform heating. It has also been reported [10] that surface geometry has a less significant impact on phase than on thermal images, making phase an attractive tool in active thermal inspection.

In PPT, acquisition is performed as in PT, and phasegrams can be reconstructed as in LT, after performing the Fourier Transform (FT) on thermal data. Contrary to Lock-In Thermography however, several frequencies became available in a single PPT test, giving access to complete (discrete) phase profiles if sampling and truncation parameters are adequately selected (see below). Nevertheless, although a number of studies have proposed interesting inversion procedures using PPT (statistical methods [11], Neural Networks [12]) or PPT variations (Wavelet Transform [13]), none of these approaches was able to provide a practical quantitative inspection technique due to the required calibrations steps and lengthy computations.

In spite of the differences in the way data is acquired between PPT and LT (transitory vs. stationary), they both share the same kind of information, *i.e.* amplitude and phase. Inversion procedures should be possible by PPT based on the thermal diffusion length equation as is done by LT, and they are, as will be stressed in section 3.2. Nevertheless, an additional difficulty arises in PPT when trying to adequately establish the temporal parameters that will produce the desired frequency response. Indeed, the frequency components are inversely related to their temporal counterparts through the Discrete Fourier Transfrom (DFT). Hence, a change in the time domain will have an impact on the frequency

spectra. This relationship is known in Signal Processing theory as the Time-Frequency Duality of the DFT [14]. The decaying thermal profiles such as the ones encountered in PPT, are non-periodic, non-band-limited functions for which, an adequate time resolution Δt (*i.e. sampling* parameter) and truncation window size *w(t)* (*i.e. truncation* parameter), should be selected during the signal discretization process. Furthermore, these sampling and truncation parameters are both function of the depth of the defect and of the thermal properties of the specimen/defect system. Although it is possible to predict the minimum *w(t)* size for a particular configuration using computer modeling [15], no analytical solution is available for the determination of Δt. Nevertheless, interactive determination is possible by following some specific guidelines as discussed in section 2.5.3 and in reference [16].

In this research, the experimental and theoretical aspects of subsurface defect characterization by PPT are explored in detail. Special attention is devoted to establishing the potentials and limitations of PPT as a reliable depth retrieval technique. The objectives of this work are described next.

RESEARCH OBJECTIVES

The main objective of this research is to:

> *Develop and test a quantitative procedure for defect depth retrieval from phase delay data obtained by Pulsed Phase Thermography.*

In order to complete this task, a series of specific objectives are required and can be stated as, to:

1. Examine the fundamental concepts behind Active Thermography (Chapter 1);
2. Review the fundamental principles behind PPT, particularly the equivalence between the continuous and discrete Fourier Transform (Chapter 2);

3. Provide a critical review of the concept of Time-Frequency Duality of the Fourier Transform as applied to the problem of the thermal profiles found in Pulsed Thermography Chapter 2, section 2.4);

4. Develop an interactive methodology to determine the optimal sampling and truncation parameters as a function of the depth of the defects (Chapter 2, section 2.5);

5. Propose and test a depth inversion procedure for depth retrieval using the phase contrast concept (Chapter 3, section 3.2);

6. Extend the depth inversion method to take into account defect size variations on badly sampled data (Chapter 3, section 3.3);

7. Evaluate the performance of the proposed quantitative techniques on the inspection of complex shape specimens (Chapter 3, section 3.4);

8. Assess the impact of the observed variability of different parameters; such as sound area location, material's thermal properties, oversampling, time and frequency resolution; on depth inversion results (Chapter 3, section 3.5).

ORGANIZATION

This thesis is organized into 3 main chapters and 7 appendices. In Chapter 1, the place of IT in the NDT&E scene is first established. Some experimental concepts such as data acquisition, defect detection and non-uniform heating by active thermography, are then discussed as an introduction to the basic theory behind PPT, offered in Chapter 2.

Chapter 2.discusses the origins of PPT as an active technique, followed by a description of how the Fourier Transform is used to process data in PPT. A fundamental concept is then carefully reviewed, namely the equivalence between the continuous and the discrete Fourier Transform. The conditions for equivalency are considered and their importance for the correct interpretation of phase (and amplitude) results is emphasized. The Time-Frequency Duality of the DFT is thoroughly examined. Although, continuous-discrete equivalency and Time-Frequency Duality of the Fourier Transform, are well-known notions in the Signal

Processing field, the analysis provided in this work constitutes a major contribution to PPT theory. As will be pointed out in Chapter 3, deep understanding of these concepts is critical for quantitative analysis by PPT.

Finally, phase contrast and blind frequency are defined in Chapter 3 prior to the introduction of the depth inversion technique by TPP based on the phase. Two cases are considered: correctly and incorrectly sampled thermal data. Complex shape inspection is also considered and several experimental uncertainties related to the phase are discussed. ▣

Chapter 1. Active Thermography

There are rays coming from the sun… invested with a high power of heating bodies, but with none of illuminating objects…. The maximum of the heating power is vested among the invisible rays…. It may be pardonable if I digress for a moment and remark that the forgoing researches ought to lead us on to others [17].
Sir William Herschel (1738–1822), German-born British Astronomer.

In 1800 in Bath UK, William Herschel (1738-1822) reproduced Newton's experience[1] of passing sunlight through a prism to separate white light into colors. He measured the temperature of each color while holding three thermometers with blackened bulbs to improve heat absorption. He observed that temperature progressively increased from the violet end to the red end of the visible spectrum. He also noticed to his surprise that temperature increases further when he positioned the thermometer just beyond the red end.

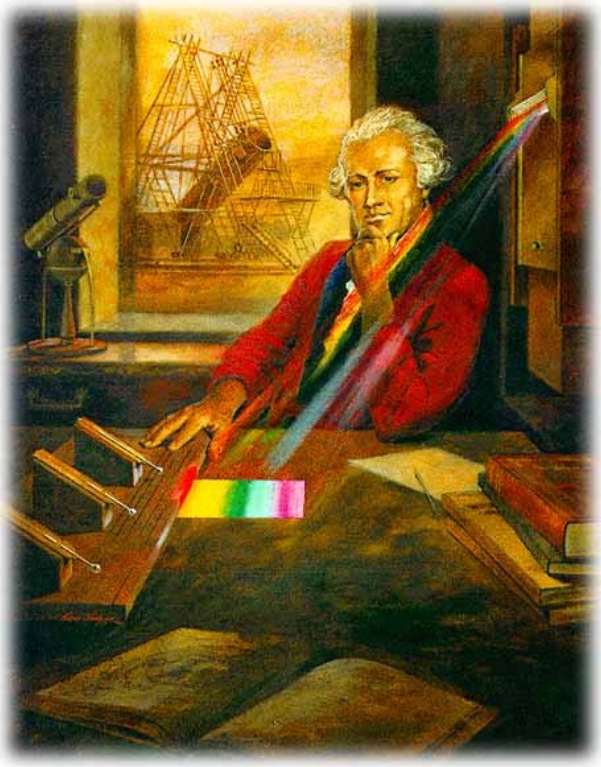

Figure 1.1. Sir William Herschel's experiment [18].

As is well known now, this invisible source of heat corresponds to the infrared part of the spectrum.►

1.1. Infrared Thermography in the NDT&E scene

NonDestructive Testing and Evaluation (NDT&E)[2] involves all inspecting techniques used to examine a part or material or system without impairing its usefulness [2]. The objective of a NDT&E technique is to provide information about (at least one of) the following parameters [2]: discontinuities and separations; structure; dimensions and metrology; physical and mechanical properties; composition and chemical analysis; stress and dynamic response; signature analysis; and abnormal source of heat.

There exists a wide variety of NDT&E techniques, none of which is able to reveal all the required information. The appropriate technique depends on the **thickness** and **nature** of the material being inspected, as well as in the **type of discontinuity** that must be detected. The National Materials Advisory Board (NMAB) *Ad Hoc* Committee on Nondestructive Evaluation adopted a classification system of 6 major categories [2]:

1. Mechanical-optical (Visual Testing);
2. Penetrating radiation (Radiographic Testing);
3. Electromagnetic-electronic (Eddy Current Testing, Magnetic Particle Testing);
4. Sonic-ultrasonic (Ultrasonic Testing);
5. **Thermal and Infrared (Infrared Thermography)**; and
6. Chemical-analytical (Liquid Penetrant Testing).

Information on the several techniques contained in these categories is abundant [5], [20], [21]. Infrared and Thermal testing involves temperature and heat flow measurements to predict or diagnose failure. IT is a nondestructive, non-contact and non-intrusive mapping of thermal patterns on the surface of the objects [2].

---

[1] Although Descartes, Robert Hooke and Edward Boyle among others scientists have used this technique before, Newton was the first to probe, in his *Experimentum Crucis* of 1665, that white light was made up of colors mixed together, and that the prism merely separated them [19].

[2] NDT&E can also be referred as NonDestructive Testing (NDT), NonDestructive Evaluation or Examination (NDE), or NonDestructive Inspection (NDI) [20].

1.1.1. The Infrared Thermography System

Figure 1.2 depicts the basic elements of an Infrared System: ❶ a thermal excitation source; ❷ a target; ❸ a radiometer (IR camera); ❹ a signal and image analysis system (PC); and ❺ the result (display). In addition, signal degradation is omnipresent at all stages.

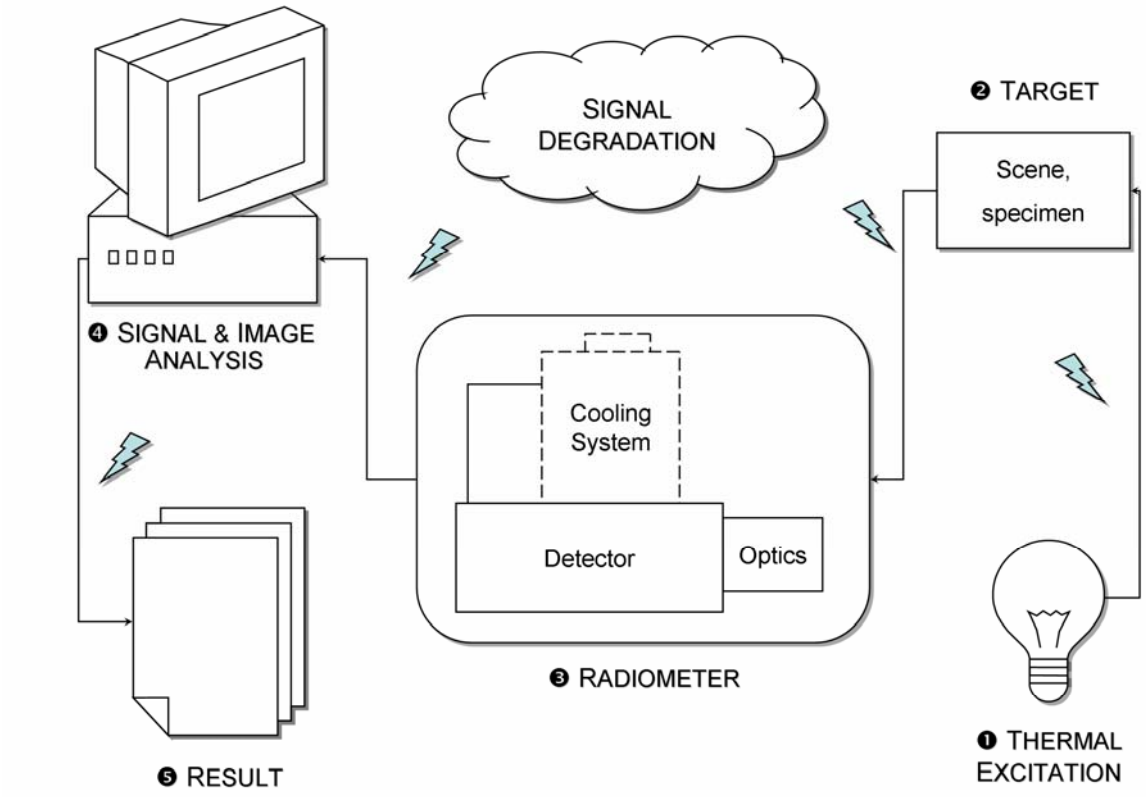

Figure 1.2. The IR thermal imaging system for NDT&E.

If a thermal gradient between the scene and the object of interest exist, the target can be inspected using the *passive* approach. However, when the object or feature of interest is in equilibrium with the rest of the scene, it is possible to create a thermal contrast on the surface using a thermal source ❶, this is known as the *active* approach in IT. Thermal excitation introduces *heat noise*, *i.e.* non-uniformities dues to imperfect heating. This is a well-known problem in active thermography (see section 1.2.6).

The target ❷ is the specimen or the scene of interest. It can be for example a subsurface flaw on a specimen or a gas leak in a complex scene. Regardless of whether the active or passive approach is used, IR signatures are weak when compared with other forms of radiation (as discussed in Appendix A and depicted in Figure A.2). The IR radiation measured by the radiometer results from the contribution of three different sources: the thermal energy emitted from the object; the energy reflected from the background; and the energy transferred through the material [22]. Additionally, the atmosphere attenuates the oncoming thermal signatures.

A radiometer (IR camera) ❸ captures the (weak and noisy) thermal signatures coming from the target. The principal components of a radiometer are (see section A.3): the optical receiver, the detector or detector matrix, and in some cases a cooling system. Here again, every element of the radiometer contributes to further degrade the signal, *i.e.* optical, electronic and electromagnetic noise (see section A.3.4). As a result, a data processing step ❹ is generally required.

Traditional and new IR image processing techniques are reviewed in references [23] and [24]. These techniques are intended to reduce noise at *pre* and *post* processing stages, to enhance image contrast and to retrieve useful information from the images. Finally, the resulting processed data must provide qualitative or quantitative outputs allowing to assess the conditions of the target ❺.

1.1.2. Conditions for using Infrared Thermography

The most important condition for IT to provide useful results is that a temperature difference or *thermal contrast* ΔT, exists between the feature of interest, *e.g.* people on a scene or an internal flaw on a specimen; and its surroundings, *e.g.* the scene or the specimen matrix. A second condition is to have the appropriate thermal imaging equipment to produce thermal images or *thermograms*. Thermal imaging apparatus is described in Appendix A, section A.3. In addition, it is

necessary to count with an experienced thermographer to interpret thermographic results.

The thermographer should have a basic knowledge of the radiation principles (Appendix A, section A.2), the fundamentals of heat transfer, the inspected material and/or process, and the equipment. Personnel qualification and certification standards (level I, II and III) for Infrared and Thermal Testing exists [2], indicating that human expertise is a critical part of the Thermography system. Analysis of raw thermal data is a qualitative inspection method relying on the training and experience of the thermographer.

Image processing techniques help on the completion of this task. The active approach is used on materials or systems that do not present significant differences in temperature with respect to their surroundings. Hence, for the active approach to be effectively applied, a fourth condition must be added, *i.e.* the thermophysical properties of the internal *defect* (*e.g.* voids, inclusions, etc.) have to be different from those of the specimen's material. Without this condition, no defect detection is possible.

Provided that these conditions are fulfilled, several techniques can be used. There are basically four techniques widely used in NDT&E, that differ from each other mainly in the way data is acquired and/or processed [5]: Pulsed Thermography (PT), Lock-In Thermography (LT), Step-Heating (SH) and Vibrothermography (VT). Pulsed Phase Thermography (PPT) can be thought as being a combination of PT and LT. Therefore, these two techniques are considered in this chapter prior to a formal presentation of PPT.

Next paragraph discusses some fundamental experimental concepts in PT, which, as will be noted below, they constitute the basis of any PPT experiment.

1.2. Pulsed Thermography (PT)[3]

1.2.1. Data acquisition

In PT, data acquisition and processing is carried out as depicted in Figure 1.3 and can be summarized as follows. First, energy sources (*e.g.* xenon flash tubes) are used to pulse-heat the specimen surface ❶. A cool pulse is also possible (*e.g.* ice, snow, air jet, thermoelectric effect, etc.). The duration of the pulse may vary from a few ms (~5-15 ms using flashes) to several seconds (using lamps), depending on the thermophysical properties of both, the specimen and the flaw.

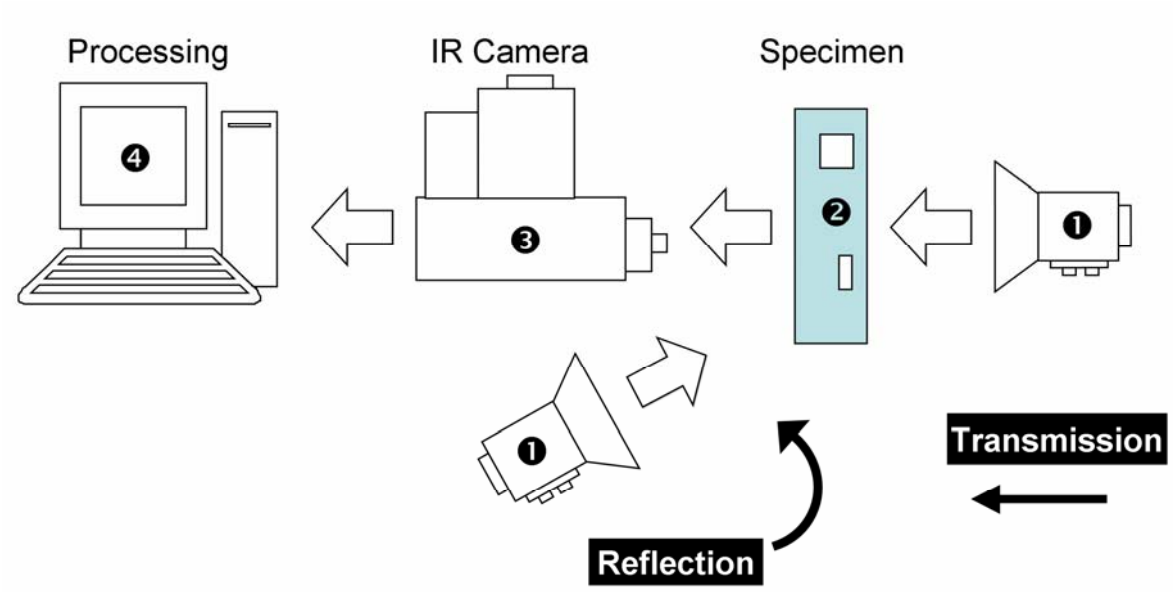

Figure 1.3. Experimental configuration in active thermography in reflection and transmission: ❶ Heat source, ❷ specimen, ❸ IR camera, and ❹ PC for data display, recording and processing.

The specimen is heated from one side while thermal data is collected either from the same side, *i.e.* **reflection mode**; or from the opposite side, *i.e.* **transmission mode**. Reflection is used when inspecting defects closer to the heated surface, whilst transmission is preferred for detecting defects closer to the non-heated

[3] Pulsed Video Thermography (PVT) [25], [26], Transient Thermography [27]-[29], Flash Thermography [30], Pulse-Echo Thermography and Thermal Wave Imaging [31]-[34] are also used.

surface (*i.e.* deeper defects). In general, resolution is higher in reflection and it is easier to deploy given that both sides of the specimen do not need to be available. Although deeper defects can be detected in transmission, depth information is loss since thermal waves will travel the same distance whether their strength is reduced by the presence of a defect or not [5]. Hence, depth quantification is not possible in transmission.

Defective zones will appear at higher or lower temperature with respect to non-defective zones on the surface, depending on the thermal properties of both the material and the defect ❷. The temperature evolution on the surface is then monitored in **transitory regime** using an infrared camera ❸. A thermal map of the surface or *thermogram* is recorded at regular time intervals. A 3D matrix is formed (see Figure 1.4a) where *x* and *y* coordinates are the horizontal and vertical pixel positions respectively, and the *z*-coordinate corresponds to the time evolution, in which the thermograms are separated Δt s from each other. The thermogram matrix in Figure 1.4a can now be processed ❹ using any of the techniques described in [23].

1.2.2. Pulsed Thermal Waves

The one-dimensional solution of the Fourier Equation for a Dirac delta function in a semi-infinite isotropic solid is given by [35]:

$$T(z,t) = T_0 + \frac{Q}{\sqrt{k\rho c_P \pi t}} \exp\left(-\frac{z^2}{4\alpha t}\right) \tag{1.1}$$

where Q is the energy absorbed by the surface [J/m^2] and T_0 is the initial temperature [K].

At the surface ($z=0$), Eq. (1.1) can be rewritten as:

$$T(0,t) = T_0 + \frac{Q}{e\sqrt{\pi t}} \tag{1.2}$$

where *e* is the effusivity.

This simple relationship characterizes the behavior of all homogeneous materials; the temperature decay curve is depicted in Figure 1.4b.

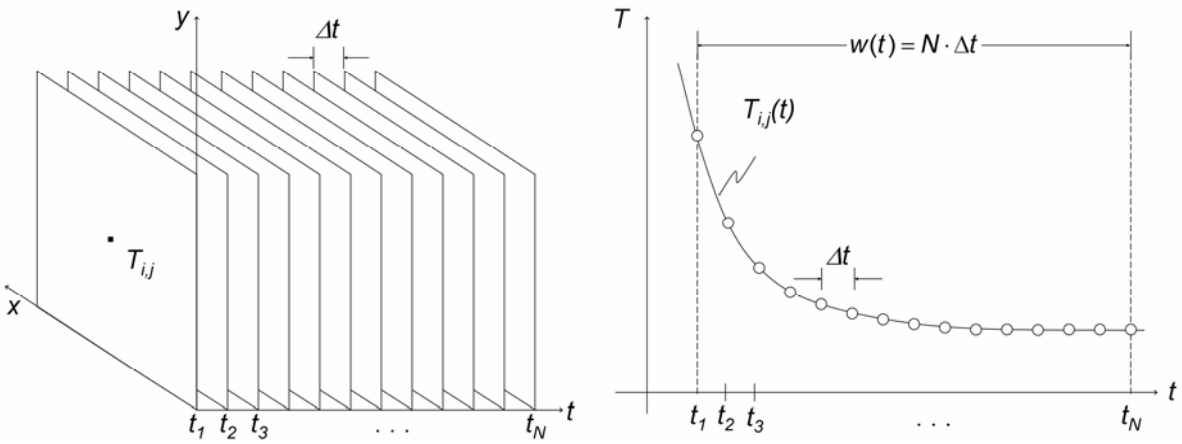

(a) **(b)**

Figure 1.4. (a) Temperature 3D matrix on the time domain, and (b) temperature profile for a non-defective pixel on coordinates (*i,j*).

Temperature profiles such as the one presented in Figure 1.4b, represent only the 'useful' fraction of the acquisition, *i.e.* the part that is going to be processed. The complete thermogram sequence contains in fact several other components as described next.

1.2.3. The complete thermogram sequence

The complete thermogram sequence is composed of 5 distinctive elements depicted in Figure 1.5. At time t_0, before heat reaches the specimen's surface, a *cold image* ❶ is captured. The cold image can be used to eliminate spurious reflections due to emissivity variations and to reduce fixed pattern artifacts (see FPN in Appendix A, section A.3.2). This is attractive for thermal data visualization and quantification although it is less useful when working with phase delay images

(see section 2.2.3). During (and shortly after) the application of a heat pulse, the acquired thermograms are temperature saturated ❷, *i.e.* the reading is out of the calibration scale and no accurate measure can be computed. The actual number of saturated thermograms depends on the sampling frequency and on the thermal properties of the material being inspected: low conductivity materials stay saturated longer than high conductivity materials, and more thermograms, saturated or not, will be recorded using high sampling rates. Saturated thermograms give no valuable information and therefore can be safely discarded from the processing stage.

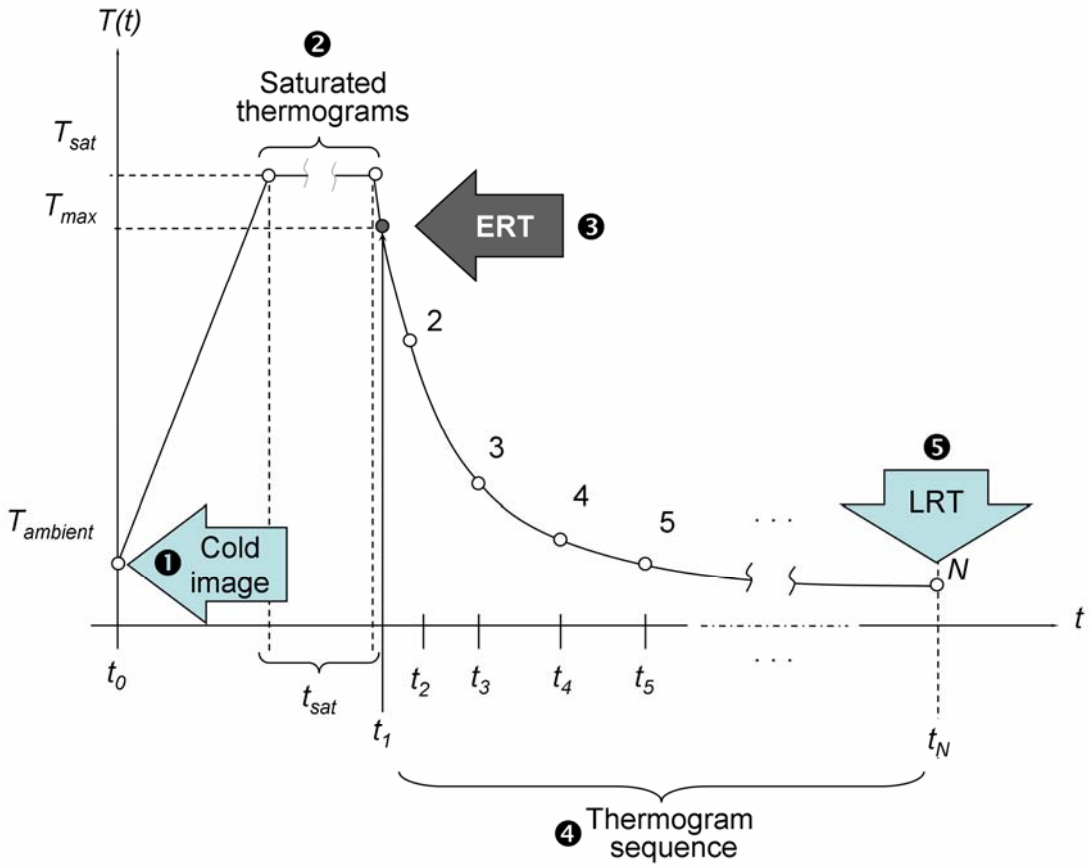

Figure 1.5. Complete thermogram sequence: ❶ cold image, ❷ saturated thermograms, ❸ ERT, ❹ thermogram sequence, and ❺ LRT.

The first useful thermogram that comes into sight after saturation is known as the *Early Recorded Thermogram* (ERT) ❸. Ideally, defects are still not visible on the

ERT, however, this condition is not always encountered in practice, especially when inspecting shallow defects on high conductivity materials using low sampling frequencies and/or when strong non-uniform heating is present. Normally, this situation does not constitute a problem for defect detection purposes. However, since depth is a function of time: $z \sim t^{1/2}$ [5], special care must be taken in order to perform quantitative analysis. Starting at the ERT at t_1, all subsequent thermograms are of interest for defect inspection and constitute the thermogram sequence ❹. The last acquired image at t_N ❺ corresponds to the *Last Recorded Thermogram* (LRT). From this point, temperature variations are considered negligible.

Deviation from the $t^{1/2}$ dependency on the useful part of the thermogram provides an indication of the presence of a defective area (see 1.2.4). This is in fact the basis for defect detection in active thermography as described next.

1.2.4. Defect detection

The temperature profile for a non-defective area (a pixel or the mean value of a pixel cluster) is a continuous non-periodical signal that decays approximately as the square root of time (Figure 1.4b). Figure 1.6 shows actual temperature profiles for a sound area (black continuous line) and for a 1 mm depth defective zone (black dotted line) from specimen PLEXI014. A semi logarithmic scale is used to increase visibility at the first instants. The sound area temperature decreases until stabilization is reached (ambient temperature). After that moment, temperature changes are negligible.

Temperature decay curves for both the defective and the sound areas behave similarly on the first instants after the application of heat since the heat front has not reached the defect yet. However, thermal effusivity *e*, which measures the material ability to exchange heat with its surroundings (see Appendix B, section B.3 and Table B.1), is 107 times greater for plastic than for air, *i.e.* Plexiglas® acts better than air as thermal sink.

Accordingly, once the thermal front has reached the defective area (air), surface temperature will be higher above the defective zone than above the sound area, from this moment to a given stabilization time.

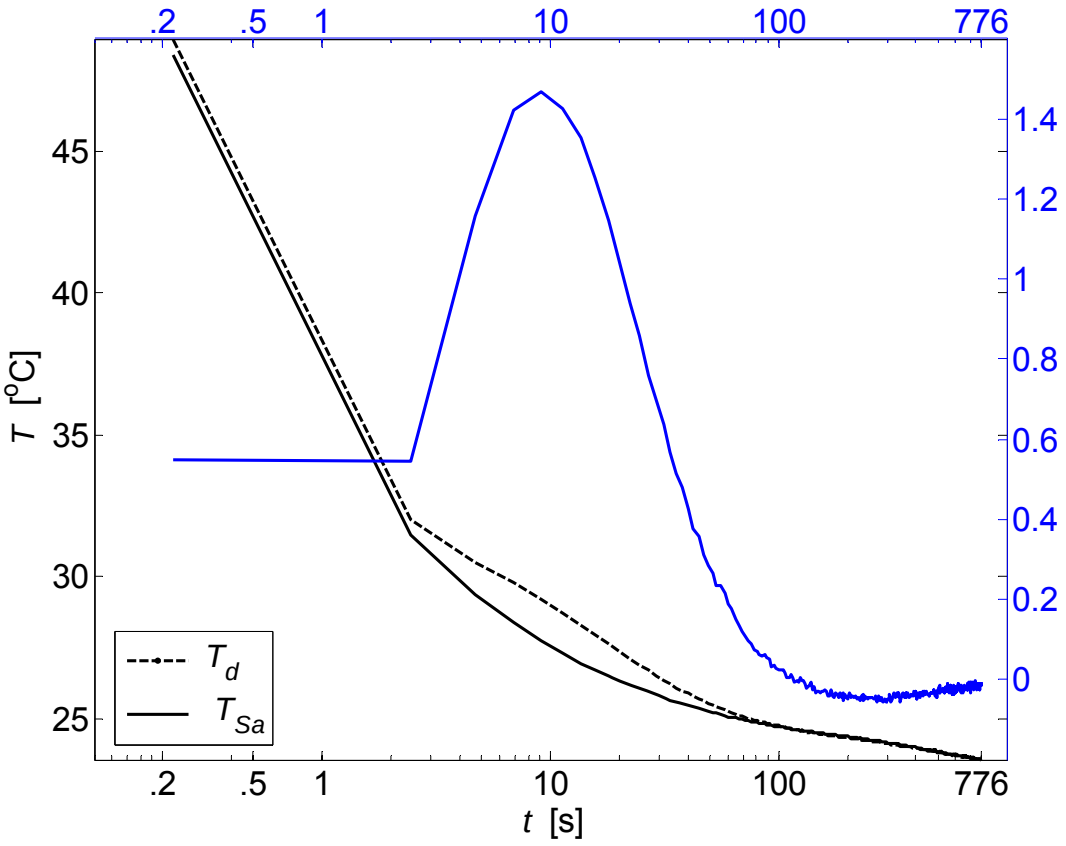

Figure 1.6. Defect detection from temperature profiles (sound area and defective zone) [36]. Temperature absolute contrast (T_d-T_{Sa}) is shown in blue. Data from a 1 mm depth flat-bottomed hole on specimen PLEXI014 (Appendix F.8), f_s=22.55 Hz, Δt=889 ms, $w(t)$=400 s. MatLab® script: `evolution.m`.

The defective temperature profile would be inverted if the flaw had a higher thermal effusivity than the specimen material. In either case, thermal contrast between defective and non-defective areas can be reconstructed as described next.

1.2.5. Absolute Thermal Contrast

Several data processing algorithms have been developed for defect characterization, *i.e.* determination of the size, depth and thermal resistance of a defect [6], [7], or for the evaluation of surface coatings [37]-[41]. Most of these techniques use thermal contrast calculations.

The basic definition of thermal contrast is the *Absolute Thermal Contrast*, which measures the difference between defective and non-defective regions [5]:

$$\Delta T = T_d - T_{Sa} \tag{1.3}$$

where T_d is the temperature of a defect, and T_{Sa} is the temperature measured at a (non-defective) sound area S_a. As summarized in [5], other thermal contrast definitions have been proposed to estimate the thermal contrast such as the Running Contrast, the Normalized Contrast and the Standard Contrast.

Figure 1.6 shows the absolute thermal contrast profile (in blue) calculated through Eq. (1.3). This simple operation is the departing point for more elaborated analysis. For instance, by locating the time and temperature values for which the thermal contrast is maximum for a pixel, it is possible to reconstruct Maximum Contrast (or Peak Contrast) *timegrams* and thermograms. It is also possible to use half the time of maximum contrast [42], the peak slope contrast [43] or the *early-time* contrast [44], *i.e.* the time at which thermal contrast begins, in order to reduce the impact of thermal diffusion. The idea is to compact the most useful information of the sequence in a single image.

Thermal contrast based analysis provide a good indication of defect characteristics (qualitative and quantitative) when working with relatively shallow defect in homogeneous materials and when non-uniformities at the surface are low (or can be corrected). However, as explained in next paragraph, the effect of non-uniform heating at the surface is always present at some extend.

1.2.6. Non-uniform surface heating

Non-uniform surface heating is an inherent source of uncertainty on active thermography. Even when a flat surface is inspected, several factors as heating source location, equipment aging, external heating or cooling sources, uneven optical properties of the surface, etc., will induce non-uniformities. Given that defect detection principle is based on temperature differences, non-uniform heating may produce confusion, especially for defect quantification.

Figure 1.7a shows the first available thermogram (or ERT, see section 1.2.3) at t=6.3 ms for an aluminum plate with 5 flat-bottom-holes at different depths. Only the shallowest defect (z=0.5 mm) is partially visible at this instant. Temperature should be the same at the first instant for an evenly heated plate. However, temperature disparities among these locations (more than 22°C difference!) are a clear indication of non-uniform heating.

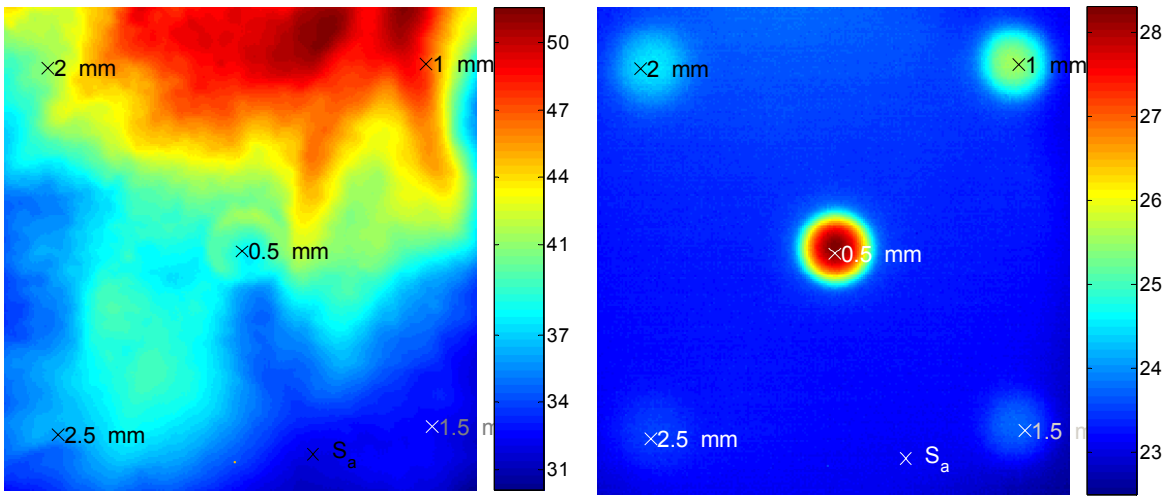

(a) **(b)**

Figure 1.7. Impact of non-uniform heating. Thermograms at (a) t=6.3 ms; and (b) t=25 ms showing defect locations. Data from specimen ALU002 in Appendix F.3 (f_s=157.83 Hz, Δt=50.3 ms, $w(t)$=6.3 s, N=250 frames).

Figure 1.7b presents another thermogram of the same sequence but at a later time (t=25 ms). Non-uniform heating is far less significant in this case, but is still present

as can be confirmed from Figure 1.8, which presents the thermal profiles of the defects and the sound area identified in Figure 1.7. As can be seen, a thermal gradient (~10°C) exists between locations at the first instant. For the aluminum-air configuration, surface temperature should be higher above the shallowest defects, since $e_{alu}=4{,}468e_{air}$, see Table B.1 in Appendix B. Accordingly, temperature profiles gradually recover their "corresponding" positions at later times. In this way, it can be noted that, temperature for the shallower defect (z=0.5 mm) is the highest at the second acquisition point (as it should be), while temperature drops sharply for the deepest defect (2.5 mm depth in red).

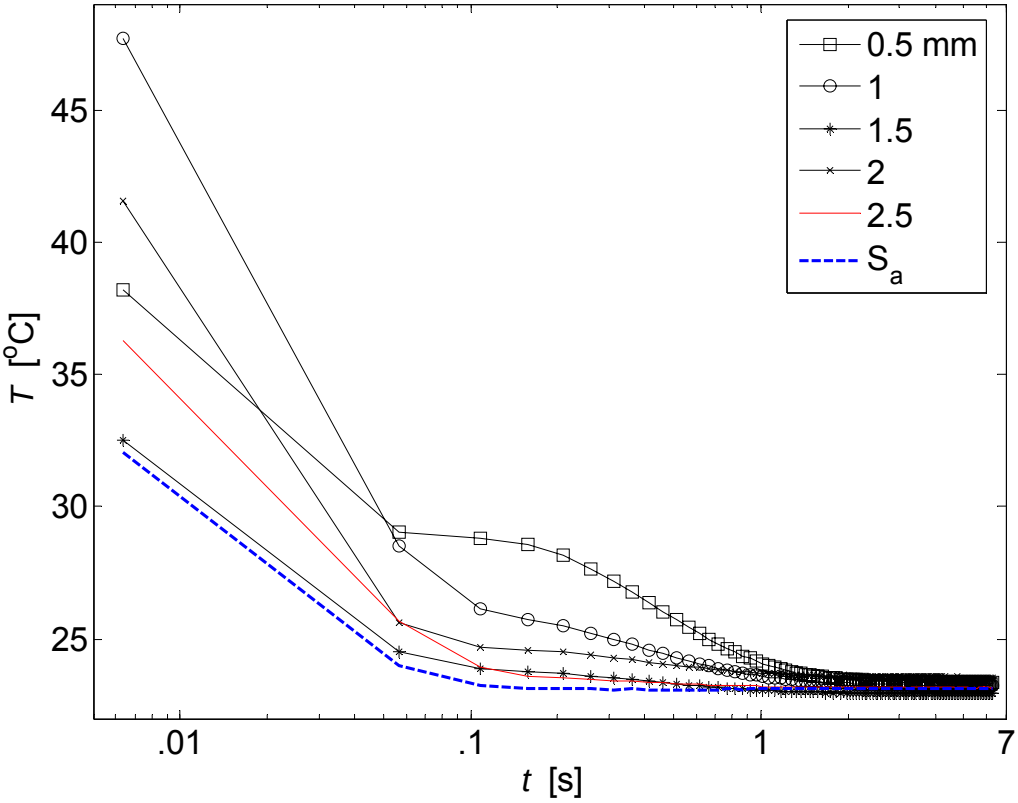

Figure 1.8. Thermal profiles for specimen ALU002 in Appendix F.3 (f_s=157.83 Hz, Δt=50.3 ms, $w(t)$=6.3 s, N=250 frames). MatLab® script: `evolution.m`.

Two additional observations can be made from Figure 1.8. First, thermal profiles for the 2 and 1.5 mm depth defects are inverted from the beginning to the end

(since temperature should be higher for shallower defects). In fact, with no additional information about the depth of the defects, Figure 1.7b might suggest that the defect identified as being at z=2 mm is in fact deeper than the one at z=1.5 mm. Thermal contrast is simply not high enough to correctly identify them. Secondly, there is a difference in the final temperature for each profile (up to 1°C), which is large enough to create uncertainty in the results. This situation is more likely to be due to an external cooling source during data acquisition (*e.g.* a ventilation fan) that cools down only part of the specimen. The impact of non-uniform heating is by far less significant on phase profiles (see Figure 2.5).

Finally, another major inconvenience of thermal contrast based methods must be noticed. The coolest surface area in Figure 1.7 was intentionally selected as sound area to increase thermal contrast with respect to defective zones. If a warmer region was selected, *e.g.* near the 0.5 mm depth defect, the sound area profile would be considerably different. This dependency on sound area location is a well-known problem of thermal contrast methods [43] and is further examined in section 3.5 for the case of phase contrast (see section 1.3.4).

It should be mentioned however, that an alternative solution has been proposed to overcome some of the problems mentioned above. The Differential Absolute Contrast (DAC) method [45], [46] estimates the sound area locally, assuming that on the first few images all points on the surface behave as a non-defective areas. DAC was originally developed as an interactive method requiring a minimum of user intervention but an automated algorithm is now available [47]. Besides of eliminating the need for a S_a definition, DAC has proven effective in reducing non-uniform heating effects.

Next paragraph presents a basic review of LT that will help on developing an inversion solution in PPT.

1.3. Lock-In Thermography (LT)[4]

1.3.1. Data acquisition

In LT, energy is delivered to the specimen's surface in the form of periodic thermal waves, several experiences must be performed to cover the entire specimen thickness. A high frequency is chosen for the first test (covering shallow defects) and then, frequency is progressively decreased until the entire thickness is included or the minimum available frequency of the equipment is set [8]. In addition, for an adequate measurement of the phase delay angle recorded at the surface, a permanent regime, in which no transient effect is present, needs to be attained each time, slowing-down the process even further. Furthermore, the maximum depth that can be detected is limited by the equipment's range of selectable frequencies. Ultrasound Lock-In Thermography is intended to solve this problem by selectively stimulating defective areas with acoustic waves [48], [49].

1.3.2. Periodic Thermal Waves

The Fourier's Law one-dimensional solution for a periodic thermal wave propagating through a semi-infinite homogeneous material may be expressed as [31]:

$$T(z,t) = T_o \exp(-\frac{z}{\mu})\cos\left(\frac{2\pi z}{\lambda} - \omega t\right) \tag{1.4}$$

where T_0 [°C] is the initial change in temperature produced by the heat source, ω [rad/s] is the modulation frequency ($\omega=2\pi f$, with f being the frequency in Hz), λ [m] is the wavelength; and μ [m] is the diffusion length given by [31]:

[4] Other designations that can be found in the literature referring to LT are Modulated Thermography [50], [51], Phase angle thermography [52], Photothermic Radiometry and Photothermal Thermography [53], [54].

$$\mu = \sqrt{\frac{2\alpha}{\omega}} = \sqrt{\frac{\alpha}{\pi f}} \tag{1.5}$$

where $\alpha=k/\rho c_P$ [m^2/s] is the thermal diffusivity, with k [W/m°C] being the thermal conductivity, ρ [kg/m^3] the density, c_P [J/kg°C] the specific heat; and f the thermal wave modulation frequency.

There are some advantages of using periodic heating instead of pulses (see Appendix C for a discussion on thermal waves). For instance, a relatively low power thermal wave can be used since energy is concentrated at a single frequency [37]. This is particularly attractive for the investigation of antique art treasures (*e.g.* frescos) [50]. However, what makes LT more attractive for NDT&E applications is related to the amplitude and phase delay properties as discussed in the following paragraph.

1.3.3. Amplitude and phase from LT

Amplitude and phase delay data are available when the periodic waveform is known [55]. For instance, as depicted in Figure 1.9, if the excitation I, and the signal response S, have both a sinusoidal form, amplitude and phase can be recovered from 4 data points per modulation cycle [56]:

$$A = \sqrt{(S_1 - S_3)^2 + (S_2 - S_4)^2} \tag{1.6}$$

$$\phi = \arctan\left(\frac{S_1 - S_3}{S_2 - S_4}\right) \tag{1.7}$$

where A is the amplitude and ϕ is the phase.

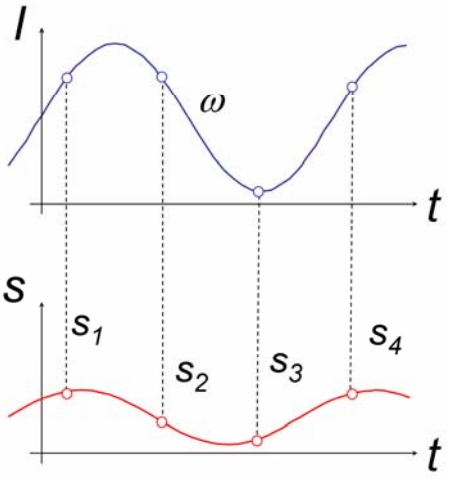

Figure 1.9. Amplitude and phase retrieval from a sinusoidal thermal excitation.

Investigations on amplitude and phase properties can be tracked back to the early studies of thermal wave imaging [9], [57], [58], [59]. These and more recent studies [55] [34], [56], [60] have pointed out the fact that phase is considerably less sensitive than amplitude to reflections from the environment [56], surface emissivity variations [59] and non-uniform heating [55]. Moreover, phase deeper probing capabilities were also noticed in all these works. The depth range z, for amplitude images is given by the thermal diffusion length equation $z \sim \mu$ [9], see Eq. (1.5). For the phase, reported values range from 1.5μ [60] to more than 2μ [9]. For these reasons, although amplitude images are sometimes of interest [61], the use of phase is more appealing in NDT&E especially for quantitative evaluation of materials since contrast changes at the defects can be more clearly observed compared with those in conventional thermal images [62] (as will be confirmed by comparing Figure 2.5a with Figure 1.7).

It is convenient to provide a formal definition for the phase contrast and the blind frequency before presenting the depth retrieval technique by LT.

1.3.4. Absolute phase contrast

Recalling from section 1.2.5, the absolute thermal contrast is defined as the surface temperature difference between a defective zone T_d, and a non-defective region or *sound area* T_{Sa} [5]: $\Delta T = T_d - T_{Sa}$. In a similar manner, a definition for the *absolute phase contrast* $\Delta\phi$, can be found in literature [63]:

$$\Delta\phi = \phi_d - \phi_{S_a} \tag{1.8}$$

where ϕ_d is the phase for a defective pixel, and ϕ_{Sa} is the phase value for a defined sound area.

The absolute phase contrast definition $\Delta\phi$, is used in combination with the blind frequency concept f_b, to solve inverse problems by LT (and by PPT as will be discussed in Chapter 3).

1.3.5. Blind frequency

In a similar manner as there exists an instant at which a defect at a particular depth is visible for the first time t_{early} [42], there is a limiting frequency at which the defect presents enough phase contrast to be detected on the frequency spectra. This frequency has been conveniently referred as the *blind frequency* f_b, [63], [64]. As is the case for temperature and time [5], phase holds a strong relationship with frequency that can be used for depth retrieval problems.

1.3.6. Quantitative Lock-In Thermography

Recent studies [1], [3], [8], [50], [51], [65], [66], propose to solve quantification problems through Eq. (1.5). For instance, depth inversion procedures are implemented with no trouble by knowing the thermal diffusivity of the material and the frequency where the defect becomes visible for the first time (*i.e.* the blind frequency, f_b [63], [64], see section 0):

$$z = C_1 \sqrt{\frac{\alpha}{\pi\, f_b}} = C_1 \mu \tag{1.9}$$

where α is the diffusivity of the material or sound area S_a, f_b is the blind frequency and C_1 is a correlation constant. From the discussion of paragraph 1.3.3, C_1=1 when working with amplitude data, whilst for the phase 1.5 < C_1< 2, with C_1=1.8 frequently adopted.

Some of these studies [8] (and references therein) and [51], considered defects having different size, thickness and thermal properties, with no reported effect on depth inversion results. The main effect of these three parameters is a change in phase intensity, the blind frequency f_b, which is the parameter used for retrieving the depth with the phase in Eq. (1.9), is less affected (see section 3.2).

Additionally, as reported in [3] and [66], diffusivity α, can be determined by knowing the sample thickness considering the frequency f_b, at which the thermal wave reaches the opposite side of the sample. To estimate f_b, a metallic ring is

positioned at the rear side of the sample while the frequency of the thermal wave excitation is varied on the front side until the ring is visible. The value is then introduced in Eq. (1.5), rearranged in the following manner:

$$\alpha = \pi \ f_b \left(\frac{L}{C_1} \right)^2 \tag{1.10}$$

where L is the (known) thickness of the sample and C_1=1.8 as before.

We end this chapter by summarizing some interesting characteristics of PT and LT in Table 1-1.

Table 1-1. Comparative characteristics of Pulsed and Lock-In Thermography.

	Pulsed Thermography	**Lock-In Thermography**
Heat source	Heat pulse	Periodic thermal waves
Regime	Transitory	Permanent
Advantages	• Fast • A single experience launches a series of thermal waves at several frequencies.	• Little impact of non-uniform heating, environmental reflections, emissivity variations and non-planar surfaces. • Low power thermal waves. • Depth inversion is straightforward
Disadvantages	• Inversion techniques are complex. • Affected by non-uniform heating.	• Requires a test for every inspected depth. • Slow: a permanent regime has to be reached

1.4. Summary

Infrared Thermography is an NDT&E technique that allows the non-contact inspection of systems and materials through a mapping of thermal patterns on the surface of the objects of interest. Defect detection principle in active thermography is based on the fact that a difference in thermal properties exists between the sound (non-defective) area and a defective region, which can be use for defect detection and quantification purposes.

Several thermographic techniques exist nowadays differing from each other mainly in the way data is acquired and/or processed. Pulsed Phase Thermography (PPT) can be thought as being a combination of Pulsed Thermography (PT) and Lock-In Thermography (LT). In one hand, data acquisition in PT is fast and allows the inspection of extended surfaces. However, non-uniformities of heating, emissivity variations, surface geometry and reflections from the environment have a great impact on thermal data. LT on the other hand, allows the reconstruction of phase images that are less affected by the problems mentioned above. Furthermore, depth quantification by LT is performed easily through the diffusion length equation. Nevertheless, long acquisition times constitute the principal drawback of LT, since a single experiment should be carried out for every inspected depth.

The idea behind PPT is to exploit the most interesting characteristics of both techniques, *i.e.* to perform data acquisition as in PT while being able to recover phase data as in LT. Next chapter describe the fundamentals of PPT.◄

Chapter 2. Pulsed Phase Thermography Reviewed

... cette pièce renferme les véritables equations différentielles de la transmission de la chaleur, soit à l'intérieur des corps, soit à leur surface: et la nouveauté du sujet, jointé à son importance, a déterminé la Classe à couronner cet Ouvrage, en observant cependant que la manière dont l'Auteur parvient à ses équations n'est pas exempte de difficultés, et que son analyse, pour les intégrer, laisse encore quelque chose à desirer, soit relativement à la généralité, soit mêmê du côté de la rigueur [67][5].
Judges (Lagrange, Laplace, Malus, Haüy, and Lacroix) comments on Fourier's 1811 essay.

In 1807, the French mathematician Joseph Fourier had completed his memoir *On the Propagation of Heat in Solid Bodies* and submitted it to the *Académie des Sciences* in Paris. The paper was at first rejected primarily because of Lagrang e disagreement on the use of the *Fourier Series*. Although Fourier was recognized with the Grand Prize in Mathematics of the Academy four years later after presenting a corrected version of his paper (for which he received a rather mixed set of remarks from the jury[5]), it was not until 1822 that his work *Théorie analytique de la chaleur* [68] was finally published. Fourier's work contained the ideas that would develop into what is now known as *Fourier Analysis* [67], [69].►

Figure 2.1. Jean Baptiste Joseph Fourier (1768-1830).

[5] … this piece encloses the real differential heat transfer equations, either inside the bodies, or on their surface, and the innovation of the subject, combined with its importance, have determined the Class to crown this Work, by observing however that the manner in which the author arrives at these equations is not exempt of difficulties and that his analysis to integrate them still leaves something to be desired on the score of generality and even rigor. [Free translation]

2.1. The link between PT and LT

As explained in Chapter 1, Pulsed Phase Thermography can be though as being the link between Pulsed and Lock-In Thermography given that it combines interesting features from both techniques. Table 1-1 in Chapter 1 enumerated the advantages and disadvantages from both techniques. Figure 2.2 depicts the basic differences in configuration.

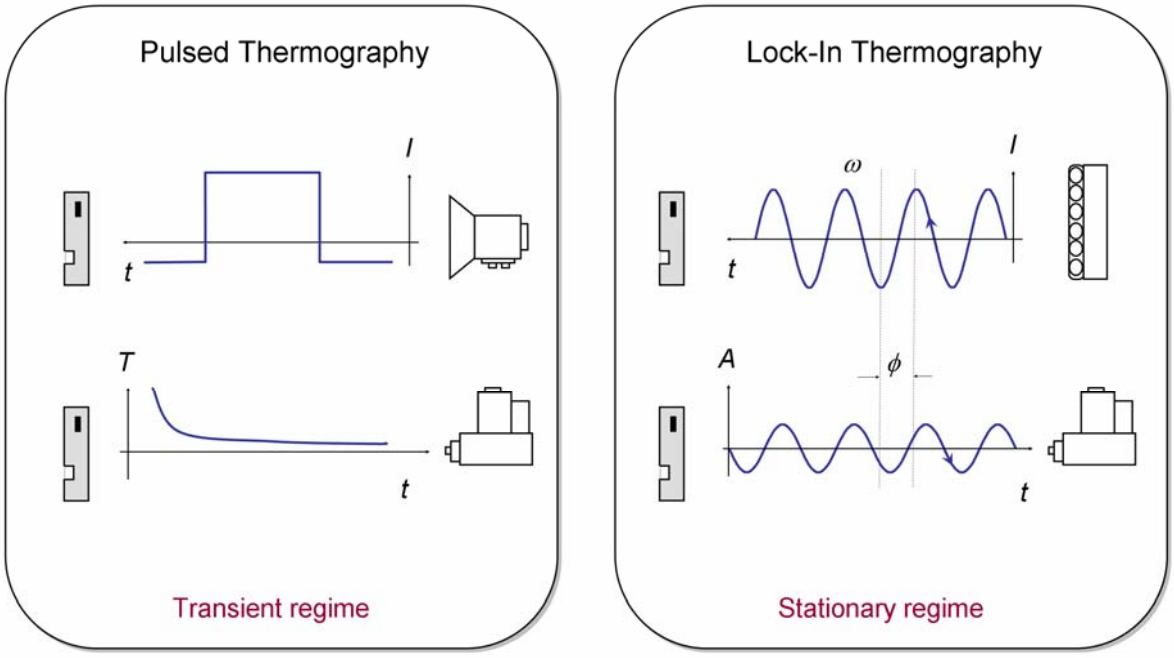

Figure 2.2. Experimental configuration: PT vs. LT.

On one hand, PT uses a thermal pulse recording the thermal evolution in transient regime. Experiments carried out under this configuration are straightforward. On the other hand, LT requires specialized equipment (sinusoidal heating source and lock-in amplifier), but depth quantification is straightforward through the diffusion length equation discussed in section 1.3.6.

Although not evident at first sight, a link between PT and LT can be established through the superposition principle [70]. It is well-know that any wave form, periodic or not, can be approximated by the sum of purely harmonic waves oscillating at different frequencies (see Appendix C.3). Figure 2.3 can help to explain this idea.

The pulsed forms on the left side (square and thermal decay) can be approximated by a sum of sinusoids (only three harmonics are included for simplicity) with frequencies ranging from 0 to ∞.

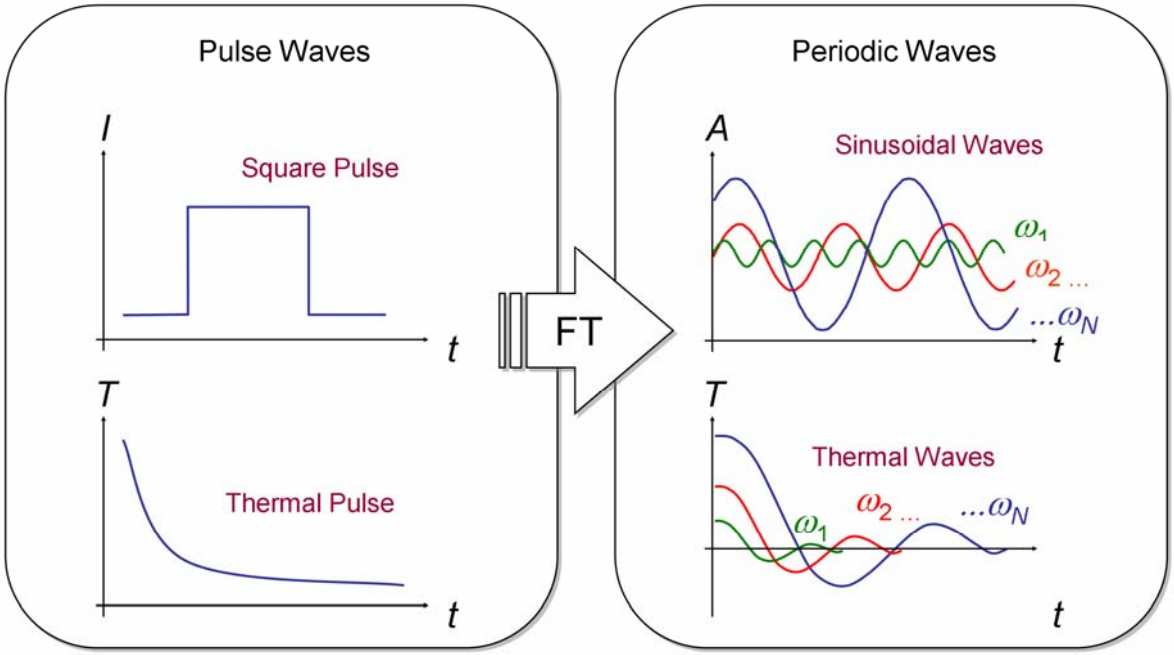

Figure 2.3. Experimental configuration: PT vs. LT.

In practice, actual frequencies (minimum, maximum), as well as frequency resolution, depend on equipment limitations as well as on sampling and truncation parameters as will be explained in Chapter 2. Hence, it is possible to extract a certain number of thermal waves from a thermal pulse, each one having a different frequency, amplitude and phase delay, though a transformation algorithm such as the Fourier Transform. As discussed in Chapter 1 and Appendix C, solutions for the temperature evolution at the surface on both pulsed and periodic thermal waves can be derived from the Fourier's Law.

In PPT, thermal data is processed with the Fourier Transform (FT) and is discussed next.

2.2. Processing with the Fourier Transform

2.2.1. The Continuous Fourier Transform

The Fourier Transform (FT), or more properly the Continuous Fourier Transform (CFT)[6] can be derived by representing the complex Fourier integral as a sum of exponential functions [14], [71]:

$$F(f) = \int_{-\infty}^{\infty} f(t) \cdot e^{(-j2\pi ft)} dt \tag{2.1}$$

where j^2=-1.

Although the CFT constitutes an invaluable tool in the analytical formulation of a solution, the Discrete Fourier Transform (DFT) is usually preferred when working with sampled signals for the actual implementation of the solution.

2.2.2. The Discrete Fourier Transform

The DFT can be derived by discretizing both time and frequency, that is [4], [14], [72], [73]:

$$F_n = \Delta t \sum_{k=0}^{N-1} T(k\Delta t) \exp^{(-j2\pi nk/N)} = \mathrm{Re}_n + \mathrm{Im}_n \tag{2.2}$$

where n designates the frequency increment (n=0,1,…N); Δt is the sampling interval; and *Re* and *Im* are the real and the imaginary parts of the transform, respectively.

---

[6] As noted at the beginning of this chapter, Joseph Fourier used the Fourier series while working on a solution for the heat conduction equation. Besides of being very practical on solving ordinary partial differential equations (such as the heat equation), Fourier series allow to represent general periodic functions from a summation of sine and cosine terms. This idea can be extended to include non-periodic signals using Fourier Integrals. The main interest of Fourier Integrals is as a tool in solving ordinary differential equations but they can also be used when discussing functions defined by integrals, *i.e.* Integral Transforms. The two most important integral transforms of this kind are (by far) are the Laplace Transform and the Fourier Transform [71].

The sampling interval Δt, is introduced in Eq. (2.2) as a scale factor in order to produce equivalency between CFT and DFT [72]. For NDT&E applications, Eq. (2.2) is not practical due to lengthy computations. The Fast Fourier Transform (FFT) algorithm [74], available on software packages such as MatLab®, greatly reduces the computation timing and is therefore privileged.

2.2.3. Amplitude and phase from PPT

Real and imaginary parts of Eq. (2.2) can be used to calculate the amplitude and the *phase delay* (the *phase angle* or simply the *phase*) of the transform and to reconstruct 3D matrices as illustrated in Figure 2.4.

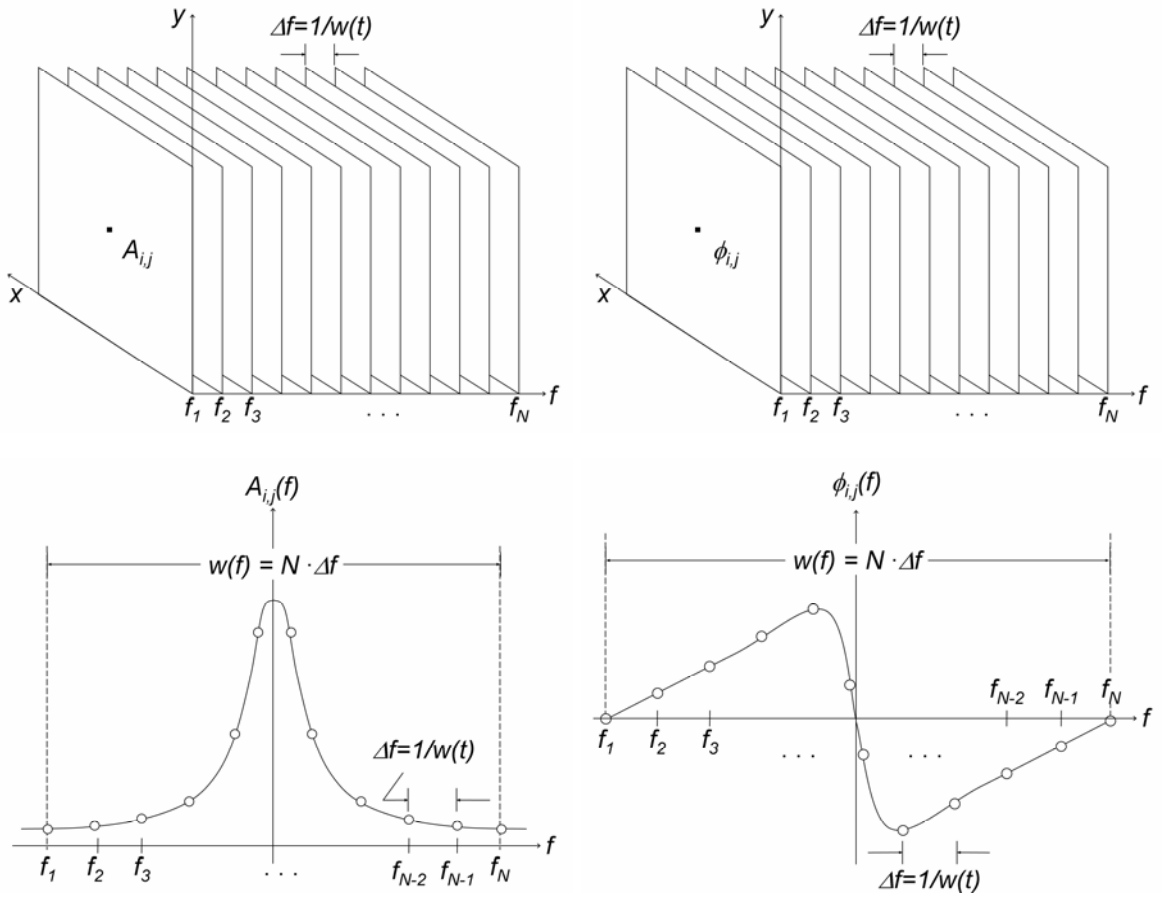

(a) **(b)**

Figure 2.4. (a) Ampligram; and (b) phasegram sequences (top) and their corresponding profiles on the frequency spectra for a non-defective pixel on coordinates (*i,j*) (bottom).

From Eq. (2.2), *modulus* or amplitude A, and phase delay ϕ, discrete values are available as follows:

$$A_n = \sqrt{\mathrm{Re}_n^2 + \mathrm{Im}_n^2} \quad \text{and} \quad \phi_n = \tan^{-1}\left(\frac{\mathrm{Im}_n}{\mathrm{Re}_n}\right) \tag{2.3}$$

Hence, matrices illustrated in Figure 2.4 can be obtained by applying Eq. (2.3) on every pixel of the thermogram sequence in Figure 1.4. Temperature profiles, as the one shown in Figure 1.4b, are *real* functions that produce a transform with an *even* (or symmetrical) real part and an *odd* (or anti-symmetrical) imaginary part. This kind of function is referred as *Hermite* function [73]. As seen in Figure 2.4, the symmetry properties of a Hermite function are reflected on the amplitude and phase of the transform, which are even and odd, correspondingly, with respect to f=0 Hz (*i.e.* $n=N/2$). Therefore, from a sequence of N thermograms, there are $N/2$ useful frequency components; the other half of the spectra only provides redundant information. Negative frequency data can thus be safely discarded.

2.2.4. Phase response to non-uniform heating

Figure 2.5 shows the phase profiles for an aluminum plate (specimen ALU002 in Appendix F.3) with 5 flat-bottomed holes. The corresponding temperature profiles were presented on Figure 1.8. As explained in section 1.2.6, non-uniform heating has a great impact on temperature profiles. Quantification using thermal data would be difficult to accomplish in these conditions. Phase on the other hand, is practically unaffected by non-uniform heating. Even if temperature profiles are practically stable shortly after 1 s of acquisition (see Figure 1.8), a larger truncation window was used, *i.e.* $w(t)$=6.3 s, to increase frequency resolution. This is done however in detriment of early time temperature data since a larger time step had to be used to reduce the total number of frames (N=250 in this case). Judging from the phase profiles in Figure 2.5, non-uniform heating has no significant impact on phase, since phase profiles are correctly distributed from the shallowest to the deepest. The impact of the missed thermal data is however reflected on the 2.5

mm depth defect phase profile (and on phase contrast profile in Figure 2.6), which does not show an inflexion point as the rest of the profiles, it resembles more to the sound area phase profile.

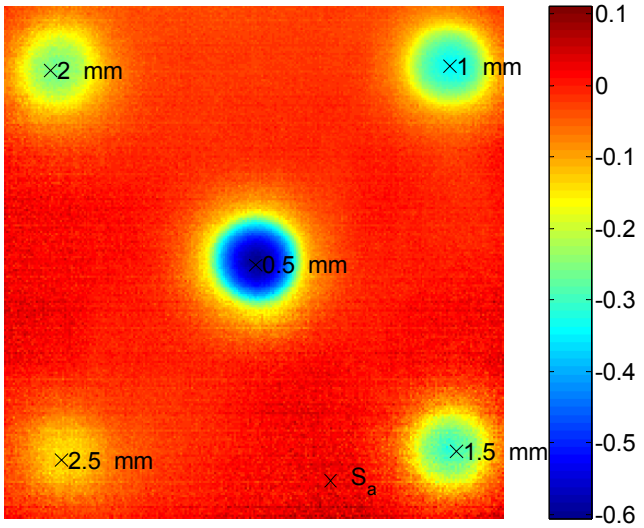

(a)

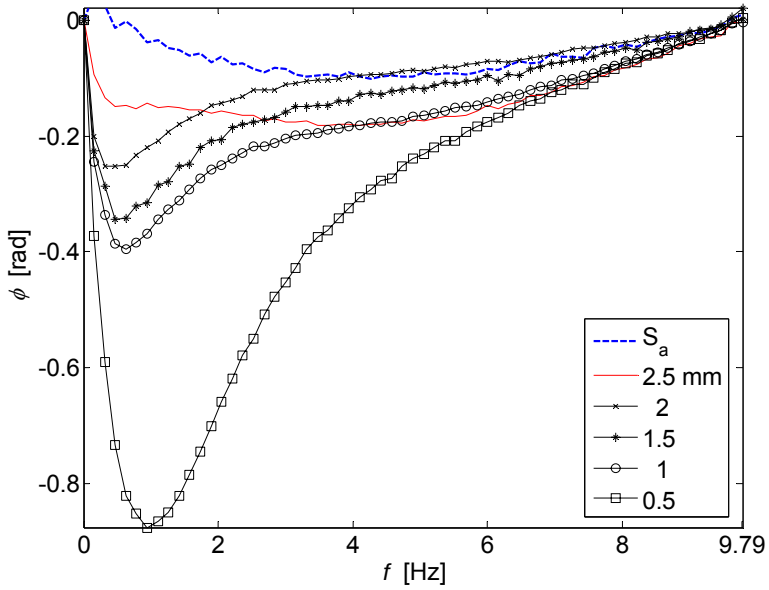

(b)

Figure 2.5. Phase response to non-uniform heating. (a) Phasegram at f=0.47 Hz; and (b) phase profiles for the 5 defects and the sound area. Data from specimen ALU002 in Appendix F.3 (f_S=157.83 Hz, Δt=50.3 ms, $w(t)$=6.3 s, N=250 frames). MatLab® script: `ppt.m`, `evolution.m`.

The selected f_s was not fast enough to capture all the temperature information to characterize the deepest defect on the frequency spectra. Using a higher sampling rate should fix this problem.

2.2.5. Phase contrast from PPT data

The absolute phase contrast for LT data was defined by Eq. (1.8) in section 1.3.4, *i.e.* $\Delta\phi=\phi_d-\phi_{Sa}$. This definition can be use for data coming from PPT data as well. Figure 2.6 shows the absolute phase contrast profiles from data in Figure 2.5b.

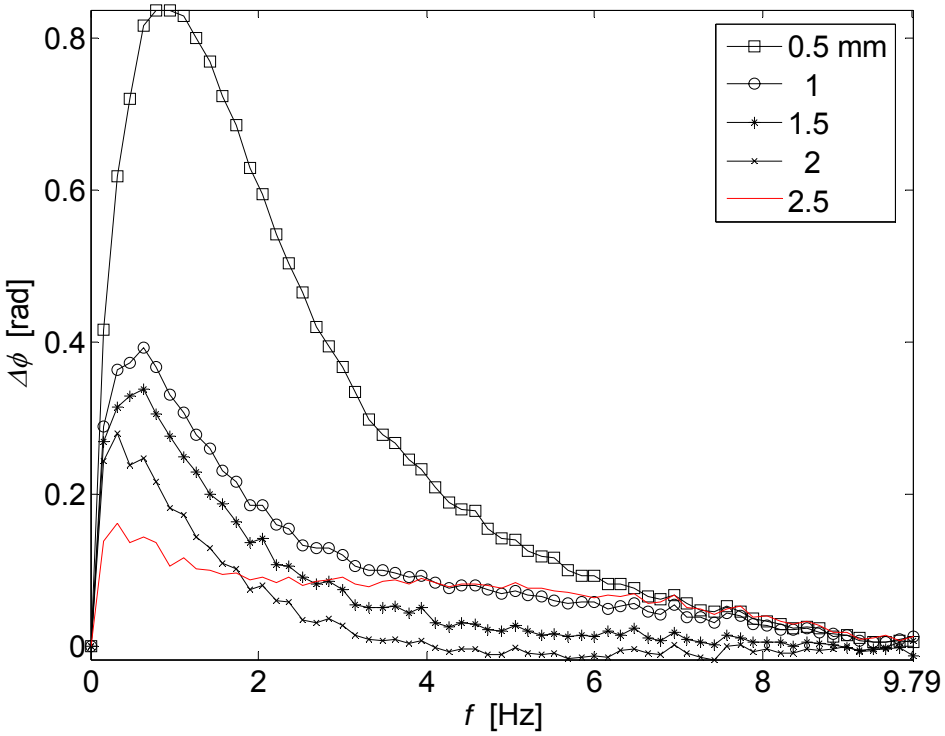

Figure 2.6. Phase contrast profiles reconstructed from data in Figure 2.5b.
MatLab® script: `evolution.m`.

Phase contrast computation will be very useful for determining the blind frequencies, which constitutes the first step of the depth retrieval procedure that is proposed in Chapter 3.

Next paragraph reviews the basic concepts that need to be addressed in order to correctly represent a continuous signal using discrete data.

2.3. Equivalence between CFT and DFT

Strictly speaking, equivalence between CFT and DFT requires compliance with the following conditions [72]:

1) the temporal function is **periodic**;
2) the frequency function is **band-limited**;
3) the **sampling theorem** is respected; and
4) the **truncation window** is non-zero over one (or integer multiple) period of the temporal signal.

The temperature profiles encountered on transient active thermography can be classed as general non-periodic signals that are neither *time-limited* (they are continuous) nor *band-limited*. Application of the DFT on this class of functions will inevitably introduce *aliasing* because of sampling, as well as *leakage* and *rippling* as a result of truncation. Nevertheless, good agreement between CFT and DFT can still be obtained. In fact, it can be demonstrated that by an appropriate selection of the acquisition parameters, DFT is a special case of the CFT [14], [72]. A brief discussion of these 4 conditions follows with help of Figure 2.7.

2.3.1. The Sampling Theorem

According to Shannon's Sampling Theorem [14], a continuous function, as in Figure 2.7a$_1$, can be completely recovered from the sampled data, *i.e.* no aliasing is produced, provided that a sampling frequency f_s, of at least twice the maximum available frequency, *i.e.* the *critical* or *Nyquist* frequency f_c, is used:

$$f_s \geq 2f_c \tag{2.4}$$

As demonstrated in [12], the selection of an adequate sampling frequency is critical for quantitative inspection, especially for high conductivity materials, requiring high sampling rates. If the sampling rate is too slow, signal degradation may be

amplified [75]. An inherent idealized condition for the application of Shannon's Sampling Theorem is that the input waveform is *band-limited*. This concept is reviewed next.

2.3.2. Band-limitedness

The Sampling Theorem requires that the function to be sampled is bandlimited, *i.e* it is zero above the Nyquist limit, f_c [14]:

$$F(f) = 0 \quad for \quad |f| \geq f_c \tag{2.5}$$

This situation is depicted in Figure 2.7c_1. In this case, the continuous function can be uniquely determined from knowledge of its sampled values. As a matter of fact, it can be demonstrated that, for band-limited functions sampled at twice the Nyquist limit, the DFT is actually a special case of the CFT [14], [72]. Unfortunately, real world signals, such as temperature decay profiles, are never band-limited. Sampling *non-band-limited* functions will unavoidably introduce aliasing. In spite of this, aliasing can be minimized to acceptable levels by complying with the Sampling Theorem [76].

In the first column of Figure 2.7, a graphical representation of the sampling process is depicted as the multiplication of the continuous temperature profile *T(t)*, in Figure 2.7a_1 by the sampling (or *Shah*) function $III_1(t)$, resulting on the discretized signal in Figure 2.7a_2. This time-domain operation produces a periodic frequency response as the continuous amplitude *A(f)* (Figure 2.7b_1) or phase $\phi(f)$ (Figure 2.7c_1) signals are convolved with the sampling function $III_1(f)$, resulting on the periodic continuous signals in Figure 2.7b_2 and Figure 2.7c_2, for amplitude and phase, respectively.

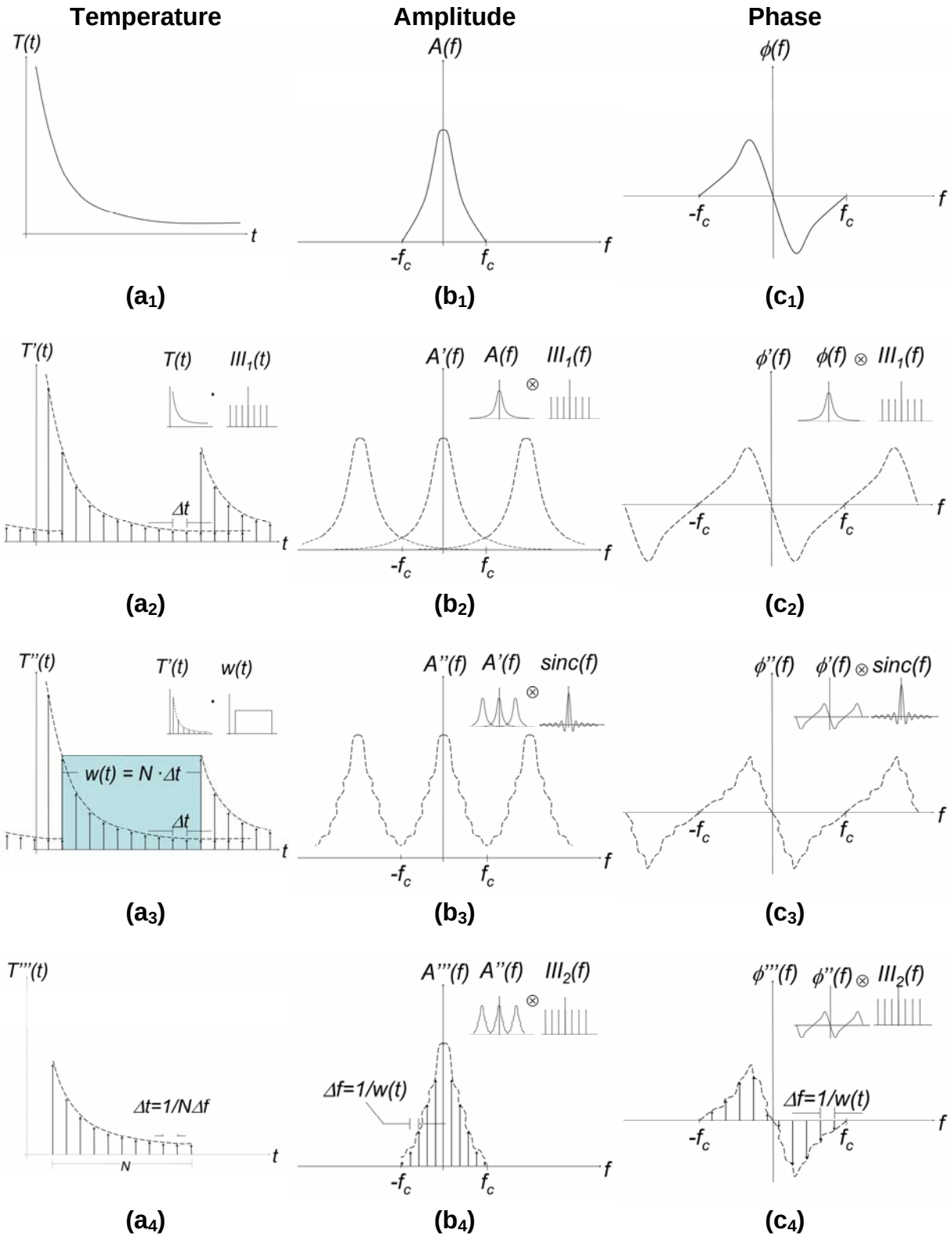

Figure 2.7. Sampling and truncation applied to thermal decay profiles.

2.3.3. Truncation and rippling

Once the continuous thermal signal has been sampled, both the beginning and the end of the acquisition sequence must be selected. This procedure is called *truncation* [14]. The analysis is then restricted over a finite number of images *N*, equally spaced by a time interval Δt, over one period of the time $N\Delta t$.

Truncation in the time domain may be seen as the multiplication of the signal by a rectangular window *w(t)*. The corresponding operation in the frequency spectra is to convolve the frequency response with the *sinc* function (see Figure 2.8), introducing in this way a *ripple effect* in the Fourier Transform, *i.e.* amplitude and phase signals are distorted with small undulations as depicted in Figure 2.7b_3 and Figure 2.7c_3.

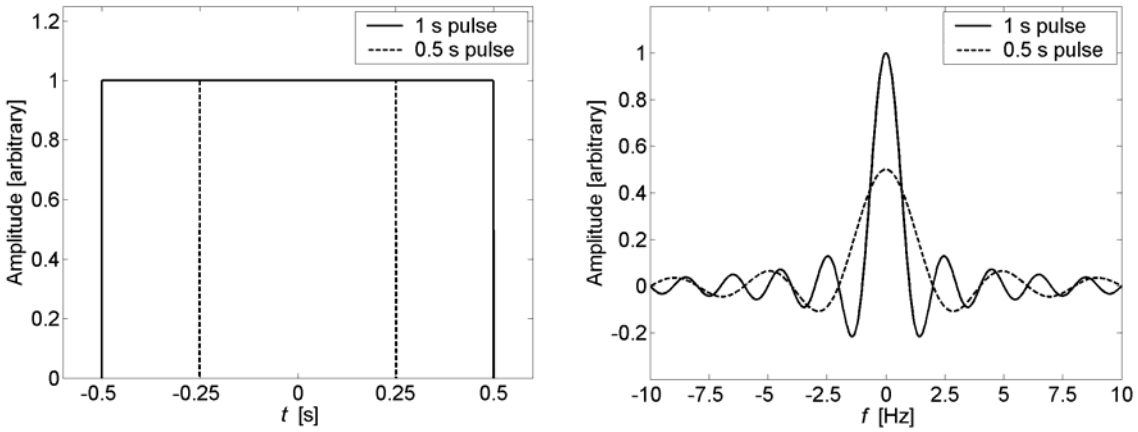

Figure 2.8. The Similarity Theorem. MatLab® script: `similarity.m`.

Recalling the Similarity Theorem [14], illustrated in Figure 2.8; as the size of a rectangular function is increased, its frequency response will approximate more and more to an impulse. Consequently, less rippling will be added to the transform if a larger *w(t)* is used. Ideally, the truncation window should be as long as possible, though buffer capacity may considerably restrict its size. The sampled temperature profile *T'(t)*, is truncated with a square window *w(t)*, in Figure 2.7a_3; producing the rippled continuous amplitude and phase responses in Figure 2.7b_3

and Figure 2.7c_3, respectively. Sampling in the time domain results in a periodic function on the frequency spectra and vice-versa [14]. Hence, to cover only the frequency range of interest ($|f| \leq f_c$), it is common practice to spread the N sampled points evenly across one cycle of the amplitude or phase signal. The final results are shown in Figure 2.7a_4, b_4 and c_4.

2.3.4. Leakage

Truncating the temporal signal at other than a period or a multiple of the period produces sharp changes in the time domain. Consequently, additional frequency components or *side-lobes* result in the frequency domain. This effect is called *leakage* [72]. Leakage can also be considered as a form of aliasing. Since the original function is non-band-limited, even if the Sampling Theorem is respected, aliasing would still be present as a combined result of leakage and ripple effects. The most that can be done to reduce leakage is to use larger *w(t)*, and to minimize ripple effects would be to sample even faster. Another possibility is to use a truncation function with smaller side-lobe characteristics than the *sinc* function. There are several of these so called *apodization functions* that could be used [77]. The price to pay is a reduction in resolution. The Hanning function has been cited as an acceptable compromise between side-lobe minimization and resolution [72].

Nevertheless, leakage is minimal in the case of the thermal profiles typically found in NDT&E since there are no sharp changes present. Instead, temperature at the surface monotonically decays with time. Hence, acceptable results are obtained using a rectangular window.

During the sampling process, the continuous temperature signal *T(t)*, is sampled at a given time resolution Δt, and truncated with a rectangular window *w(t)*, as depicted in Figure 2.7. The choice of Δt and *w(t)* in the time domain, is intimately related to the frequency response (frequency resolution and maximum available frequency) through the DFT. This Time-Frequency Duality [73] is discussed in detail in the next paragraph.

2.4. Time-Frequency Duality

Section 2.3 provide us with some important guidelines that should be follow to assure the equivalency between the continuous and discrete Fourier Transform. Special attention must be taken in order to establish *how fast* and for *how long* the continuous temporal signal needs to be sampled, since as will be discussed in this chapter, time and frequency are intimately related through the Fourier Transform. This is known as the Time-Frequency Duality. However, the sampling rate and the truncation window size depend on the inspected depth (among other factors), which complicates their estimation. Fortunately, it is possible to estimate this factors through an interactive procedure as will be discussed in section 2.5. It is convenient to further examine the role of the acquisition, sampling and truncation parameters on a PPT experience before presenting this interactive methodology.

2.4.1. Acquisition parameters

The first parameters that need to be determined in any PPT experience are the frame rate f_s, and the acquisition time t_{acq}. These two parameters are intimately related and are limited by the maximum storage capacity of the IR system: $N_{max}=f_s \cdot t_{acq}$. Appropriate selection of f_s primarily depends on the thermal properties of the specimen. In general, high conductivity materials require a faster f_s (to avoid loss of information), but lower t_{acq} (given that thermal variations ends more rapidly) than poor thermal conductors. Thermal modeling [80], [81] may be useful as a first step on deciding the f_s value. Other factors such as defect-to-sound area diffusivity ratios, and equipment limitations, will as well have an influence.

Proper selection of the acquisition parameters, f_s and t_{acq}, is critical to minimize error in reproducing the real continuous signal. As acknowledged in [15], thermal data capture should begin before heat reaches any defect and it should end after all thermal contrast signals become negligible. A simple guideline is to verify (when possible) that the LRT is at (nearly) the same temperature as the cold image, *i.e.* at room temperature. In this way, spacing between thermograms may be optimized with the maximum leakage reduction.

2.4.2. Sampling and truncation parameters

The maximum time resolution corresponds to $\Delta t=1/f_s$, and the maximum window size is $w(t)=t_{acq}$, though in most cases, thermal data acquired in such conditions contains much more information that what is actually required at PPT processing stages as will be stressed in paragraph 2.5.3. The width of the truncation window $w(t)$, is given by [73]:

$$w(t) = N\Delta t \tag{2.6}$$

Hence, sampling requires that specific values for two of the following three parameters are established: the size of the truncation window $w(t)$, the total number of points that are going to be sampled N, and the spacing between them Δt. Once the parameters on Eq. (2.6) are selected for the time domain, the frequency spectra counterparts are defined as well (see Table 2-1). For instance, the sampling rate is given by [73]:

$$f_s = N\Delta f = \frac{1}{\Delta t} \tag{2.7}$$

Therefore, N points should also be used to compute the transformation, since more points would introduce redundancy, and fewer points would not take advantage of all the available information [73]. However, as stated before (section 2.2.3), only half the spectra needs to be conserved, reducing the total number of frequency components to $N/2$. Moreover, because of the periodicity requirements for the CFT-DFT equivalency (section 2.3), calculations must be confined to cover only one period of the frequency spectra. In such a case, we should evenly spread the $N/2$ point over one cycle centered upon the origin. The $N/2$ frequency components are separated Δf from each other, where [73]:

$$\Delta f = \frac{1}{N\Delta t} = \frac{1}{w(t)} \tag{2.8}$$

From Eq. (2.8), frequency domain sample spacing Δf, is inversely related to the width of the time domain truncation window *w(t)*, and to the time domain sample spacing Δt. Therefore, to estimate finely spaced frequency components (small Δf), we need to use a large *w(t)*.

Table 2-1. Sampling and truncation parameters in time and frequency domains.

Parameter	***Time***	***Frequency***	***Eq. #***
Resolution	Δt	$\Delta f = \frac{1}{w(t)}$	(2.9)
Truncation window	$w(t) = N \cdot \Delta t$	$f_{\max} = \frac{1}{2\Delta t} = f_c$	(2.10)
Sampled points	N	$N/2$	(2.11)
Single element value	$t_n = n \cdot \Delta t$	$f_n = \frac{n}{N \cdot \Delta t}$	(2.12)
Minimum value	$t_1 = \Delta t$	$f_1 = \frac{1}{N \cdot \Delta t} = \Delta f$	(2.13)
Maximum value	$t_N = t_0 + w(t)$	$f_N = \frac{1}{2 \cdot \Delta t} = \frac{f_s}{2} = f_c$	(2.14)

Frequency components can be calculated directly from the time domain counterparts using this relationship [5], [10]:

$$f = \frac{n}{N \cdot \Delta t} = \frac{n}{N} f_s \tag{2.15}$$

The range of available frequencies can be established through a careful examination of Eq. (2.15). For a predetermined sampling rate ($f_s=1/\Delta t$), the total number of images *N*, dictates the minimum available frequency ($f_{min}=f_s/N$); while the maximum available frequency is given by half the sampling rate ($f_{max}= f_s/2$, since $n_{max}=N/2$), *i.e.* the Nyquist frequency f_c. Therefore, if we are interested on low-frequency components, as we usually do in NDT&E applications to go deeper below the surface as will be discussed in Chapter 3, we should use large Δt and/or

large *N*. Hence, the sampling and truncation parameters, *i.e.* the pair: Δt - *w(t)*, can be optimized for every inspected depth. The other sampling parameters together with their corresponding frequency counterparts can be estimated from these two, and are summarized in Table 2-1.

2.4.3. The impact of *w(t)* on phase

The size of *w(t)* has a great impact on the resulting spectra. This is illustrated in Figure 2.9. The temperature profiles for a sound area and a 1 mm depth flat-bottomed hole on a Plexiglas® plate (specimen PLEXI014 in Appendix F.8) are shown in Figure 2.9a. The truncation window size varies from 22 to 533 s (indicated with arrows) while the time resolution is the same in all cases (Δt=889 ms). Phase profiles in Figure 2.9b correspond to the positive part of the phase spectra calculated by PPT, using the four truncation windows identified in Figure 2.9a. As a result, from Eq. (2.10), the number of points are re-adjusted in accordance with *w(t)*. The % error is estimated with respect to the 533 s profiles, which has the highest time resolution and is thus closer to the actual continuous phase profile. As can be seen, for a constant time resolution (Δt=889 ms), there is a loss of information related to the use of smaller *w(t)*. Accordingly, incomplete thermogram sequences, *i.e.* sequences for which the final temperature is not reached, will increase the error on the phase estimations, especially at low frequency components.

It can be concluded from this graph that a *w(t)*=133 s would be enough (*i.e.* the maximum error is ~7% for the minimum peak phase) to correctly sample a 1 mm defect on a Plexiglas® matrix, even if the ambient temperature has not been reached yet. Using a smaller *w(t)*, could save a considerable amount of memory for the computations (*e.g.* 4 times smaller using 133 instead of 533 s). However, larger *w(t)* would be needed when inspecting deeper defects, which implies that the search for the optimal sampling and truncation parameters should be done individually.

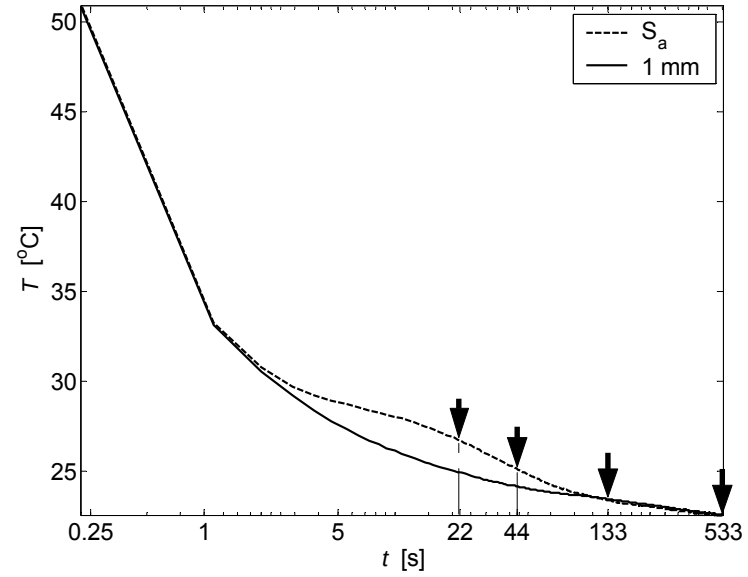

(a)

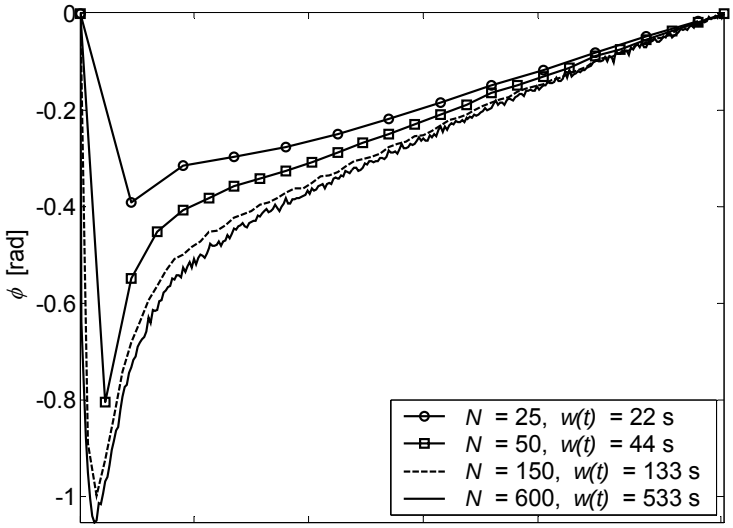

(b)

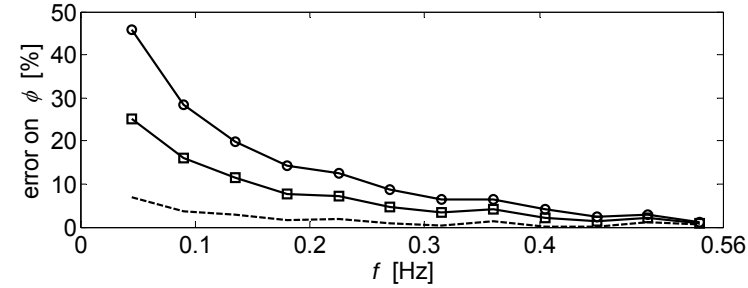

(c)

Figure 2.9. Impact of the size of the truncation window on phase for a 1 mm depth flat-bottomed hole on a Plexiglas® at f_S=22.55 Hz, Δt=889 ms. (a) temperature profile; (b) phase profiles; and (c) % error evaluated with respect to the 533 s phase profile. Data from specimen PLEXI014 in Appendix F.8.

A compromise between Δt, *w(t)* and available computer power should be made depending on the probing requirements. For instance, a similar analysis on the 3.5 mm depth defect on the same Plexiglas® plate (specimen PLEXI014 in Appendix F.8), allowed to determine that a *w(t)*=533 s is needed. To compensate (in part) for the increase on the number of points *N* to be processed (600 instead of 150 as for the 1mm case above), time resolution can be reduce by a factor of 3, *i.e.* Δt=2.67 s instead of Δt=889 ms in Figure 2.9.

Thus, the acquisition time t_{acq} is dictated by the depth of the deepest defect (since it is the last one to be reached by the heat front), whereas the limiting f_s must take account of the range of inspected depths and the computer memory.

The material thermal properties are critical when choosing, not only Δt but also *w(t)*. Acquisition, sampling and truncation parameters used to inspect specimen PLEXI014 are compared in Table 2-2 with those used for specimen ALU002 (Appendix F.3) presented in Figure 1.7 and Figure 2.5. In the case of aluminum, Δt=50.3 ms and *w(t)*=6.3 s were required to detect flat-bottomed holes from 0.5 mm to 2 mm (the 2.5 mm depth defect could be detected in Figure 2.5a but it could not be correctly characterized as seen in Figure 2.5b). This contrasts with the parameters used in the Plexiglas® specimen, which were Δt=889 ms and *w(t)*=533 s for defects ranging from 1.0 to 3.5 mm.

Table 2-2. Comparative table of sampling and truncation requirements on Plexiglas® and aluminum.

	k **[W/mK]**	***f_s*** **[Hz]**	***Δt*** **[ms]**	***N*** **[-]**	***w(t)*** **[s]**	***z*** **[mm]**
Plexiglas®	0.2	22.55	889	86	533	1.0 - 3.5
Aluminum	237	157.83	50.3	250	6.3	0.5 - 2.0

Thus, the much higher time resolution requirement on high conductivity materials is compensated in part by the need of a smaller truncation window. More frames had to be included for aluminum to incorporate more temperature data especially at the beginning of the sequence, where thermal changes are critical. The number of frames *N* could be further reduced without loss of pertinent information using a higher sampling rate with a shorter *w(t)*.

2.4.4. Energy redistribution

After performing the PPT on the thermogram sequence, the resulting amplitude and phase delay data are distributed along frequency components ranging from "0" to a maximum frequency f_{max}. Figure 2.10a shows the phase profiles for the 6 defects in specimen PLEXI014 using a time resolution of Δt=889 ms. According to Eq. (2.14), the maximum available frequency is given by $f_{max}=1/2\Delta t$, thus f_{max}=0.56 Hz for this particular experience. It would be however possible to decrease the time resolution value without compromising the precision of the result, provided that f_{max} is kept above the Nyquist limit, f_c. This situation is illustrated in Figure 2.10b for a time step 8 times larger than in Figure 2.10a (Δt=7.11 s Hz, f_{max}=0.07 Hz).

Phase profiles are presented on the same scale as in Figure 2.10a for comparison. A zoomed frame is also shown to increase detail. In both graphs, Figure 2.10a and Figure 2.10b (zoomed portion), clear depth discrimination can be observed from "0" to a *limiting* frequency (*i.e.* the *blind frequency*, as will be explained in section 3.2), which depends on the depth of each defect, while phase values are all mixed together from the limiting frequency to f_{max}, and no depth distinction can be made.

Decreasing time resolution has a "zoom-in" effect; energy is however redistributed on a shorter scale. There is also a change on phase values. For instance, minimum peak phase for the 1 mm defect goes from -1.05 rad in Figure 2.10a to -0.46 in Figure 2.10b. Nevertheless, blind frequency values are about the same in both cases with a slight shift to lower frequencies due to a loss of thermal information as can be seen in Table 2-3, which presents a comparative analysis of

the phase profiles shown in Figure 2.10. Minimum peak phase, blind frequencies and the inverse square root blind frequencies for both cases, Δt=889 ms and Δt=7.11 s, are included in this table.

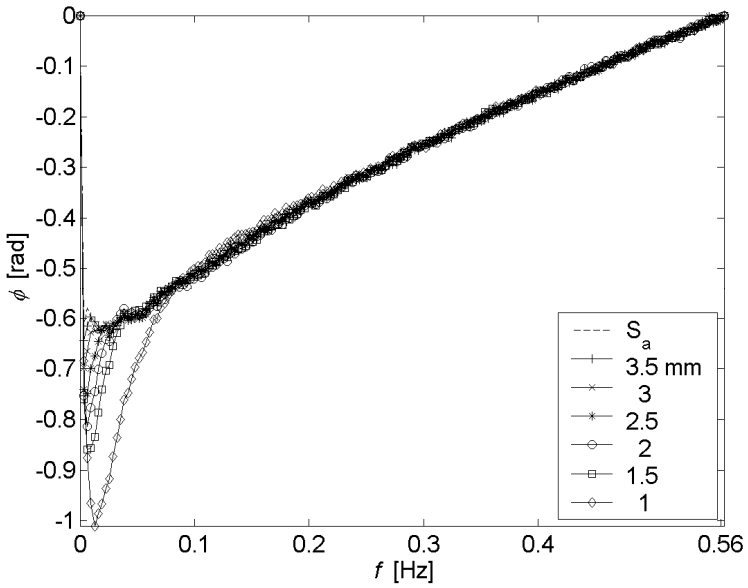

(a)

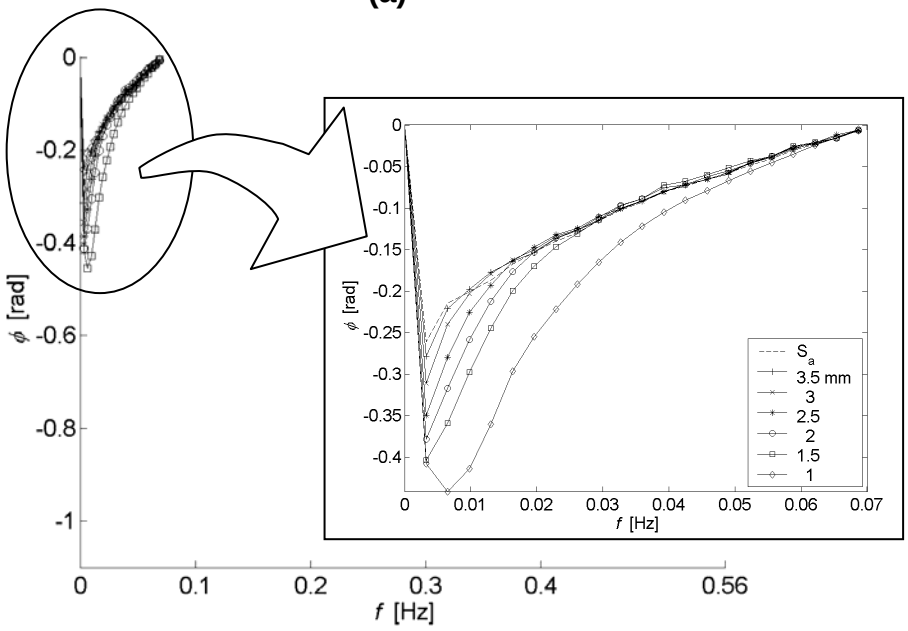

(b)

Figure 2.10. Energy redistribution on phase profiles for a Plexiglas® plate with 6 flat-bottomed holes using f_s=22.55 Hz, $w(t)$=533 s, and (a) Δt=889 ms, N=350; and (b) Δt=7.11 s, N=43. Data from specimen PLEXI014 in Appendix F.8.

The depth inversion technique proposed in Chapter 3 is based on the dependency of the depth of a defect z, with the square root of the blind frequency f_b. Hence, differences between the two studied situations are evaluated as a percent of discrepancy in $f_b^{-1/2}$. From this table, increasing the time step from 889 ms to 7.11 s, *i.e.* 8 times larger, will produce up to a 12.4% error in the worst case. It can be concluded that profiles in Figure 2.10a are *over-sampled* since similar results can be obtained using a time resolution considerably smaller (by a factor of 8), as in Figure 2.10b. Again, this is conditioned to the fulfillment of the Sampling Theorem. Consequently, the blind frequency f_b, depends on the studied depth as well as on the material thermal properties.

Table 2-3. Comparative results for the phase profiles in Figure 2.10.

z [mm]	Δt=889 ms			Δt=7.11 s			error in $f_b^{-1/2}$ [%]
	ϕ_{min} [rad]	f_b [Hz]	$f_b^{-1/2}$ [Hz$^{-1/2}$]	ϕ_{min} [rad]	f_b [Hz]	$f_b^{-1/2}$ [Hz$^{-1/2}$]	
3.5	-0.64	0.0096	10.18	-0.28	0.0098	10.10	0.9
3.0	-0.70	0.0129	8.82	-0.31	0.0131	8.74	0.9
2.5	-0.75	0.0193	7.20	-0.35	0.0164	7.82	-8.6
2.0	-0.82	0.0289	5.88	-0.38	0.0229	6.61	-12.4
1.5	-0.86	0.0354	5.32	-0.40	0.0327	5.53	-4.0
1.0	-1.01	0.0804	3.53	-0.44	0.0687	3.82	-8.2

Usually, acceptable qualitative results, *i.e.* defects are visible, can be obtained by PPT with little attention on the way in which the thermal profiles have been obtained. However, as will be discussed in Chapter 3, quantitative analysis by PPT requires that the sampling and truncation parameters to be selected following the guidelines presented in section 2.4 prior to the application of the FFT.

The analysis presented thus far suggests that sampling and truncation parameters are directly related to the depth and to the thermal characteristics of the defect being inspected. Of course, these parameters are generally not available in the first

place. An interactive procedure can be implemented taking advantage of these facts, *i.e.* (1) defects are visible even in the case of badly sampled so the defective zones can be located first; and (2) with the information about the defect locations, the sampling and truncation parameters can be re-adjusted individually for quantitative analysis by taking into account the CFT-DFT equivalency and the Time-Frequency Duality of the DFT as described next.

2.5. Interactive Defect Characterization by PPT

2.5.1. Optimizing frequency resolution

Figure 2.11 illustrates a well-known fact in signal processing with the DFT, *i.e.* that a change in one or both elements of the pair the Δt-$w(t)$, will inexorably have an impact in the frequency response[14], [72], [73]. Figure 2.11a depicts an example of a correctly sampled temperature profile, which produces an adequate frequency response in Figure 2.11b, *i.e.* the resulting phase profile shows the characteristic minimum peak phase at low frequency and then goes quasi-linearly to zero at higher frequencies. Note that only half the spectra (and half the points) are required in Figure 2.11b as discussed in section 2.2.3.

Figure 2.11c reveals that, a reduction in time resolution ($\Delta t=1/f_s$) from Δt_1 to $\Delta t_2=2\Delta t_1$; will produce a reduction of the maximum available frequency, from f_{c1} to $f_{c2}=f_{c1}/2$ in Figure 2.11d, from Δf_1 to $\Delta f_2=2\Delta f_1$. Although the minimum peak phase value is affected in the process, reducing the truncation window size (above the Nyquist limit) does not affect the frequency resolution. On the other hand, a decrease in the truncation window size say from $w(t)_1$ to $w(t)_2=w(t)_1/2$; will deteriorate the frequency resolution by half after the application of the FT in Figure 2.11f. The impact at low frequencies is more important since the information for the minimum peak phase might be lost in the process. At high frequencies, this procedure may even be benefic in some cases since noise content is reduced. These two situations can be conveniently exploited to optimize frequency resolution.

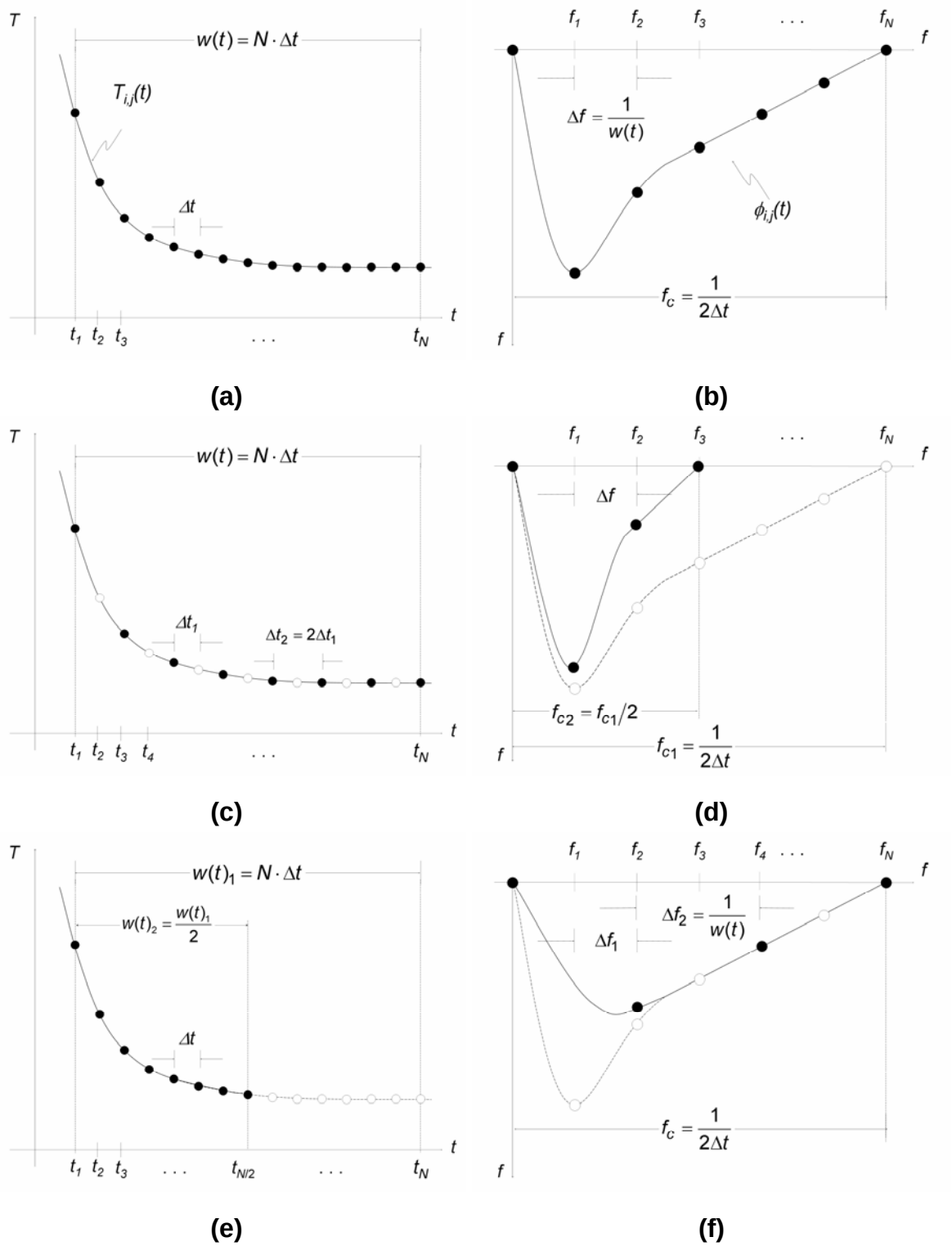

Figure 2.11. Time-Frequency Duality of the FT applied to surface temperature decay profiles. (a) Continuous temporal signal *T(t)*, sampled at Δt, and truncated at *w(t)*; (b) frequency response $\phi(f)$. Increasing Δt in (c) produces a reduction of f_{max} in (d). Decreasing *w(t)* in (e); diminishes frequency resolution in (f).

2.5.2. Time and frequency resolution fine-tuning

The maximum time resolution that can be used corresponds to the inverse of the sampling rate: $1/f_s$. Once data is acquired, it would be desirable to use all the available information. However, it is sometimes useful to sacrifice time resolution (reducing N in consequence) to increase the area to be simultaneously processed. For instance, discarding one of every two points will increase Δt by a factor of 2, and at the same time, N will be reduced by the same factor, as portrayed in Figure 2.11c and Figure 2.11d.

Even though this procedure does not have a net effect on frequency resolution, *i.e.* $w(t)$ is unchanged as can be confirmed from examination of Eqs. (2.9) and (2.10) in Table 2-1; energy is redistributed over frequency components on a shorter scale ('zoom-in' effect) since the maximum available frequency is now reduced by half the original value, as discussed previously. The overall effect is that the amount of data is reduced (by half in this case). If thermal contrast is good enough to allow defect detection, a convenient size for $w(t)$ can be chosen before processing by locating directly in the temperature profile the time at which thermal changes are negligible. In the same manner, time resolution Δt, can be diminished to reduce the number of discrete points without compromising frequency resolution, if the frame rate is kept above the Nyquist limit, f_c [73]. Nevertheless, it is not always possible to visualize defects from raw thermal data.

Contrast between defective and sound areas is greatly improved when using the phase instead of the temperature, thus the interest in such techniques as PPT. Hence, it is possible to locate defective areas with a relatively modest computer power using low time resolution and/or short truncation windows for a first defect visualization of the entire specimen surface.

Considering the time domain, acquisition should ideally last until thermal changes in the specimen are negligible, *e.g.* when surface temperature is in equilibrium with its surroundings. However, it could take long time before reaching these conditions, especially for low conductivity materials. In practice, acquisition is truncated at a

more reasonable time, *e.g.* when surface temperature shows no thermal contrast with respect to a (contiguous) non-defective area.

On the frequency side, the typical minimum peak phase at low frequency gives an indication that the selected *w(t)* produced good enough frequency resolution (see the change in the minimum phase value in Figure 2.11f). From Eq. (2.9) in Table 2-1, it can be seen that frequency resolution Δf, improves for larger *w(t)*. As a result, *w(t)* should be as large as possible to decrease Δf, especially when dealing with deep defects that are detectable only at very low frequencies. However, there is no use in extending the size of *w(t)* beyond the stabilization time, *i.e.* when thermal changes are no longer significant. Only important variations in time domain are of interest on the frequency spectra following the FT. Therefore, it would be attractive to be able to locate the pertinent information for a particular depth prior to the application of the FT. Although it is possible to predict the minimum *w(t)* size for a particular configuration using computer modeling [15], Δt prediction is difficult to implement given the multitude of factors (thermal properties of the specimen and defect, defect depth, surface shape, etc.) that are involved. As a consequence, Δt is generally established empirically. An interactive approach is possible as summarized in Figure 2.12 and described next.

2.5.3. Interactive Methodology

❶ACQUISITION

The frame rate f_s, and the acquisition time t_{acq}, should be selected bearing in mind that the goal is to characterize defects at different depths in a single test. A compromise should be made between f_s, t_{acq} and storage capacity N_{max}, ($N_{max}=f_s \cdot t_{acq}$). Whenever possible, f_s, and t_{acq} should be chosen in function of the thermal properties of the material being inspected and the defect properties. Some primitive information about the sample and defects will be helpful at this point. Thermal modeling may be useful as well. In addition, it should be considered that deep defects (thin or thick) require longer t_{acq} than shallow defects; and thin defects

require higher f_s values than thick defects (L is the sample thickness in the diagram of Figure 2.12).

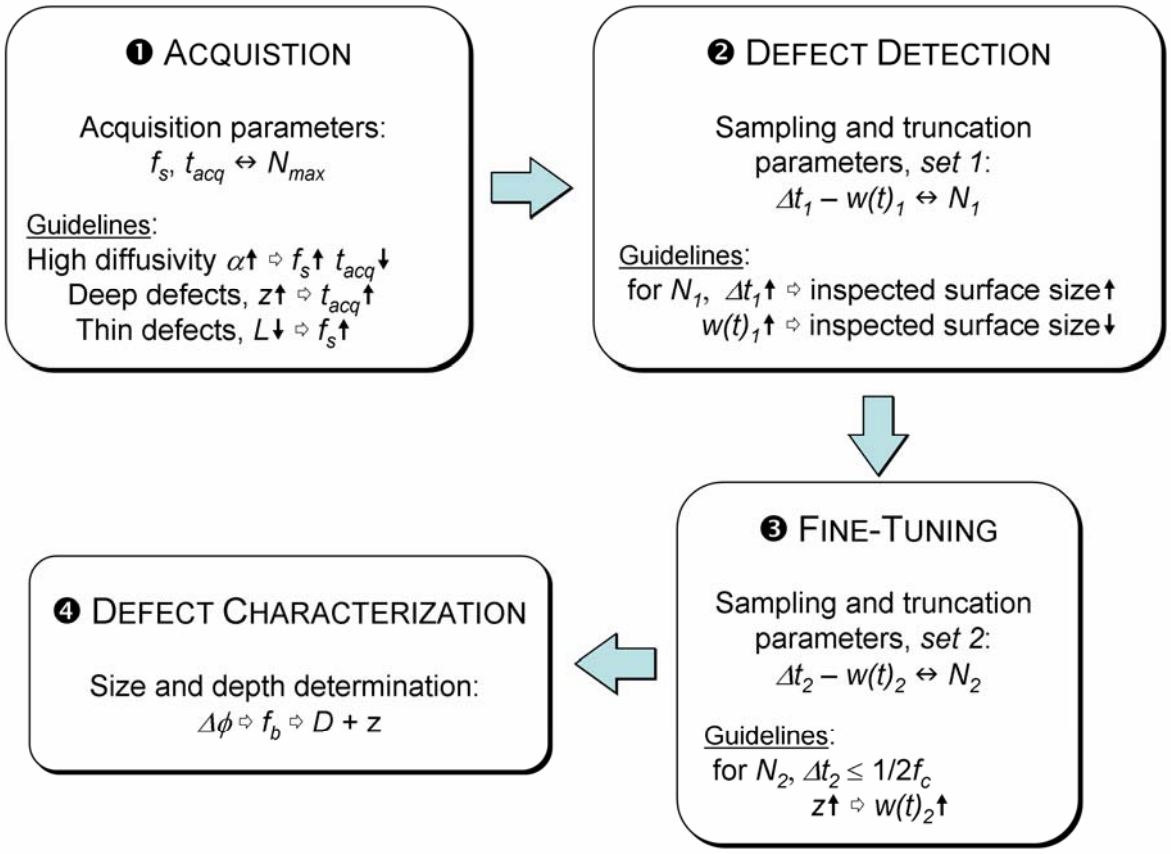

Figure 2.12. Schematization of the proposed interactive methodology for optimized defect characterization by PPT.

❷ DEFECT DETECTION

Once the acquisition process is completed, a great amount of data covering a wide span of depths will be available for processing. In order to cover the entire surface (or a considerable part of it) a compromise between computer power, depth range, time and frequency resolution is needed. A first pair Δt_1 - $w(t)_1$ is chosen for defect detection purposes only by taking into consideration all the available information about the system being inspected: $w(t)_1$ should be as large as possible to increase frequency resolution and to be able to characterize a wide range of depths, and Δt_1 should be short enough to capture early thermal changes.

From these two facts, it is more convenient to sacrifice time resolution (with the subsequent reduction in f_{max}, as seen in Figure 2.11c and d), instead of decreasing the size of *w(t)* (which will decrease frequency resolution, see Figure 2.11e and d) to cover a wider range of depths without compromising too much in defect detectability. This will guarantee that most defects, deep and shallow, will be detected even if it might not be possible to quantify them at this point. In the process, important information to characterize shallower defects (having higher Nyquist frequencies than deep defects) will be left aside (for the moment). Computations taking into consideration these data will be undertaken afterward as described below. Once defects are located using a given Δt_1 - $w(t)_1$ pair, thermal data can be 'selected' from the original sequence and then processed at a different Δt_2 - $w(t)_2$ pair, whose values will depend on the depth been inspected.

❸ FINE-TUNING

The next step is to analyze defective zones individually now that their locations are known. For instance, defects that are thick and shallow will show greater thermal contrast for longer time than defects that are thin and deep. If thermal contrast is high enough, the size of *w(t)* can be estimated by examination of the thermal profiles, but in general, the characteristic peak at minimum phase can be more easily retrieved from the phase profiles giving an indication of the correct size of *w(t)*.

The optimal time resolution can also be derived from examination of the phase profiles $\Delta t \leq 1/2f_c$, *i.e.* phase contrast should be zero at a frequency lower than f_c, if not; this could mean that time resolution should be increased. Also, a deep defect will require a longer *w(t)* than a shallow one, see flow diagram in Figure 2.12.

❹ DEFECT CHARACTERIZATION

Finally, phase contrast can be used for f_b retrieval using the technique presented in paragraph 3.2. Before presenting the depth inversion method, it is convenient to review the interactive methodology through a descriptive example.

2.5.4. Example of Interactive Optimization

Carbon Fiber Reinforced Plastic (CFRP) specimen, CFRP006 in Appendix F.9, was inspected from the right side and characterized following the interactive methodology proposed in section 2.5.3. The four steps are detailed next.

❶ ACQUISITION

After preliminary tests at different sampling rates, it was determined that a frame rate of f_s=157 Hz and an acquisition time of t_{acq}=6.6 s, were adequate for this specimen. Only 1048 frames were conserved (instead of 1080) after discarding pre-flashed (cold) and saturated thermograms.

❷ DEFECT DETECTION

Figure 2.13 shows different phasegrams at selected frequencies using a time resolution of Δt=76 ms, *i.e.* twelve times lower than the best possible resolution (Δt=1/157=6.3 ms). This was done simply by excluding from the computations 11 of every 12 frames in the sequence. As a result, *N* was reduced by a factor of 12. The truncation window was left at the maximum available value, *i.e.* $w(t)$=6.6 s, but it would be possible to use narrower window if required since only defect visualization is of interest at this stage. It can be said (through visual examination of Figure 2.13a through f) that the supplied energy was enough to detect 24 of the 25 defects, *i.e.* all defects from 0.2 to 1.0 mm in depth and from 3 to 15 mm in diameter with the exception of the 3 mm defect at 1.0 mm depth (the smallest defect at the deepest depth). However, as will be seen in paragraph 3.2 (Figure 3.6a), it was possible to characterize all defects after optimization.

The fiber structure is visible in phasegrams presented in Figure 2.13a through e, but it is more clearly seen at lower frequencies, which correspond to deeper depths, where there is more non-defective fiber matrix between the defects and the surface. In addition, noise increases at higher frequencies, as a result, fiber structure is no longer visible in the 7.53 Hz phasegram in Figure 2.13f.

❸ FINE-TUNING

The phasegram in Figure 2.14a highlights the locations of the five biggest defects (D=15 mm) with depths ranging from 0.2 to 1.0 mm. The corresponding temperature profiles are shown in Figure 2.14b, the phase profiles in Figure 2.14c and the phase contrast profiles in Figure 2.14d. The average values of 10 pixels inside the zones of interest were used to reconstruct these profiles.

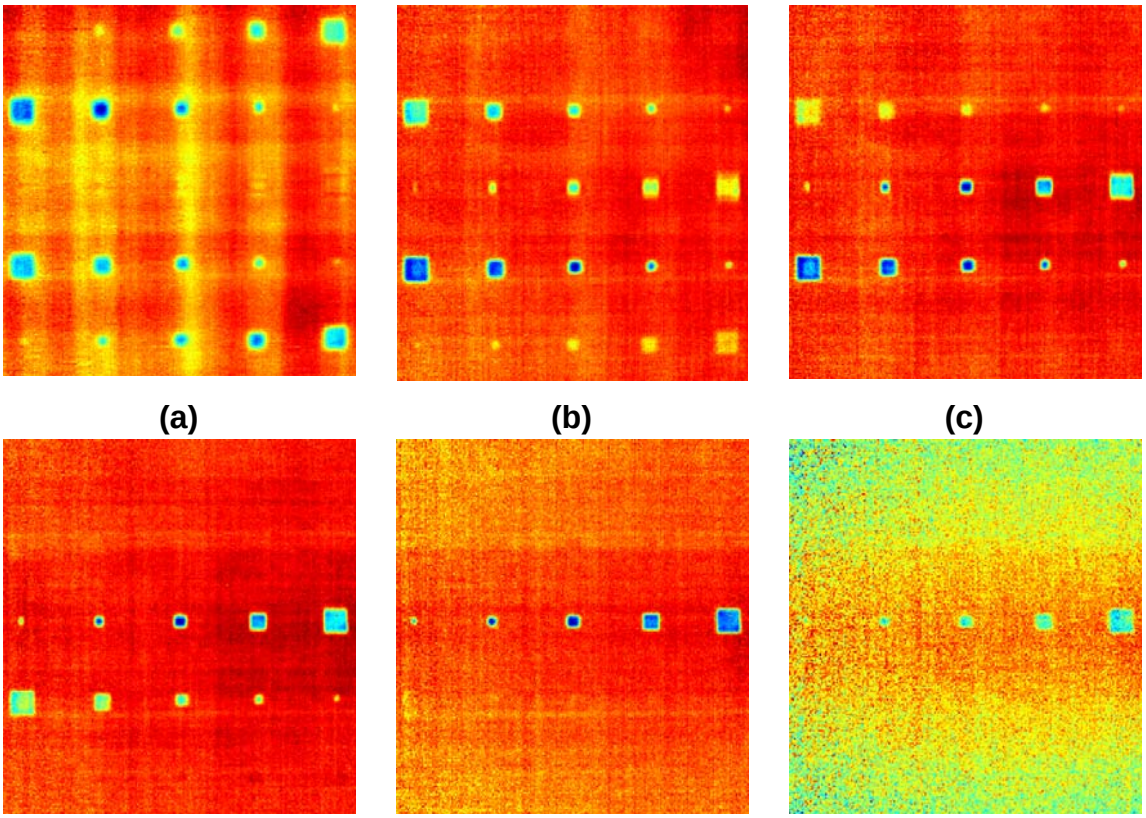

Figure 2.13. Phasegrams for specimen CFRP006 at f_s=157 Hz, Δt=76 ms, $w(t)$=6.6 s and N=87. Phasegrams at selected frequencies after applying the FT, (a) f=0.15 Hz; (b) f=0.45 Hz; (c) f=0.75 Hz; (d) f=1.20 Hz; (e) f=2.71 Hz; and (f) f=7.53 Hz.

The temperature profiles in Figure 2.14b reveal strong non-uniform heating effects, clearly seen at early times (9°C difference between profiles), but also at the end of the profiles (2°C difference between profiles). Moreover, thermal profiles at different depths do not exhibit their 'expected' behavior, *i.e.* shallow defects should yield a higher contrast than deep defects, which is not the case in Figure 2.14b. In

spite of this, *w(t)*=6.6 s seems to be enough time to capture the most significant thermal variations, as the rate of cooling has considerably slowed down at this point. Based on this facts, acquisition conditions (f_s=157 Hz and t_{acq}=6.6 s) were judged to be adequate to perform quantitative analysis for this particular case.

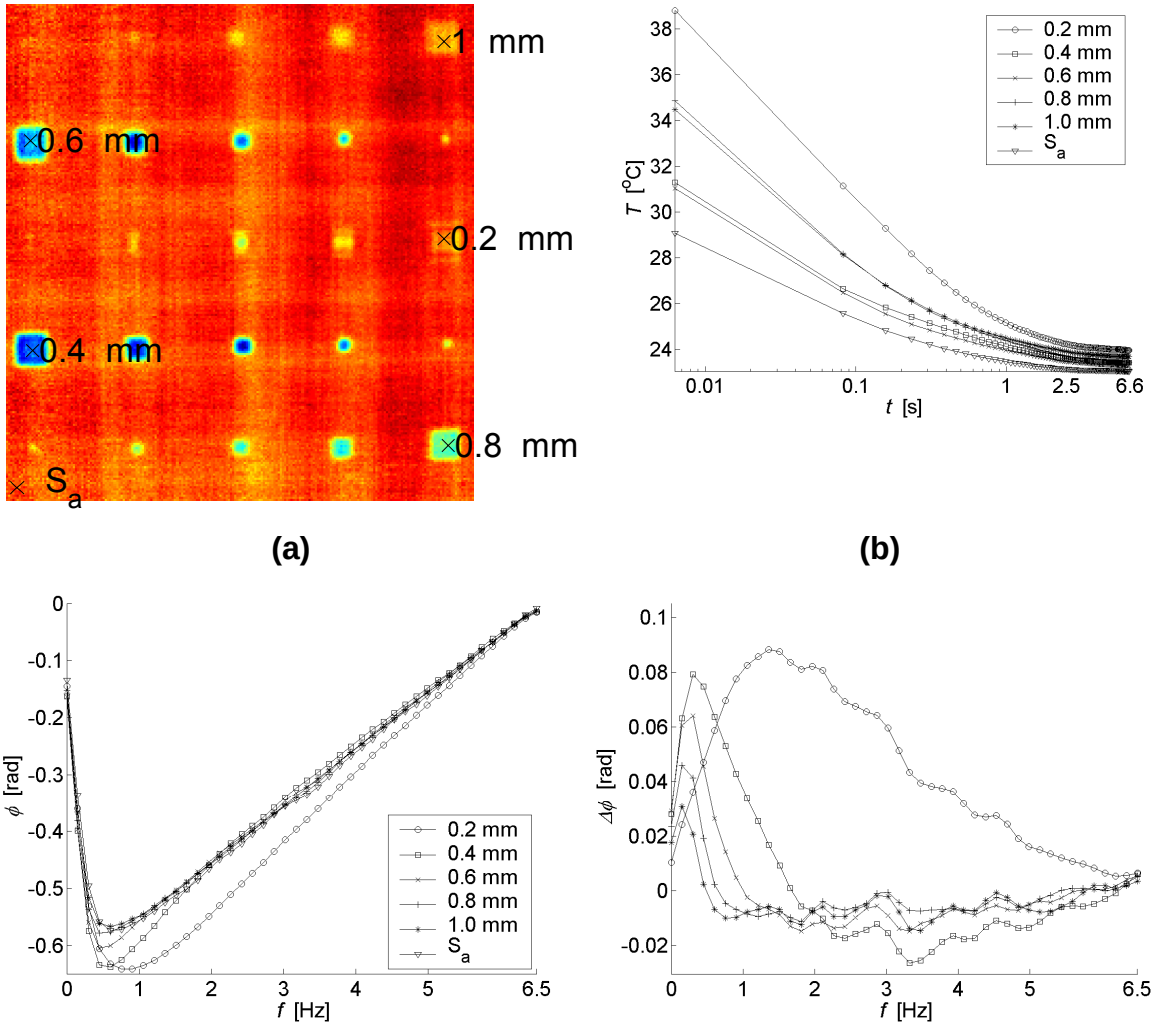

Figure 2.14. Specimen CFRP006 tested at f_s=157.83 Hz, Δt=76 ms, *w(t)*=6.6 s and *N*=87. (a) Phasegram at 0.30 Hz showing depths for the *D*=15 mm defects; (b) temperature; (c) phase and (d) phase contrast profiles for the 5 selected defective zones (from 0.2 to 1.0 mm) and a non-defective sound area (S_a).

On the other hand, from the phase contrast profiles in Figure 2.14d, it can be deduced that the Sampling Theorem is respected only for the 4 deepest defects

since the maximum available frequency is higher than the Nyquist limit in all these cases, *i.e.* $\Delta\phi$=0, $f_{max}>f_c$. Hence, the 4 deepest defects are correctly characterized at these conditions: Δt=76 ms, *w(t)*=6.6 s. In fact, time resolution could even be further reduced (*e.g.* by half) without compromising frequency resolution.

On the contrary, better time resolution is needed for the shallowest defect. Phase contrast for the shallowest defect (0.2 mm in depth) goes to zero only at the maximum available frequency. There are two possibilities in this case, it is possible that the selected sampling pair in the time domain corresponds exactly to a maximum frequency on the frequency spectra equal to the Nyquist limit, *i.e.* $f_{max}=f_c$, or it is possible that the Nyquist limit has been missed for this defect depth. From these two possibilities, the second one appears more reliable given the 'abnormal' phase contrast behavior, *i.e.* phase contrast should present a maximum peak contrast at a low frequency if the trend of the rest of the contrast profiles in Figure 2.14d was to be followed. Since the zones of interest have already been located (Figure 2.14a), an analysis beginning at this extreme value is performed next exclusively on the shallower defect, in order to characterize it.

The thermal decay profiles for the defective region (0.2 mm depth) and for a contiguous sound area are presented in Figure 2.15. The sound area in this case was selected right next to the defective area to effectively minimize non-uniform heating effects. Two cases are shown, Case 1: Δt=6.3 ms, *w(t)*=6.3 s, *N*=1000; and Case 2: Δt =25.4 ms, *w(t)*=3.17 s, *N*=125. Despite the appearances, the number of points between 0 and 3.17 s is the same as in between 3.17 and 6.34, since a semi-logarithmic scale is used for convenience. Phase and phase contrast profiles for these two situations are shown in Figure 2.16. Profiles in Figure 2.16a corresponds to Case 1; while conditions for Figure 2.16b are for Case 2.

As a first observation, noise presence in Figure 2.16a is substantial, particularly at high frequencies. Continuous phase and phase contrast profiles, obtained after performing PPT on synthetic data obtained by Thermographic Signal

Reconstruction (TSR) [43], [82]-[86], see Appendix D, are also included in these figures. A high degree polynomial (9^{th} degree) was used to fit all profiles.

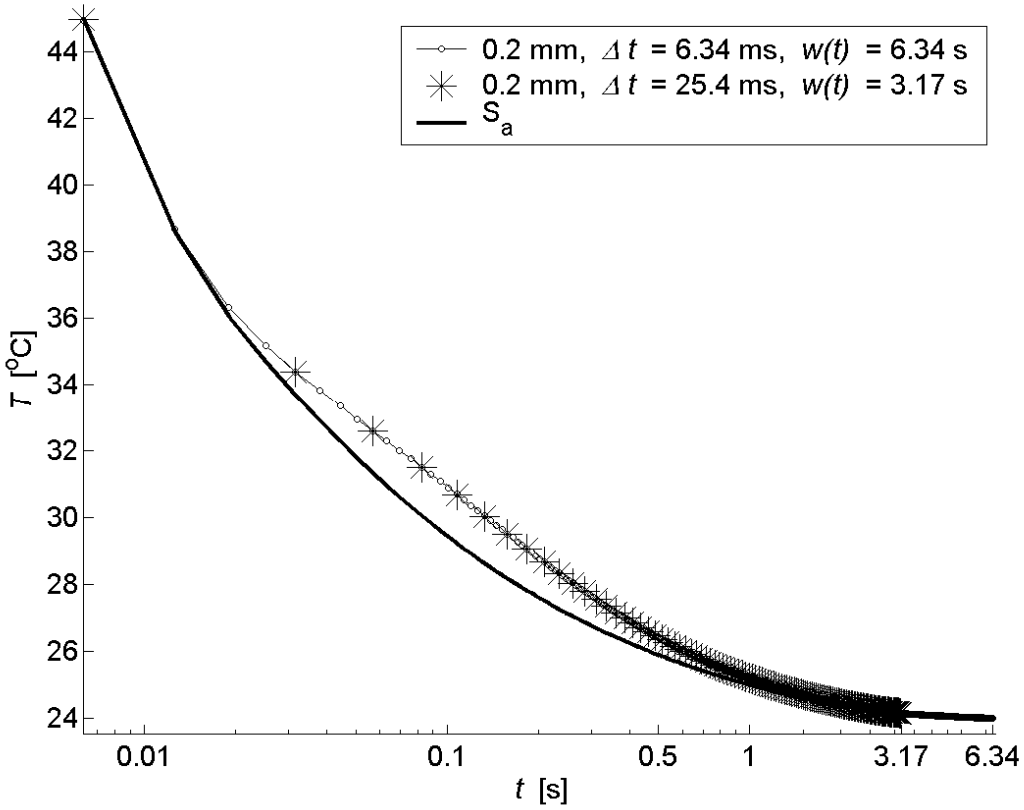

Figure 2.15. Thermal profile for a sound area Sa, and the 0.2 mm defect using two set of parameters: Case 1: Δt=6.34 ms, $w(t)$=6.34 s, N=1000; and Case 2: Δt =25.4 ms, $w(t)$=3.17 s, N=125.

Case 2 presents considerably less noise than Case 1. There is a small variation on the estimation of f_b, as a combined effect of the presence of noise, and the reduction of frequency (by a factor of 2) and time (by a factor of 4) resolutions. However, this variation is of the same order of magnitude as the error caused by using phase contrast calculations.

Indeed, changes in f_b caused by selecting a different sound area can be as large as those produced by reducing time and/or frequency resolution (as will be shown in section 3.5).

Hence, both conditions can be used for characterization with Case 2 (Figure 2.16b) being considerably less expensive in computational time and space.

❹ DEFECT CHARACTERIZATION

Depth retrieval was performed using phase contrast calculations as described in section 3.2. Results from least squares regression are presented in paragraph3.2.2.

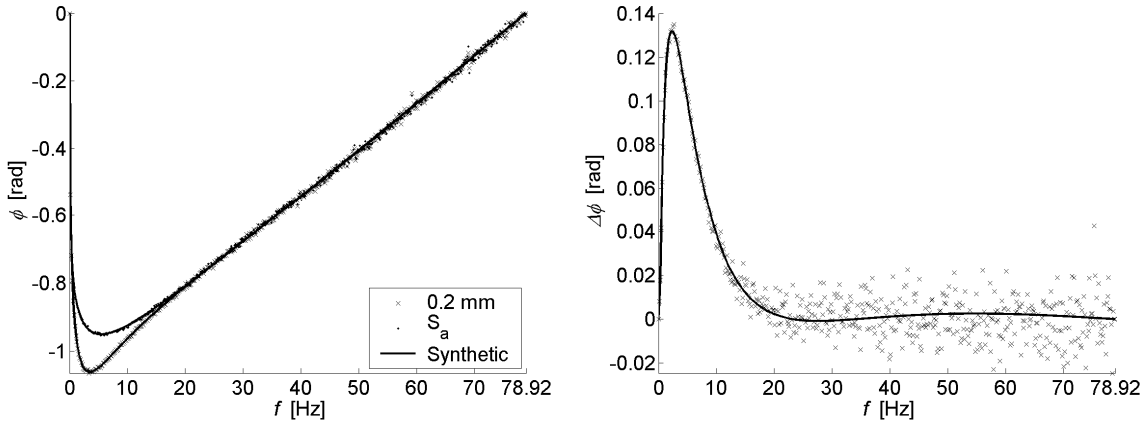

(a)

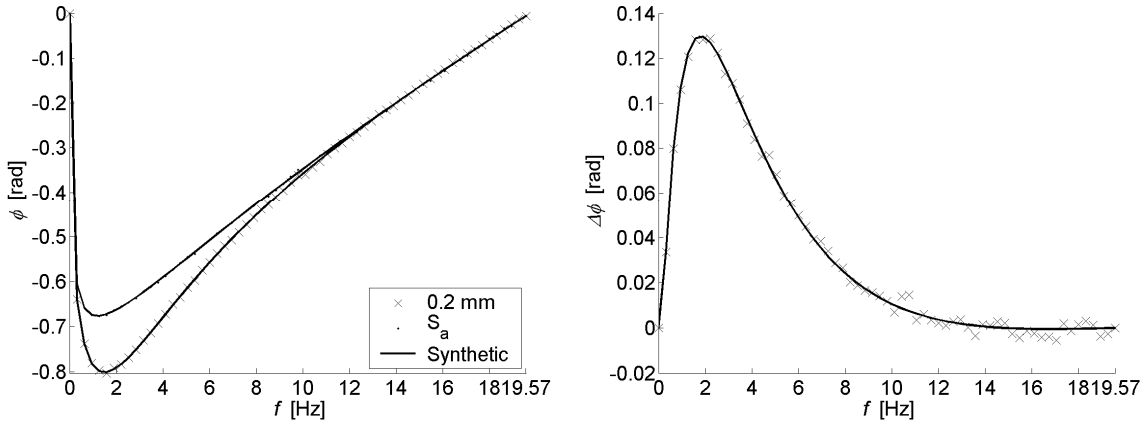

(b)

Figure 2.16. Phase (left) and phase contrast (right) profiles for the 15 mm defect at 0.2 mm depth for (a) Case 1: Δt=6.34 ms, $w(t)$=6.34 s, N=1000; and (b) Case 2: Δt =25.4 ms, $w(t)$=3.17 s, N=125. The solid curves are results obtained by applying the PPT to reconstructed data using a 9th degree polynomial.

Depth inversion with the phase is the subject of Chapter 3.

2.6. Summary

Defect detection and quantification is rarely a straightforward procedure because of all the signal degradation sources enumerated in Appendix A, section A.3.4. Preprocessing by traditional image enhancement techniques may help to increase contrast between defective and non-defective areas. However, more sophisticated techniques [22] are often required. PPT is one of such techniques aimed to increase defect/non-defect contrast by retrieving the frequency spectra from the time-domain temperature data using a transformation algorithm. Given the phase characteristics addressed in section 1.3.3 and further discussed in section 2.2.3, defect/non-defect contrast should be greater for phasegrams than for raw thermograms. Different schemes are possible, for instance, the Fast Fourier Transform (FFT) [4].

Pulsed Phase Thermography (PPT) is a FFT-based processing method for which, data acquisition is carried out in a similar way as in classical Pulsed Thermography. PPT's greatest innovation is that from this pulsed data, amplitude and phase delay information can be retrieved at different frequencies after the application of the FFFT algorithm. Non-uniform heating, reflections from the environment, surface emissivity variations and surface geometry have a less significant impact on phase than on raw temperature. These PPT characteristics are complemented by its rapidity of deployment (as in PT), greatly relaxing experimental constrains without loosing critical information.

The decaying thermal profiles such as the ones encountered in PPT, are non-periodic, non-band-limited functions for which, an adequate time resolution Δt and truncation window size *w(t)*, should be selected during the signal discretization process. Furthermore, these sampling and truncation parameters are both function of the depth of the defect and of the thermal properties of the specimen/defect system. The Time-Frequency Duality plays a critical role on defect characterization by PPT. In summary, the size of the truncation window *w(t)*, should be as large as possible to retrieve all the important information prior to the application of the FT.

Nevertheless, the size of *w(t)* could be reduced with little impact on phase profiles in order to save computer memory. On the other hand, time resolution Δt, has a greater impact on phase profiles. Increasing Δt has a 'zoom-in' effect on phase. Energy is however re-distributed on a shorter scale. This situation could be used with profit to reduce high frequency noise, and to reduce the amount of processed data, if needed.

Although determination of Δt is possible through modeling [15], no analytical solution is available for the estimation of *w(t)*, given the several factors having an impact on phase results [15]. A 4-step methodology was proposed to interactively determine the adequate sampling and truncation parameters in function of the inspected depth. The methodology was tested on a CFRP plate with Teflon® insertions at different depths. This functionality will prove effective for depth inversion purposes as will be pointed out in Chapter 3.◄

Chapter 3. Quantitative Pulsed Phase Thermography

The fundamental problem of communication is that of reproducing at one point either exactly or approximately a message selected at another point. [78].
Claude Elwood Shannon (1916-2001), American mathematical engineer

Claude Shannon put together[7] the Sampling Theorem concepts in his classical paper of 1949 [79]. Shannon's Sampling Theorem, as it is known today, acts as a link between an analog (continuous) signal and a sequence of numbers (discrete signal). It allows the replacement of a continuous bandlimited signal by a discrete sequence of its samples without any (significant) loss of information, specifying at the same time the lowest rate required to reproduce the original signal, *i.e.* the Nyquist limit. This is of particular importance when working with the Fourier Transform.

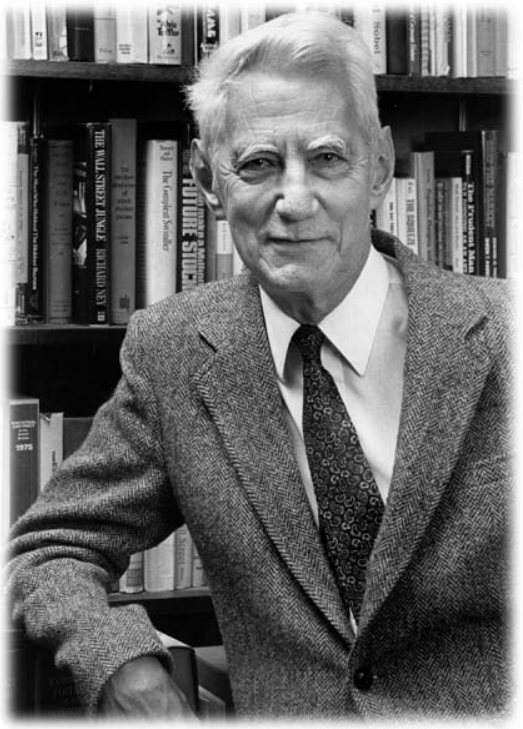

Figure 3.1. Claude Elwood Shannon (1916-2001).

Contrary to what is usually observed when a new idea is born,Shannon's theory was an immediate success among his colleagues. Practical applications have evolved ever since from telephone channels, to optical communications and now to wireless systems.►

[7] Although the problem was already formulated by Nyquist (1928), Whittaker (1929), Kotel'nikov (1933) and Gabor (1946); Shannon was the first to present it as a formal statement [76].

3.1. Introduction

PPT combines interesting capabilities of two older active techniques: acquisition is fast as in PT (performed in transient regime); and amplitude and phase data is available as in LT (performed in permanent regime). As discussed in section 2.2.3, phase is of special interest in NDT&E. In contrast, inversion procedures in PT are complex, whilst depth inversion by LT is a more mature technique for which depth inversion is straightforward [1], [8], [50], [51], [65], [66]. It would be desirable to preserve the easiness of deployment of PT with the quantification capabilities of LT. Several techniques have been considered for quantitative PPT, for instance: statistical methods [11], Neural Networks [12], and wavelets [13]. However, the required calibration steps and lengthy computation subroutines complicate their use in most of the NDT&E applications. On the other hand, as stated before, the Fourier Transform is the spectra representation of the time function and contains exactly the same information [72]. Hence, an inverse solution from PPT results could somehow be derived. A solution can be foreseen by examining quantitative LT studies.

In spite of the differences in the way data is acquired (permanent periodic waves vs. transient pulse-heating), the implementation of quantitative techniques using the phase is as straightforward for PPT as it is for LT, as it will be demonstrated in this chapter. Hence, much of this work was inspired from LT studies prepared by several recognized authors, although no experimental work by LT has been done specifically during this investigation. Nevertheless, two additional aspects, reviewed in Chapter 2, should be taken into consideration when extracting the information from the thermal sequences: (1) the equivalency between CFT and DFT; and (2) the Time-Frequency Duality of the DFT. In fact, besides the quantitative approach proposed in section 3.2, other inversion techniques might benefit from these two concepts since they provide the guidelines to correctly choose the acquisition, sampling and truncation parameters. We begin our discussion by briefly describing the depth retrieval procedures by LT.

3.2. Depth inversion by Pulsed Phase Thermography

Figure 3.2 shows the phase and phase contrast profiles for the case of thick defects (flat-bottomed holes) at two different depths. The phase profiles for the positive part of the spectra for two defects at different depths (ϕ_{z1}, ϕ_{z2}), and for a sound area (ϕ_{zs}), are shown at the bottom part of this graph. Phase contrast ($\Delta\phi_{z1}$, $\Delta\phi_{z2}$) can be calculated from the phase profiles through Eq. (1.8).

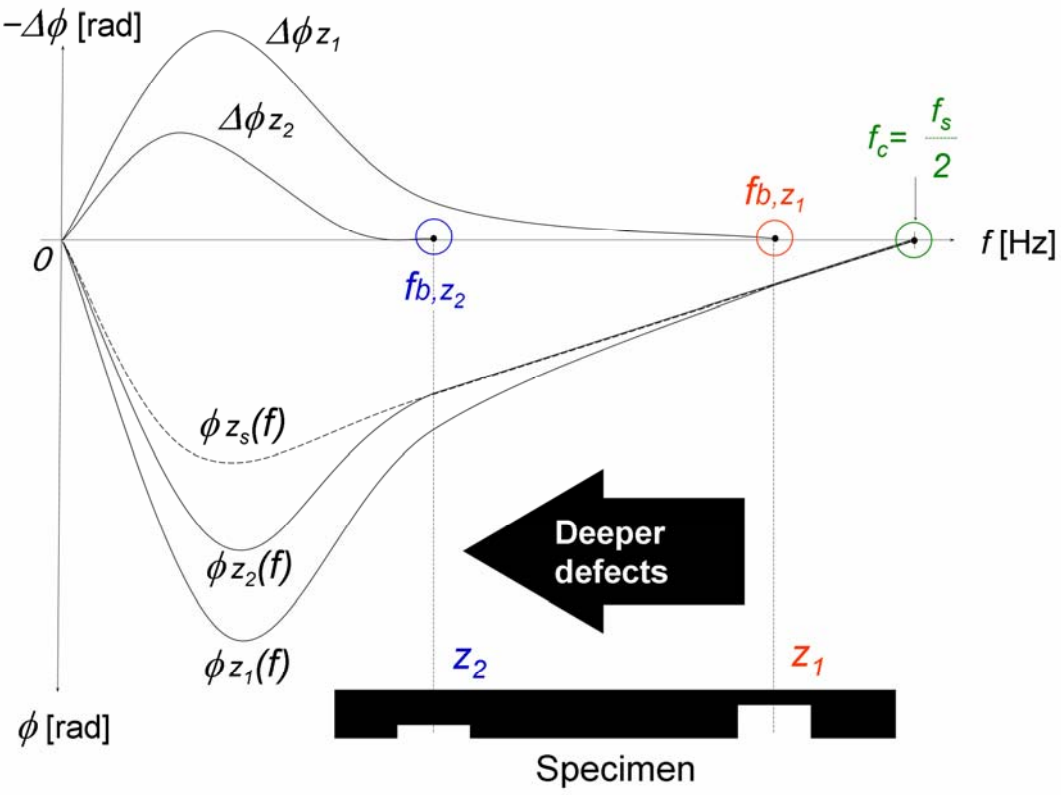

Figure 3.2. Depth quantification with the phase contrast and blind frequency.

The negative value for the phase contrast is used for convenience and is shown on the top of Figure 3.2. Defects are visible from '0' to a given frequency, *i.e.* the blind frequency ($f_{b,z1}$ and $f_{b,z2}$) which is lower for deeper defects ($f_{b,z1} > f_{b,z2}$). No depth discrimination can be made at frequencies higher than f_b, since profiles merge with the sound area phase profile into a straight line for $f > f_b$. Consequently, shallow defects have a larger frequency range of visibility than deep defects.

This analysis suggests that there exists an “optimal” sampling rate to retrieve all the important spectral information for a flaw at a particular depth, which will correspond to the blind frequency at that particular depth f_b. This is the basis for the quantitative technique presented next.

Given that (amplitude and) phase information is available in PPT, inversion procedures should be possible through Eq. (1.9), after determining the f_b, as is done by LT; with the advantage that, in PPT, several frequencies are available at once, and hence, complete (discrete) phase profiles can be reconstructed in a single test. Nevertheless, as discussed in section 2.1 and at the beginning of this chapter, an additional difficulty arises in PPT when trying to adequately establish the temporal parameters that will produce the appropriate frequency response. Indeed, the frequency components are inversely related to their temporal counterparts through the DFT. Hence, a change in the time domain will produce an effect on the frequency spectra. This situation has to be carefully addressed when selecting the sampling and truncation parameters in the absence of what phase results will be compromised. Interactive determination of both Δt and $w(t)$ is possible by following the guidelines provided in section 2.5.3 and in reference [16]. Accordingly, for correctly sampled data, the defect depth can be related to its corresponding blind frequency f_b.

The following example is intended to verify the validity of Eq. (1.9) on a homogenous material (steel) with flat bottomed-holes. In paragraph 3.2.2, we extend the technique to anisotropic composite materials (CFRP and GFRP) having thin defects. In these two cases, sampling and truncation parameters were carefully selected following the Interactive procedure of section 2.5.3. In section 3.3, we will consider the situation of an aluminum plate with flat-bottomed holes for which these guidelines were not respected.

3.2.1. Steel

Quantitative analysis was performed on two steel plates, specimens ACIER001 and ACIER002 in Appendices F.1 and F.2, respectively. Same size (30x30 mm^2) but different depths (from 1 to 4.5 mm) flat-bottom holes were machined on the rear side of each plate. A sampling rate f_s=45.1 Hz was used in both cases. For all the studied depths, the maximum possible truncation size was used to increase frequency resolution, *i.e.* $w(t)$= 23.9 s (since the buffer capacity is N=1080). In contrast, time resolution Δt, was optimized for each specific depth following the methodology proposed in section 2.5.3.

Conditions for specimen ACIER001 were: Δt=355 ms and $w(t)$=22 s, reducing the total number of images to N=62 images. Figure 3.3a and Figure 3.3b show the raw phase and phase contrast profiles, respectively for the four defective zones highlighted on the phasegram in Figure 3.3c (the phase average within the area enclosed by the 'Xs' was used). As can be seen, data is covered by noise and, even though a relationship between depth and their corresponding f_b values may be distinguished (phase and phase contrast intensities vary with the corresponding depths), it is difficult to perform accurate f_b estimations in these conditions.

Thermographic Signal Reconstruction (TSR) as proposed in [43], [82]-[85], see Appendix D, was applied to raw thermal data using a 7^{th} degree polynomial. Such a relatively high degree polynomial proves effective for signal de-noising with reduced 'ringing' effects as seen in Figure 3.3d and Figure 3.3e. Another possibility is to reconstruct phase or phase contrast profiles directly following a similar procedure as with thermal data in Appendix D. However, ringing effects are far more important in this case and higher polynomials have to be used (reducing the de-noising effect as a consequence) since phase changes with frequency are very sharp at low frequencies, whilst temperature slowly decreases through time.

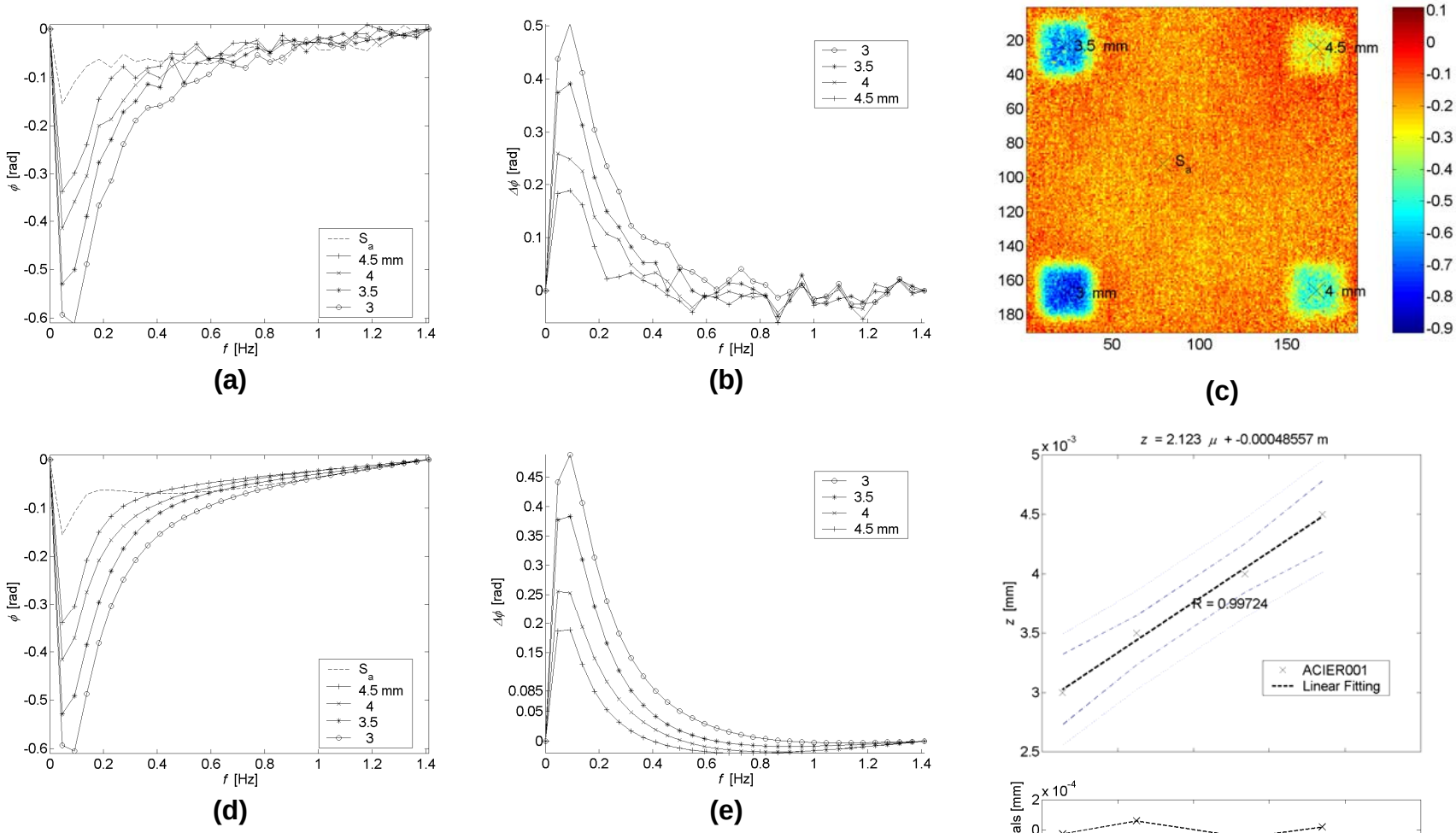

Figure 3.3. Quantitative results for specimen ACIER001: (a) raw phase; (b) raw phase contrast; (c) phasegram *f*=0.27 Hz showing defect depths and locations (d) reconstructed phase; (e) reconstructed phase contrast; (f) correlation results.

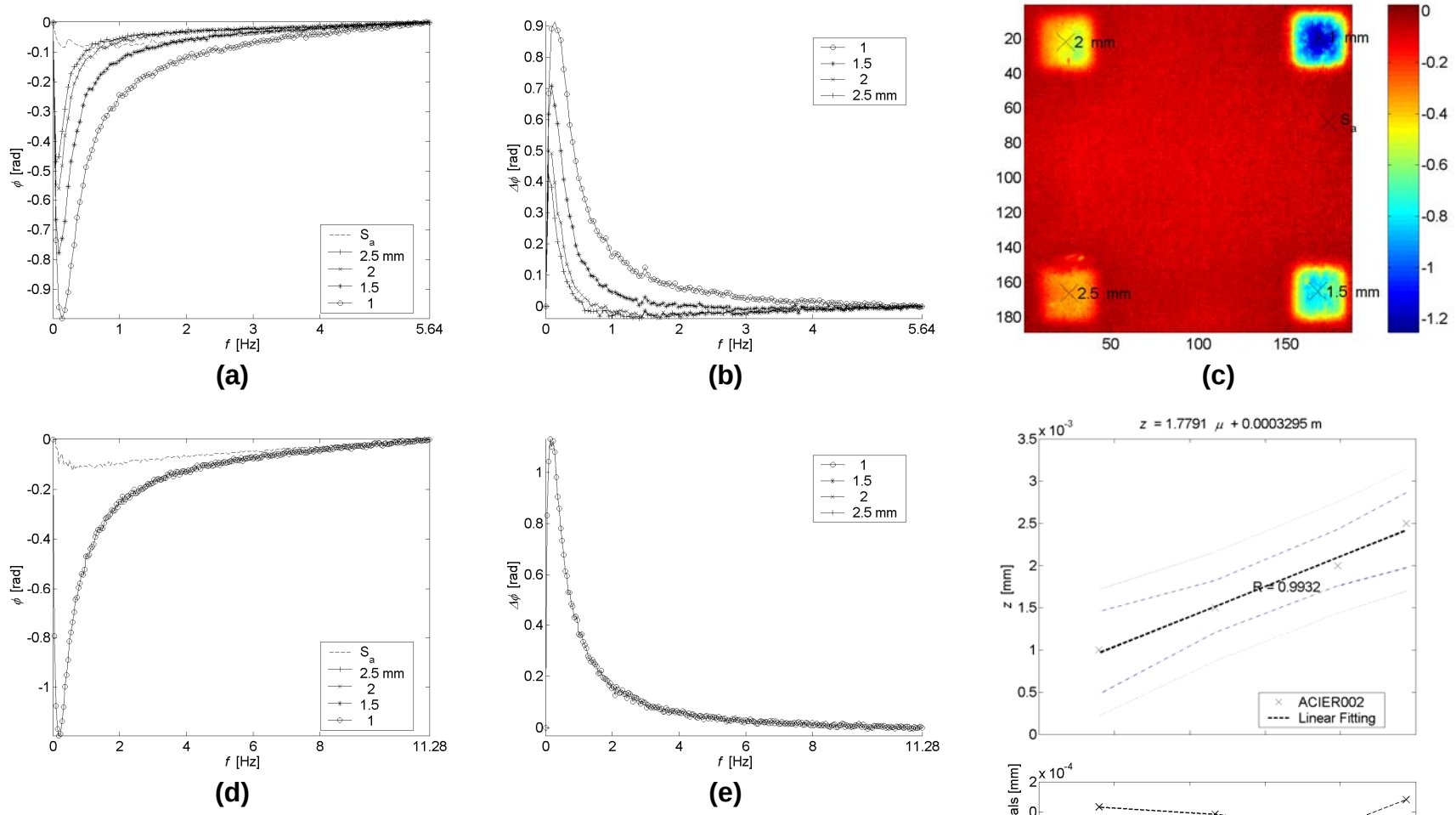

Figure 3.4. Quantitative results for specimen ACIER002: (a) phase; and (b) phase contrast for all defects (Δt=88 ms, $w(t)$=22 s, N=250); (c) defect depths and locations on phasegram at f=0.27 Hz (d) phase; and (e) phase contrast for the shallowest defect (Δt=44 ms, $w(t)$=22 s, N=500);.(f) correlation results.

Initial parameters for specimen ACIER002 were: Δt=88 ms, $w(t)$=22 s, and N=250. Raw phase and phase contrast profiles are shown in Figure 3.4a and Figure 3.4b, respectively, and the defects depths and locations are marked in the phasegram of Figure 3.4c. As a first observation, noise content is considerably less important than for specimen ACIER001, given that the inspected depths are closer to the surface and a better contrast is obtained with similar energy delivered to the surface. In addition, sampling and truncation parameters were adequate for the three deeper defects (1.5, 2.0 and 2.5 mm depth) since the corresponding f_b occur before the maximum available frequency (f_{max}= 5.64 Hz). However, f_b for the shallowest defect (1.0 mm depth) is too close to the maximum available frequency: f_b(1.0 mm) $\sim$ 5.64 Hz. Hence, time resolution was enhanced for the shallowest defect exclusively to increase the maximum available frequency f_{max} (as discussed in section 2.5.1). In this case: Δt=44 ms, $w(t)$=22 s and N=500.

The estimated blind frequency for the shallowest defect is f_b=9.65 Hz, which is below the maximum available frequency (f_{max}=11.28 Hz). Hence, it can be safely stated that f_{max} in this case is above the Nyquist limit as it should be. Phase and phase contrast results for the 1 mm depth defect are shown in Figure 3.4d and Figure 3.4e, respectively. No smoothing by TSR was required for specimen ACIER002 given the low noise levels. Hence, more information about the depth is available early in the sequence, which is traduced as less noisy profiles in the frequency domain.

Individual results for specimens ACIER001 and ACIER002 are presented in Figure 3.3f and Figure 3.4f, respectively. Data for both specimens are merged together in Figure 3.5. Correlation results by linear least squares regression of z on μ, are highly correlated (R=0.99), according to the following expression:

$$z_{\substack{ACIER001 \\ ACIER002}} = 1.72\sqrt{\frac{\alpha}{\pi\, f_b}} \quad [\mathrm{m}] \tag{3.1}$$

where the estimated C_1 is slightly lower than previous reported values of 1.8.

The quantitative analysis just presented, especially for specimen ACIER002, strengthens the significance of using an appropriate methodology for the determination of the sampling and truncation parameters.

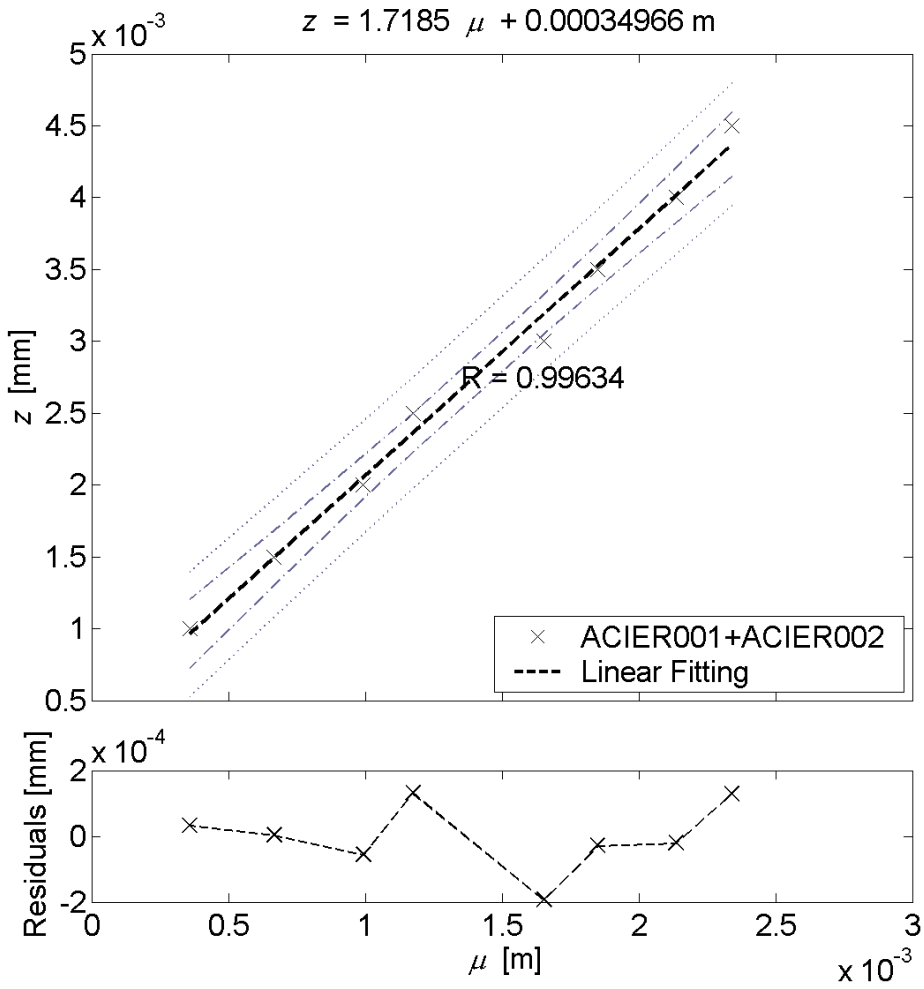

Figure 3.5. Correlation results for steel plates from 1.0 to 4.5 mm depth. Data from specimens ACIER001 and ACIER002 in Appendixes F.1 and F.2, respectively.

Phase contrast is just one way of obtaining the blind frequencies (real or apparent). Another option is to estimate the inflexion points of the phase profiles, which correspond to the f_b for a given defect. The advantage of this technique is that there is no need to define a sound area since phase profiles will behave the same up to f_b, and that automation is possible [87].

3.2.2. Composites

Continuing with the example of section 2.5.4, phase contrast is used to retrieve the blind frequencies of all 25 Teflon® inclusions on specimen CFRP006 in Appendix F.9. Figure 3.6a presents the correlation results. Defects have the same thickness but different depths and sizes, though they all fit into a linear correlation allowing depth discrimination. Experimental data is fitted by linear least squares regression (black dotted line) resulting on a high correlation coefficient (R=0.98). The goodness of the fitting results is evaluated through prediction bounds as described in Appendix E. For instance, Figure 3.6a includes the prediction bounds for a 95% confidence interval for two situations: fitted data and new observations.

Same analysis was performed on Glass Fiber Reinforced Plastic (GFRP) specimen, GFRP006 in Appendix F.9, with similar results (Figure 3.6b), though data is more disperse (R=0.94) and the prediction bounds are further apart than the corresponding bounds for CFRP006. Glass Fiber inspection is more demanding than Carbon Fiber in terms of speed and storage capacity. Hence, error is greater for specimen GFRP006.

The regression results shown in Figure 3.6a and b, were used to estimate the constant C_1 of Eq. (1.9), resulting in the following expressions:

$$z_{CFRP006} = 1.73\sqrt{\frac{\alpha}{\pi\ f_b}} \quad [\text{m}] \tag{3.2}$$

$$z_{GFRP006} = 2.26\sqrt{\frac{\alpha}{\pi\ f_b}} \quad [\text{m}] \tag{3.3}$$

for CFRP and GFRP, respectively. These results are close to the previously reported C_1 values ($1.5 < C_1 < 2$), in spite of the anisotropic nature of the inspected materials.

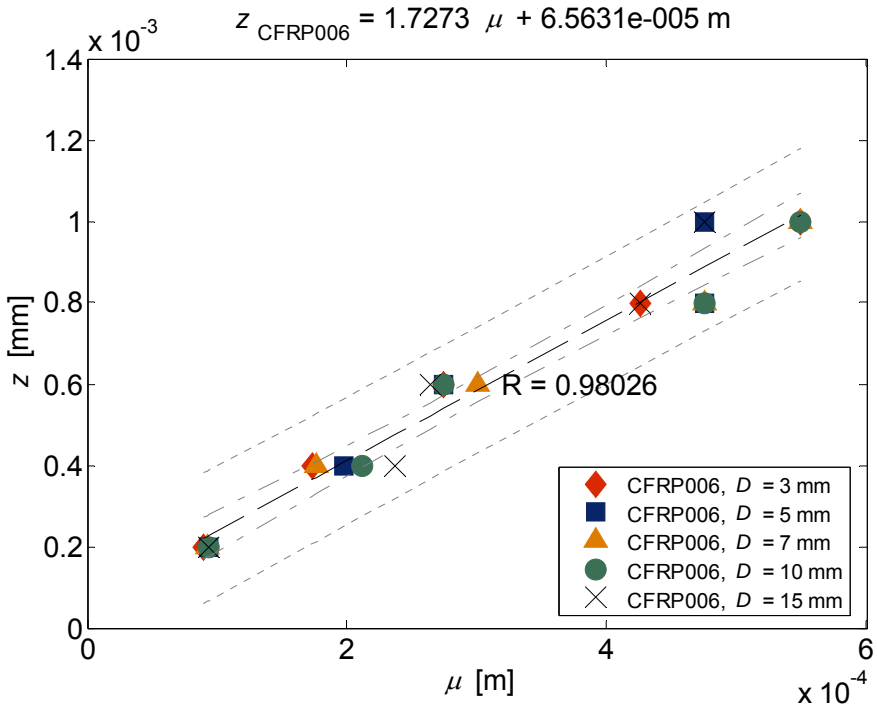

(a)

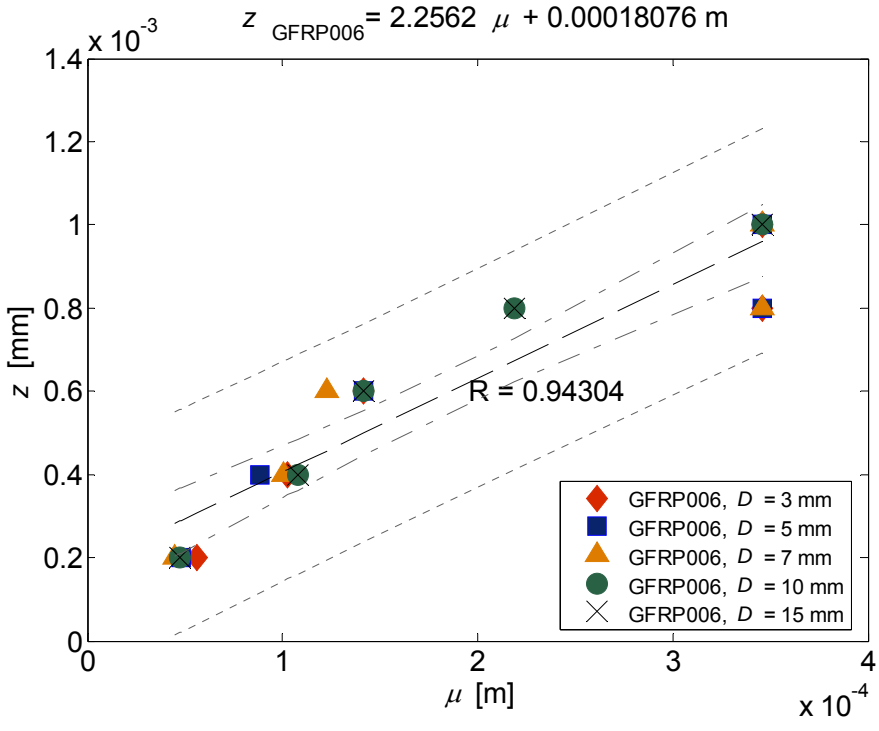

(b)

Figure 3.6. Correlation results for depth inversion on specimens (a) CFRP006, and (b) GFRP006, both specimens described in Appendix F.9.

Thus, provided that thermal data is correctly sampled and truncated, the f_b determined from phase profiles can be used for quantification. For instance, the absolute phase contrast $\Delta\phi$, can be used. In the next paragraph, quantification analysis is presented for two steel plates.

Plexiglas® and aluminum were also tested. Data acquisition for Plexiglas® was carried out following the guidelines proposed in section Chapter 2 and the results are presented in section 3.4.1. On the contrary, thermal data was badly sampled for aluminum. As discussed next, it is still possible to characterize internal defects in these conditions.

3.3. Badly sampled data

3.3.1. Aluminum

Eq. (1.9) can be used provided that thermal data is correctly sampled and truncated prior to the application of the FT. However, this is not always the case. On one hand, there are times when acquisition is performed without considering the Time-Frequency Duality relationship discussed in section 2.1; and on the other hand, it is not always possible to produce the desired frequency output because of equipment limitations.

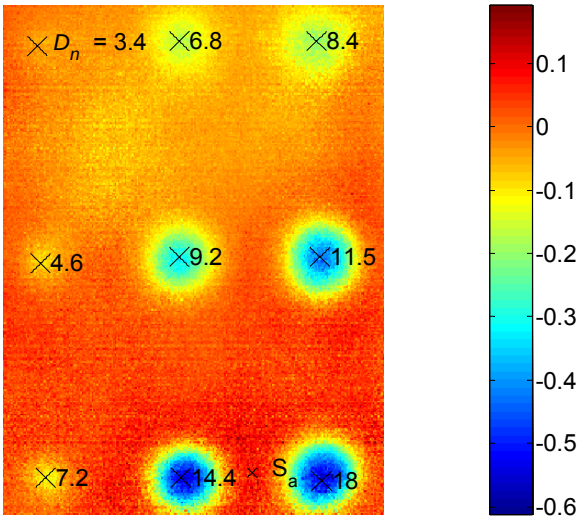

Figure 3.7. Phasegram at f=0.45 Hz showing defect locations and depths. Data from specimen ALU003 in Appendix F.5 (f_s=157.83 Hz, Δt=101 ms, $w(t)$=6.6 s).

In spite of this, data recorded on these conditions will still contain important depth information; see for instance the phasegram in Figure 3.7 showing the defect locations and depths from specimen ALU003, and their corresponding raw phase and phase contrast profiles in Figure 3.8a and Figure 3.8b, respectively.

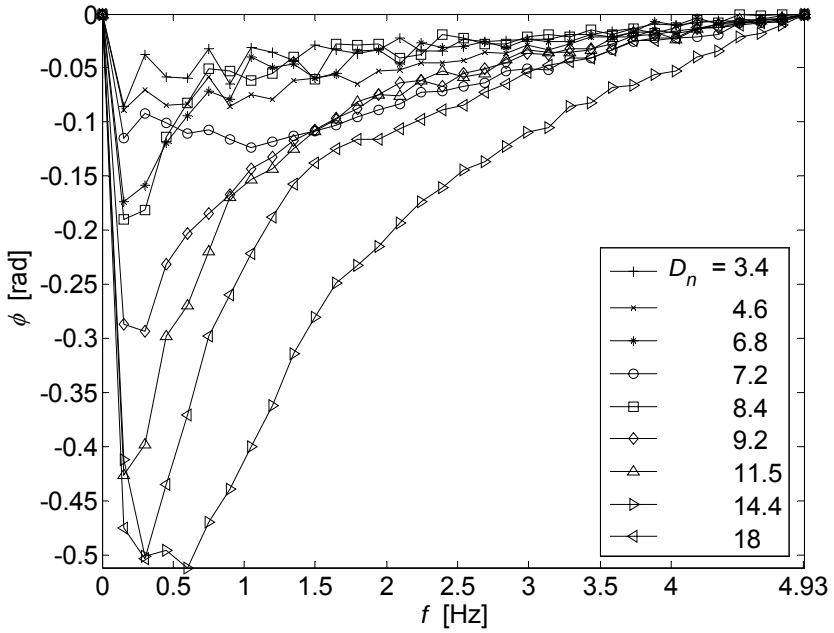

(a)

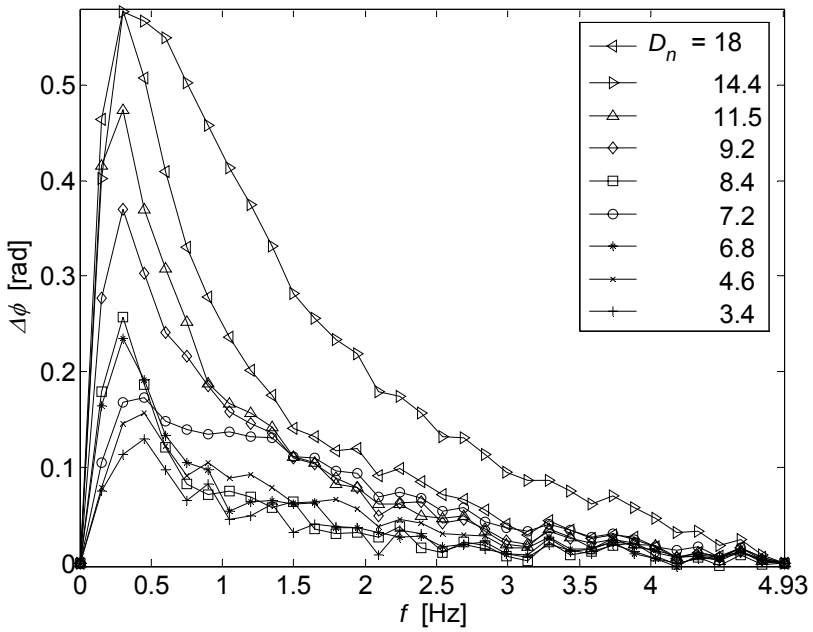

(b)

Figure 3.8. Raw (a) phase and (b) phase contrast profiles [88]. Data from specimen ALU003 in Appendix F.5 (f_S=157.83 Hz, Δt=101 ms, $w(t)$=6.6 s).

As can be noted, despite the high noise content, a difference in phase intensity (as a function of the depth) can still be distinguished. However, all profiles tend to zero

at the highest available frequency (4.93 Hz). This situation is more obvious in the phase contrast profiles in Figure 3.8b, which is a clear indication that a poor time resolution was used in at least 8 of the 9 defect profiles since no depth discrimination can be made from the corresponding f_b values. At best, time resolution was adequate for the defect with the lowest *normalized* diameter D_n, *i.e.* the one with the lowest time resolution requirements (D_n is used to account for the effect of size variations, see section 3.3.2). However, is more likely that time resolution was not good enough for any of the 9 defects. A new test at higher frame rate (and at least the same acquisition duration) would be required to confirm this observation. As a result, Eq. (1.9) cannot be used since it is impossible to determine the f_b values under these conditions. In spite of this, available data still shows a distinguishable pattern. For instance, maximum phase contrast increases with the depth. As seen in Figure 3.9, this relationship holds down to a minimum phase contrast threshold. Phase contrast profiles were smoothed in this figure using a Gaussian filter with a variance σ=1.

Hence, establishing a minimum phase threshold (0.1 rad in Figure 3.9), an *apparent* blind frequency f'_b can be estimated. An alternative relationship between phase and frequency can be derived knowing that for a thermal wave, phase ϕ is defined as [31]:

$$\phi = \frac{z}{\mu} \tag{3.4}$$

where z is the depth; and μ is the thermal diffusion length given by Eq. (1.5) [9]. A link between the defect depth z and the f_b can thus be derived:

$$z \propto \phi \cdot \mu = \phi \sqrt{\frac{\alpha}{\pi f}} \tag{3.5}$$

which is very similar to Eq. (1.9) except that the phase $\phi(z)$ is a function of the depth and that the frequency f, can not correspond to the blind frequency since there is no way to determine it with badly sampled data. Instead, we define the

apparent blind frequency f'_b, as the cutting frequency at a phase threshold (see Figure 3.9), and include this definition in Eq. (3.5) together with the minimum phase $\phi_{\min}$, which is still a function of the depth, to arrive to this expression:

$$z = C'_1 \cdot \phi_{\min} \sqrt{\frac{\alpha_d}{\pi\ f'_b}} = C'_1 \cdot \phi_{\min} \cdot \mu'_d \tag{3.6}$$

where C'_1 is the regression coefficient; $\phi_{\min}$ is the minimum phase for a defect; α_d is the thermal diffusivity of the defect; f'_b, is the apparent blind frequency; and $\mu'_d=(\alpha_d / \pi\ f'_b)^{1/2}$ is the *apparent* diffusion length.

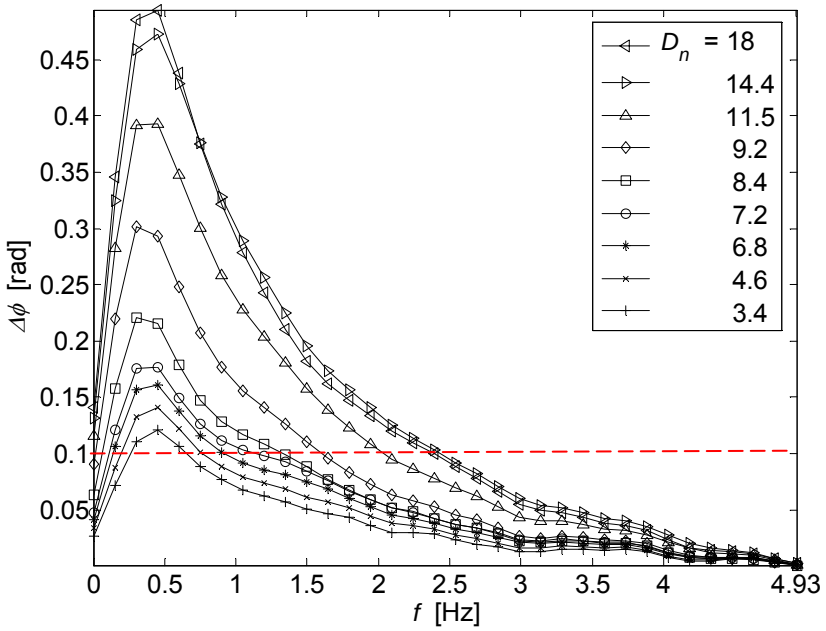

Figure 3.9. Phase contrast smoothed with a Gaussian (σ=1) showing a phase detection threshold of 0.1 rad. Data from specimen ALU003 in Appendix F.5.

The regression coefficient C'_1 is on a different scale than the corresponding constant on Eq. (1.9). The apostrophe is added to pinpoint that the result is based on an apparent blind frequency. The inclusion of the minimum phase of the defect on Eq. (3.6) is very convenient for the case of incorrectly sampled data for which f_b determination is not possible. Instead, the minimum phase will provide part of the required information about the depth. However, phase intensity is also related to

the defect size (and thickness). Subsequently, Eq. (3.6) will collapse for the case of same depth but different size defects as is the case for specimen ALU003 presented in Figure 3.8. The use of normalized parameters is proposed then to account for size variations.

3.3.2. Normalized diameter, D_N

Indeed, Eq. (3.6) is inappropriate when inspecting defects at the same depth but considerably different sizes. A possibility is to use the normalized diameter D_n, defined as [6], [7]:

$$D_n = \frac{D_{eq}}{z}\left(\frac{\alpha_{||}}{\alpha_{\perp}}\right)^{1/2} \tag{3.7}$$

where D_{eq} is the equivalent diameter (defined below); $\alpha_{\perp}$ and $\alpha_{||}$ are the thermal diffusivities perpendicular and parallel to the heat flow, respectively. For homogeneous materials, *e.g.* aluminum, $\alpha_{\perp}=\alpha_{||}$, hence $D_n=D_{eq}/z$.

3.3.3. Equivalent diameter, D_{EQ}

Although, shape of real defects is commonly irregular, it can be approximated from a single or a combination of different regular geometrical forms. In practice, it is possible to recover the shape from thermogram or phasegram using traditional segmentation techniques [89]-[91]. For instance, this is possible to do in step ❷ (defect detection) of the proposed methodology in section 2.5.3. A circle is a common shape approximation for which D_{eq} is the actual diameter of the circle, D. A shape factor (*e.g.* rectangle perimeter/circle perimeter = $2/\pi^{1/2}$) is proposed to compensate for additional thermal wall effects, such as cooling or resistance to heat flow, with respect to a circular defect of equivalent area when defects have geometrical forms other than a circle:

$$D_{eq} = \left(\frac{defect \quad perimeter}{circle \quad perimeter} \right) \cdot D \tag{3.8}$$

For instance, the equivalent diameter for a rectangle defect is calculated by multiplying the length of one of its sides by the factor: perimeter/circle perimeter=$2/\pi^{1/2}$.

3.3.4. Normalized diffusion length, μ_N

Normalized variables are commonly used as a way to broaden the validity of numerical or experimental procedures to include other defect geometries. In our case, the definition of a normalized diffusion length μ_n proves very handy:

$$\mu_n = \frac{\mu_d}{\mu_{S_a}} = \left(\frac{\alpha_d}{f_b} \cdot \frac{f_c}{\alpha_{S_a}} \right)^{1/2} \tag{3.9}$$

with μ_d and μ_{Sa} being the diffusion lengths for a defective and for a sound area, respectively.

3.3.5. Depth inversion with badly sampled data

Substituting the normalized diameter D_n and the normalized diffusion length μ_n, on Eq. (3.6), a relationship accounting for defect size variations can be derived:

$$D_n = C'_{n,1} \cdot \phi_{\min} \cdot \mu'_n \tag{3.10}$$

where $C'_{n,1}$ is the regression coefficient and μ'_n is the normalized diffusion length evaluated at the apparent blind frequency.

Figure 3.10 presents the regression results using f'_b values estimated from Figure 3.9. Results show that the normalized diameter D_n is highly correlated (R~0.96) to the product of the defect minimum phase and the normalized diffusion length μ'_n, both calculated at f'_b.

An important point has to be noted. For a complete defect characterization through Eq. (3.10) with badly sampled data, information about the defect size and defect thermal properties is required. The defect size can be determined through the phasegram sequence following classical feature segmentation algorithms, while the thermal properties (to calculate μ'_n) of the defect can be known *a priori*, *e.g.* looking for air gaps or water inclusions. With no information available about the defect, characterization with Eq. (3.10) would not be possible.

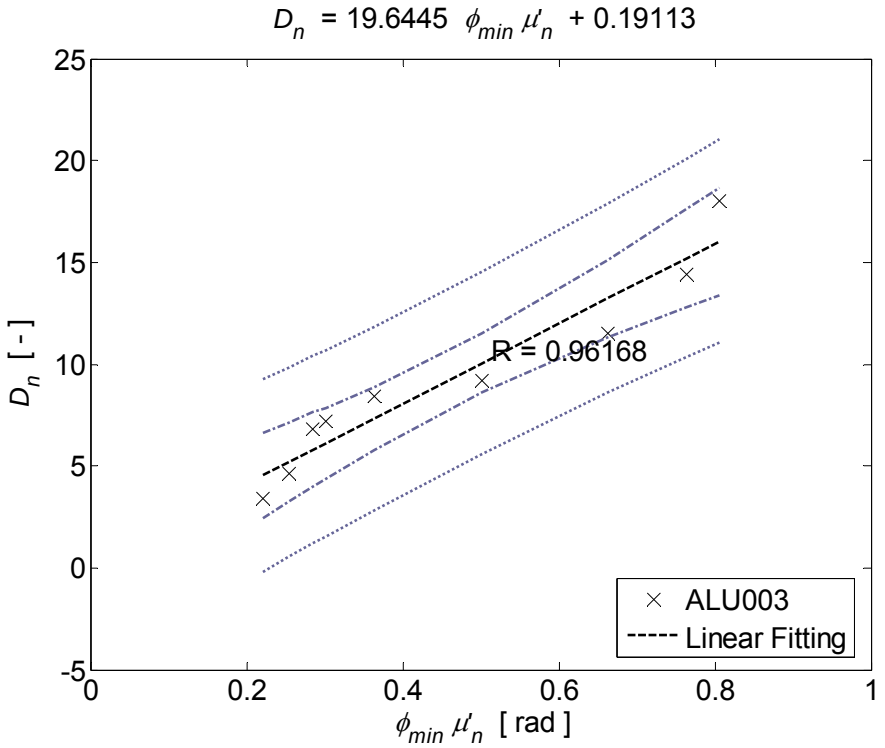

Figure 3.10. Llinear correlation using normalized parameters and a phase detection threshold of 0.1 rad. Data from specimen ALU003 in Appendix F.5.

IT techniques are usually applied under the assumption that the part being inspected has a planar surface. However, when complex shape objects are examined, the surface shape produces a signal distortion that may lead to faulty defect detection.

3.4. Non-planar quantitative inspection by PPT

Heat emission (as well as heat absorption) is at its maximum when the normal to the surface is parallel to the direction of the flow of energy (see Figure 3.11). Therefore, the emitted (or absorbed) signal is weaker when there is an angle between the normal to the surface and the direction of flow.

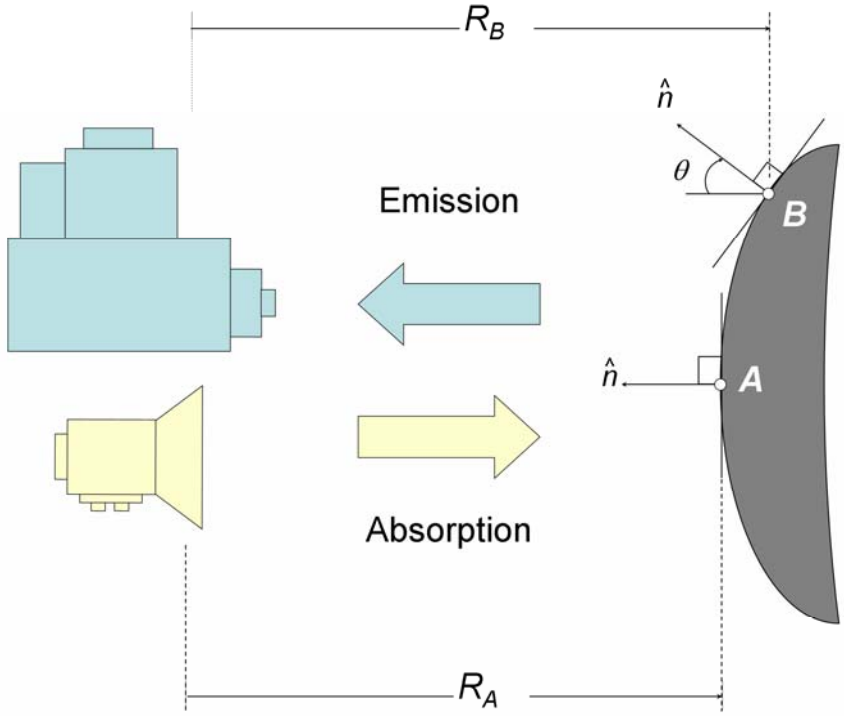

Figure 3.11. Complex shape inspection problem in IT.

This intensity reduction, caused exclusively by the surface geometrical variations, can lead to incorrect subsurface defect detection. Moreover, the points furthest away from the source (or sensor) will absorb (or will emit) less energy compared to the closer ones. In reference to Figure 3.11 shown above, in addition to the angle between the normal at the point B and the direction of flow, B is located further from the source (and from the sensor) in comparison to point A. Without shape information on the object, defects located under the surface just below point B will be difficult to detect by IT. Aircraft industry is a good example of application. Aircraft fuselage and wings are never completely flat. Visual techniques, ultrasounds, eddy currents and X-rays, are used. However, these techniques are

slow and they are prone to subjective interpretation and human errors. IT allows the examination of surface portions up to 4 m^2 at once, thus greatly reducing the inspection time making the technique especially interesting for the examination of aeronautical parts.

Some interesting solutions have been proposed [5], p.430: point-source heating, video thermal stereo vision [92], direct thermogram correction, and Shape-from-Heating (SfH) [93]-[100]. SfH is the most complete among these methods; it is based on Shape-from-Shading theory [101], and offers 1D [94]-[96] and 2D [93], [97] solutions for shape correction. SfH retrieves the surface shape from the Early Recorded Thermogram (ERT), *i.e.* the first useful thermogram after thermal excitation in which no defect is still visible. Subsequent thermograms on the sequence are corrected using this information.

On the other hand, as discussed in section 2.2.3, surface geometry has little impact on phase. Hence, if we are not interested in actually recovering the surface shape, phase results from PPT could be exploited for complex shape inspection. As a first case, a Plexiglas® plate was tested to asses the impact of the surface orientation.

3.4.1. Surface orientation: Plexiglas®

Figure 3.12 presents the quantitative analysis based on phase for specimen PLEXI014 (Appendix F.8). Phase and phase contrast profiles are shown in Figure 3.12a and Figure 3.12b, respectively. Defects depths and locations are indicated on the phasegram (f=0.0032 Hz) in Figure 3.12c, and the correlation results are displayed in Figure 3.12d. As was the case for the correctly sampled cases studied above, excellent agreement between z and μ is observed (R~1).

It should be mentioned at this point that, following the reasoning exposed in section 2.1, data is over-sampled since all the important information is contained at frequencies below approximately 0.1 Hz as can be deduced from the phase and phase contrast profiles.

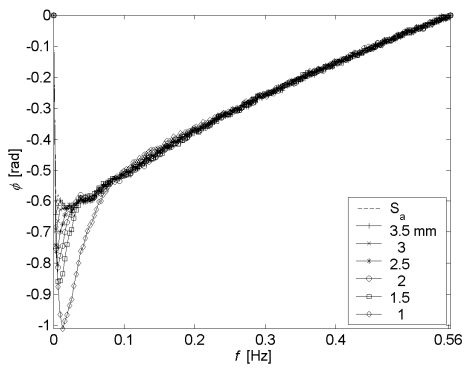

(a)

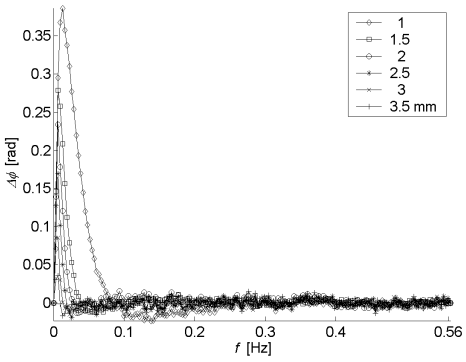

(b)

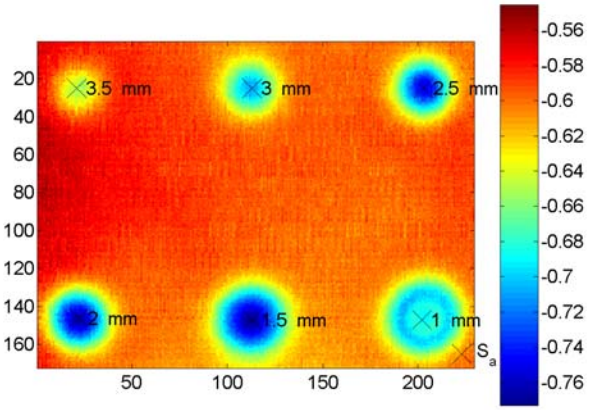

(c)

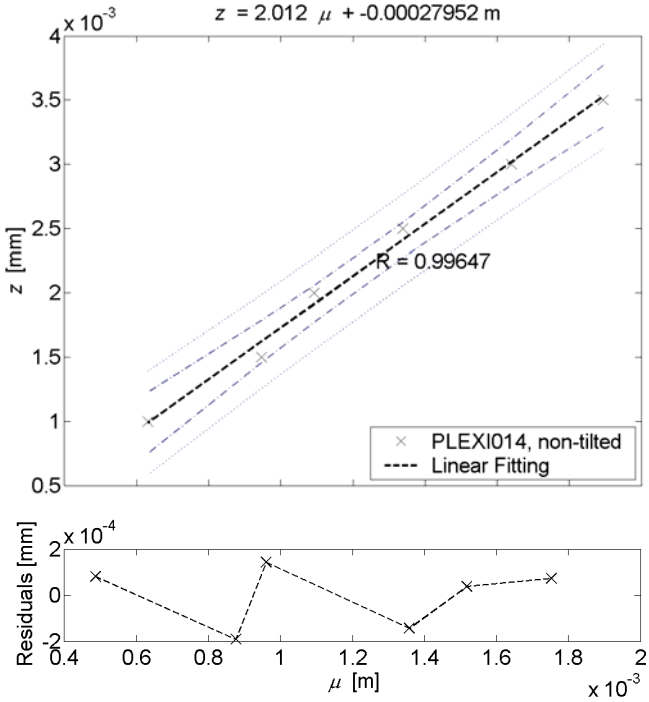

(d)

Figure 3.12. Surface orientation, non-tilted plate: (a) Phase; and (b) phase contrast profiles; (c) phasegram at f=0.0032 Hz; and (d) correlation results. Data from specimen PLEXI014 in Appendix F.8 (f_s=22.55 Hz, $w(t)$=311 s, Δt=889 ms Hz, N=350).

This situation will be further examined in section 3.5.4. For the purposes of this section, over-sampling is of no consequence. Quantitative analysis was repeated on the same specimen (PLEXI014 in Appendix F.8), only this time, the plate was tilted at a 30^o angle with respect to the camera. Results are presented in Figure 3.13.

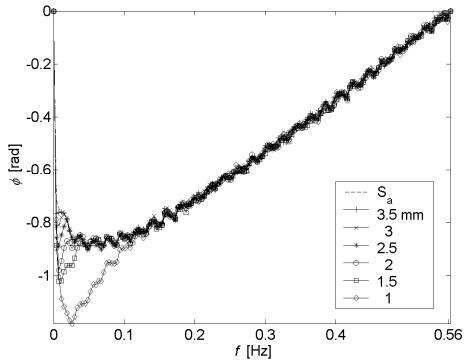

(a)

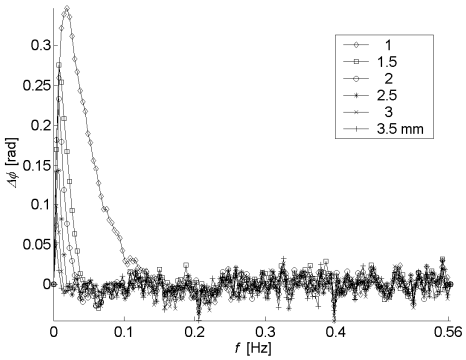

(b)

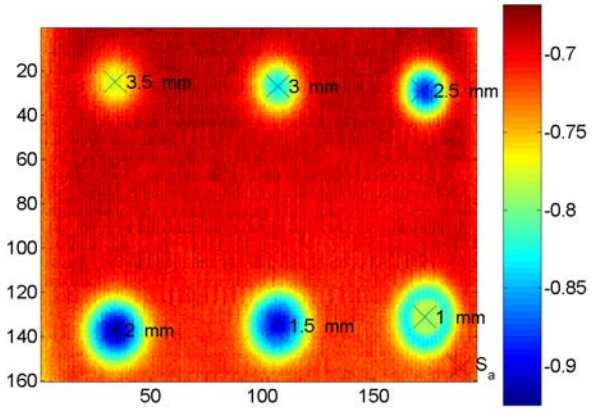

(c)

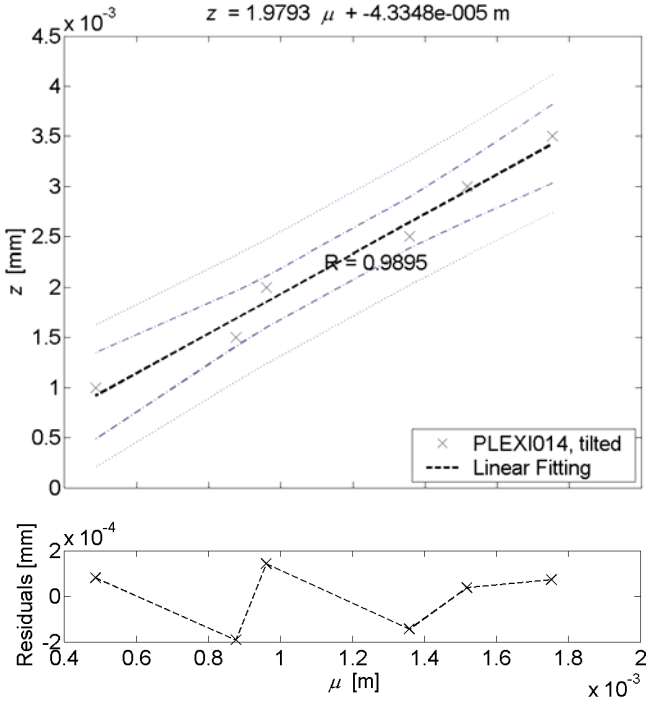

(d)

Figure 3.13. Surface orientation, tilted plate: (a) Phase; and (b) phase contrast profiles; (c) phasegram at f=0.0038 Hz; and (d) correlation results. Data from specimen PLEXI014 in Appendix F.8 (f_s=22.55 Hz, $w(t)$=267 s, Δt=889 ms Hz, N=300).

Besides a slight variation on the number of thermal data used as input, depth inversion with the phase was performed in exactly the same way.

Correlation results for the tilted and non-tilted Plexiglas® plates showed in both cases a higher C_1 value than for CFRP, GFRP and steel studied in section 3.2:

$$z_{PLEXI014,\ non-tilted} = 2.01\sqrt{\frac{\alpha}{\pi\ f_b}} \quad [\text{m}] \tag{3.11}$$

$$z_{PLEXI014,\ tilted\ (30^o)} = 1.98\sqrt{\frac{\alpha}{\pi\ f_b}} \quad [\text{m}] \tag{3.12}$$

Figure 3.13 lead to some interesting observations. First, phase profiles show a periodic pattern as can be seen in Figure 3.13a. After some additional tests were carried out, it was concluded that an overheating of the power supply of the IR camera induced the signal degradation. In any case, correlation results on Figure 3.13d agrees closely to the non-tilted case, which led us to think that both, surface orientation (up to 30^o with respect to the camera) and low frequency periodic degradation, have little impact on depth inversion results. On the contrary, defect shape is affected by the inspection angle as seen in the phasegram of Figure 3.13c when compared with the corresponding non-tilted phasegram in Figure 3.12c. Defects at the right of the phasegram are further away from the camera, so optical distortion is larger. Finally, although correlation coefficient is also high for the tilted plate (R~0.98), data is more disperse and prediction bound are further apart than for the non-tilted case.

3.4.2. Surface Shape: CFRP

A series of tests were performed on a set of specimens made on Carbon Fiber (CFRP) having three different shapes: planar (CFRP006 in Appendix F.9), curved (CFRP007 in Appendix F.10) and trapeze (CFRP008 in Appendix F.11). All specimens contain 25 Teflon® inclusions at different depths ($0.2 < z < 1.0$ mm) and sizes ($3 < D < 15$ mm). Figure 3.14 presents representative thermograms (left) at t=6.3 ms, and phasegrams (right) at f=0.3 Hz. Figure 3.14a corresponds to a planar plate (specimen CFRP006). Non-uniform heating is evident in the thermogram (left), but the phasegram (right) is unaffected. Results for CFRP007 are shown in Figure 3.14b. The thermogram (left) is affected by both the shape of

the surface and by non-uniform heating. The specimen was inspected from the concave side, although the form of thermogram might indicate the opposite.

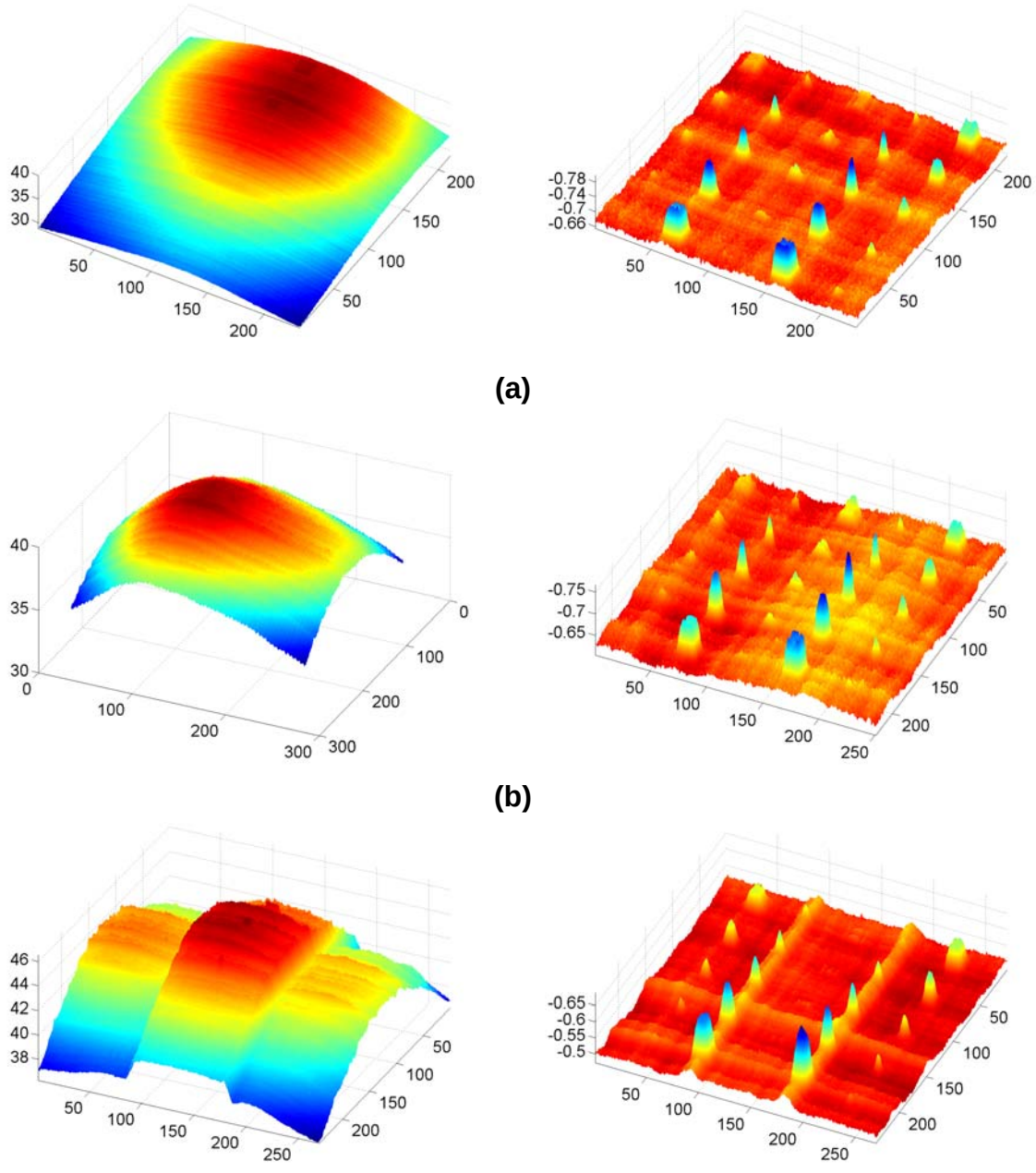

Figure 3.14. Complex shape inspection. Thermograms at t=6.3 ms (left) and phasegrams at f=0.3 Hz for: (a) a planar plate (specimen CFRP006 in Appendix F.9); (b) a curved plate (specimen CFRP007 in Appendix F.10); and (c) a trapezoidal plate (specimen CFRP008 in Appendix F.11).

This situation highlights an important ambiguity when working with thermogram from complex shapes: Without additional information about the specimen, it is difficult to know whether a surface is concave or convex. On the contrary, the phasegram (right) is practically undisturbed by non-uniformities, and surface shape, and knowing if the shape is concave or convex is not important in this case. However, if the shape of the surface is of interest, methods based on thermal data, *e.g.* Shape-from-Heating can be used to extract the surface shape information, although the ambiguity of whether the surface is concave or convex persists. Another possibility is to work with amplitude data, which conserve surface shape and non-uniformities information. Results for the third specimen are presented in Figure 3.14c. This specimen was inspected from the concave side as well. Again, thermal information (left) is ambiguous. The phasegram (right) show more signs of the surface shape in this case. Sharp surface changes (30^o angle) can be seen along two of the defects columns (at 0.4 and 0.6 mm depth). Nevertheless, defects can be easily detected. In all phasegrams in Figure 3.14, the fiber (0^o,90^o) structure of the CFRP composites can be seen.

Quantitative PPT was performed on these three plates. The results for the planar plate were presented in Figure 3.6a. Figure 3.15 and Figure 3.16 show the results for the curved specimen and for the trapezoidal plate, respectively. Besides a slight change in slope and offset (shown in each figure), correlation results for all three specimens (CFRP006, CFRP007 and CFRP008) fit into a linear relationship of the form of Eq. (1.9). The following expression can be used to estimate the depth of a defect by knowing its blind frequency and the thermal properties of the specimen:

$$z_{CFRP} = 1.47\sqrt{\frac{\alpha}{\pi\, f_b}} \tag{3.13}$$

Quantitative results from all three specimens are merged together in Figure 3.17 confirming the agreement with Eq. (3.13). Differences in the estimated f_b values are due to the several uncertainties involved in PPT calculations described in section 3.5.

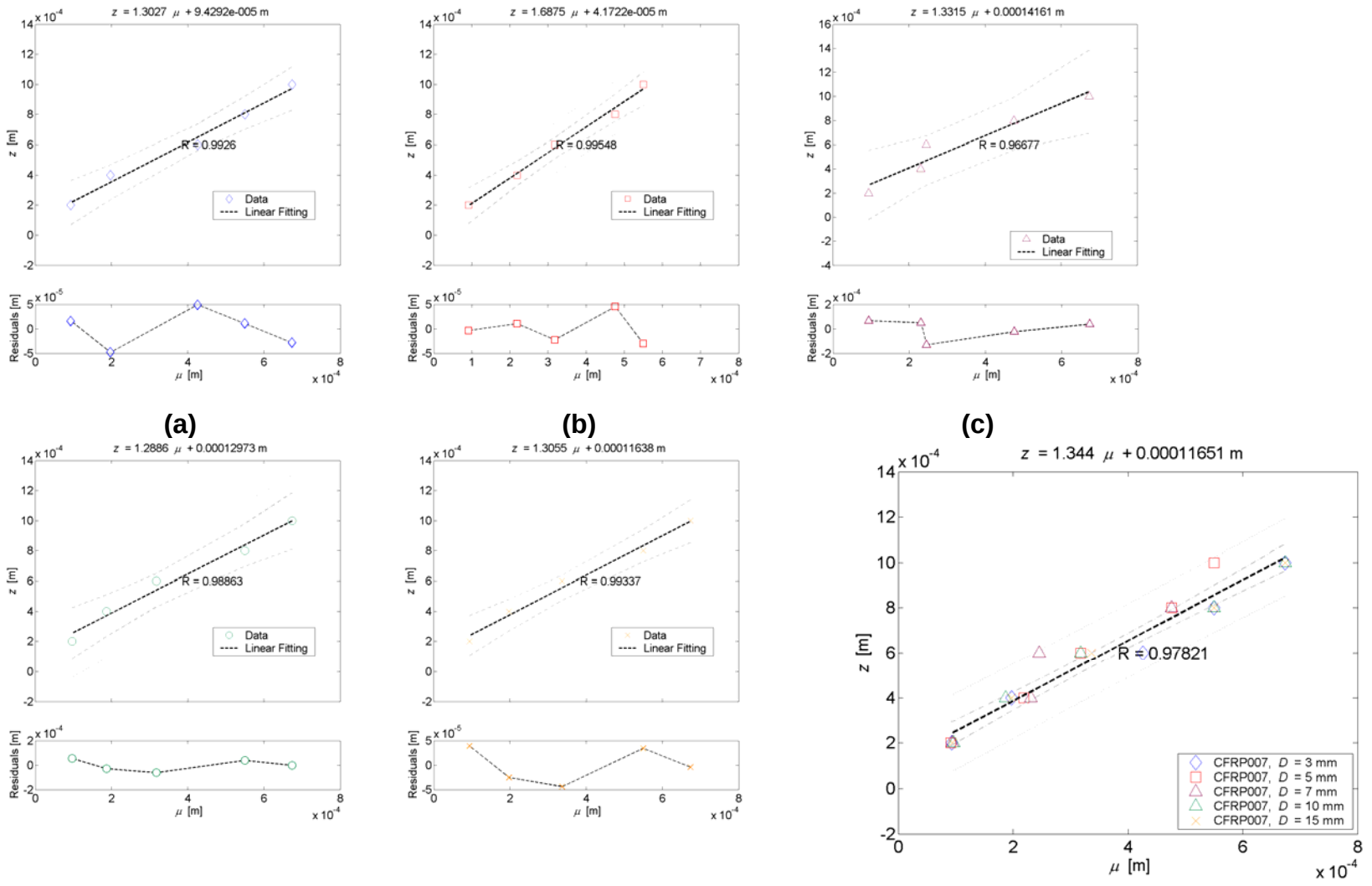

Figure 3.15. Quantitative results for CFRP007: *D* = (a) 3 mm; (b) 5 mm; (c) 7 mm; (d) 10 mm; and (e) 15 mm.

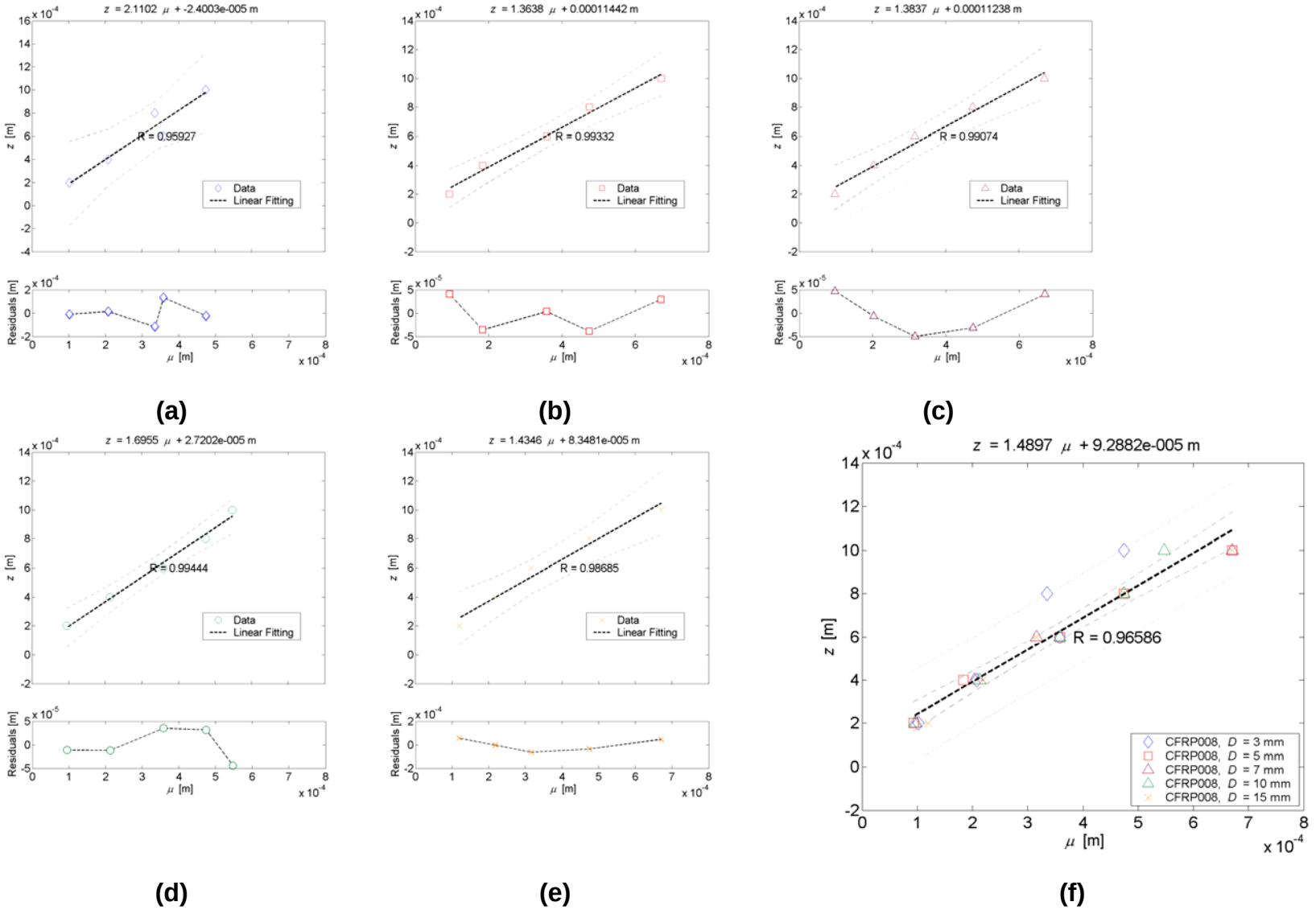

Figure 3.16. Quantitative results for CFRP008: *D* = (a) 3 mm; (b) 5 mm; (c) 7 mm; (d) 10 mm; and (e) 15 mm.

In Figure 3.17 experimental data came from three plates having different surface shapes. Still, depth can be predicted with good accuracy from Eq. (3.13) with no more information than the blind frequency for the different defects and the specimen thermal diffusivity. Shallow defects are better fitted as expected (there are 15 points in the 0.2 mm depth cluster at the lower left corner). More variability can be seen as depth increases. For instance, at z=0.8 mm, data is distributed in the range: $3.2 \times 10^{-4} < \mu < 5.5 \times 10^{-4}$ m.

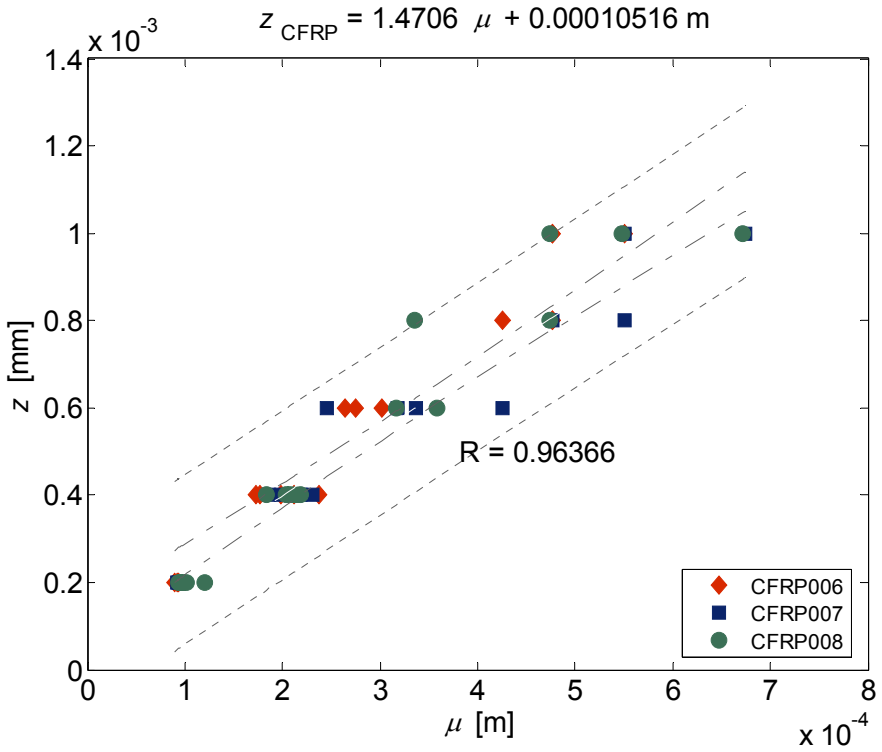

Figure 3.17. Comparison of complex shape results for specimens CFRP007 and CFRP008 with planar results on specimen CFRP006.

It should also be pointed out that the depth range considered for this experience is relatively short (from 0.2 to 1.0 mm). Discrimination between considerably larger defects in homogeneous materials is by far more evident as can be confirmed from the steel results presented in section 3.2.1.

A similar analysis wa performed to three GFRP specimens having similar geometries and defect distributions as the CFRP (see Appendices F.9 to F.11). Results are shown in Figure 3.18.

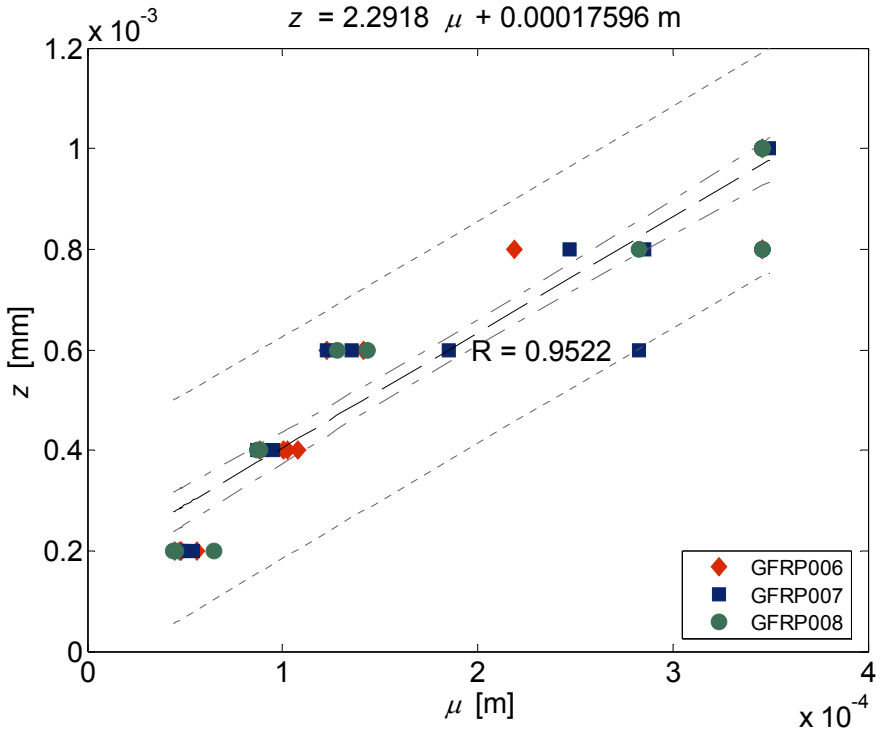

Figure 3.18. Comparison of complex shape results for specimens GFRP007 and GFRP008 with planar results on specimen GFRP006.

Incidentally, the thermal properties used for all the examples presented here correspond to those found in the literature and summarized in Appendix B. However, reported diffusivity values diverge greatly from one source to another, especially for composite materials. This is primarily due to variability in composition from one manufacturer to the other, but also to differences in the way thermal properties are determined. Moreover, it is observed from the results presented up to now that the estimation of C_1 presents some variability. Several factors contribute to this discrepancy as described next.

3.5. Uncertainties

Several sources of uncertainty affect the inversion results. First, as in any thermographic experience, there is noise in all of its forms: electronic, optical, heating, environmental, structural, etc. see section A.3.4. For the configuration used on this study, the Signal-to-Noise Ratio (SNR) was estimated to be SNR=65, which is within the values commonly found in FPA configurations [5].

Although the composition, and therefore the thermal properties of the materials, is not perfectly homogeneous; diffusivity data available on the literature, and brought together in Appendix B, was used for the estimation of the C_1 values. Hence, an error is introduced with this material homogeneity hypothesis, especially on the case of Carbon Fiber and Glass Fiber composites, which are anisotropic. Furthermore, phase contrast calculations are subjected to some variability, since non-defective area is not perfectly homogeneous.

The following paragraphs review some of the common uncertainty sources that are found in any PPT experience.

3.5.1. Impact of the selected sound area, S_a

An important source of variability comes from the fact that (phase) contrast calculations are used to determine the blind frequencies. As is well known for the thermal case [43], (temperature) contrast depends on the selected sound area. This is primarily due to non-uniform heating and emissivity variations on the surface. Contrast calculations using the phase greatly increase the accuracy of the results, since phase is less affected by these two problems as pointed out above. Still, phase shows some variability on non-defective zones that contribute to the uncertainty of the results. See for instance the phasegram in Figure 3.19a.

To assess the impact of contrast calculations on depth retrieval, a series of tests were performed on specimen PLEXI014 (Appendix F.8) using different sound

areas, ranging from the coolest to the warmest regions on the plate as indicated in Figure 3.19a.

The phasegram in Figure 3.19a shows the defect depths and locations as well as the locations of the four different sound areas: $S_{a,1}$, $S_{a,2}$, $S_{a,3}$ and $S_{a,4}$.

The correlation results for the four cases are compared in Figure 3.19b.

Individual correlation results; including the regression coefficients, the correlation coefficients, the prediction bounds for the fitted data and for new observations, and the residuals, as described in Appendix E; are presented in Figure 3.20.

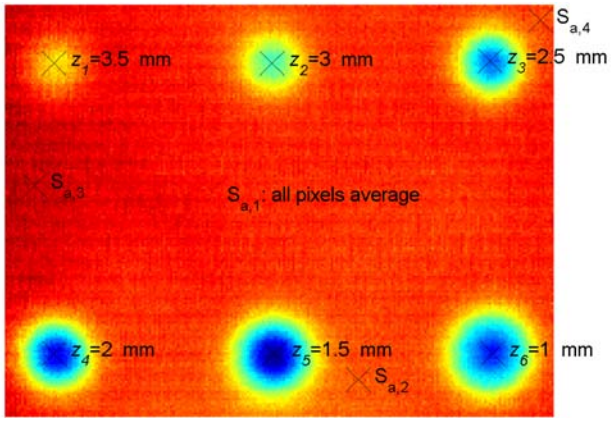

(a)

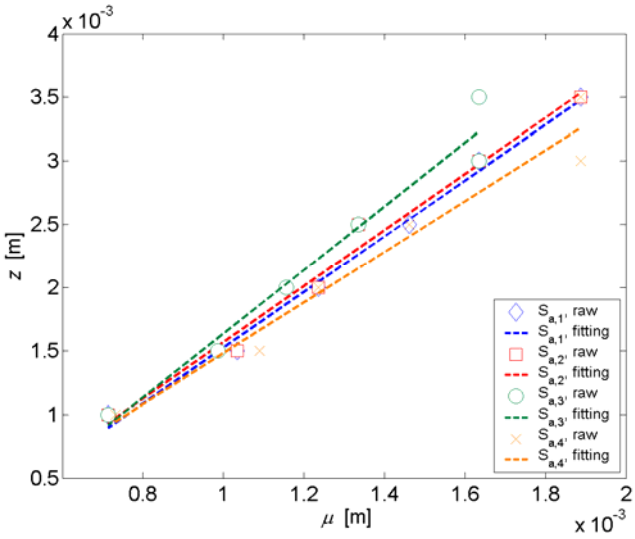

(b)

Figure 3.19. Impact of S_a on quantitative results: (a) Defect and sound areas locations on phasegram at f=0.0032 Hz; (b) correlation results.

Data is more disperse for deeper defects. Through examination of the individual correlation curves, it is found that frequency resolution was not good enough in the last two cases (Figure 3.20c and d) to discriminate between the two deepest defects. Correlation coefficients are high in all cases but data dispersion is

progressively higher and prediction bounds wider from Figure 3.20a to Figure 3.20d.

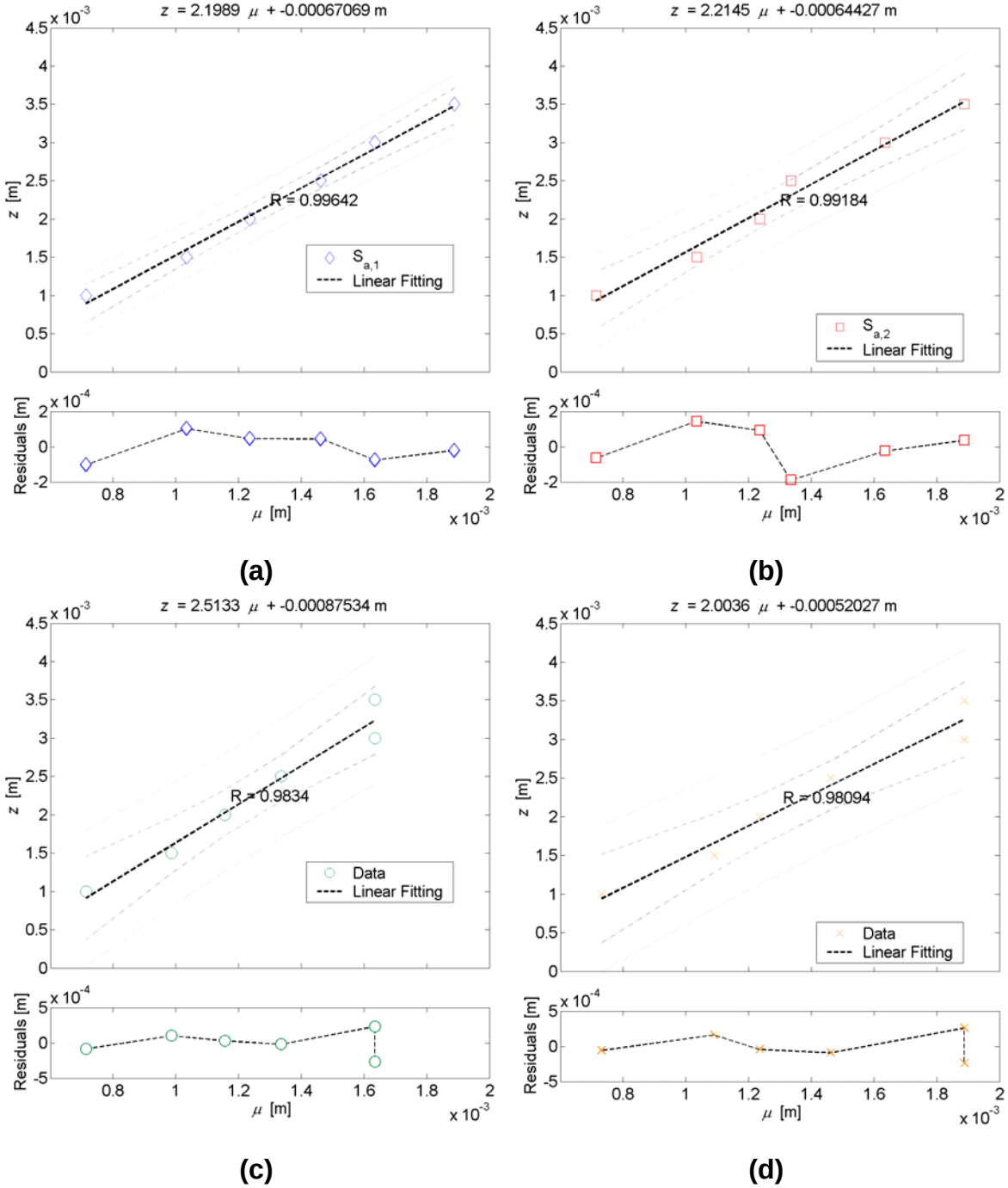

Figure 3.20. Impact of S_a on quantitative results: (a) $S_{a,1}$; (b) $S_{a,2}$; (c) $S_{a,3}$; and (d) $S_{a,4}$ (see Figure 3.19). Data from specimen PLEXI014 in Appendix F.8.

Hence, from the results presented in Figure 3.20, the estimated regression coefficients C_1, can vary from 2.00 to 2.51. Judging from the prediction bounds, selecting $S_{a,1}$ (Figure 3.20a), *i.e.* the average of the entire surface, as sound area produces the most reliable results in this case (for which the overall surface occupied by defects is much smaller that the field of view).

3.5.2. Impact of the truncation window size, *w(t)*

Specimen PLEXI014 (Appendix F.8) was used again to estimate the impact of changing the size of the truncation window on depth inversion results. Four cases were evaluated: $w(t)_1$=400 s, $w(t)_2$=300 s, $w(t)_3$=200 s and $w(t)_4$=100 s, all merged together in Figure 3.21. As before, error is greater for deeper defects.

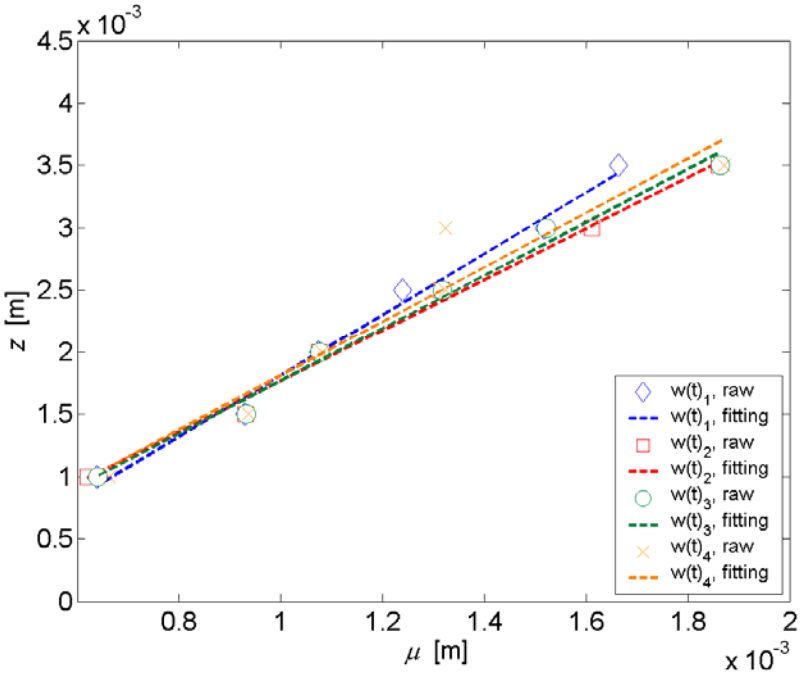

Figure 3.21. Impact of *w(t)* on quantitative results : $w(t)_1$=400 s, $w(t)_2$=300 s, $w(t)_3$=200 s, $w(t)_4$=100 s. Data from specimen PLEXI014 in Appendix F.8.

The main effect of reducing the size of *w(t)* is a loss of frequency resolution Δf, as expected from Eq. (2.9), which can be confirmed in Figure 3.22d. Reducing the truncation window size below $w(t)_4$=100 s will further degrade the quantification results.

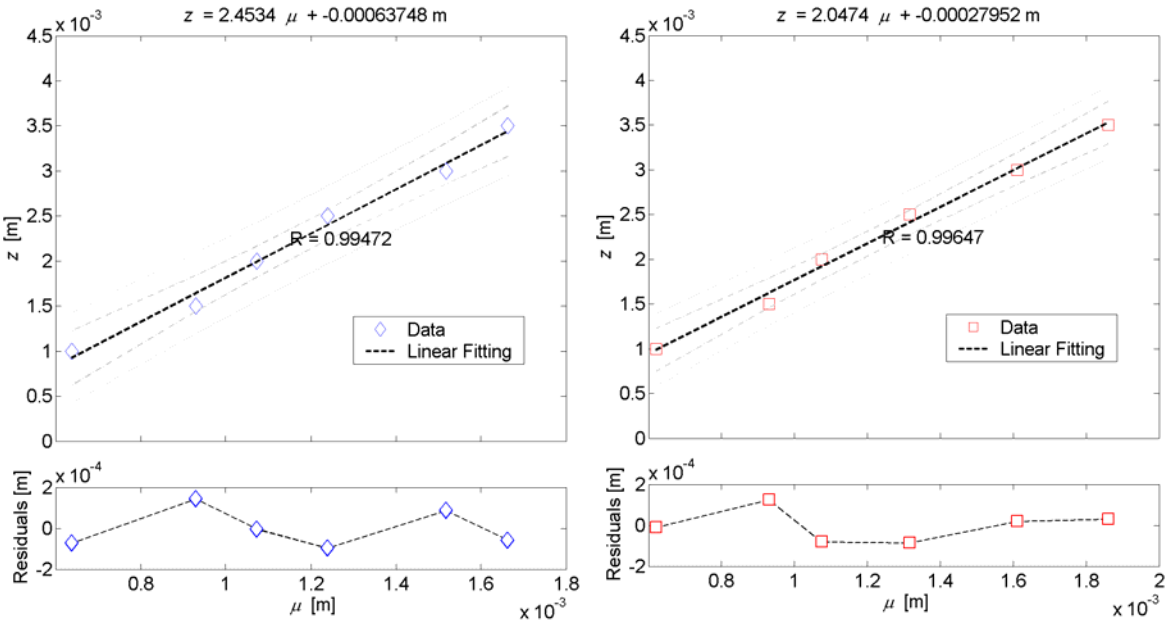

(a)

(b)

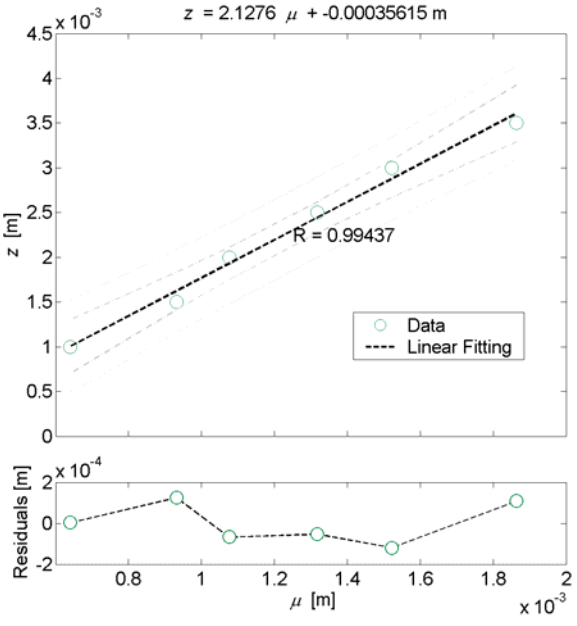

(c)

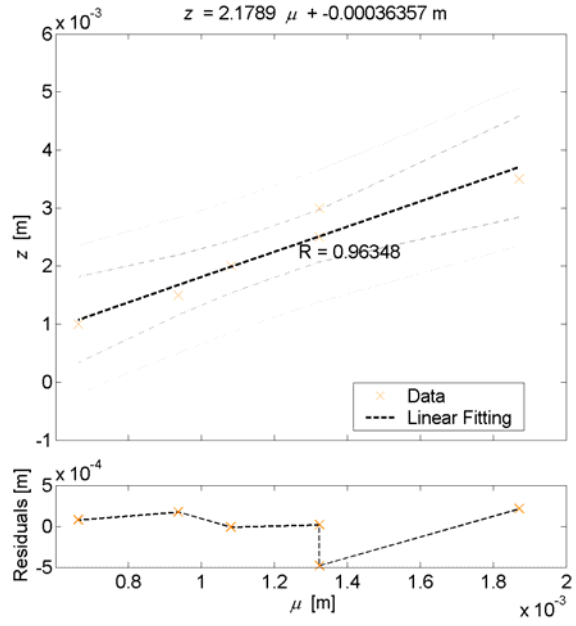

(d)

Figure 3.22. Impact of *w(t)* on quantitative results: (a) $w(t)_1$=400 s; (b) $w(t)_2$=300 s; (c) $w(t)_3$=200 s; and (d) $w(t)_4$=100 s (see Figure 3.19). Data from specimen PLEXI014 in Appendix F.8.

3.5.3. Impact of the time resolution, Δt

Because of the Time-Frequency Duality of the FT, time resolution Δt, can be reduced up to a point that the resulting frequency components will still contain the most pertinent information for depth discrimination. Figure 3.23 and Figure 3.24 illustrate this fact for four conditions: Δt_1=0.88 s, Δt_2=1.77 s, Δt_3=3.55 s and Δt_4=7.11 s, with $w(t)$=311 s.

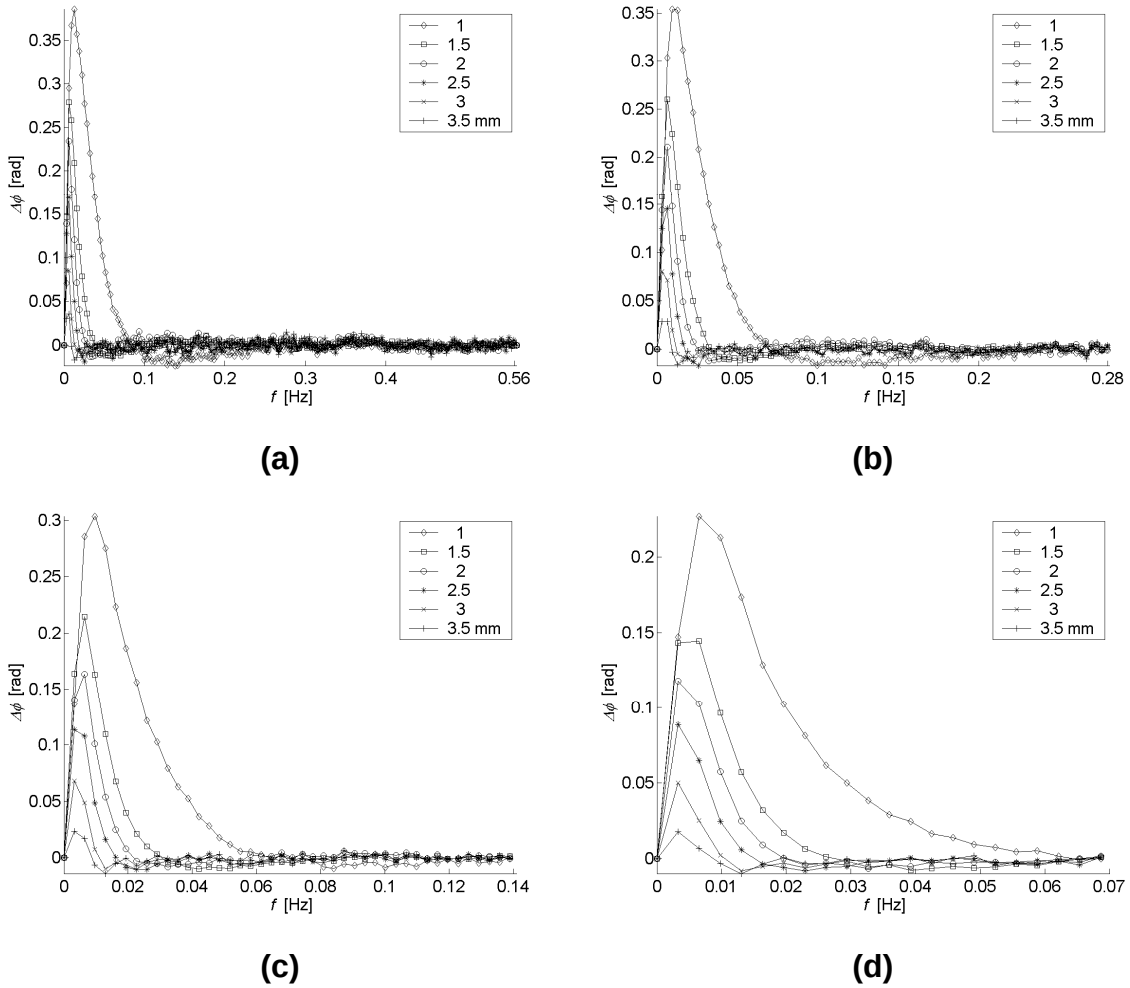

Figure 3.23. Impact of Δt on quantitative results using phase contrast: (a) Δt_1=0.88 s; (b) Δt_2=1.77 s; (c) Δt_3=3.55 s; and (d) Δt_4=7.11 s. Data from specimen PLEXI014 in Appendix F.8.

In Figure 3.23, phase contrast profiles using the four different time resolutions are shown. Frequency resolution is unchanged since the truncation window has the

same size in all cases, see Eq. (2.9). The main effect of reducing the time resolution is to redistribute the phase values over a smaller number of frequency components (equally spaced). This redistribution has a small impact on low frequency components (see the reduction on phase contrast intensity from Figure 3.23a to Figure 3.23d). In contrast, high frequency elements, which do not provide any useful information, are taken out of the results. Another sign of the impact of increasing Δt can be highlighted considering the phase contrast curve for the 1 mm depth defect, in this case, there are 4 discrete frequencies before the maximum contrast in the Δt_1=0.88 s case against 2 frequencies in the Δt_4=7.11 s case. Nevertheless, the effect is negligible as can be seen from Figure 3.24. The correlation curves for all the cases considered in Figure 3.23, are regrouped in Figure 3.24. Contrary to the varying sound area and the truncation window size cases, the fact of worsen time resolution has a greater impact on shallow defects, since the blind frequencies are higher and are thus more affected.

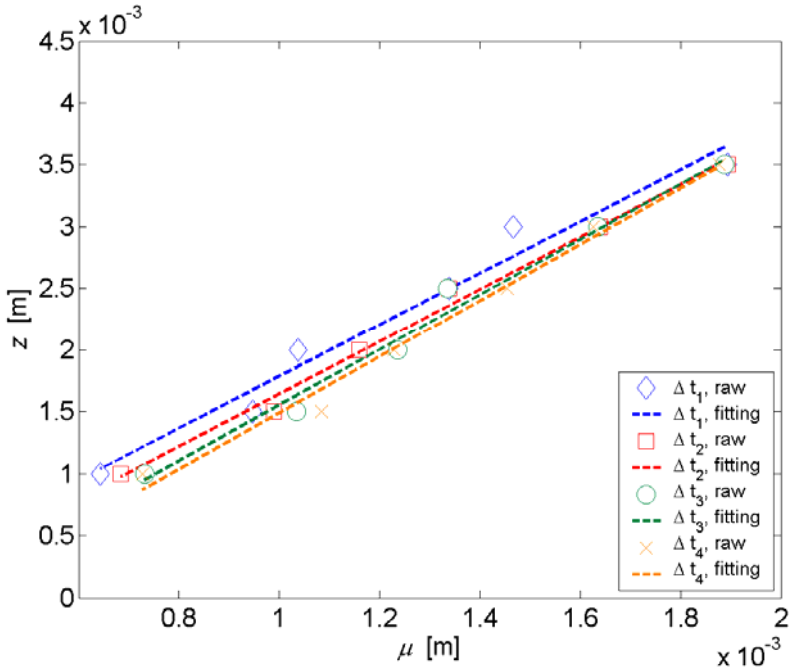

Figure 3.24. Impact of Δt on quantitative results.

All four cases produce approximately the same results (see individual results in Figure 3.25). However, the case with Δt_4=7.11 s is the more interesting from the computer memory point of view (since it uses $^1/_8$ of the data utilized in the Δt_1=0.88 s case).

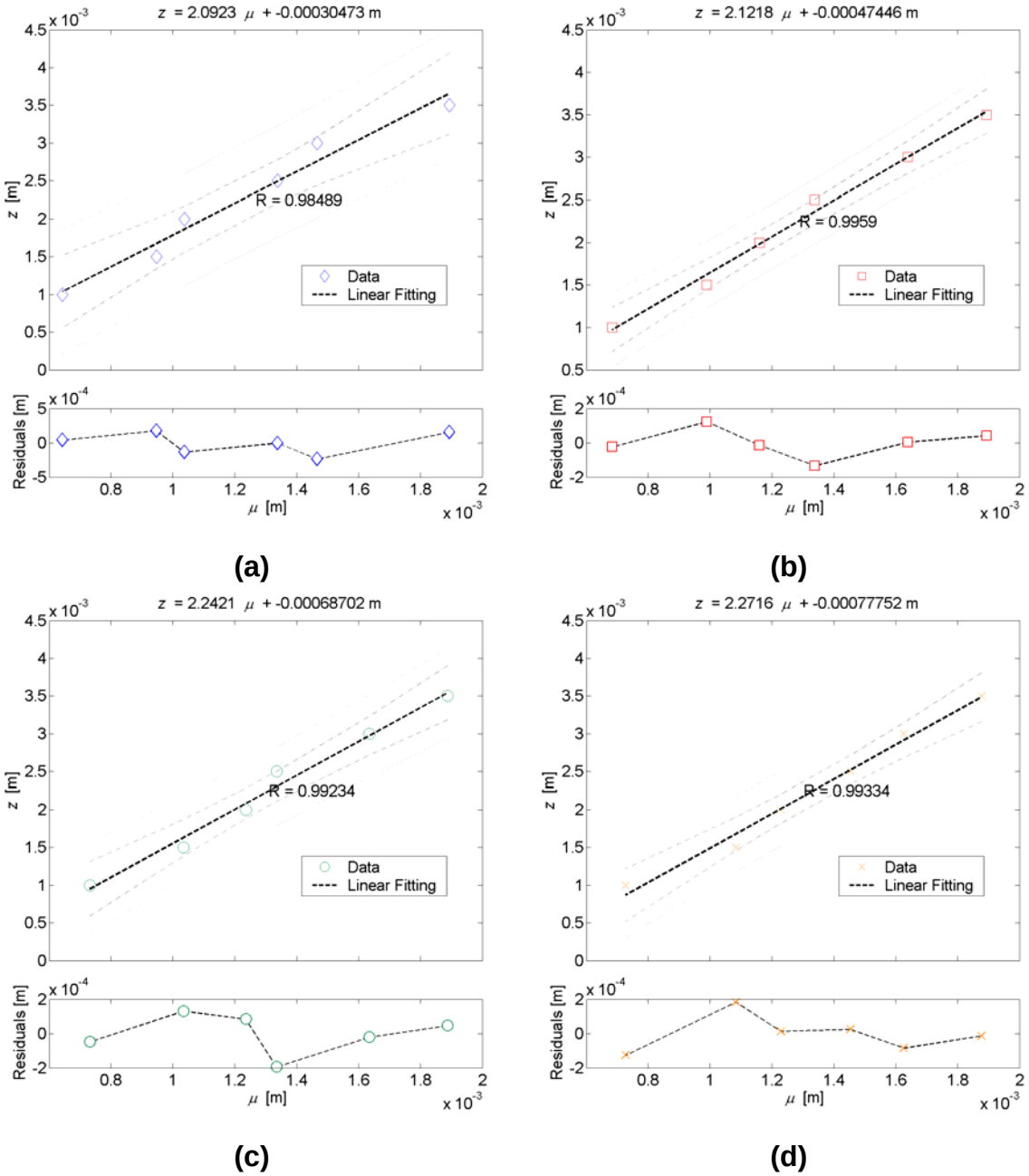

Figure 3.25. Impact of Δt on quantitative results: (a) Δt_1=0.88 s; (b) Δt_2=1.77 s; (a) Δt_3=3.55 s; and Δt_4=7.11 s. Data from specimen PLEXI014 in Appendix F.8.

Hence, even though reducing the time resolution leads to a loss of temporal information, and consequently to a reduction in phase results accuracy, the impact is mostly positive, *i.e.* a reduction in the amount of data, if the maximum available frequency is kept above the Nyquist limit.

3.5.4. Impact of oversampling

Figure 3.26 presents an example of oversampling. Figure 3.26a shows the temperature profile for a 1.0 mm defect on specimen PLEXI014 (Appendix F.8). Noise levels are relatively low as can be confirmed from the thermal contrast profile in Figure 3.26b. However, the situation is different in the frequency domain. If the whole sequence is considered, phase and phase contrast profiles (Figure 3.26c and d) will contain much more information than what is actually required, since the most useful information is confined to low frequencies. Moreover, signal degradation increases with frequency, to a point that phase information is covered by noise at high frequencies as can be seen in Figure 3.26d. However, it is known from the Time-Frequency Duality of the FT that a reduction in time resolution results in a reduction in the maximum available frequency, see Eq. (2.10). For instance, if time resolution is reduced by a factor of 4, *i.e.* only ¼ of the thermal data is conserved (by leaving out of the PPT calculations 3 of every 4 thermograms in the sequence), is like applying a zoom to the important portion of the phase (Figure 3.26e) and phase contrast (Figure 3.26f) profiles, leaving most of the noisy part out of the profiles.

Hence, although similar results (f_b estimation) are obtained from both conditions, a high resolution (Δt_1=0.22 s) is unnecessary, and data is said to be *oversampled*. Instead, a lower time resolution (Δt_2=0.88 s or even lower) is a better choice since it produces similar results with reduced computer memory, storage and power requirements.

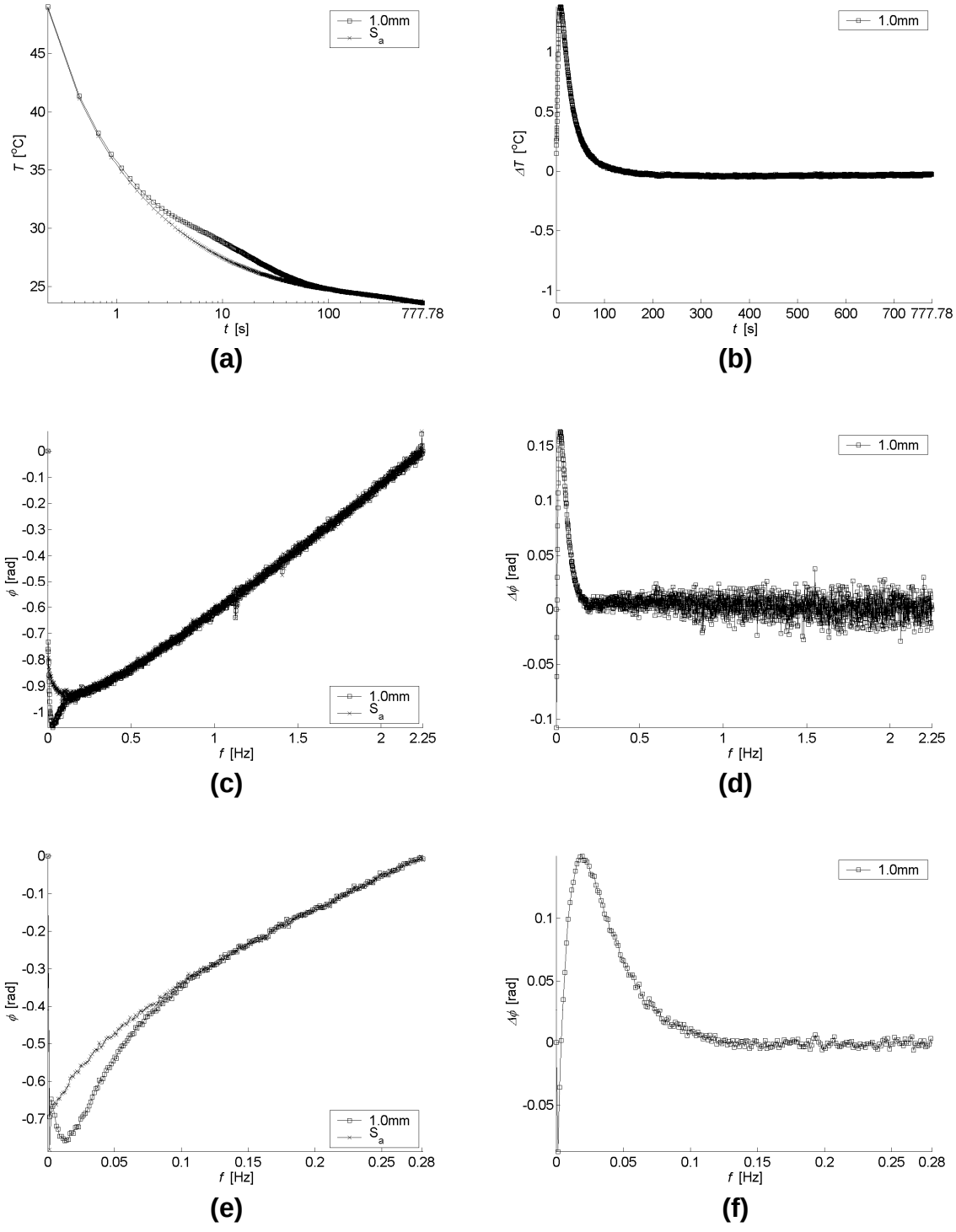

Figure 3.26. The impact of oversampling: (a) temperature profiles for a sound area and a 1.0 mm depth defect, Δt=0.22 s; (b) thermal contrast profile; (c) oversampled phase profiles; (d) the corresponding phase contrast profiles; (e) phase and (f) phase contrast profiles with Δt=0.88 s.

3.5.5. Impact of the thermal properties

The combination of the material and defect thermal properties will produce different thermal decay profiles at the surface. The 'shape' of the temperature decay produces characteristic phase profiles. To give an idea of the 'expected' phase behavior from different defect-material systems, several combinations are presented in Figure 3.27, Figure 3.28, and Figure 3.29.

In Figure 3.27, thermal profiles for a defect at 1.0 mm depth and a sound area from specimen PLEXI014 (in black), are compared with same depth defects in different materials. In Figure 3.27a, Plexiglas® is compared with steel (specimen ACIER002 in Appendix F.2). Steel shows a much greater decay rate at the first instants and it quickly stabilizes to a *quasi*-constant temperature. When a defect is present, air in this case, the temperature stabilization rate is reduced. It should be noticed that time scales are considerably different in both cases. Hence, these differences in time and shape of the temperature profiles produce differences in frequency scale and phase shape in the frequency spectra as can be seen in Figure 3.27 (right).

In the case of aluminum in Figure 3.27b (specimen ALU002 in Appendix F.3), thermal behavior is similar in shape to Plexiglas®, but on a considerably different time scale. This would produce similar results in the frequency spectra (similar in shape but on a different frequency scale). However, the acquisition time was not enough to retrieve all the required thermal information, and as a consequence, aluminum phase profiles appear slightly distorted. Acquisition should last longer to avoid this situation.

Figure 3.27c present a comparison between two Plexiglas® plates (PLEXI014 as before and specimen PLEXI013 in Appendix F.6). Besides the differences on the initial temperature of the plate and on the final stabilization temperature, similar thermal profiles were obtained from both experiments (same time and temperature scales were used). Temperature differences at the beginning are due to variability on the instant of the first acquired image, *i.e.* the ERT, which is normally observed from one experience to another.

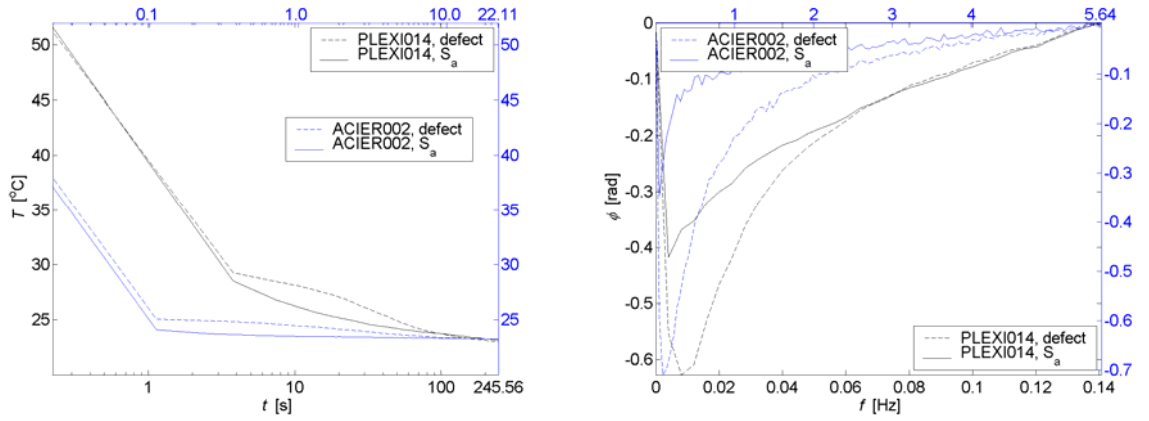

(a)

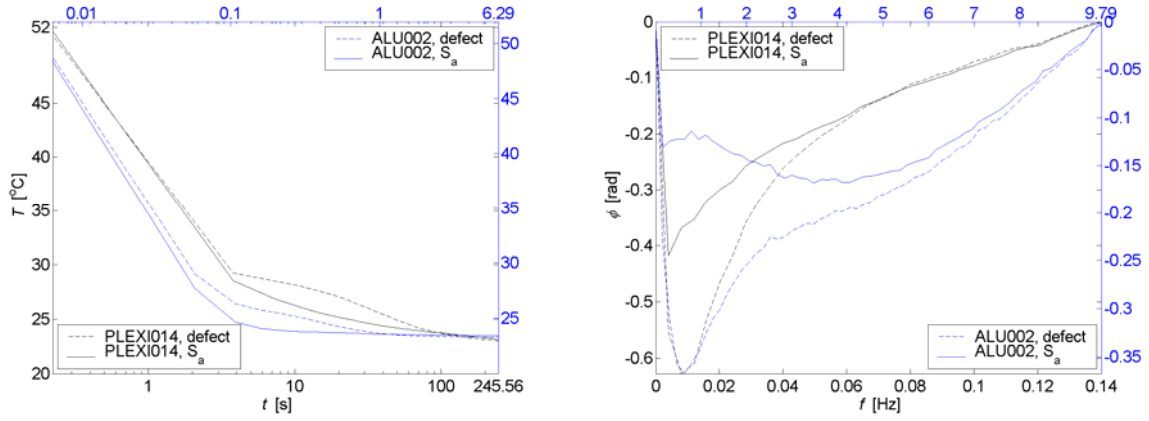

(b)

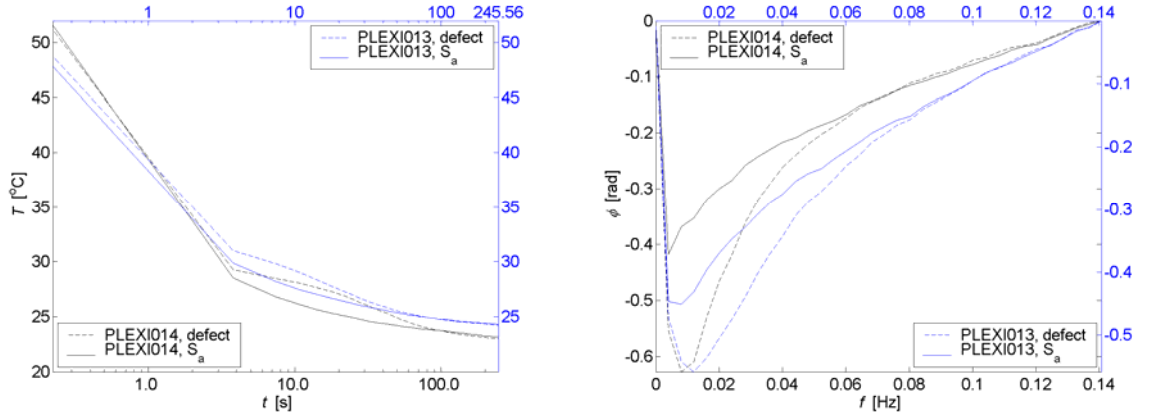

(c)

Figure 3.27. Comparison between thermal (left) and phase (right) profiles behavior of Plexiglas® (specimen PLEXI014 in Appendix F.8) with respect to: (a) steel (specimen ACIER002 in Appendix F.2) (b) aluminum (specimen ACIER002 in Appendix F.3), and (c) Plexiglas® (specimen PLEXI014 in Appendix F.6).

More importantly, the differences in the stabilization time at the end are observed because of defects size variations (10 mm in PLEXI014 vs. 5 mm in PLEXI013). Thermal diffusion is greater for the bigger defect (PLEXI014).

The main effect of these differences in temperature profiles is translated as a change in phase slope, but also a relatively small variation in the f_b value (where defective phase profiles diverge from the sound area phase profiles). These observations expose one important source of uncertainty on depth quantification by PPT: a rather small temperature variation in the time domain (due to differences in defect size, non-uniform heating and/or initial acquisition time), will have an effect on f_b estimations (from $f_b \approx 0.06$ Hz for specimen PLEXI014 to $f_b \approx 0.08$ Hz for specimen PLEXI013, see Figure 3.27).

Figure 3.28a compares temperature and phase profiles for specimens PLEXI014 and CFRP006. In specimen CFRP006 square Teflon® inclusions were positioned between Carbon-Fiber plies. In this case, besides a change of material, there are also differences in the defect thermal properties (Teflon®), shape (square), thickness (few microns), size (7 mm) and depth (0.2 mm). Same situation is presented in Figure 3.28b for a Glass-Fiber specimen (GFRP006) having the same geometry as specimen CFRP006.

A comparison between two plates having the same geometry but different thermal properties (CFRP006 vs. GFRP006 both described in Appendix F.9) is proposed in Figure 3.29.

The impact on phase of a sharp temperature change (as for specimen GFRP006 at the beginning of Figure 3.29a), is more clearly seen in Figure 3.29b. Phase differences between the defect and sound area profiles are almost imperceptible in Glass-Fiber when compared to Carbon-Fiber.

However, as pointed out in section 3.2, Eqs. (3.2) and (3.3), blind frequency estimations are very similar for both specimens, confirming that f_b is unaffected by the thermal properties of the material.

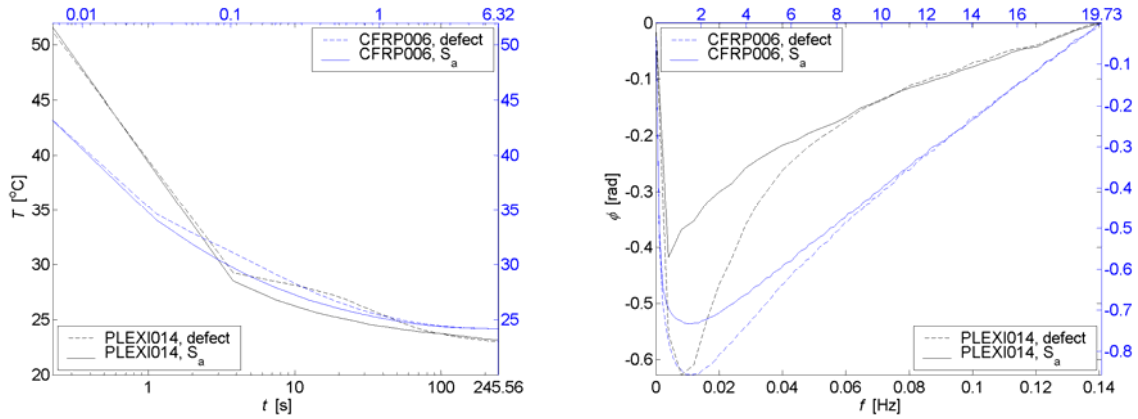

(a)

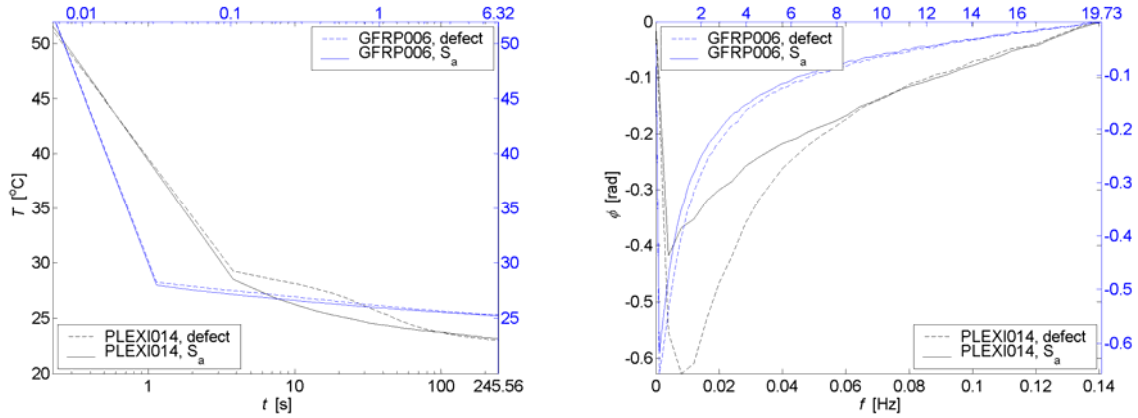

(b)

Figure 3.28. Comparison between thermal (left) and phase (right) profiles behavior of Plexiglas® (specimen PLEXI014 in Appendix F.8) with respect to: (a) specimen CFRP006, and specimen GFRP006 (both described in Appendix F.9).

Another important source of uncertainty needs to be highlighted at this point. The thermal profiles in Figure 3.29a indicate that Glass Fiber have a higher thermal conductivity than Carbon Fiber (since GFRP cools down faster and both specimens have the same number of plies and fiber orientation). Nevertheless, thermal characteristics of these materials found on the literature and summarized in Appendix B denote the opposite: $k_{CFRP}>k_{GFRP}$. Without accurate information about the thermophysical properties, it is difficult to correctly assess their impact on quantification results.

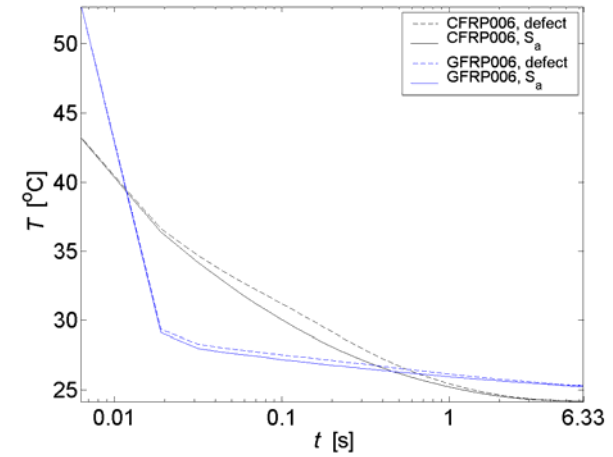

(a)

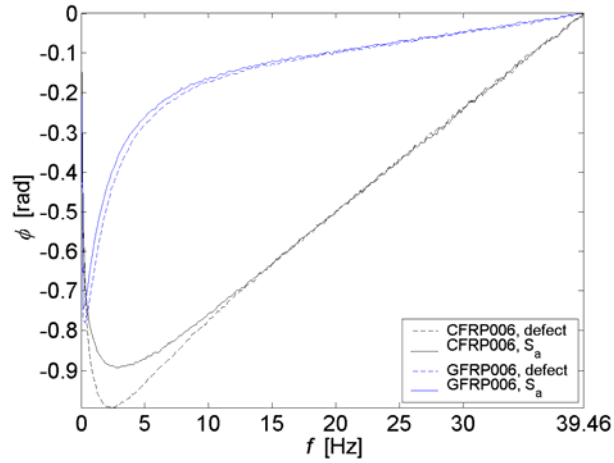

(b)

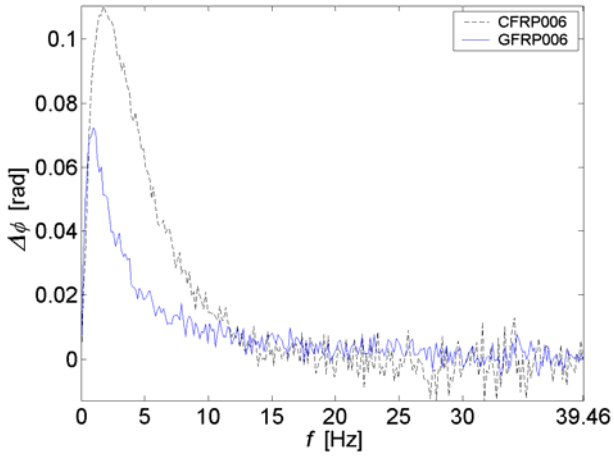

(c)

Figure 3.29. Comparison between Carbon and Glass fibers composites (specimens CFRP006 and GFRP006 in Appendix F.9): (a) Temperature; (b) phase and (c) phase contrast profiles.

3.6. Summary

As a conclusion for this chapter, it can be said that PPT is a useful quantitative tool for NDT&E applications. Data acquisition in PPT is as simple as in PT, whilst depth retrieval is carried out straightforwardly, through Eq. (1.9), as in LT. Nevertheless, there are two differences between quantitative LT and quantitative PPT. First, contrary to LT, thermal data should be prepared carefully prior to the application of the PPT algorithm. The basic guidelines were provided in section 2.5.3. Second, a single PPT test allows defect characterization at several depths, so complete (discrete) phase profiles become available after performing one experience. On the contrary, LT requires that individual tests be performed for every inspected depth. On the other hand, LT proves more effective for the inspection of materials that require a more succinct control of the amount of energy delivered, *e.g.* art and cultural heritage pieces, although some studies [102], [103] suggests that PT can be successfully implemented as well.

Eq. (1.9) can be used if thermal data is correctly sampled and truncated prior to the application of the FT. The experimental results obtained during this research, confirm that C_1 in Eq. (1.9) is close to previously reported values ($1.5 < C_1 < 2$). The inversion procedure was also tested in complex shape specimens showing excellent agreement with no-complex results. In the case of badly sampled data, depth inversion is still possible, though Eq. (1.9) could not be used. An alternative relationship can be derived combining the phase definition for a thermal wave $\phi=z/\mu$, with the diffusion length equation to arrive to Eq. (3.10): $D_n=C'_{n,1}\ \phi_{min}\ \mu'_n$; in which the minimum phase ϕ_{min}, the normalized apparent diffusion length evaluated at f'_b ,$\mu'_n=\mu_d/\mu_{Sa}$, and the normalized diameter D_n, are included to account for defect size variations. However, depth retrieval through Eq. (3.10), requires that the size, shape and thermal diffusivity of the defect to be estimated. Size and shape information can be extracted from the phasegram sequence.

Finally, several uncertainties related to the phase retrieval technique were identified in order to assess their impact on the quantification results.◄

Conclusions

Active Thermography was reviewed in Chapter 1. Infrared Thermography stands among the different NDT&E techniques, as an attractive tool for fast inspection of large surfaces. The different active methods in use nowadays vary in the way energy is sent to the specimen surface. Pulse heating is commonly used in PPT using photographic flashes; an IR camera and a PC. The heat source produces an additional source of signal degradation, namely non-uniform heating. External (heating or cooling sources) might contribute as well to signal degradation. The principle of defect detection is based on the assumption that a defect will possess different thermal properties than the sound material. This will produce a thermal difference on the surface.

A detailed review of PPT theory was provided in the first part of Chapter 2. PPT's greatest innovation is that from this pulsed data, amplitude and phase delay information can be retrieved at different frequencies after the application of a transformation algorithm. Fourier Transform can be used on this purpose. The use of the Fourier Transform was proposed in 1996 [4] to perform PPT calculations, even though; other transformation algorithms can be used (*e.g.* wavelets [13]). The availability of phase images as in LT is complemented by its rapidity of deployment as in PT, which allows to greatly relax experimental constrains without loosing critical information.

The second part of Chapter 2 provides new elements to the PPT Theory. Notably, the Time-Frequency duality of the DFT is analyzed with respect to pulsed thermographic data. The first parameters that need to be determined in any PPT experience are the frame rate f_s, and the acquisition time t_{acq}. Appropriate selection of the pair f_s - t_{acq} must also take into account the thermal properties of the material being inspected; f_s must be large enough to record any significant temperature changes, while the size of t_{acq} is dictated by the depth of the deepest defect. Ideally, t_{acq} should be large enough to allow the specimen to cool down to ambient temperature. Both parameters are related in such a way that the much higher sampling rate requirement on high conductivity materials is compensated in part by

the need of smaller t_{acq} windows. Once data has been recorded, sampling parameters should be chosen carefully to diminish divergence between DFT and CFT. Sampling gives rise to aliasing, while truncation produces leakage and rippling. These problems can be minimized by respecting the Sampling Theorem (*i.e.* $f_s>2f_c$), and though a deep understanding of the Time-Frequency Duality of the DFT.

For instance, the size of the truncation window *w(t)*, should be as large as possible to retrieve all the important information and to minimize leakage and rippling effects. Nevertheless, *w(t)* could be reduced with little impact on phase results in order to save computer memory, provided that the maximum available frequency is kept above the Nyquist limit. Conversely, time resolution Δt, has a greater impact on phase. If Δt increases, *i.e.* time resolution deteriorates, is like applying a 'zoom-in' on phase but with an energy re-distribution at a shorter scale. Time resolution degeneration can be beneficial in some situations, *e.g*. for the suppression of high frequency noise on phase and to reduce the amount of processed data.

Although it has been shown [15] that is possible to determine Δt through modeling, no analytical solution is available for the estimation of *w(t)*. In this sense, a 4-step methodology was proposed to interactively determine the sampling and truncation parameters in function of the inspected depth and the inspected material/defect system. The methodology was used through all the quantitative results on Chapter 3.

Quantification is the ultimate step in NDT&E. Quantification includes determination of depth, size and thermal properties of the specimen. Problems such as signal degradation and complex shape complicate the inversion process. Even though inversion methods exist, reported accuracies change dramatically. As explained in Chapter 3, phase delay data can be used to solve inverse problems. For instance, with the correct combination of sampling parameters, we demonstrated that depth retrieval from phase data is a straightforward procedure, *i.e.* using the thermal diffusion length definition: $\mu=(\alpha/\pi f_b)^{1/2}$. Depth inversion with the phase reduces to

the estimation of f_b. The f_b corresponds to the limiting frequency at which a particular defect produces enough phase contrast to be visible. Defect is not detectable at frequencies higher than f_b. The phase contrast is proposed to estimate f_b, although other techniques are possible (*e.g.* automatic determination of the inflexion points in the phase profiles [87]).

The depth retrieval procedure assumes that thermal data is correctly sampled and truncated, which is not always the case. Nevertheless, when working with badly sampled data, a distinctive relationship between depth and phase can still be observed. An alternative relationship between phase and frequency can be derived from the phase definitions for a thermal wave, combined with the thermal diffusion length equation, to arrive to an expression of the form: $D_n=C_{n,1}\ \phi_{peak}\ \mu'_n$; where the minimum phase $\phi_{\min}$, the normalized apparent diffusion length $\mu'_n=\mu_d\ /\mu_{Sa}$, evaluated at the apparent blind frequency f'_b, and the normalized diameter $D_n=D_{eq}/z$; are included to account for defect size variations.

Finally, one of the principal attractions of using phase data on qualitative and quantitative inspections is that surface shape has a considerably lesser impact on phase than on temperature. Phase is more likely to respond to differences on material thermal properties rather than to geometrical features [10], which makes PPT an attractive tool for the inspection of complex shape specimens. In this work, we describe the complex shape problem in order to assess the impact of the surface shape on active thermography. No significant impact on quantitative results was observed when inspecting slightly shaped specimens ($< 30^o$). This is of paramount importance when non-planar surface, *e.g.* wings, fuselage and other aeronautical parts are tested. Experimental procedures are relaxed as well since the specimen inspection orientation is less critical.

More research needs to be done in order to include defect thickness determination on the quantification procedures.

SUMMARY OF CONTRIBUTIONS

This research work has been the source of several scientific communications. Next paragraphs enumerate them with some detail on the main contributions in the field of active thermography.

The following article was first submitted as a 6 pages conference paper (paper **A**) and poster for the QIRT Congress 2004 (Quantitative InfraRed Thermography). It was subsequently selected for publication (extended to 23 pages) on the first issue of the first scientific journal devoted entirely to quantitative IR thermography, *QIRT Journal* (paper **B**) In this article, a detailed review of Pulsed Phase Thermography was presented, the Time-Frequency Duality is analyzed and the depth inversion technique was introduced, constituting the basis of Chapter 2:

A. Ibarra-Castanedo C. and Maldague X. "Pulsed Phase Thermography Reviewed," *Proceedings of QIRT 7 – Quantitative Infrared Thermography*, 2004. *poster*

B. Ibarra-Castanedo C. and Maldague X. "Pulsed Phase Thermography Reviewed," *QIRT Journal*, **1**(1):47-70, 2004.

Next group of communications were presented by myself at *Thermosense*, a conference part of the Defense and Security Symposium (formerly *Aerosense*), which is held annually in Orlando. In paper **C**, normalized parameters are introduced to account for defect size variations on badly sampled data. The last two articles were intended to validate the depth inversion technique on steel plates (paper **D**), and on Plexiglas and Aluminum Samples (paper **E**):

C. Ibarra-Castanedo C. and Maldague X. "Pulsed Phase Thermography Inversion Procedure using Normalized Parameters to Account for Defect Size Variations," *Proceedings of SPIE - The International Society for Optical Engineering, Thermosense XXVII,* **5782**:334-341, 2005. *20 minutes oral presentation*

D. Ibarra-Castanedo C., Avdelidis N. P. and Maldague X. “Quantitative Pulsed Phase Thermography Applied to Steel Plates,” *Proceedings of SPIE - The International Society for Optical Engineering, Thermosense XXVII,* **5782**:342-351, 2005. *20 minutes oral presentation*

E. Ibarra-Castanedo C. and Maldague X. “Defect Depth Retrieval from Pulsed Phase Thermographic Data on Plexiglas and Aluminum Samples,” *Proceedings of SPIE - The International Society for Optical Engineering, Thermosense XXVI,* **5405**:348-355, 2004. *20 minutes oral presentation*

The following group of articles was prepared in collaboration with Dr. Avdelidis. In the first 4 papers (**F** to **I**), the capabilities of PPT as an inspection technique is compared favorably to other active thermography techniques for the evaluation of aircraft composite patches. Paper **J** is a corrected and extended version of paper **D**, and paper **K** was intended for detecting the tesserae (small squares of stone or glass used in making mosaic patterns) beneath a plastered surface:

F. Avdelidis N. P., Ibarra-Castanedo C., Maldague X., Marioli-Riga Z. P., Almond D. P., “A Thermographic Comparison Study for the Assessment of Composite Patches,” *Journal of Infrared Physics and Technology*, **45**(4): 291-299, 2004.

G. Avdelidis N. P., Almond D. P., Dobbinson A., Hawtin B. C., Ibarra-Castanedo C., Maldague X. Invited Review Paper: "Aircraft composites assessment by means of transient thermal NDT", *Progress in Aerospace Sciences*, **40**(3):143-162, 2004.

H. Avdelidis N. P., Ibarra-Castanedo C., Maldague X., Almond D. P. and Moropoulou A. “Thermal NDT&E of Composite Aircraft Repairs,” *CD of Proceedings of WCNDT- World Conference on Nondestructive Testing*, Montreal (QC), August 30 - September 3, 2004.

I. Avdelidis N. P., Almond D. P., Dobbinson A., Hawtin B., Ibarra-Castanedo C. and Maldague X. “Thermal

Transient Thermographic NDT & E of Composites," *Proceedings of SPIE - The International Society for Optical Engineering, Thermosense XXVI,* **5405**:403-413, 2004.

J. Ibarra-Castanedo C. Avdelidis N. P. and Maldague X. "Complex-Shape Inspection of Composite Materials by Quantitative Pulsed Phase Thermography," submitted to *Materials Evaluation*.

K. Avdelidis N. P., Ibarra-Castanedo C., Koui M., Maldague X., and Moropoulou A. "Thermography Approaches on Plastered Mosaics," submitted to *8th International Workshop on Advanced Infrared Technology and Applications (AITA 8*), Roma - Italy, September 7 - 10, 2005.

Next group of articles was written in collaboration with Daniel Gonzalez. Mr. Gonzalez is currently pursuing a Ph. D. at the Photonic Engineering Group, University of Cantabria, in Spain and he paid two visits to the CVSL as part of his research agenda. Different ways to process thermographic data automatically were reviewed, using thermal data as in papers **M** and **O**; or pulsed phase data as in papers **L** and **N**:

L. Ibarra-Castanedo C., González D. A. and Maldague X. "Automatic Algorithm for Quantitative Pulsed Phase Thermography Calculations," *CD of Proc. of WCNDT - World Conference on Nondestructive Testing*, Montreal (QC), August 30 - September 3, 2004. *25 minutes oral presentation*

M. González D. A., Ibarra-Castanedo C. Pilla M., Klein M., J. M. López-Higuera and Maldague X. "Automatic Interpolated Differentiated Absolute Contrast Algorithm for the Analysis of Pulsed Thermographic Sequence," *Proceedings of QIRT 7 – Quantitative Infrared Thermography*, 2004. *poster*

N. González D. A., Ibarra-Castanedo C., Madruga F. J., Maldague X., "Differentiated Absolute Phase Contrast

Algorithm for the Analysis of Pulsed Thermographic Sequences," *Infrared Physics & Technology*, *in press*.

O. González D. A., C. Ibarra-Castanedo, López-Higuera J. M., Maldague X. "New Algorithm based on the Hough Transform for the Analysis of Pulsed Thermographic Sequences", *V International Workshop Advances in Signal Processing for Non Destructive Evaluation of Materials (IWASPNDE)*, Quebec, 2005, *in press*.

The following papers present a basic review of IR image processing methods. The most used methods together with in-progress techniques are described and some experimental results are included. Paper **P** was presented by Prof. Maldague at NDE 2004 National Indian Society annual conference in Pune, India. Paper **Q** was exposed at the 7th International Workshop on Advanced Infrared Technology and Applications (AITA) by Prof. Maldague and later selected for publication at the *Journal of Infrared Physics and Technology*. This article includes as well a presentation of the depth inversion technique. Paper **R** is a review of thermographic methods and was presented as a 10-pages conference paper and as a 142 x 107 cm poster at Thermosense 2003:

P. Ibarra-Castanedo C., González D. and Maldague X. "Infrared Image Processing for Nondestructive Applications," keynote lecture, 25 p. *NDE 2004 National Indian Society annual conference*, 9-11 Dec. 2004, Pune (India).

Q. Ibarra-Castanedo C., González D., Klein M. Pilla M., Vallerand S. and Maldague X. "Infrared Image Processing and Data Analysis," *Journal of Infrared Physics and Technology*, **46**(1-2):75-83, 2004.

R. Ibarra-Castanedo C., Galmiche F., Darabi A., Pilla M., Klein M., Ziadi A., Vallerand S., Pelletier J.-F. and Maldague X. "Thermographic Nondestructive Evaluation: Overview of Recent Progress," *Proceedings of SPIE - The International Society for*

Optical Engineering, Thermosense XXV, **5073**:450-459, 2003. *poster*

Paper S was presented at the Canadian Conference on Electrical and Computer Engineering 2004 in Niagara Falls Ontario, as a 4-pages conference paper and a 142 x 107 cm poster, both in French. The Time-Frequency Duality of the DFT with respect to TPP was reviewed. Paper T was exposed (by myself) at the Annual Congress of the Canadian Association of Physicists 2002 in Quebec City, and presents a study of the Thermographic Signal Reconstruction technique described in Appendix D, applied to PPT data:

S. Ibarra-Castanedo C. and Maldague X. "Traitement numérique de données thermiques par thermographie de phase pulsée quantitative pour l'évaluation non-destructive des matériaux," *Proceedings of CCECE-Canadian Conference on Electrical and Computer Engineering*, Niagara Falls (ON), May 2-5, 2004. *poster in French*

T. Ibarra-Castanedo C., Galmiche F. and Maldague X. "Synthetic Data in Infrared Thermography for NonDestructive Evaluation," *Proc. Annual Congress of the Canadian Association of Physicists (CAP)*, Quebec City (Quebec) Canada, June 2-5, 2002, p 88. *30 minutes oral presentation*

The interactive technique reviewed in section Chapter 2, is described in next paper that was submitted to *Research in Nondestructive Evaluation* journal:

U. Ibarra-Castanedo, C. and Maldague X. "Interactive Methodology for Optimized Defect Characterization by Quantitative Pulsed Phase Thermography," to be submitted to *Research in Nondestructive Evaluation*.

Finally, the following paper was prepared in collaboration with Dr. Ermano Grinzato and his team, Dr Avdelidis and the CVSL. It constitutes an investigation on complex shape composite specimens using PPT:

v. Ibarra-Castanedo C., Avdelidis N. P., Grinzato E. G., Bison P. G., Marinetti S., Maldague X. “Quantitative Assessment of Flat & Complex Shape Composites Using Pulsed Phase Thermography,” *5th International Workshop Advances in Signal Processing for Non Destructive Evaluation of Materials (IWASPNDE)*, Université Laval, Quebec City, QC, CA, 2-4 August, 2005. *submitted*.

Bibliography

[1] **MEOLA C., CARLOMAGNO G. M. AND GIORLEO G. 2004,** "The Use of Infrared Thermography for Materials Characterization", *J. Mater. Process. Technol.*, **155-156**:1132–1137.

[2] **AMERICAN SOCIETY FOR NONDESTRUCTIVE TESTING - ASNT,** "Infrared and Thermal Testing", Nondestructive Handbook on Infrared Technology, Volume 3, ASNT Handbook Series, X. Maldague technical ed., P. O. Moore ed., 3rd edition, Columbus, Ohio, ASNT Press, 2001, 718 p.

[3] **GIORLEO G., MEOLA C. AND SQUILLACE A. 2000,** "Analysis of Defective Carbon-Epoxy by Means of Lock-in Thermography", *Res. Nondestr. Eval.,* **12**:241-250.

[4] **MALDAGUE X. P. AND MARINETTI S. 1996,** "Pulse Phase Infrared Thermography," *J. Appl. Phys*., **79**(5):2694-2698.

[5] **MALDAGUE X. P. 2001,** Theory and Practice of Infrared Technology for Nondestructive Testing, John Wiley & Sons, N. Y.

[6] **KRAPEZ J. C. AND CIELO P. 1991,** "Thermographic Nondestructive Evaluation: Data Inversion Procedures. I: 1D Analysis," *Res. Nondestr. Eval.*, **3**(2):81-100.

[7] **KRAPEZ J. C., MALDAGUE X. AND CIELO P. 1991,** "Thermographic Nondestructive Evaluation: Data Inversion Procedures. II: 2D Analysis and Experimental Results," *Res. Nondestr. Eval.*, **3**(2): 101-124.

[8] **MEOLA C. AND CARLOMAGNO G. M. 2004,** "Recent Advances in the Use of Infrared Thermography", *Meas. Sci. Technol.,* **15**:27–58.

[9] **BUSSE G. AND ROSENCWAIG A. 1980,** "Subsurface Imaging with Photoacoustics," *Appl. Phys. Lett.*, **36**(10):815-816.

[10] **MALDAGUE X. AND COUTURIER, J-P. 1997,** "Review of Pulse Phase Infrared Thermography," *Proc. 4th International Workshop on Advanced Infrared Technology and Applications (AITA)*, Firenze, Italy, September 15-16, **53**(1):271-286.

[11] **VALLERAND S. AND MALDAGUE X. 2000,** "Defect Characterization in Pulsed Thermography: A Statistical Method Compared with Kohonen and Perceptron Neural Networks," *NDT&E Int*., **33**(5):307-315.

[12] **MALDAGUE X. LARGOUËT Y. AND COUTURIER, J-P. (1998).** "A Study of Defect Depth Using Neural Networks in Pulsed Phase Thermography: Modeling, Noise, Experiments," *Rev. Gén. Therm.*, **37**:704-717.

[13] **GALMICHE F. AND MALDAGUE X. 2000,** "Depth defect retrieval using the wavelet pulsed phased thermography," *Proc. 5th Conference on Quantitative InfraRed Thermography (QIRT)*, *Eurotherm Seminar 64*, D. Balageas, G. Busse, C. Carlomagno (eds.), Reims, France, July 18-21, 2000, 194-199.

[14] **BRACEWELL R. 1965,** The Fourier Transform and its Applications, McGraw-Hill, USA.

[15] **MARINETTI S., PLOTNIKOV Y. A., WINFREE W. P., BRAGGIOTTI A. 1999,** "Pulse phase thermography for defect detection and visualization," *Proc. SPIE, Thermosense XXI*, **3586**:230-238.

[16] **IBARRA-CASTANEDO, C. AND MALDAGUE X. 2005,** "Interactive Methodology for Optimized Defect Characterization by Quantitative Pulsed Phase Thermography," submitted to *Res. Nondestr. Eval*.

[17] **HUDSON R. D. 1969,** "Infrared System Engineering", John Wiley & Sons Inc., USA.

[18] **INFRARED PROCESSING AND ANALYSIS CENTER (IPAC) 2004,** "Discovery of Infrared," from Cool Cosmos at the Infrared Processing and Analysis Center & the SIRTF Science Center: <http://coolcosmos.ipac.caltech.edu/ cosmic_classroom/ir_tutorial/discovery.html>, accessed on June 23, 2004.

[19] **BRITISH BROADCASTING CORPORATION (BBC) 2004,** "Sir Isaac Newton (1643 - 1727)," from BBC - History: <http://www.bbc.co.uk/history/historic_figures/ newton_isaac.shtml>, accessed June 24, 2004.

[20] **CANADIAN INSTITUTE FOR NDE (CINDE) 2004,** "What is NDT?," [online]: <http://www.cinde.ca/ ndt.shtml>, accessed on July 5, 2004.

[21] **AMERICAN INSTITUTE OF PHYSICS (AIP) 2004,** *Review of progress in quantitative nondestructive evaluation*, *Proc. AIP - American Institute of Physics* [online]: <http://www.aip.org/> accessed on July 5, 2004.

[22] **RUDDOCK W. 2004,** "Infrared Instruments Come of Age," from InfraredThermography.com by Advanced Infrared Resources [online]: <http://www.infraredthermography.com/mvarticle.htm>, accessed on June 28, 2004.

[23] **IBARRA-CASTANEDO C., GONZÁLEZ D., KLEIN M. PILLA M., VALLERAND S. AND MALDAGUE X. 2004,** "Infrared Image Processing and Data Analysis," *Infrared Phys. Technol.*, 46(1-2):75-83.

[24] **IBARRA-CASTANEDO C. AND MALDAGUE X. 2002,** "Infrared Image Processing for Nondestructive Applications," keynote lecture, 25 p., CD of Proceedings: *NDE 2004 National Indian Society annual conference*, 9-11 Dec. 2004, Pune (India).

[25] **REYNOLDS W. N. 1986,** "Thermographic Methods Applied to Industrial Materials," *Can. J. Phys.*, **64**: 1150-1154.

[26] **MILNE J. M. AND REYNOLDS W. N. 1984,** "The Non-Destructive Evaluation of Composites and other Materials by Thermal Pulse Video Thermography," *Proc. SPIE*, *Thermosense VII*, **520**: 119-122.

[27] **ALMOND D. P. AND LAU S. K. 1994,** "Defect Sizing by Transient Thermography I: An analytical Treatment," *J. Phys. D: Appl. Phys.*, **27**: 1063-1069.

[28] **ALMOND D. P. AND LAU S. K. 1993,** "Edge Effects and a Method of Defect Sizing by Transient Thermography," *Appl. Phys. Lett.*, **62**(25): 3369-3371.

[29] **SAINTEY M. B. AND ALMOND D. P. 1995,** "Defect Sizing by Transient Thermography II: A Numerical Treatment," *J. Phys. D: Appl. Phys.*, **28**: 2539-2546.

[30] **PARKER W. J., JENKINS R. J., BUTLER C. P. AND ABBOTT G. L. 1961,** "Flash Method of Determining Thermal Diffussivity, Heat Capacity, and Thermal Conductivity," *J. Appl. Phys.*, **32**(9):1679-1684.

[31] **FAVRO L. D. AND HAN X. 1998,** "Thermal Wave Materials Characterization and Thermal Wave Imaging," in Birnbaum G., Auld B. A. (eds.): Sensing for Materials Characterization, Processing and Manufacuring, ASNT TONES, **1**:399-415.

[32] **FAVRO L. D., HAN X., WANG Y., KUO P. K. AND THOMAS R. L. 1995,** "Pulse-echo thermal wave imaging," in Review of Progress in Quantitative Nondestructive

Evaluation, D.O. Thompson and D.E. Chimenti (ed.), **14**:425-429.

[33] **FAVRO L. D., HAN X, KUO P. K. AND THOMAS R. L. 1995,** "Imaging the early time behavior of reflected thermal wave pulses," *Proc. SPIE*, *Thermosense XVII,* **2473**:162-166.

[34] **HAN X., FAVRO L. D., KUO P. K. AND THOMAS R. L. 1996,** "Early-Time Pulse-Echo Thermal Wave Imaging," in D. O. Thompson and D. E. Chimenti (ed.): Review of Progress in Quantitative Nondestructive Evaluation, **15**:519-524.

[35] **CARSLAW H. S. AND JAEGER J. C. 1986,** *Conduction of Heat in Solids*, 2nd edition, Clarendon Press, Oxford.

[36] **IBARRA-CASTANEDO C. AND MALDAGUE X. 2004,** "Pulsed Phase Thermography Reviewed," *QIRT J.*, **1**(1):47-70.

[37] **LAU S. K., ALMOND D. P. AND PATEL P. M. 1991,** "Transient Thermal Wave Techniques for the Evaluation of Surface Coatings," *J. Phys. D: Appl. Phys.*, **24**:428-436.

[38] **LAU S. K., ALMOND D. P. AND MILNE J. M. 1991,** "A Quantitative Analysis of Pulsed Video Thermography," *NDT&E Int.*, **24**(4):195-202.

[39] **MACLACHLAN SPICER, J. W. KERNS W. D. AAMODT L. C AND MURPHY J. C. 1989,** "Measurement of Coating Physical Properties and Detection of Coating Disbonds by Time-Resolved Infrared Radiometry," *J. Nondestruc. Eval*., **8**(2):107-120.

[40] **AVDELIDIS N. P. AND ALMOND, D. P. 2004,** "Transient thermography as a through skin imaging technique for aircraft assembly: Modelling and experimental results," *Infrared Phys. Technol.*, **45**(2):103-114.

[41] **AVDELIDIS N. P. AND ALMOND, D. P. 2004,** "Through skin sensing assessment of aircraft structures using pulsed thermography," *NDT&E Int.*, **37**(5): 353-359.

[42] **KRAPEZ J.C., BALAGEAS D., DEOM A. AND LEPOUTRE F. 1994,** "Early Detection by Stimulated Infrared Thermography. Comparison with Ultrasonics and Holo/Shearography" in X. P. V. Maldague (ed.): Advances in signal processing for Nondestructive Evaluation of Materials, Kluwer Academic Publishers, Netherlands, 303-321.

[43] **MARTIN R. E., GYEKENYESI A. L. AND SHEPARD S. M. 2003,** "Interpreting the Results of Pulsed Thermography Data," *Mater. Eval.*, **61**(5):611-616.

[44] **KRAPEZ J.C., BOSCHER D., DELPECH P., DÉOM A., GARDETTE G. AND BALEGEAS D. 1992,** "Time-Resolved Pulsed Stimulated Infrared Thermography applied to Carbon-Epoxy Non Destructive Evaluation," *Proc. 1st Conference on Quantitative InfraRed Thermography (QIRT)*, *Eurotherm Seminar 27*, Château-Malabry, France, July 7-9, 1992, 195-200.

[45] **PILLA M 2002,** "A Novel Contrast Method for Pulse Thermography Data", *Ph.D. Thesis*, Politecnico di Milano.

[46] **PILLA M., KLEIN M., MALDAGUE X. AND SALERNO A. 2002,** "New Absolute Contrast for Pulsed Thermography," *Proc. 7th Conference on Quantitative InfraRed Thermography (QIRT)*, *Eurotherm Seminar 64*, Dubrovnik, Croatie.

[47] **GONZÁLEZ D. A., IBARRA-CASTANEDO C. PILLA M., KLEIN M., J. M. LÓPEZ-HIGUERA AND MALDAGUE X. 2004,** "Automatic Interpolated Differentiated Absolute Contrast Algorithm for the Analysis of Pulsed Thermographic Sequence," *Proc. 7th Conference on Quantitative InfraRed Thermography (QIRT)*, Rhode Saint

Genèse, Belgium, July 5-8, 2004, H.16.1-H.16.6.

[48] **ZWESCHPER T., DILLENZ A., RIEGERT G., SCHERLING D. AND BUSSE G. 2003,** "Lockin Thermography Methods for the NDT of CFRP Aircraft Components," [online]: http://www.ndt.net/article/ecndt02/249/249.htm, NDT.net, February.

[49] **ZWESCHPER T., RIEGERT G. DILLENZ A. AND BUSSE G. 2003,** "Ultrasound Burst Phase Thermography (UBP) for Applications in the Automotive Industry," *Rev. Quant. Nondestr. Eval.*, **22**:531-536.

[50] **CARLOMAGNO G. M. AND MEOLA C. 2002,** "Comparison between thermographic techniques for frescoes NDT," *NDT&E Int.*, **35**(8):559-565.

[51] **GIORLEO G. AND MEOLA C. 2002,** "Comparison between Pulsed and Modulated Thermography in Glass-Epoxy Laminates," *NDT&E Int.*, **35**(5):287-292.

[52] **DILLENZ A., ZWESCHPER T., RIEGERT G. AND BUSSE G. 2003,** "Progress in phase angle thermography," *Rev. Sci. Instrum.*, **74**(1):417-419.

[53] **BUSSE G. 1994,** "Nondestructive Evaluation of Polymer Materials," *NDT&E Int.*, **27**(5):253-262.

[54] **DANJOUX R., COLLET D. AND BEAUDOIN J. L. 1994,** "New Developments in the Detection of Defects by Photothermal Thermography" in X. P. V. Maldague (ed.): *Advances in signal processing for Nondestructive Evaluation of Materials*, Kluwer Academic Publishers, Netherlands, 145-160.

[55] **WU D. AND BUSSE G. 1998,** "Lock-in Thermography for NonDestructive Evaluation of Materials," *Rev. Gén. Therm.*, **37**:693-703.

[56] **BUSSE G., WU D. AND KARPEN W. 1992,** "Thermal Wave Imaging with Phase Sensitive Modulated Thermography," *J. Appl. Phys.*, **71**(8):3962-3965.

[57] **BUSSE G. 1979,** "Optoacoustic Phase Angle Measurement for Probing a Metal", *Appl. Phys. Lett*., **35**:759–760.

[58] **BUSSE G. 1982,** "Optoacoustic and Photothermal Material Inspection Techniques", *Appl. Optics*., **21**(1):107–110.

[59] **ROSENCWAIG A. AND BUSSE G. 1980,** "High-Resolution Photoacoustic Thermal-Wave Microscopy", *Appl. Phys. Lett*., **36**(9):725–727.

[60] **THOMAS R. L., POUCH J. J., WONG Y. H., FAVRO L. D. AND KUO P. K. 1980,** "Subsurface Flaw Detection in Metals by Photoacustic Microscopy", *J. Appl. Phys.*, **51**(2): 1152–1156.

[61] **BALAGEAS D. L., LEVESQUE P., AND DÉOM A. A. 1993,** "Characterization of Electromagnetic Fields using a Lock-In Infrared Thermographic System," Lee R. Allen (ed.), *Proc. SPIE*, *Thermosense XV*, **1933**:274-285.

[62] **SAKAGAMI T. AND KUBO S. 2002,** "Development of a New Non-Destructive Technique for Quantitative Evaluations of Delamination Defects in Concrete Structures Based on Phase Delay Measurement using Lock-In Thermography," *Infrared Phys. Technol.*, **43**:211-218.

[63] **BAI W. AND WONG B. S. 2001,** "Evaluation of Defects in Composite Plates under Convective Environments using Lock-In Thermography," *Meas. Sci. Technol.* **12**:142-150.

[64] **WONG B. B., TUI C. G., LOW B. S. AND BAI W. 1999,** "Thermographic and Ultrasonic Evaluation of Composite Materials", *Insight*, **41**:504–509.

[65] **MEOLA C., CARLOMAGNO G. M., SQUILLACE A. AND GIORLEO G. 2004,** "The Use of

Infrared Thermography for Nondestructive Evaluation of Joints", *Infrared Phys. Technol.*, **46**:93-99.

[66] **MEOLA C., CARLOMAGNO G. M., SQUILLACE A. AND GIORLEO G. 2002,** "Non-destructive Control of Industrial Materials by Means of Lock-In Thermography," *Meas. Sci. Technol.*, **13**:1583-1590.

[67] **KESTON D. 1998,** "Joseph Fourier - Politician & Scientist," [online]: <http://www.todayinsci.com/F/Fourier_JBJ/FourierPoliticianScientistBio.htm> accessed on April 26, 2004.

[68] **FOURIER, J. B. J. 1822,** "Théorie analytique de la chaleur", Paris, Firmin Didot.

[69] **O'CONNOR J. J. AND ROBERTSON E. F. 2005,** "The MacTutor History of Mathematics archive: Jean Baptiste Joseph Fourier," [online]: <http://www-groups.dcs.st-and.ac.uk/~history/Mathematicians/Fourier.html> accessed on April 26, 2004.

[70] **FISHBANE P. M., GASIOROWICZ S. AND THORTON S. T. 1996,** *Physics for Scientists and Engineers*, 2nd edition, Prentice-Hall, Inc, Upper Saddle River, NJ.

[71] **KREYSZIG E. 1993,** *Advanced Engineering Mathematics*, 7th ed., John Wiley and Sons, Inc.

[72] **BRIGHMAN E. O. 1974,** *The Fast Fourier Transform*, Prentice-Hall, Inc., Englewood Cliffs, N. J.,

[73] **CASTLEMAN K. R. 1996,** *Digital Image Processing*, Prentice-Hall, Upper Saddle River, N. J.

[74] **COOLEY J.W. AND TUKEY J.W. 1965,** "An Algorithm for the Machine Calculation of Complex Fourier Series," Mathematics of Computation, **19**(90):297-301.

[75] **GALMICHE F., LECLERC M. AND MALDAGUE X. (2001).** "Time Aliasing Problem in Pulsed Phased Thermography," *Proc. SPIE Int. Soc. Opt. Eng., Thermosense XXIII*, **4360**:550-553.

[76] **UNSER M. 2000,** "Sampling - 50 Years After Shannon," *Proc. IEEE*, **88**(4):569-587.

[77] **WEISSTEIN E. W. 1999-2005,** "Apodization Function," from MathWorld--A Wolfram Web Resource: http://mathworld.wolfram.com/Apodization Function.html, accessed on January 11, 2005.

[78] **SHANNON C. E. 1948**, "A mathematical theory of communication,'' *Bell System Technical Journal*, **27**:379-423 and 623-656, July and October.

[79] **SHANNON C. E. 1949,** "Communication in the presence of noise," *Proc. IRE*, **37**:10–21.

[80] **VAVILOV M. 2000,** "Advanced modeling of thermal NDT problems: From buried landmines to defects in composites," *Proc. SPIE Int. Soc. Opt. Eng., Thermosense XXIV*, **4710**: 507-521.

[81] **THERMOCALC-3D SOFTWARE, 1998,** Version 3.0, Innovation Inc.

[82] **SHEPARD S. M. 2001,** "Advances in Pulsed Thermography", *Proc. SPIE, Thermosense XXIII*, **4360**: 511-515.

[83] **SHEPARD S. M., AHMED T., RUBADEUX B. A. AND WANG D. 2001,** "Synthetic Processing of Pulsed Thermographic Data for Inspection of Turbine Components", *Insight: Non-Destructive Testing and Conditioning Monitoring*, **43**(9):587-589.

[84] **SHEPARD S. M. AND LHOTA J. R. 2003,** "Spatial-Temporal Signal Processing for Subsurface Thermographic Imaging", *Proc. SPIE, Thermosense XXV*, **5073**: 401-405.

[85] **SHEPARD S. M., LHOTA J. R., RUBADEUX B. A., AHMED T., WANG D. 2002,** "Enhancement and reconstruction of thermographic NDT data", *Proc. SPIE, Thermosense XXIV*, **4710**:531-535.

[86] **IBARRA-CASTANEDO C., GALMICHE F. AND MALDAGUE X. 2002,** "On Synthetic Data in Infrared Thermography for NonDestructive Evaluation", *Proc. Annual Congress of the Canadian Association of Physicists (CAP)*, Quebec City (Quebec) Canada, June 2-5, 2002, p 88.

[87] **IBARRA-CASTANEDO C., GONZÁLEZ D. AND MALDAGUE X. 2004,** "Automatic Algorithm for Quantitative Pulsed Phase Thermography Calculations," *Proc. 16th World Conference on Nondestructive Testing (WCNDT)*, Montreal (QC), August 30 - September 3, 2004, CD of proceedings.

[88] **IBARRA-CASTANEDO C. AND MALDAGUE X. 2005,** "Pulsed Phase Thermography Inversion Procedure using Normalized Parameters to Account for Defect Size Variations" *Proc. SPIE: Thermosense XXVII*, **5782-43**, *in press*.

[89] **RUSS J. C. 2002,** *The Image Processing Handbook* [online], 4th edition, CRC Press, Boca Raton, Fla. Available from: <http://www.engnetbase.com/ejournals/books/book%5Fsummary/summary.asp?id=792>, accessed on January 11, 2005.

[90] **GONZALEZ R. C. AND WOODS R. E. 2002,** *Digital Image Processing*, 2nd edition, Prentice-Hall, Upper Saddle River, N. J.

[91] **PRATT W. K. 1991,** *Digital Image Processing*, Wiley, N. Y.

[92] **NOUAH A. 1992,** "Exploitation de la vision dans les bandes visible et infrarouge pour l'évaluation non-destructive des matériaux", *M. Sc. Thesis* Université Laval.

[93] **PELLETIER J-F. AND MALDAGUE X. 1997,** "Shape-from-Heating: A Two-Dimensional Approach for Shape Extraction in Infrared Images", *Opt. Eng.*,**36**(2):370-375.

[94] **BARKER E. 1994,** "Étude de la géométrie des objets en thermographie infrarouge à l'aide d'une image thermique numérique unique", *M. Sc. Thesis*, Université Laval.

[95] **BARKER E., MALDAGUE X. AND LAURENDEAU D. 1994,** "Objects Shape Determination from a Single Infrared Thermal Image", dans Snell J.R. (éds.), *Proc. SPIE : Thermosense XVI,* **2245**(Mar): 95-105,.

[96] **BARKER E., MALDAGUE X. AND LAURENDEAU D. 1995,** "Shape Reconstruction from a Single Thermal Image", *Opt. Eng.,* **34**(1): 154-159,.

[97] **PELLETIER J-F. AND MALDAGUE X. 1996,** "Infrared Thermography : Nonplanar Inspection", in Burleigh, J.J., Spicer J. W. (eds.), *Proc. SPIE: Thermosense XVIII,* **2766**(Mar) :264-275.

[98] **PITRE L., MALDAGUE X. AND LAURENDEAU D. 1993,** "Range finder based guidance of PUMA robot for the infrared inspection of non-planar materials", Canadian Conference on Electrical and Computer Engineering,**1**:108-110.

[99] **MALDAGUE X., FORTIN L. AND PICARD J. 1991,** "Applications of Tridimensional Heat Calibration to a Thermographic NDE Station", *Proc. SPIE: Thermosense XIII,* **1467**(Avr): 239-251.

[100] **MALDAGUE X., BARKER E., NOUAH A., BOISVERT E., DUFORT B., FORTIN L. AND LAURENDEAU D. 1994,** "On Methods for Shape Correction and Reconstruction in Thermographic NDE", in X. P. Maldague (eds) : *Advances in signal processing for Non Destructive Evaluation of Materials*, Kluwer Academic Publishers, Pays-Bas.

[101] **HORN B. K. P. AND BROOKS M. J. 1989,** *Shape from Shading*, MIT Press, Cambridge, MA.

[102] **AVDELIDIS N. P. DELEGOU, E. T., ALMOND, D. P. AND MOROPOULOU, A. 2004,** "Surface roughness evaluation of marble by 3D laser profilometry and pulsed thermography," *NDT&E Int*, **37**(7): 571-575.

[103] **AVDELIDIS N. P. AND MOROPOULOU, A. 2004,** "Applications of infrared thermography for the investigation of historic structures" *Journal of Cultural Heritage*, **5**(1):119-127.

[104] **PLANCK M. 1950**, "Scientific Autobiography and Other Papers", trans. Frank Gaynor:33–34.

[105] **KARLSSON E. B. 2004,** "The Nobel Prize in Physics," from Nobel e-Museum - The Official Web Site of The Nobel Foundation, <http://www.nobel.se/physics/articles/karlsson/index.html>, accessed June 18, 2004.

[106] **NATIONAL AERONAUTICS AND SPACE ADMINISTRATION (NASA) 2004,** "Electromagnetic Spectrum," from Imagine the Universe!: <http://imagine.gsfc.nasa.gov/docs/science/know_l1/emspectrum.html>, accessed on July 6, 2004.

[107] **PIOTROWSKI J. AND ROGALSKI A. 2004,** "Uncooled Long Wavelength Infrared Photon Detectors", *Infrared Phys. Technol.*, **46**:115-131.

[108] **ROGALSKI A. AND CHRZANOWSKI K. 2002,** "Infrared Devices and Techniques", Contributed Paper: *Opto-electronics Review*, **10**(2):111-136.

[109] **RUDDOCK W. 2004,** "Infrared Imaging and Open Heart Surgery," from InfraredThermography.com by Advanced Infrared Resources [online]: <http://www.infraredthermography.com/IR%20Heart.htm>, accessed on June 28, 2004.

[110] **INCROPERA F. P. AND DE WITT D. P. 1990,** *Fundamentals of Heat and Mass Transfer*, 3rd edition, John Wiley & Sons, USA.

[111] **RUDDOCK W. 2004,** "Infrared Thermography vs. The Visible," from InfraredThermography.com by Advanced Infrared Resources: <http://www.infraredthermography.com/irvsvis.htm>, accessed on June 28, 2004.

[112] **PLANCK, M. 1988,** *The Theory of Heat Radiation*, in The History of Modern Physics, 1800-1950, **11**, American Institute of Physics, Tomash Publishers, N. Y.

[113] **EVERETT INFRARED (EIR) 2004,** "Physics of Electro-Optic Detectors," [online]: <http://www.everettinfrared.com/detectors.htm>, accessed on July 9, 2004.

[114] **TISSOT J. L. 2004,** "IR Detection with Uncooled Sensors", *Infrared Phys. Technol.*, **46**:147-153, 2004.

[115] **MARINETTI S., MALDAGUE X., PRYSTAY M. 1997,** "Calibration Procedure for Focal Plane Array Cameras and Noise Equivalent Material Loss for Quantitative Thermographic NDT," Mater. Eva., **55**(3):407–412.

[116] **BEIN B. K., GIBKES J., GU J. H., HUETTNER R., PELZL J., BALAGEAS D. L. AND DEOM A. A. 1992,** "Thermal Wave Characterization of Plasma-Facing Materials by IR Radiometry," *J. Nucl. Mater.*, **191-194**:315-319.

[117] **BUREAU INTERNATIONAL DES POIDS ET MESURES (BIPM) 2004,** "The BIPM and the evolution of the definition of the metre," from <http://www1.bipm.org/en/si/history-si/evolution_metre.html>, accessed June 24, 2004.

[118] **MATLAB 2005,** from The MathWorks, Inc. 1994-2005 [online]: <http://www.mathworks.com/>, accessed on January 11, 2005.

[119] **SPIEGEL M. R., SCHILLER J. J., SRINIVASAN R. A. 2000,** *Schaum's outline of theory and problems of probability and statistics*, McGraw-Hill, N. Y.

OTHER CONSULTED BIBLIOGRAPHY:

BALAGEAS D. L., DÉOM A. A., BOSCHER D. M., 1987, "Characterization and Nondestructive Testing of Carbon-Epoxy Composites by a Pulsed Photothermal Method," Materials Evaluation, **45**(4):466–465.

BENNETT C. A. AND PATTY R. R. 1996, "Thermal Wave Interferometry: A Potential Application of the Photoacustic Effect," *Appl. Opt.*, **21**(1):49-54.

BRITANICA 2004, "Thermometry" from Encyclopædia Britannica Premium Service: <http://www.britannica.com/eb/article?tocId= 9072086>, accessed on November 17, 2004.

BURKE J. 2004, "Physics 12 Course Notes", from Riverview Rural High School Physics EPSS (Electronic Performance Support System): <http://www.cbv.ns.ca/rv/physics/Physics12/physics12notes.pdf>, accessed on July 28, 2004.

CCD ASTRONOMY 2004, "CCD Revolution," [online]: <http://www.astrosurf. com/re/ ccdrev .html>, accessed on June 30, 2004.

COUTURIER J.-P. AND MALDAGUE X. 1997, "Pulsed Phase Thermography of Aluminum Specimens," *Proc. SPIE, Thermosense XIX*, **3056**:170-175.

HOUNSFIELD G. N. 2004, "Computed Medical Imaging," from Nobel e-Museum - The Official Web Site of The Nobel Foundation: <http://www.nobel.se/medicine/laureates/1979/hounsfield-lecture.html>, accessed on July 5, 2004.

LUDWIG N. AND TERUZZI P. 2002, "Heat losses and 3D diffusion phenomena for defect sizing procedures in video pulse thermography," *J. Appl. Phys.*, v **43**:297-301.

MACLACHLAN SPICER, J. W. KERNS W. D. AAMODT L. C AND MURPHY J. C. 1991, "Time-Resolved Infrared Radiometry (TRIR) of Multilayer Organic Coatings using Surface and Subsurface Heating," *Proc. SPIE*, *Thermosense XIII*, **1467**:311-321.

MARINETTI, S., GRINZATO E., BISON P. G., BOZZI E., CHIMENTI M., PIERI G. AND SALVETTI O. 2004, "Statistical Analysis of IR Thermographic Sequances by PCA", *Infrared Phys. Technol.*, 46:85-91.

MILLS A. F. 1999, "Basic Heat and Mass Transfer," 2nd edition, Prentice Hall Inc. USA.

MONCHALIN J.-P. 2004, "Non Contact Generation and Dtection of Ultrasound Lasers," *Proc. 16th World Conference on Nondestructive Testing (WCNDT)*, Montreal (QC), August 30 - September 3, 2004, CD of proceedings.

RAJIC N. 2002, "Principal Component Thermography For Flaw Contrast Enhancement and Flaw Depth Characterisation in Composite Structures," *Compos. Struct.*, **58**: 521-528.

RAJIC N. 2002, "Principal Component Thermography", Airframes and Engines Division, DSTO Aeronautical and Maritime Research Laboratory, Fishermans Bend, Victoria, Australia.

RAO B. P. C. 2004, "Visual Techniques in NDT," Encyclopaedia of Materials: Science and Technology, Elsevier Science Ltd, September 2001, 6043-6046, [online]: <http://www.geocities.com/raobpc/Visual.html> accessed on November 29, 2004.

SPRING R. AND SNELL J. 2004, *Infrared thermography*, The Engine Yearbook 2004.

VAVILOV V. 2004, "Evaluating the Efficiency of Data Processing Algorithms in Transient Thermal NDT", *Proc. SPIE, Thermosense XXVI*, **5405**:336-347.

VAVILOV V. P. 1994, "Advances in Signal Inversion with Application to Infrared Thermography" in X. P. V. Maldague (ed.): Advances in signal processing for Nondestructive Evaluation of Materials, Kluwer Academic Publishers, Netherlands, 161-184.

WETSEL G. C. AND MCDONALD F. A. 1984, "Resolution and Definition in Photothermal Imaging," *J. Appl. Phys.*, **56**(11): 3081-3085.

ZALAMEDA J. N., RAJIC N., AND WINFREE W. P. 2003, "A comparison of image processing algorithms for thermal nondestructive evaluation," *Proc. SPIE, Thermosense XXV*, **5073**:374-385.

Appendix A. Fundamentals of Infrared Radiation

The outside world is something independent from man, something absolute, and the quest for the laws, which apply to this absolute, appeared to me as the most sublime scientific pursuit in life [104].
Max Planck (1858 to 1947), German Scientist.

Max Planck was told by one of his professors that *"physics was essentially a complete science with little prospect of further developments"* [104]. Fortunately, Planck decided to pursue a career in Physics after all. In a paper published in 1900, he proposed a mathematical solution to characterize the radiant energy distribution over the entire frequency spectra, a problem that had puzzled scientists for years[8]. To explain his results, he came up with the revolutionary idea that energy is radiated in discrete units named *quanta*, rather that as a steady stream as described by classical Physics; and he introduced a universal constant that he called *quantum of action*, which is better known as the *Planck's constant*, *h*. Although not fully understood at the beginning, Planck's concepts were gradually adopted by the scientific community forming the basis of *Quantum Theory* and marking the beginning of a new era in Physics. ►

Figure A.1. Max Karl Ernst Ludwig Planck (1858 to 1947).

[8] Theory on Radiation is the result of over 40 years of research contributions from many dedicated scientists starting with Kirchhoff's enouncement of his law in 1859 and his *blackbody* definition in 1860, followed by the work of Stefan (1879) and Boltzmann (1884); and Wien in 1893; among others, and that culminated with the enouncement of Planck's law in 1900.

A.1 The Electromagnetic Spectrum

All matter regardless of its state or composition continuously emits electromagnetic (EM) radiation. Radiation can be viewed either as the transportation of tiny particles called *photons* or *quanta*; or as the propagation of EM *waves*. This so-called Wave-Particle Duality [105], is very convenient in describing EM behavior. For instance, the amount of radiated energy by a photon E, *i.e.* a particle measure, can be directly related to the corresponding wavelength λ, or frequency f, of a wave, through the following relationship:

$$E = hf = \frac{hc}{\lambda} \tag{A.1}$$

where h = 6.6256 x 10^{-34} Js is a universal (or Planck's) constant, and c=2.9979 x 10^{8} m/s is the speed of light. From this equation, the relationship between frequency and wavelength can be obtained:

$$f = \frac{c}{\lambda} \tag{A.2}$$

Hence, EM waves at different λ or f, are basically the same kind of physical 'objects', *i.e.* EM radiation, the difference among them is in the amount of photon energy E [106], related to each particular λ and f, respectively, through Eq. (A.1).

The EM *spectrum*, depicted in Figure A.2, can be thought as a map containing all types of EM radiation. The most energetic forms are located at the short wavelength end of the spectrum, left part of Figure A.2, between 10^{-14} and 10^{-8} m. Gamma (γ) Rays and X-Rays are widely used in medicine, security and nondestructive testing. On the other hand, wavelengths ranging from 1 mm to several hundred meters, right part of Figure A.2, are transparent to the atmosphere, so they are mostly used for data transmission, *e.g.* radio, TV, mobile phones, etc. Many other kinds of waves used in numerous applications are enclosed between these two extremes.

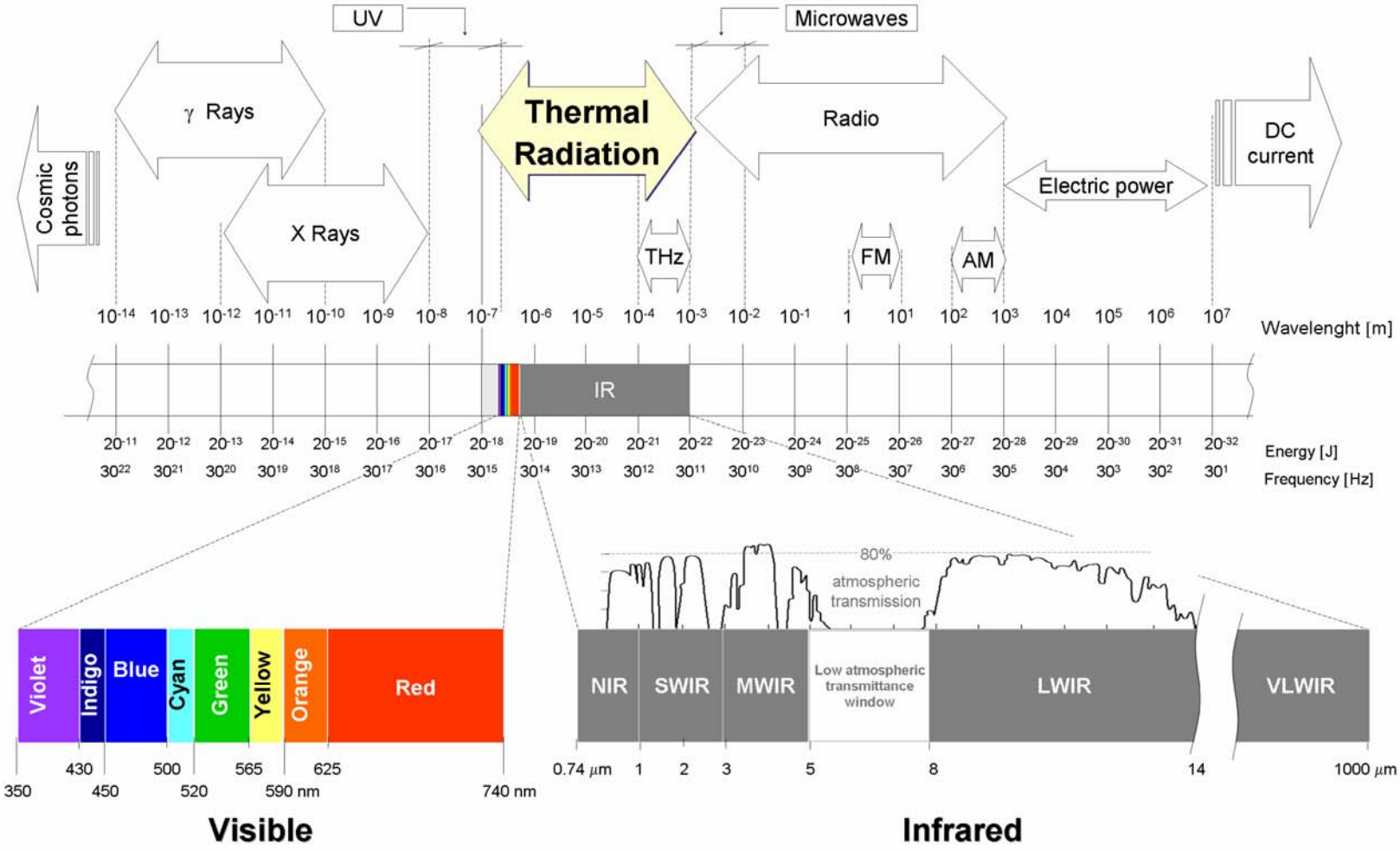

Figure A.2. The electromagnetic spectrum.

Whenever there is a thermal difference (above 0 K) between two objects, radiation will be exchanged in the form of heat. The *thermal radiation* band is enclosed between 0.1 and 1000 μm of the spectrum (highlighted in Figure A.2). The thermal spectrum can be divided into three spectral bands: the ultraviolet (UV) spectrum, the visible band and the infrared (IR).

The infrared part of the spectrum (0.74 - 1000 μm) can be further subdivided into five parts, summarized in Table A.1: Near Infrared (NIR) from 0.74 to 1 μm; Short Wavelength Infrared (MIR) from 1 to 3 μm; Medium Wavelength Infrared (MWIR) from 3 to 5 μm; Long Wavelength Infrared (LWIR) from 8 to 14; and Very long Wavelength Infrared (VLWIR) from 14 to 1000 μm. Although this subdivision is somehow arbitrary and varies from one source to another, it is based on the atmosphere high transmissivity 'windows', *i.e.* the wavelength bands where atmosphere interferes the less with the incoming IR radiation, and on the detector's spectral sensitivities. High atmospheric transmission windows (80%) can be identified above the IR spectrum in Figure A.2 for a 18,000 m horizontal path at sea level containing 17 mm of precipitate water [17].

Table A.1. Infrared spectral bands. Adapted from [5], [17], [107], [108], [109].

Spectral bands	**Range [μm]**	**Common detector materials***	**Applications**
NIR	0.74 - 1	Si	Telecommunications
SWIR	1 - 3	InGaAs, PbS	Remote sensing
MWIR	3 - 5	InSb, PbSe, PtSi, HgCdTe	High temperature inspection (indoors, scientific research)
LWIR	8 - 14	HgCdTe	Ambient temperature (outdoor, industrial inspection)
VLWIR	14 - 1000	-	Spectrometry, astronomy

*Si: silicon; In: Indium; Ga: gallium; As: arsenic; Pb: lead; S: sulfur; Sb: antimony; Se: selenium; Pt: platinum; Hg: mercury; Cd: Cadmium; Te: tellurium.

Infrared radiation is invisible to the unaided eye, hence, energy radiated in the IR band needs to be transformed into a visible image through specialized imaging equipment (see section A.3). As shown in Table A.1, the detectors materials (and combinations) are selected to perform at these particular bands.

A.2 Theory of Heat Radiation

A.2.1 Blackbody Radiation

In 1860, Gustav Robert Kirchhoff (1824-1887) defined a **blackbody** as a surface that neither reflects nor transmits incident radiation. Instead, a blackbody absorbs all incident radiation irrespective of direction and wavelength. In addition to be a perfect absorber, a blackbody is also a perfect *radiator*. Therefore, all radiation leaving a blackbody is emitted by the surface and no surface can emit more energy than a blackbody. In addition, a black surface is a *diffuse emitter*, *i.e.* the emitted radiation is a function of the wavelength and temperature but independent of the direction.

In 1900, Max Planck found an expression describing the spectral distribution of the radiation intensity from a blackbody, known today as *Planck's Law* [110]:

$$E_{\lambda,b}(\lambda,T) = \frac{C_1 \lambda^{-5}}{\exp(C_2/\lambda T - 1)} \tag{A.3}$$

where C_1=3.742 x 10^8 W $\mu m^4/m^2$ is the first radiation constant, and C_2=1.4389 x 10^4 μm K is the second radiation constant.

Figure A.3 shows the Planck's distribution for different representative temperatures: from the Cosmic Microwave Background (CMB)[9] radiation, to the emitted surface temperature of a Blue Star (the most energetic kind of star at about

[9] The CMB is regarded as the best available evidence of the "Big Bang". This radiation is essentially a blackbody with temperature at about 2.735 K, which peaks in the microwave portion of the spectrum (see Figure A.2and Figure A.3).

40,000 K). Also shown in this graph, is the Planck distribution for the Sun's surface temperature (5,800 K), for a common incandescent light bulb temperature (3,000 K), for the minimum temperature at which an object will glow in the visible spectrum (~800 K) and for a 0°C blackbody (273.15 K).

A double logarithm scale is used for sake of clarity. Some interesting observations can be retrieved from this graph: (1) emitted radiation continuously varies with the wavelength; (2) the total amount of emitted energy increases with temperature; (3) the peak of the curve shifts to the lower wavelength end of the spectra; (4) there is more energy difference per degree at shorter wavelengths.

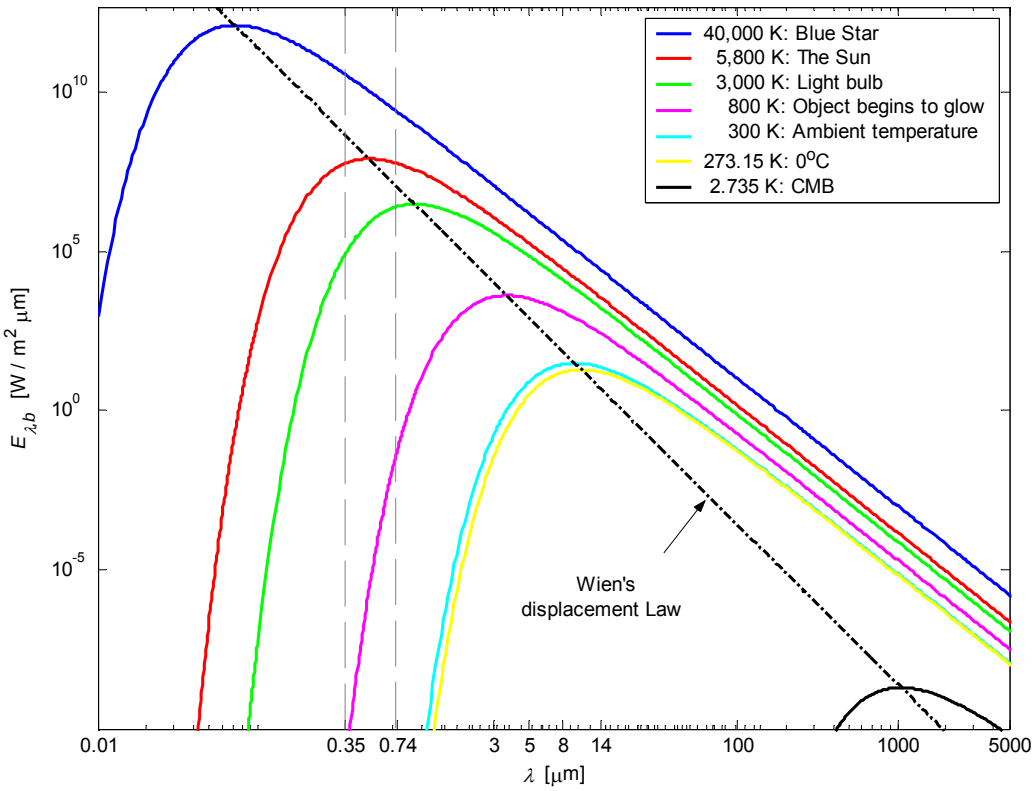

Figure A.3. Planck's distribution at different temperatures. MatLab® function: `planck_distribution.m`.

In 1879, Josef Stefan (1835-1893) experimentally determined a simple expression relating radiant emission from a surface to its temperature. Stefan's results were theoretically confirmed in 1884 by one of his former students, Ludwig Boltzmann

(1844-1906). The resulting expression, known as Stefan-Boltzmann Law, states that the total radiant emission, integrated over all frequencies (or wavelengths), is proportional to the fourth power of its absolute temperature [110]:

$$E_b = \sigma T^4 \tag{A.4}$$

where σ=5.6697 x 10^{-8} W/m^2 K^4 is the Stefan-Boltzmann constant. Eq. (A.4) can be obtained by integrating Planck's Law, Eq. (A.3), over the entire spectrum ($0<\lambda<\infty$).

Planck's Law gives the intensity radiated by a blackbody as a function of frequency (or wavelength), whilst Stefan-Boltzmann's Law gives the total flux integrated over all frequencies (or wavelengths). Now, the frequency (or wavelength) at which Planck's distribution has the maximum specific intensity (marked as a straight dotted line in Figure A.3) is given by Wien's displacement Law. In 1893, Wilhelm Wien (1864-1928) measured the spectral distributions for a blackbody at different temperatures. Wien found that the peak energy was proportional to their corresponding wavelength for varying temperature, that is [110]:

$$\lambda_{\max} T = C_3 \tag{A.5}$$

where C_3=2897.8 μm K, is the third radiation constant. This relationship can be obtained by differentiation of Eq. (A.3) with respect to λ, and setting the result equal to zero.

Wien's Law gives an indication of the 'color' of the thermal radiator. Wavelengths in the visible area of the electromagnetic spectrum, *i.e.* between 350 and 740 nm, see Figure A.2, are associated with high temperatures. Objects will begin to glow at about 800 K (527°C), first in the red band, then orange, yellow, and so on, each color shifting indicating higher temperatures. The Sun, whose surface temperature is at about 5,800 K, radiates energy mostly in the yellow portion of the visible spectra. Stars that are more energetic emit energy at even higher temperatures (as high as 40,000 K!). Most of what we see however is the reflection of these

extremely high temperature objects on lower temperature surfaces. In general, thermographic instruments, either in the MWIR or LWIR (see Figure A.2 and Table A.1) can sense the emitted energy from objects that are at a temperature of approximately 240 K (-35^{o}C) or higher [111].

Planck's law is an invaluable tool to estimate spectral distribution for a blackbody, which corresponds to the theoretical maximum possible emission from any real object. Of importance in NDT&E, the energy emitted by a body (real or blackbody) is a function of his surface temperature. However, the energy detected by an IR detector, depends as well on the real object surface properties, as discussed next.

A.2.2 Real Surface Emission

EMISSIVITY, ε

Kirchhoff defined *emissivity* ε, as the ratio of thermal radiation emitted by a *real* surface at a given temperature to that of a blackbody at the same conditions (temperature, wavelength and direction) [110]:

$$\varepsilon\ (\lambda,T_S)=\frac{E\ (T_S)}{E_b(T_S)} \tag{A.6}$$

This relationship represents an average over all possible directions and wavelengths and can be used, together with Planck's distribution law, Eq. (A.3), to compute the emissive power. Hence, spectral distribution for real surfaces does depend on the wavelength but it differs from Planck's Law distribution shown in Figure A.3.

Four types of sources can be distinguished according to their spectral emissivity variations [17], [112]: a blackbody (perfect radiator), for which $\varepsilon(\lambda,T_S)=\varepsilon=1$; a *graybody* for which $\varepsilon(\lambda,T_S)=\varepsilon=constant<1$; a *whitebody* (perfect reflector) [112], for which $\varepsilon(\lambda,T_S)=\varepsilon=0$; and a *selective radiator*, for which $\varepsilon(\lambda,T_S)$ varies with λ.

ABSORPTIVITY, α

Absorptivity α, measures the fraction of absorbed energy by a surface. For a blackbody α=1, whilst α=0 corresponds to a whitebody. For real surfaces, absorptivity range between 0 and 1. More formally, the ratio of radiant emission from a real surface *E*, to absorptivity α, is a constant for all materials equal to the incident radiant energy to a surface or *irradiation G*, at the same temperature T_S, that is [110]:

$$\frac{E(T_S)}{\alpha} = G \tag{A.7}$$

As was the case for emissivity, absorptivity depends on direction and wavelength, but is practically unaffected by surface temperature.

REFLECTIVITY, ρ

Reflectivity is defined as the fraction of the incident radiation reflected by a real surface. Although reflectivity depends on the direction of both, the incident and reflected radiation, it is convenient to work with integrated average to avoid complication. If a surface reflects radiation in all directions regardless of the direction of the incident radiation, the surface is said to be **diffuse**. Conversely, if radiation is reflected with an angle equal to the incident angle, the surface is **specular** [110].

Absorptivity and reflectivity are responsible for our perception of color. As discussed above, color is not the result of emission, since only objects at high temperature (higher than ~800 K) glow in the visible portion of the spectra. Instead, color is the result of a balance between reflection and absorption. A surface is white if it reflects all incident radiation, and it is black if it absorbs all the irradiation in the visible spectra. Color, however, does not give an indication of the absorbed or reflected irradiation since most of the energy may be in the IR band. The typical example is the snow, which is highly reflective at visible wavelengths (between 350

and 750 nm), but strongly absorbs and emits IR radiation, approximating a blackbody at longer wavelengths [5].

TRANSMISSIVITY, τ

Transmissivity is defined as the ratio of the directly transmitted radiation after passing through a participating medium (atmosphere, dust, fog) to the amount of radiation that would have passed the same distance through a vacuum. Dissolved colloidal and suspended particles cause further attenuation by absorbing and scattering the incident light beam. Higher attenuations are observed at long wavelengths. Transmissivity is of importance when selecting the spectral band of operation of the IR equipment as discussed in paragraph A.3.

ENERGY BALANCE

In active thermography applications, we are interested in capturing the *emissions* coming from a surface following an external excitation. However, not all the incident energy is re-emitted by the surface as depicted in Figure A.4. On the contrary, one part of the energy is *absorbed*, one part is *transmitted*. In addition, not all the emitted energy is the result of the active thermal excitation. Part of the energy that is being emitted by a surface is the *reflection* from several external sources, other than the active thermal excitation, and another part is energy coming form the inside. As a result, surface emission is a complex process resulting from a balance between transmission, absorption, and reflection.

As illustrated in Figure A.4, a fraction of irradiation G is *absorbed* αG; another fraction is *reflected* ρG; and for semitransparent media, another fraction is *transmitted* through the surface τG. Symbols α; ρ; and τ.; correspond to the absorptivity, the reflectivity and the transmissivity, respectively, which are the surface properties defined below. By the energy conservation principle [110]:

$$G = \alpha G + \rho G + \tau G \tag{A.8}$$

it follows that:

$$\alpha + \rho + \tau = 1 \tag{A.9}$$

For opaque materials τ=0, from Eq. (A.9), therefore:

$$\varepsilon = (1 - \rho) \tag{A.10}$$

which is convenient when reflectance is easier to measure than emissivity [17].

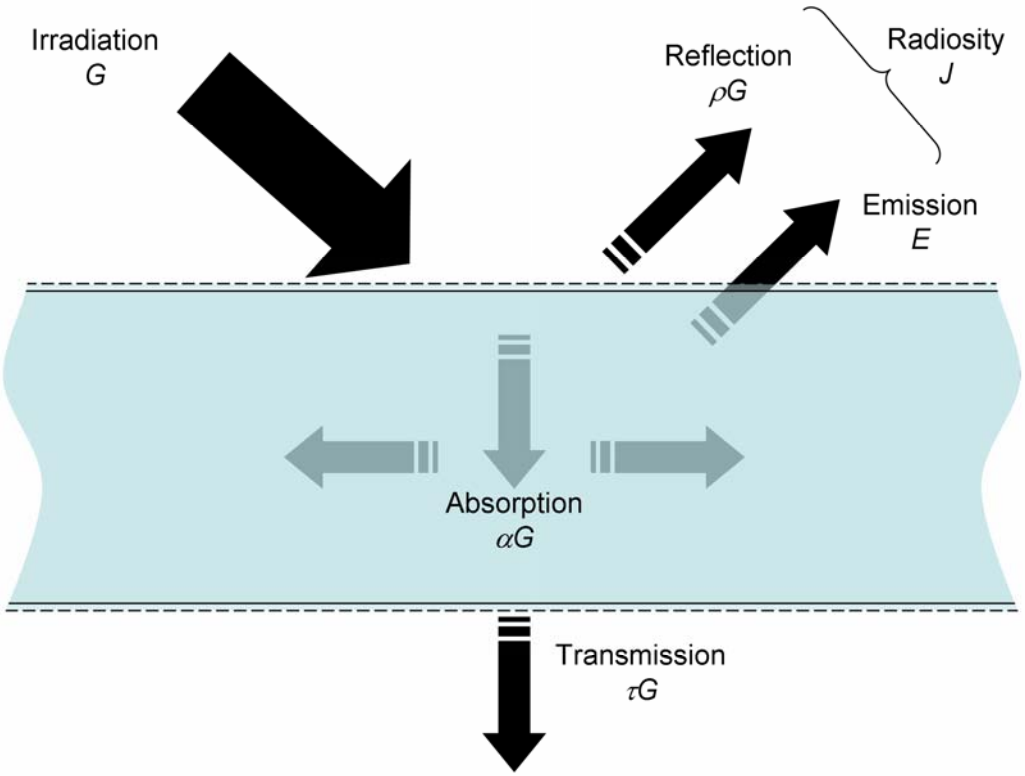

Figure A.4. Energy balance in a semitransparent medium.

As seen in Figure A.4, *Radiosity J*, is the sum of two contributions: direct emissions from a surface *E*, and reflected irradiation from the incident ray ρG. For a blackbody however at a given temperature [110]: $G=E_b$, when combined with Eq. (A.6) and Eq. (A.7), it follows that:

$$\varepsilon = \alpha \tag{A.11}$$

which is commonly referred as Kirchhoff's Law.

The validity of Eq. (A.11), is restricted to blackbody emission. Nevertheless, it is still applicable for the case of diffuse surfaces, which are independent of the direction distribution of the emitted radiation [110].

In order to increase emissivity to a value near to 1, it is a common practice to *blackpaint*[10] the specimen's surface whenever possible prior to inspection. This procedure contributes at the same time to diminish emissivity variations on the surface and to eliminate reflections from the environment. There are other techniques that can be considered when blackpainting is not practical or possible to implement [5].

A.3 IR Imaging Equipment

IR Imaging Systems usually operate in two[11] high transmissivity atmosphere windows (Table A.1): LWIR (8-14 μm) and MWIR (3-5 μm). It can be seen from Wien's Law, Eq. (A.5) and Figure A.3, that high temperature bodies have their peak emission at short wavelengths, while objects emitting at ambient temperature have their maximum emission at longer wavelength bands. Therefore, the MWIR band is preferred when inspecting high temperature objects and the LWIR band when working with near room temperature objects. Other important criteria for band selection are [5]: the operating distance, indoor-outdoor operation, temperature and emissivity of the bodies of interest. For instance, long wavelengths (LWIR) are preferred for outdoor operation since they are less affected by radiation from the Sun. LWIR cameras are typically uncooled systems using a microbolometer Focal Plane Arrays commonly used in industrial IR applications, although cooled LWIR cameras using Mercury Cadmium Tellurium (MCT) detectors exists as well. On the contrary, the majority of the MWIR cameras

[10] Other painting colors besides black show a very good emissivity coefficient (ε~0.94) and can be used as well.

[11] The near IR system (approximately between 0.9 and 1.7 μm) is a new addition to the infrared imaging camera field. The main use of this camera is however restricted to the telecommunications industry [109].

require cooling, using either liquid nitrogen or a Stirling cycle cooler. Cooling to approximately -196^{o}C, offer excellent thermal resolution, but it might restrict the span of applications to controlled environments.

A.3.1 Detectors

An **infrared detector** or **sensor** is a device that converts radiant energy into some other measurable form, *e.g.* an electrical current. There are two classes of infrared sensors: *thermal* and *photonic* (or *quantum*) detectors. A thermal detector responds to incident radiation by raising its temperature. When a thermal detector is at equilibrium there is no thermal conduction, the sensor simply *radiates* energy at the same rate as it *absorbs* it. The detector's temperature will increase whenever the incident radiation rises above the equilibrium state, the detector absorbs more energy than it radiates. The excess temperature is then removed away by conduction. Types of thermal detectors include thermocouples, bolometers, pneumatic detectors, pyroelectric detectors and liquid crystals. A detailed description of these and other detectors can be found in references [5] and [17]. Thermal detectors response is theoretically independent of wavelengths and they display high sensitivity at room temperature.

A photonic[12] detector is made from semiconductor materials and operates on the principle that incident radiation excites electrons from the valence to the conduction atomic bands [113]. Even though they provide superior sensitivity and response speed than thermal sensors, photon detectors typically require cryogenic cooling to minimize the noise to obtain the high relative sensitivity.

In summary, thermal detectors exhibit a modest performance, with slower response than photonic sensors, but they are less expensive and do not require

[12] Photonic detectors are subdivided in (1) photoemissive detectors, based on the emission of carriers from a metal to a semiconductor material through absorption of radiation; and (2) quantum detectors, which can be photoconductors (the electrical conductivity increases with temperature) or photovoltaic (or photodiode) detectors (a current proportional to incident radiation flows through the diode junction of the semiconductor) [5].

cryogenic cooling as their photonic counterparts. Developments in both fields predicts that uncooled photon detectors and thermal detectors with better performance will soon emerge [5], [107], [114].

A.3.2 Focal Plane Arrays (FPA)

Focal Plane Arrays (FPAs) are today's most common IR imaging configuration. An FPA is made up of rows and columns of individual IR detectors. The fill factor is an important parameter in selecting FPAs, it provides the IR-sensitive material to total surface (including the signal transmission paths) ratio. The higher the fill factor, the higher the sensitivity, the cooling efficiency and the overall image quality of the system. If FPAs have both IR-sensitive material and signal transmission paths on the same layer they are called *monolithic* FPAs. Conversely, a *hybrid* array has the IR-sensitive detector material on one layer and the signal-transmission and processing circuitry on another layer bonded together by small collecting bumps. Hence, monolithic FPAs are easier and less expensive to manufacture than hybrid FPAs, but they generally have lower performance since having the detector material and signal pathways on the same level significantly reduce the fill factor (~55% for a monolithic FPA vs. ~90% for a hybrid FPA).

The readout device is also important. An FPA can use one of two technologies, a Charge Coupled Device (CCD) or a Complementary Metal Oxide Semiconductor (CMOS). The principal advantages of CMOS with respect to CCDs are: lower fabrication cost, possibility of developing a single-chip camera, lower voltages and have lower power requirements (portability), possibility to read out a portion of the array rather than the entire array (windowing). On the other hand, CMOS have much higher noise than CCDs, since CMOS have more on-chip circuitry and uses amplifiers for each pixel, producing nonuniformities known as Fixed Pattern Noise (FPN). FPN can be removed by recording the pattern and post processing with software to remove it [23], but this further reduces the useful dynamic range. Furthermore, the sensitivity and the filling factor (< 30%, the amplifiers also take up more area) of the CCD is much greater. CMOS is expected to dominate in the low-

end consumer market (camcorders, snapshot cameras, toys, etc.) and other specialty applications such as surveillance. However, CCDs will remain unchallenged for scientific and technical applications requiring high fidelity, resolution, and dynamic range for some time to come [107], [114].

One of the most interesting characteristic of today's IR imaging systems based on FPA arrays, is that they confer the capability to manage data in several ways.

A.3.3 Representing IR Images

IT data may be represented in several manners. A common approach is to display a two-dimensional (2D) map, where each element gives the intensity (*e.g.* temperature, time, amplitude, phase, etc.) of a point on the specimen's surface (or scene). Figure A.5a shows a 2D view of a Plexiglas® specimen with 9 flat-bottomed circular holes and a vertical strip on the right machined in the back (see details for specimen PLEXI013 in Appendix F.7). Figure A.5d is a zoomed portion of Figure A.5a where the picture elements or *pixels* can be distinguished (coordinates are indicated on the left and below).

One-dimensional (1D) profiles can be used in two ways. Spatial profiles are useful to highlight geometrical features as in Figure A.5b and c, or it is also possible to retrieve information from the signature evolution through time as in Figure A.5e. More importantly, 1D temporal profiles give useful information about the defect depth as will be stressed in section 1.2.4. It is also possible to represent data as three-dimensional (3D) views, see Figure A.5f, in which x and y coordinates correspond to the pixel location p, and the z coordinate is the intensity value at p.

Finally, animated films are also possible. This is particularly interesting since allows to follow intensity and spatial variations through time in either 1D, 2D or 3D views.

No matter what type of representation is being used, there are always many sources of signal degradation as discussed in next paragraph.

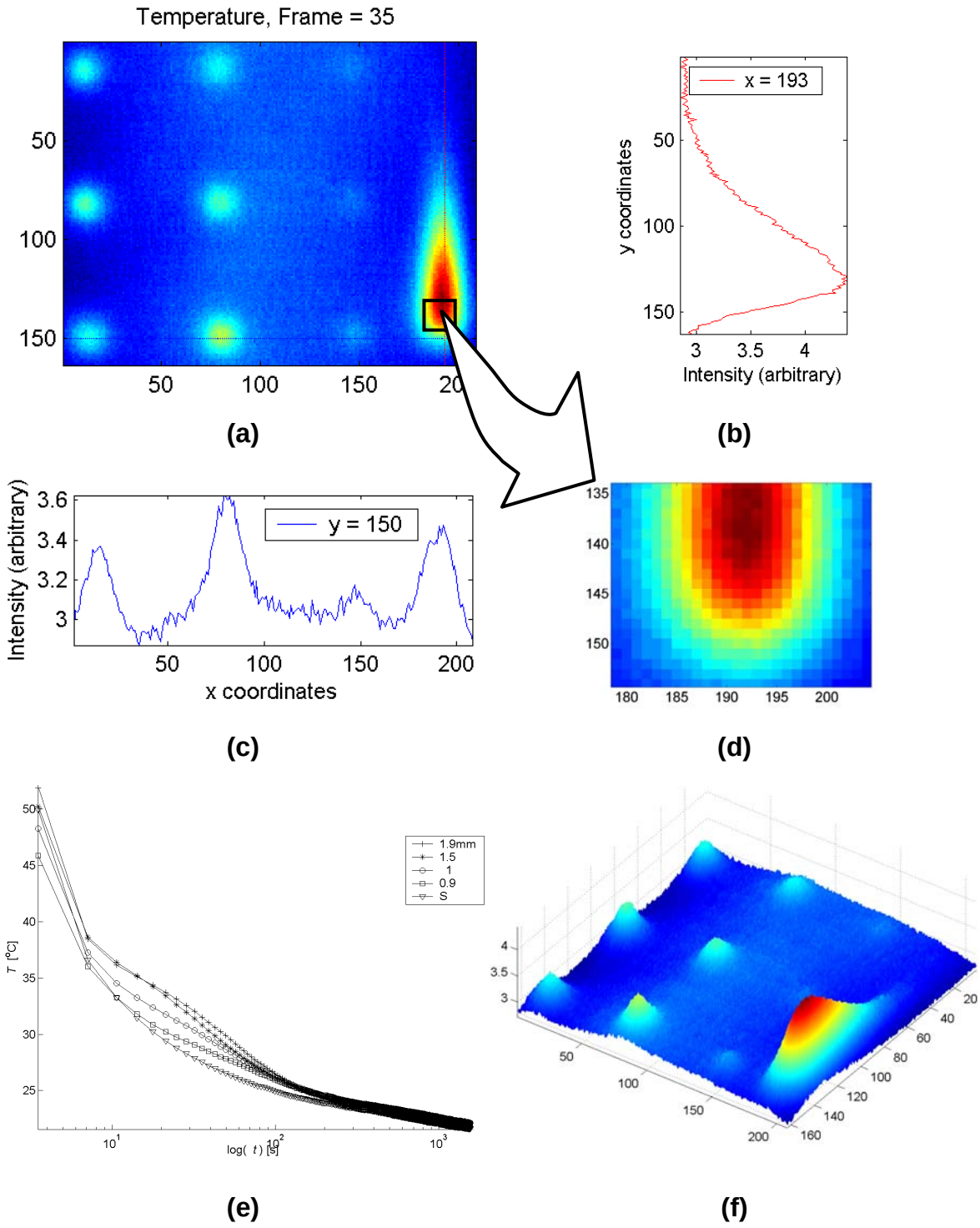

Figure A.5. IR image representations: (a) 2D view; (b) 1D spatial profiles along *x*=193 and (c) along *y*=150; (d) zoomed portion of (a); (e) 1D temporal thermal profiles for the 4 shallowest defects; and (f) 3D view. Data from PLEXI013 in Appendix F.8. MatLab® scripts: (a) `profiles.m`, (c) `evolution.m`, and (d) `disp3D.m`.

A.3.4 Signal Degradation

Besides being weak by nature (when compared to more energetic forms of EM radiation like X-Rays, see Figure A.2), IR signals are affected by numerous sources of noise that contribute to degrade the signal even further. First, there is the **electronic** noise from the IR detector, which can be of three kinds: *shot* noise, caused by the random variation of the incident radiation; *thermal* (or Johnson) noise, resulting from the random motion of electrons in resistive materials (cooling the detector can help to reduce it); and *flicker* (or 1/*f*) noise, which depends on the observation frequency as $1/f^n$ (where n is typically between 0.9 and 1.35) [5].

Noise can also be **optical**, resulting from the random fluctuations of the incident radiation; **heating**, because of non-uniform thermal excitation and spurious reflections; **environmental**, electromagnetic interference induced by power lines, radio and TV broadcast, and by heavy machinery; and **structural**, random variability of thermophysical properties.

In addition, the characteristics of the detectors, *e.g.* detectivity, responsivity among many others [5], will dictate the overall performance of the detectors. For instance, cooled photonic detectors respond faster and with greater sensitivity than the uncooled counterparts.

Furthermore, there are other kinds of effects caused either by the lens or by the way it is been used. Those so-called **aberrations** might degrade the signal. Typical aberrations are chromatic, spherical, coma, astigmatism, curvature of field, distortion and vignetting [5]. Most of these aberrations can be corrected using (a combination of) lenses having opposing aberrations. **Vignetting** is of particular interest in IT, since it is temperature dependent. Fortunately, this kind of aberration can be corrected by processing the signal [115].

Several image-enhancing techniques have been proposed to enhance IR signatures as discussed in [23] and [24].

A.4 Summary

IR radiation from a body (blackbody or real) is a function of its surface temperature. A blackbody radiates energy as described by Planck's Law, Eq.(A.3). A real object on the other hand, emits only a portion of the IR radiation that a blackbody would emit at the same temperature. This fraction is given by the emissivity coefficient, Eq. (A.6). Besides the object's surface emissivity, the radiation that is actually detected by an IR sensor depends on the surface properties of the object: absorptivity, and reflectivity and transmissivity (τ=0 for opaque bodies); and on the medium (atmosphere) absorptivity and transmissivity. Blackpainting the specimen surface increases the surface emissivity and at the same time decreases the reflections from the environment. An energy balance allows to separate the portion of the radiated energy that is actually been emitted by an object from the portions that are been absorbed by the atmosphere, and reflected from the environment.

Imaging equipment for NDT&E applications is designed to work in either the MWIR or LWIR (see Figure A.2), since atmosphere transmissivity is high in this spectral windows. LWIR is favored when inspecting room temperature objects and outdoor applications, whilst MWIR is a better choice for high temperature objects. FPA is the preferred IR imaging configuration nowadays, allowing to represent IR data in several different ways. There are basically two technologies CMOS and CCDs. The former is gaining ground on industrial and surveillance applications, but the later is still unchallenged for scientific and technical applications requiring high fidelity, resolution, and dynamic range.

In any case, IR signatures are weak and noisy. As a result, image-processing techniques are required to enhance the signal and to increase contrast.

Appendix B. Thermophysical properties

B.1 Conductivity, *k*

Thermal conductivity *k* [W/m°C] is a thermophysical property of matter defined as:

$$k \equiv \frac{q_n}{\left(\partial T / \partial n\right)} \tag{B.1}$$

Conductivity gives an indication of the energy diffusion rate by conduction for a particular material. For the same thermal gradient, heat flux will increase with *k*. In general [110]: $k_{solids} > k_{liquids} > k_{gas}$.

B.2 Diffusivity, α

Thermal diffusivity α [m^2/s], measures the material's ability to conduct heat in relation to its capacity to store it [110]:

$$\alpha = \frac{k}{\rho\, c_P} \tag{B.2}$$

where *k* [W/m K] is the thermal conductivity, ρ [kg/m^3] the density and *c* [J/kg K] the specific heat.

Materials with large α respond faster to thermal changes than (reach thermal equilibrium before) low α materials. Thermal diffusivity is therefore an important quantity in all transient conduction problems.

B.3 Effusivity, *e*

Effusivity *e*, [$Ws^{½}/m^2 \cdot K$], is a thermophysical property relevant to transient surface heating processes [116], which is present in all materials (solids, liquids, pastes, powders, and gases). Effusivity measures the material ability to exchange heat with its surroundings and is defined as:

$$e = \sqrt{k\rho\ c_P} \tag{B.3}$$

B.4 Density, ρ; and specific heat, c_P

Density ρ, is a measure of mass per unit volume. Specific heat c_P, is the ratio of the amount of heat required to raise the temperature of a unit mass of a substance by one unit of temperature to the amount of heat required to raise the temperature of a similar mass of a reference material, usually water, by the same amount. They are both considered thermodynamic properties in the sense that they pertain to the equilibrium state of the system. When combined ($\rho \cdot c_P$), they provide an indication of the ability of the material to store thermal energy, *i.e.* their heat capacity [110]. Specific values for representative materials are shown in Table B.1.

Table B.1. Thermophysical properties of common NDT&E materials.

	Material	***k*** **(W/m K)**	ρ **(kg/m^3)**	***c*** **(J/kg K)**	α **(m^2/s) x 10^{-7}**	***e*** **(Ws$^{1/2}$/m^{2}K)**	e/e_{air} **(-)**	e/e_{teflon} **(-)**
Common materials	Aluminum (pure)	237	2702	903	971	24047	4468	32
	Steel							
	Mild	46	7900	440	132	12645	2349	17
	AINSI 302 @ 300 K	15.1	8055	480	39	7641	1420	10
	CFRP							
	|| fibers	7	1600	1200	36.5	3666	681	5
	⊥ fibers	0.8	1600	1200	4.2	1239	230	1.6
	GFRP							
	|| fibers	0.38	1900	1200	1.7	931	173	1.2
	⊥ fibers	0.3	1900	1200	1.3	827	154	1.1
	Plexiglas®	0.19	1190	1470	1.1	577	107	0.76
	Kevlar®	0.04	1440	1400	0.2	284	53	0.38
Simulated Defects	Air	0.024	1.2	1006	1988	5	1	0.01
	Teflon®	0.25	2170	1050	1.1	755	140	1

Appendix C. Thermal Waves

C.1 Wave propagation

Figure C.1 depicts the simple harmonic motion for two sinus waves. The *phase delay* ϕ, represents the fraction of the period that a particular wave lags or leads an un-shifted wave. The magnitude of an oscillation is called the *amplitude A*. Amplitude determines how loud is a sound or how bright is a light. The time it takes for a wave to repeat is called the *period T*; and its reciprocate is the *frequency f*, *i.e.* how many complete cycles pass through a point in one second. Frequency is an important characteristic of waves, giving for instance the *color* of light, *i.e.* its corresponding location on the electromagnetic spectrum; or the *pitch* (or note) of a sound. Light and sound however, are different kinds of waves.

Sound cannot travel unless there is a media, such as air or water, to move through. Light on the other hand does not require the presence of matter to propagate; it does so at a speed of light in vacuum. In fact, all kinds of EM waves travel through vacuum at the speed of light, see Eq. (A.1).

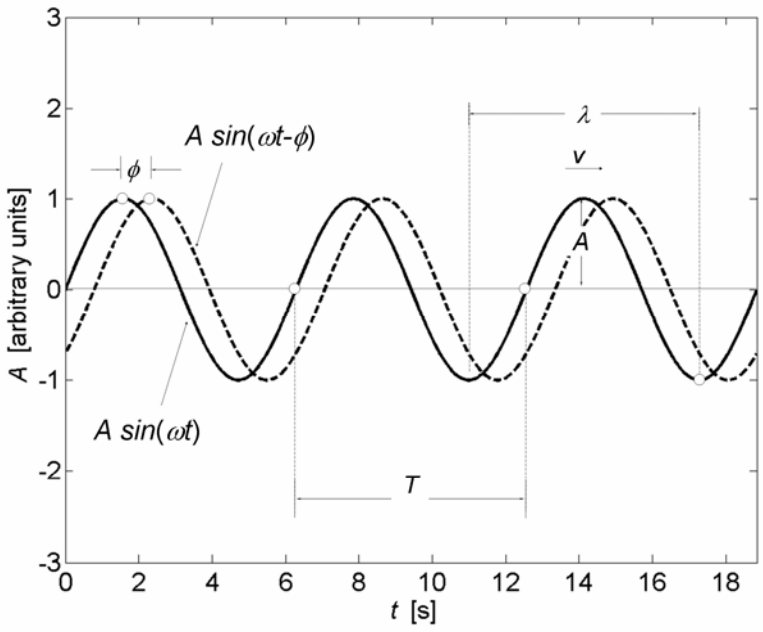

Figure C.1. A sinusoidal wave and its properties.

Another important property of EM waves is the wavelength λ, which gives the distance between corresponding points separated by one period *T*. Wavelength and frequency give the same information, though λ is traditionally used to denote

the color, since it can be measured directly[13]. However, frequency ***f*****,** would be a better choice since unlike the wavelength, frequency does not change from one medium to another [112].

Thermal waves can be classified as **periodic** or **pulsed** [31]. A pulse can be seen as the sum of many sinusoidal waves at several frequencies. Hence, it is possible to reconstruct any stimulation pattern from a summation of several periodic waves.

C.2 Periodic Thermal Waves

The Fourier's Law one-dimensional solution for a periodic thermal wave propagating through a semi-infinite homogeneous material may be expressed as [31]:

$$T(z,t) = T_o \exp(-\frac{z}{\mu})\cos\left(\frac{2\pi z}{\lambda} - \omega t\right) \tag{C.4}$$

where T_0 [°C] is the initial change in temperature produced by the heat source, ω [rad/s] is the modulation frequency ($\omega=2\pi f$, with f being the frequency in Hz), λ [m] is the wavelength; and μ [m] is the diffusion length given by [31]:

$$\mu = \sqrt{\frac{2\alpha}{\omega}} = \sqrt{\frac{\alpha}{\pi f}} \tag{C.5}$$

where $\alpha=k/\rho c_P$ [m^2/s] is the thermal diffusivity, with k [W/m°C] being the thermal conductivity, ρ [kg/m^3] the density, c_P [J/kg°C] the specific heat; and f the thermal wave modulation frequency.

The thermal wavelength is defined as [31]:

---

[13] Albert A. Michelson developed an interferometric method to measure distance using wavelengths of light. In 1893, the Bureau International de Poids et Mesures (BINP) used Michelson's interferometer to defined the meter unit in terms of the number of wavelengths of the red line of cadmium radiation instead of the meter prototype [117].

$$\lambda \equiv 2\pi\mu \tag{C.6}$$

Figure C.2 shows two thermal waves having the same amplitude but different frequencies. Thermal wave propagation through a solid is a strongly damped phenomena in all cases, however, the high frequency thermal wave experience a greater decay than the low frequency wave. Hence, from Eqs. (C.4) to (C.6), it can be observed that after traveling a distance equal to μ, the thermal wave has already damped to exp(-1) ≈ 0.37 of its initial value, and by a factor of exp(-2π) ≈ 1/535.5 after penetrating a distance equal to λ. These situations are illustrated in Figure C.2, the dotted line corresponds to a pure exponential decay.

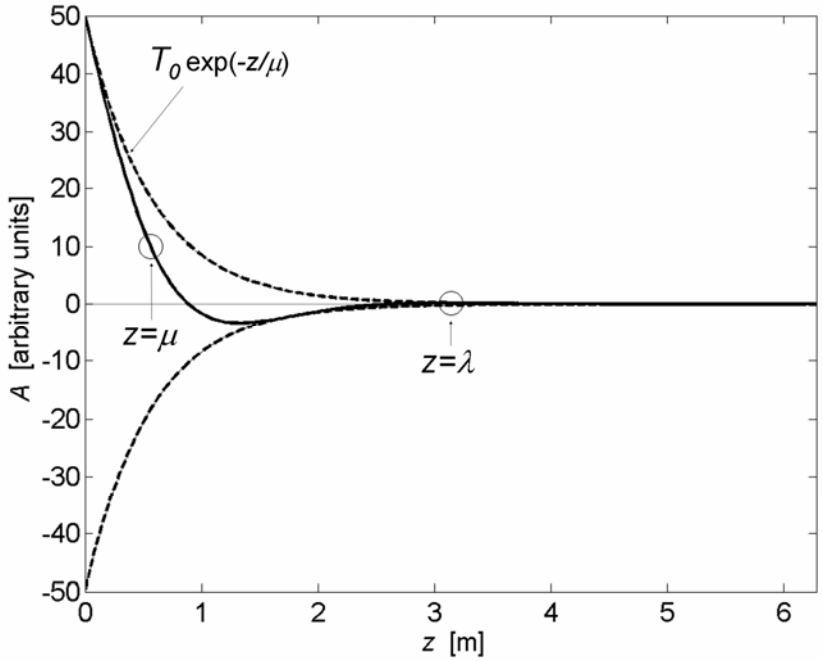

Figure C.2. Periodic thermal wave after reaching a solid barrier for the low frequency wave. MatLab® script: `thermal_wave.m`.

Furthermore, the propagation speed is also different for the two thermal waves, since it depends on the modulation frequency [31]:

$$v = \lambda\left(\frac{\omega}{2\pi}\right) = \sqrt{2\omega\alpha} \tag{C.7}$$

Consequently, low frequency thermal waves penetrate deeper into the material but they do so at lower speeds than high frequency waves.

C.3 Pulses

The *Superposition Principle* [70] states that any wave can be approximated by the sum of purely harmonic (sinusoidal) waves with different frequencies. Figure C.3 illustrates this principle using the *Fourier expansion* form for a square pulse, *S*:

$$S_n(z) = \frac{1}{2} + \frac{2}{\pi}\sum_{k=1}^{n}(-1)^{(k-1)}\frac{\cos(2k-1)\omega z}{(2k-1)} \tag{C.8}$$

where *n* represents the number of waves included in the approximation. The more sine waves are included, the better the sum of sine approximates a square pulse as can be seen in Figure C.3.

As discussed in Chapter 2, Fourier analysis is used to decompose temperature signatures into frequency components, which is the basis of Pulsed Phase Thermography.

From the above discussion it can be noticed that pulse propagation through the specimen is described by a relationship different from (C.4). The concept of an *impulse* is very convenient in the derivation of a solution. An impulse or *Dirac's delta function* $\delta(t)$, is defined as an intense unit-area pulse of so brief duration that no measuring equipment is capable of distinguishing it from even shorter pulses [14], *i.e.* $\delta(t)$ corresponds to a pulse of null duration.

The one-dimensional solution of the Fourier Equation for a Dirac delta function in a semi-infinite isotropic solid is given by [35]:

$$T(z,t) = T_0 + \frac{Q}{\sqrt{k\rho c_P \pi t}}\exp\left(-\frac{z^2}{4\alpha t}\right) \tag{C.9}$$

where Q is the energy absorbed by the surface [J/m^2] and T_0 is the initial temperature [K].

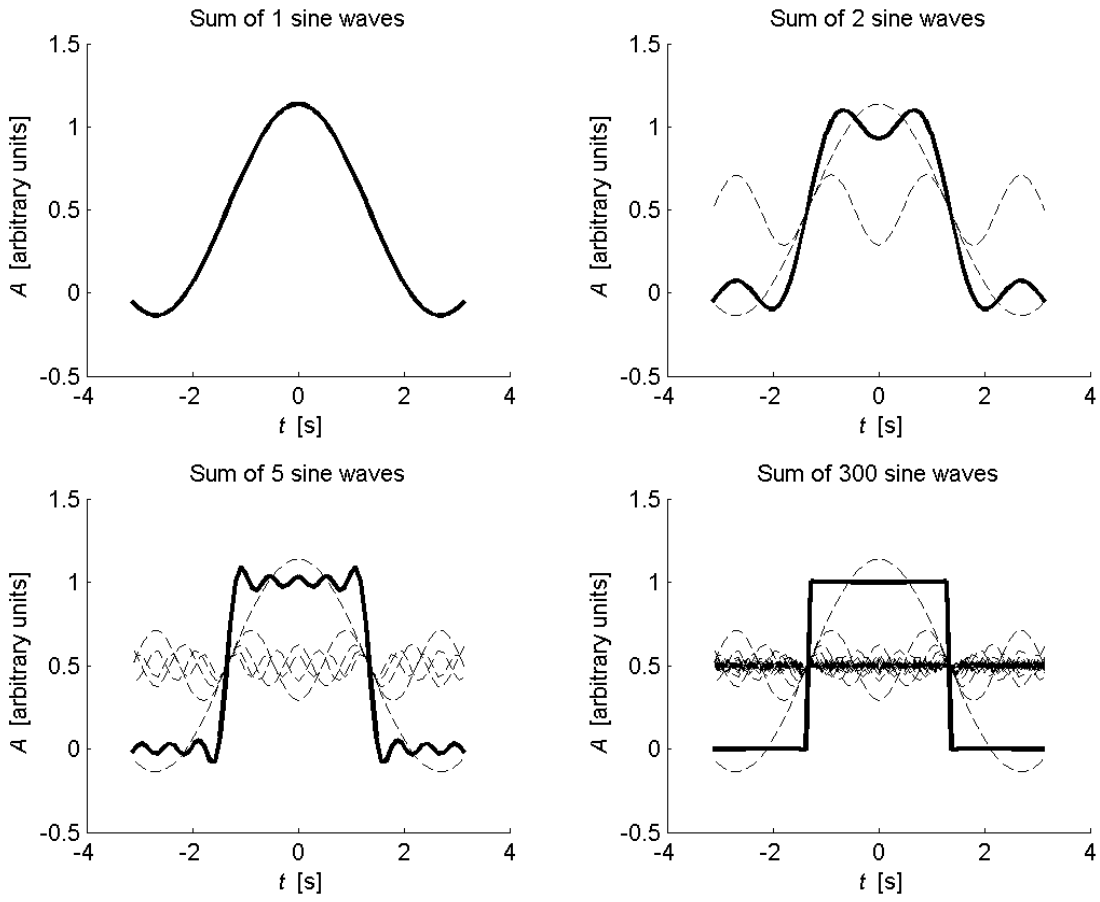

Figure C.3. Sum of 1, 2, 10 and 300 sine approximating to a square pulse. MatLab® script: `square_pulse.m`.

At the surface ($z=0$), Eq. (C.9) can be rewritten as:

$$T(0,t) = T_0 + \frac{Q}{e\sqrt{\pi t}} \tag{C.10}$$

where e is the effusivity.

This simple relationship characterizes the behavior of all homogeneous materials. Deviation of the $t^{1/2}$ dependency gives an indication of the presence of a defective area (see 1.2.4).

Appendix D. Thermographic Signal Reconstruction

Thermographic Signal Reconstruction (TSR) [82] is an attractive technique that allows to increase spatial and temporal resolution of a sequence, reducing the amount of data to be manipulated at the same time. TSR is based on the assumption that, non-defective pixels temperature profiles should follow the decay curve given by the one-dimensional solution of the Fourier Equation at the surface for a semi-infinite body stimulated by a Dirac delta function, *i.e.* Eq.(C.10):

$$\Delta T(t) = \frac{Q}{e\sqrt{\pi t}} \tag{C.10}$$

where $\Delta T = T - T_0$, with T being the temperature of the pixel or region of interest at time t, and T_0 is the initial (cold) temperature at the same region, *i.e.* at time t_0.

Taking the natural logarithm of both sides, Eq. (C.10) can be rewritten as [82]:

$$\ln(\Delta T) = \ln\left(\frac{Q}{e}\right) - \frac{1}{2}\ln(\pi t) \tag{D.11}$$

Eq. (D.11) represents the "normal" behavior for a non-defective pixel, *i.e.* it should follow a straight-line decay on a logarithmic scale corresponding to -½ slope. The offset is then given by input energy Q, and the effusivity of the specimen e. From this reasoning, Shepard [82] proposes to use a low order (N^{th}) polynomial function to fit the experimental data:

$$\ln(\Delta T) = a_0 + a_1 \ln(t) + a_2 \ln^2(t) + \ldots + a_N \ln^N(t) \tag{D.12}$$

Typically, n is set to 4 or 5 to avoid "ringing" and insure a good correspondence between fitting accuracy and signal de-noising for different NDT&E applications [82]-[86]. MatLab® provides a direct polynomial fitting function `polyfit()`. Hence, for a 5th degree polynomial for example, synthesized data can be obtained from [82]:

$$\Delta T(t) = \exp\left[a_0 + a_1 \ln(t) + a_2 \ln^2(t) + a_3 \ln^3(t) + a_4 \ln^4(t) + a_5 \ln^5(t)\right] \quad \text{(D.13)}$$

Figure D.4 shows the 6 coefficient images for a 5th degree polynomial fitting on temperature data for specimen PLEXI013 (see Appendix F.6). It is noticed that coefficient images show already significant contrast improvement with respect to raw data (see Figure A.5a).

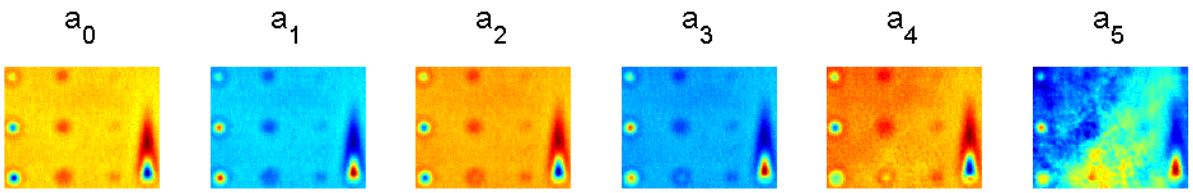

Figure D.4. Coefficient images for a 5th degree polynomial. MatLab® key functions: `polyfit()`,`polyval()`.

There are some advantages of using synthetic data provided by Eq. (D.13) with respect to raw thermal data. Besides signal de-noising (especially at high frequencies), data storage is considerably reduced. For instance, a typical thermogram sequence can have 500 frames or more on a 320x256 pixels configuration, *i.e.* a 320x256x500 matrix. Using a 4th degree polynomial, data will be reduced to 1/100 of its original size since only the coefficients of the polynomial function are needed to reconstruct the thermal profiles for each pixel, *i.e.* 320x256x5 matrix.

Finally, analytical processing becomes also possible. For example, actual temperature for a time between acquisitions can be estimated from the polynomial coefficients. Time derivatives can be calculated as well.

First time derivatives indicate the rate of cooling while second time derivatives refer to the rate of change in the rate of cooling. Therefore, time derivatives should be more sensitive to temperature changes than raw thermal images [43].

The first time derivative for the N^{th} degree polynomial in Eq. (D.12) can be expressed as:

$$\frac{d}{dt}\ln(\Delta T) = a_1 + a_2 \ln(t) + ... \qquad \text{(C.14)}$$

$$... + a_{N-1} \ln^{N-2}(t) + a_N \ln^{N-1}(t)$$

which can also be written as a summation series as follows [85]:

$$\frac{d}{dt}\ln(\Delta T) = \sum_{n=1}^{N} n a_n \ln^{(n-1)}(t) \qquad \text{(C.15)}$$

Figure D.5a corresponds to a typical temperature decay for a defective (dotted line) and a non-defective (plain line) area. The first time derivative as calculated with Eq. (C.15), is shown in Figure D.5b, and the second time derivative in Figure D.5c.

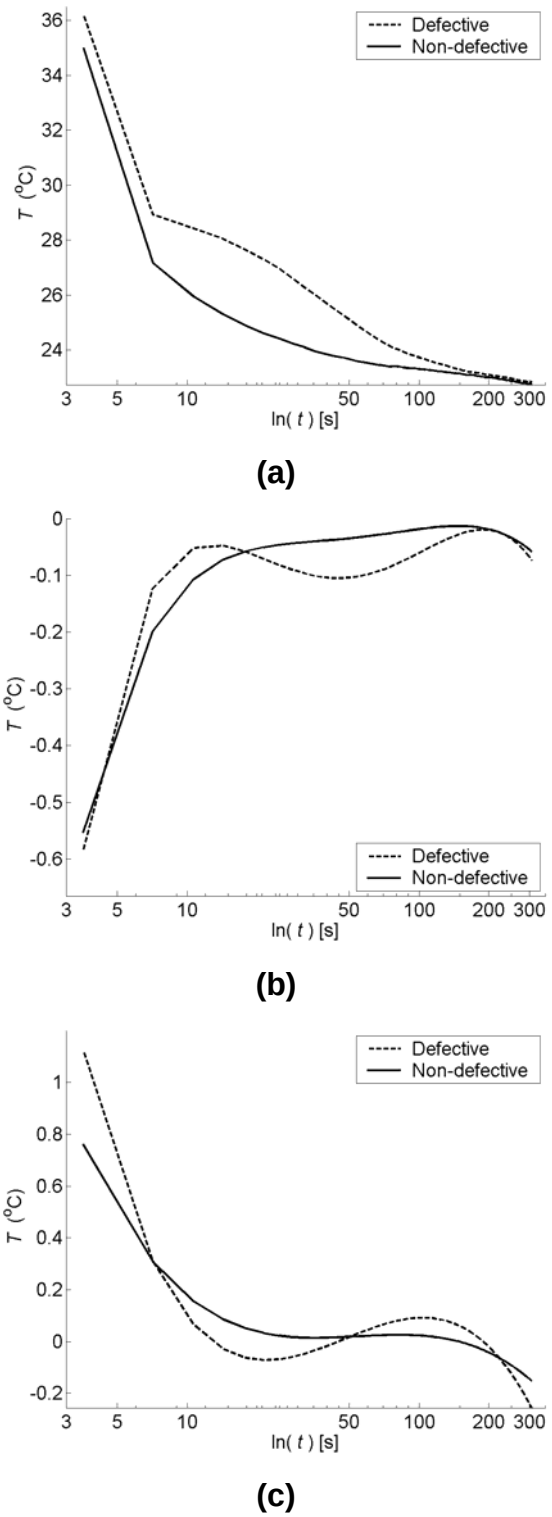

Figure D.5. (a) Temperature, (b) 1st, and (c) 2nd time derivatives.

Second time derivative can be expressed as:

$$\frac{d^2}{dt^2}\ln(\Delta T) = \sum_{n=2}^{N}(n-1)n a_n \ln^{(n-2)}(t) \tag{D.16}$$

Eqs. (C.15) and (D.16) can be easily integrated on the automatic computation of the first and second derivatives coefficients. For instance, first and second time derivatives at different times are shown in Figure D.6, respectively, for specimen ALU005 in Appendix F.6.

Specimen ALU005 consists of two concentric flat-bottomed holes of different depths. Thermograms in Figure D.6a and Figure D.6b, show a cropped portion of the plate to include the two concentric holes. In this case, the first time derivative is more effective in discriminating both defects (see thermogram at t=0.31046 s). Another possibility is to use synthetic data to feed the PPT algorithm as is shown in Figure D.6d. PPT synthetic results are almost the same as raw PPT results at low frequencies. However, de-noising capabilities of synthetic data are demonstrated at high frequencies. When compared to time derivative images, synthetic PPT phasegrams show more subsurface details.

Another example of the usefulness of TSR, as a processing technique alone or when combined to PPT, is seen in Figure D.7 for a steel plate with simulated corrosion (not shown in Appendix). To simulate corrosion of different degrees of severity, three slots of equal depth where first machined on the rear part of the plat at approximately 1 mm depth, *i.e.* 5.5 mm depth from the front side. Then, an acid solution was applied and left for several hours. The process was repeated several times in random areas of the three slots resulting on more realistic irregularly corroded areas. For instance, the right slot presented corrosion from 5.5 mm (at the bottom) to 0 mm (at the top), where a hole was present at the top of this slot as can be clearly seen in Figure D.6a, Figure D.6b and Figure D.6c. These images correspond all three to t=1.42 s (the best overall contrast of the thermal sequence), but different processing techniques were used as described below.

Figure D.6a corresponds to a raw thermogram, which is affected by Fixed Pattern Noise (FPN), contributing to hide defect information. Corrosion is better seen in Figure D.6b, which is obtained by subtracting a pre-flash (cold) image from the thermogram in Figure D.6a. This simple arithmetic operation is good enough to reveal almost entirely the artificially corroded areas on the three slots.

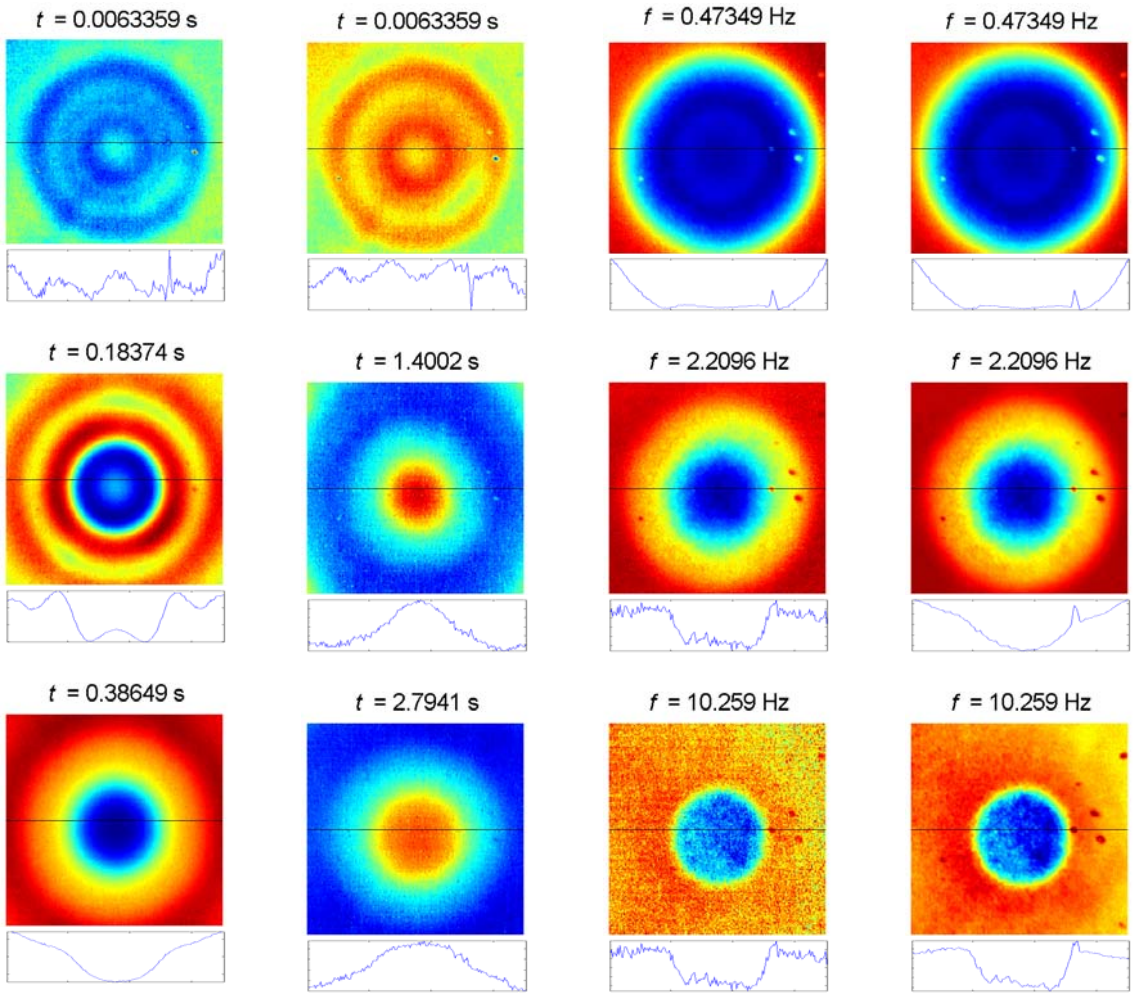

Figure D.6. (a) First time derivative; and (b) second time derivative obtained from a 7th degree polynomial. PPT results from (c) raw thermal data; and (d)synthetic data. Data from specimen ALU005 in Appendix F.6. MatLab® key functions: `disp_imgs()`, `ppt()`, `polynomial()`, `derivatives()`.

However, information about the subsurface condition of the plate is still missing. Figure D.6c corresponds to the second coefficient image (the one showing the

higher contrast of all 6 coefficient images) as obtained by TSR fitting raw thermal data (after cold image subtraction) with a 5th degree polynomial. Figure D.6d is the first time derivative image at t=1.42 s (calculated from the polynomial coefficients). Besides an increase in thermal contrast and resolution, more internal information becomes available. Although the hole may still be distinguished at this particular time, this image reveals deeper information more clearly.

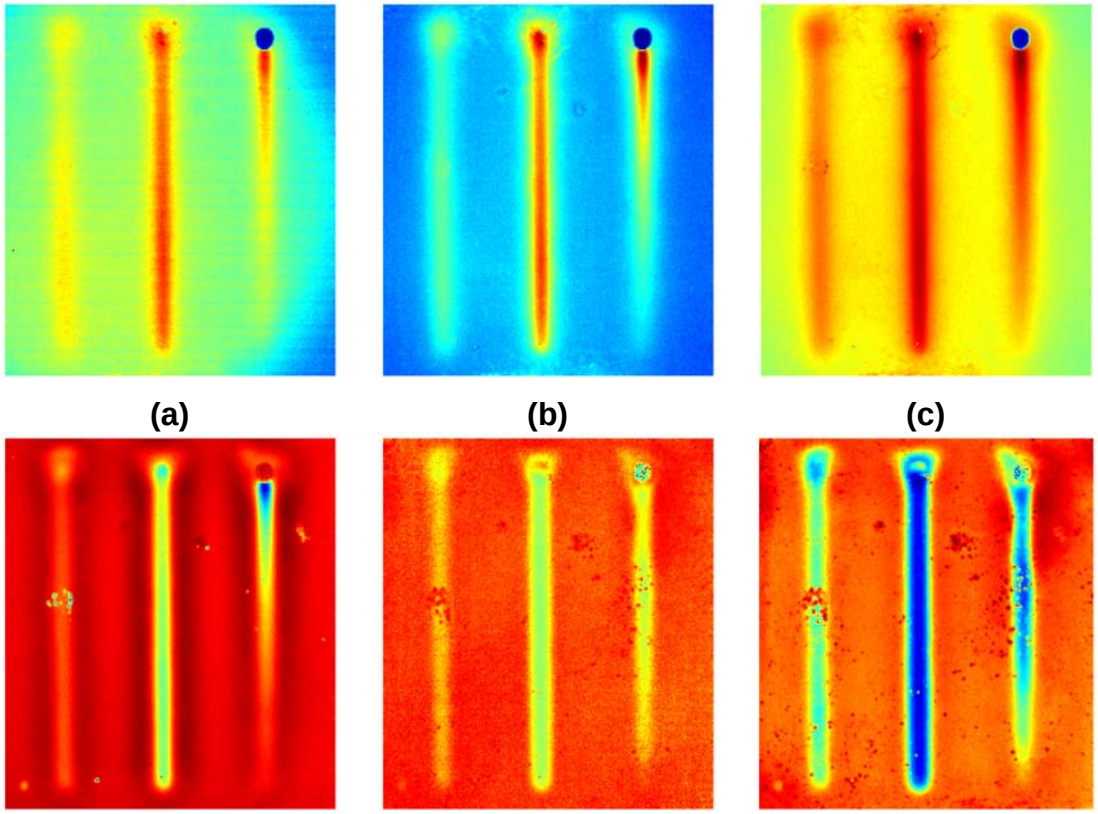

Figure D.7. Simulated corrosion on a steel plate (specimen ACIER005 in Appendix F.3). Thermograms at t=1.42 s obtained (a) from the raw temperature sequence, (b) after subtracting the cold image from the raw sequence, (c) after reconstruction using a 5th degree polynomial, (d) first time derivative calculated from the synthetic sequence. Phasegrams at f=0.55Hz after performing PPT on (e) the raw temperature sequence; and (f) the synthetic thermal sequence.

Although the 1st time derivative image showed considerable enhanced contrast with respect to the raw thermograms, additional subsurface information can be recovered with the phase. Phasegram in Figure D.6e corresponds to f=0.55Hz. At

this frequency, it was possible to see some (deeper) internal features due to material imperfections (small clusters at different locations) that were not detected in Figure D.6d. These internal features are also seen in Figure D.6f with enhanced contrast. Figure D.6f is the phasegram at f=0.55Hz obtained after applying the PPT on reconstructed data.

Appendix E. Evaluation of the fitting accuracy

Several tools can help to evaluate the 'goodness' of the fittings. For instance, the correlation coefficient, the residuals and the prediction bounds are used through all of the correlation results presented in this work. Contrary to the regression coefficient *R*, which is a numerical measure, the residuals *r*, and the prediction bounds *P*, can be thought as graphical measures because they allow to view the entire data set at once, and they can easily display a wide range of relationships between the model and the data. A brief description of these parameters follows.

CORRELATION COEFFICIENT

The correlation coefficient is a normalized measure of the strength of the linear relationship between two variables. Uncorrelated data results in a correlation coefficient of 0; equivalent data sets have a correlation coefficient of 1 [118]. The correlation coefficient is defined as [119]:

$$R = \sqrt{\frac{\sum\left(y_{est} - \bar{y}\right)^2}{\sum\left(y - \bar{y}\right)^2}} \tag{E.17}$$

where y_{est} is the estimated value of y, and $\bar{y}$ is the mean value of y.

RESIDUALS

The residuals are also useful. The residuals from a fitted model *r*, are defined as the differences between the response data *y*, and the fit to the response data at each predictor value y_{est}:

$$r = y - y_{est} \tag{E.18}$$

This simple calculation helps to determine if the model is correct, *i.e.* the residuals appear to behave randomly, or if it fits the data poorly, *i.e.* the residuals display a systematic pattern.

PREDICTION BOUNDS

Prediction bounds can be calculated for a new observation or for the fitted curve. In both cases, the prediction is based on an existing fit to the data. Additionally, the bounds can be *simultaneous* and measure the confidence for all predictor values, or they can be *no simultaneous* and measure the confidence only for a single predetermined predictor value. In the correlation graphs of Chapter 3, simultaneous prediction bounds of two kinds are used: (1) for a *new observation* considering *all* predictor values $P_{s,o}$ (the widest bounds in all graphs); and (2) for the *function* and *all* predictor values $P_{s,f}$ (the narrowest bounds in all graphs), both defined correspondingly as:

$$P_{s,o} = y_{est} \pm f\sqrt{s^2 + xSx'} \tag{E.19}$$

$$P_{s,f} = y_{est} \pm f\sqrt{xSx'} \tag{E.20}$$

where s^2 is the mean square error, S is the covariance matrix, x is the predictor value, x' is its transpose, and f is the inverse of the F cumulative distribution function. Function `finv()` from MatLab® is used to compute f. See reference [119] for details.

Appendix F. Plate Specifications

F.1 ACIER001

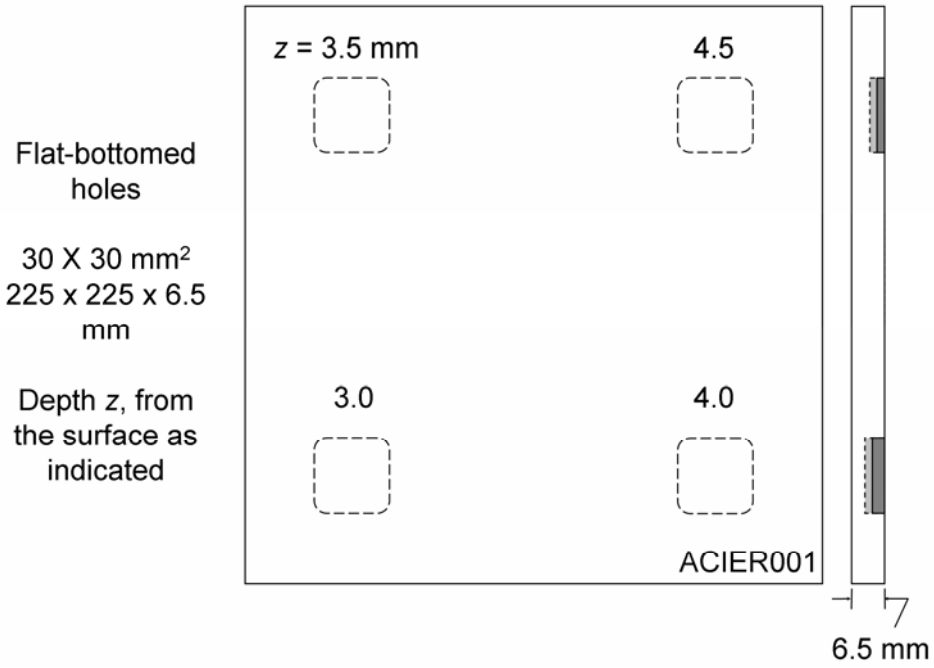

F.2 ACIER002

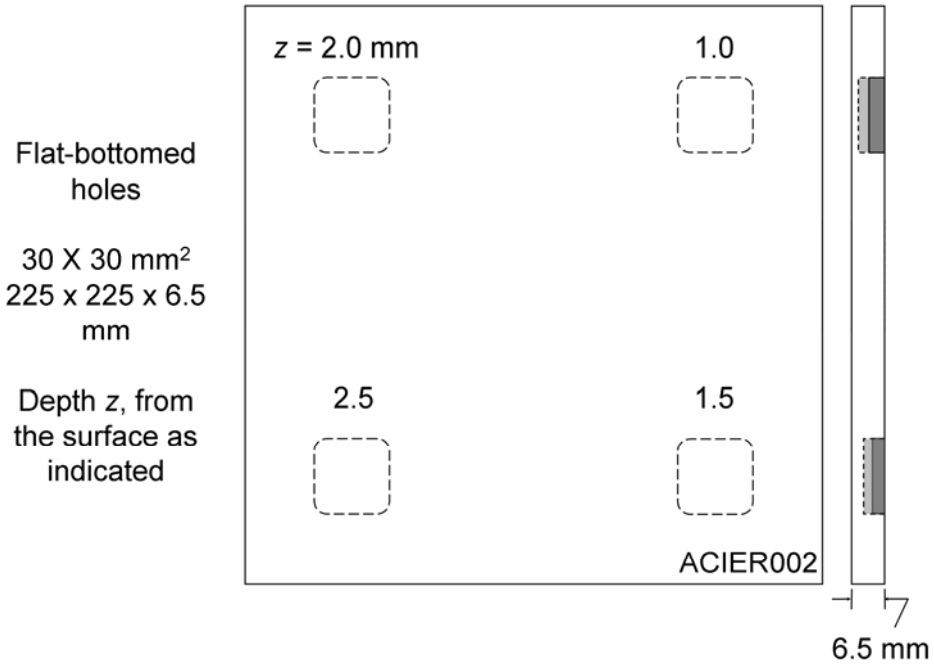

F.3 ACIER005

F.4 ALU002

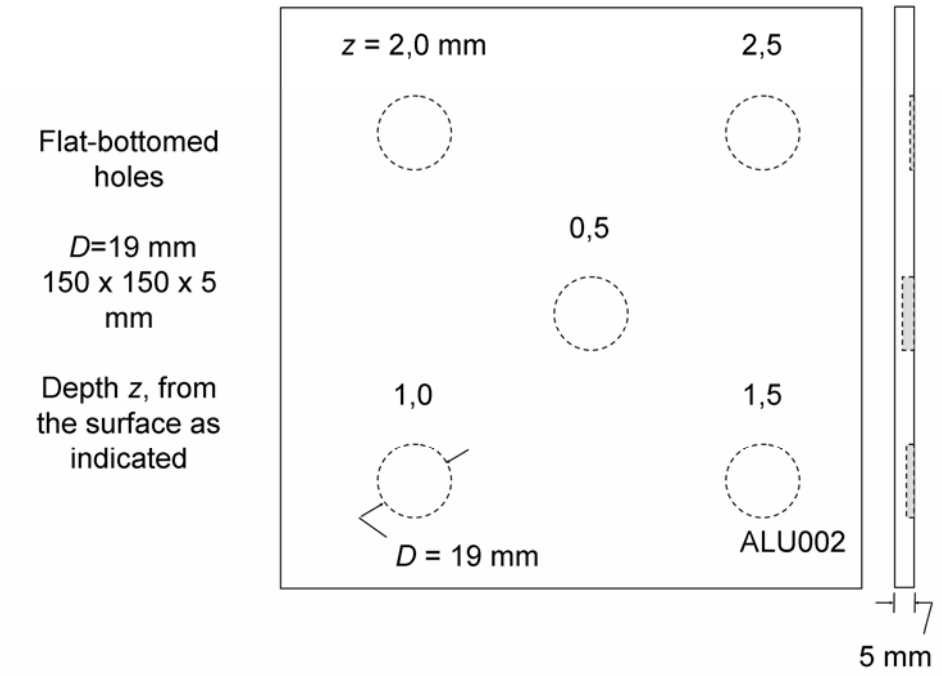

F.5 ALU003

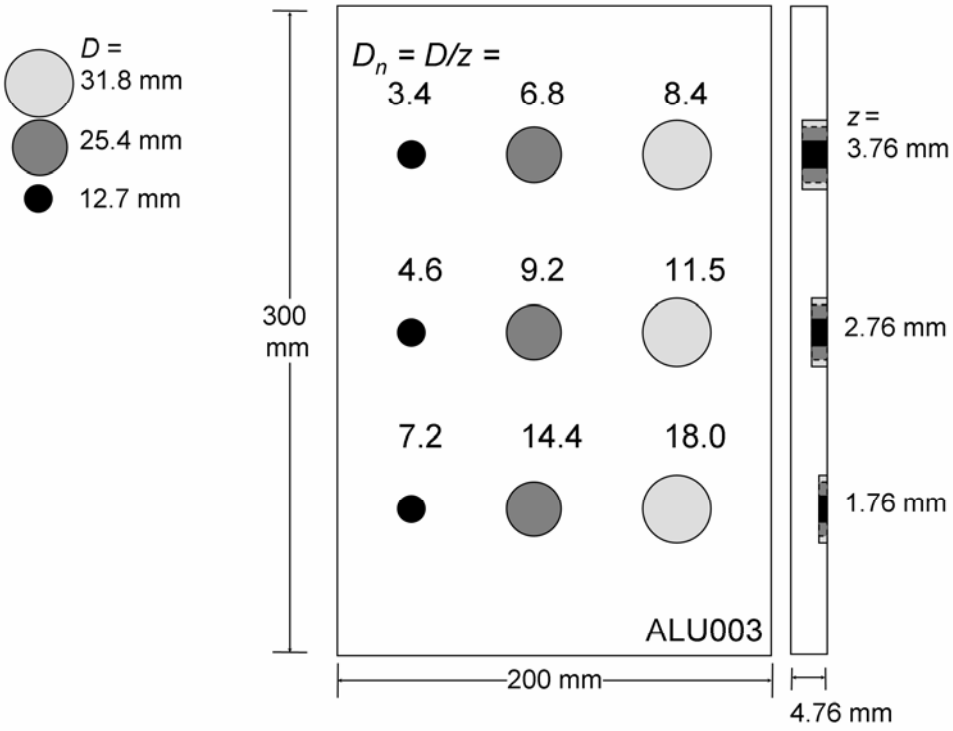

F.6 ALU005

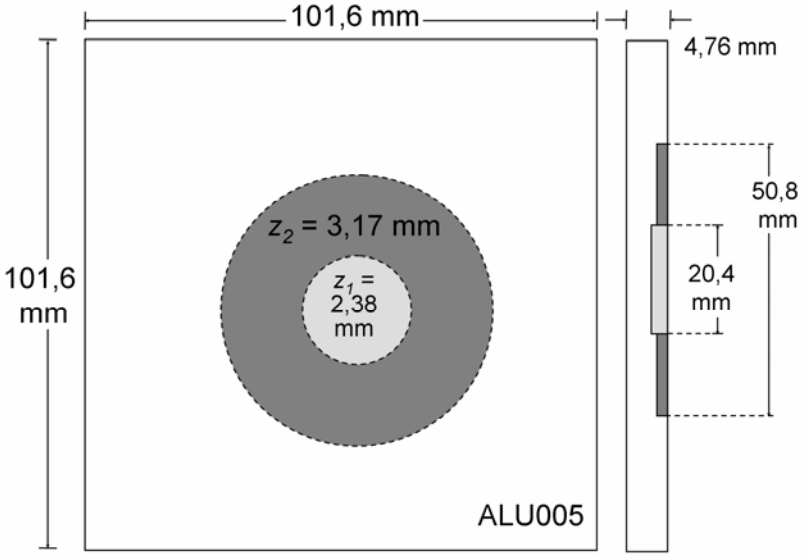

F.7 PLEXI013

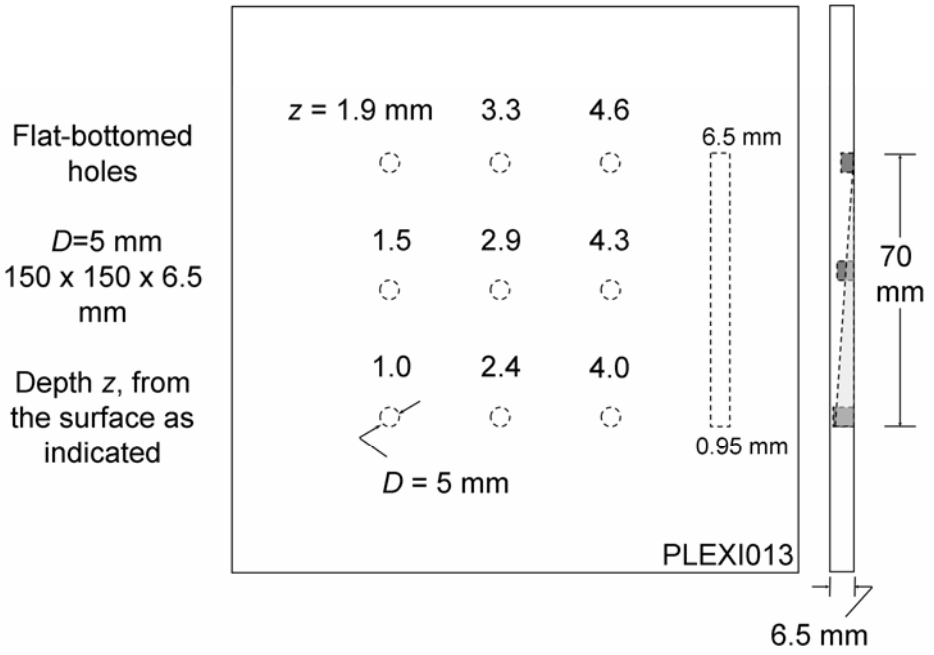

F.8 PLEXI014

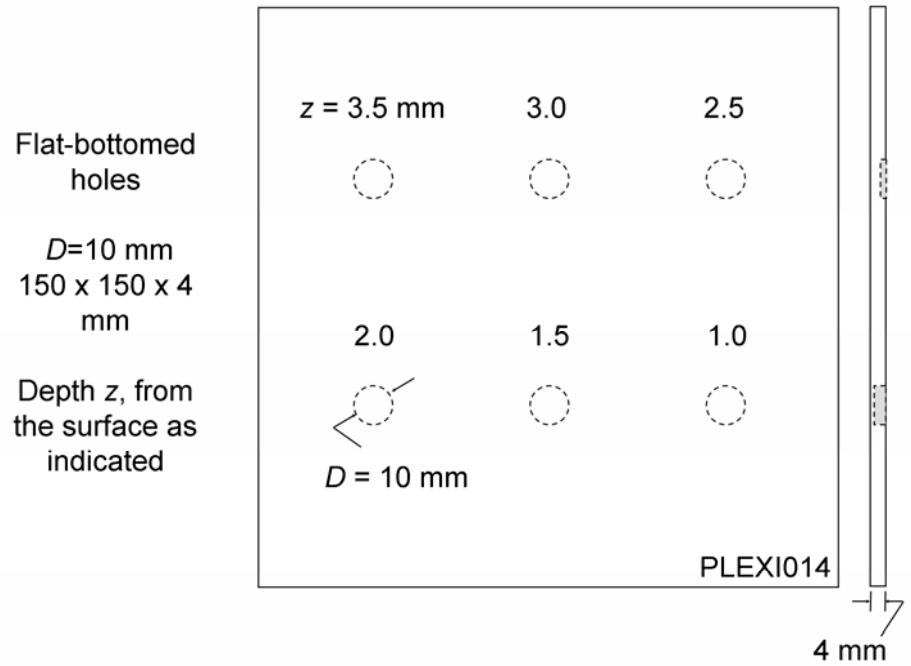

F.9 CFRP006 and GFRP006

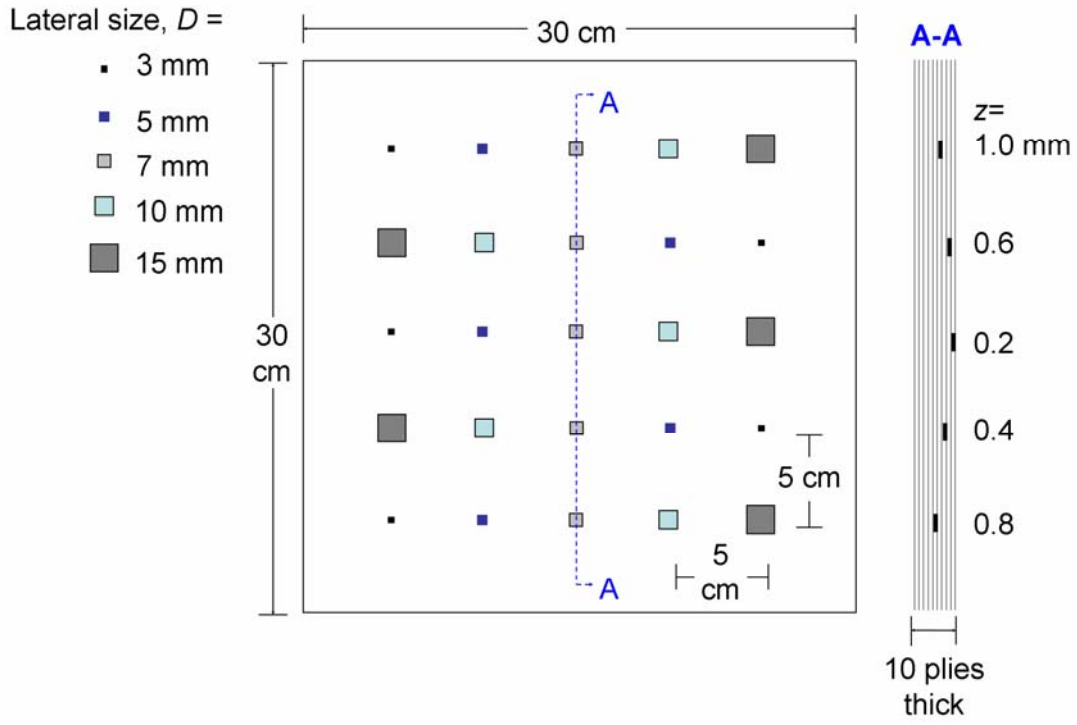

F.10 CFRP007 and GFRP007

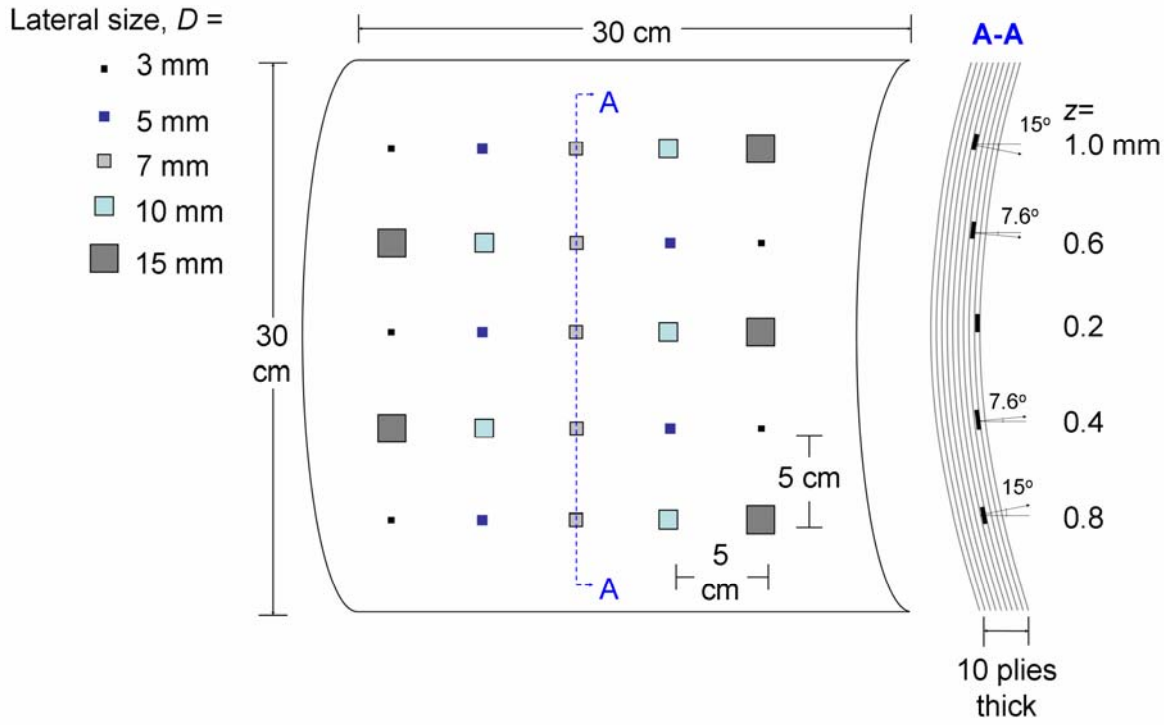

F.11 CFRP008 and GFRP008

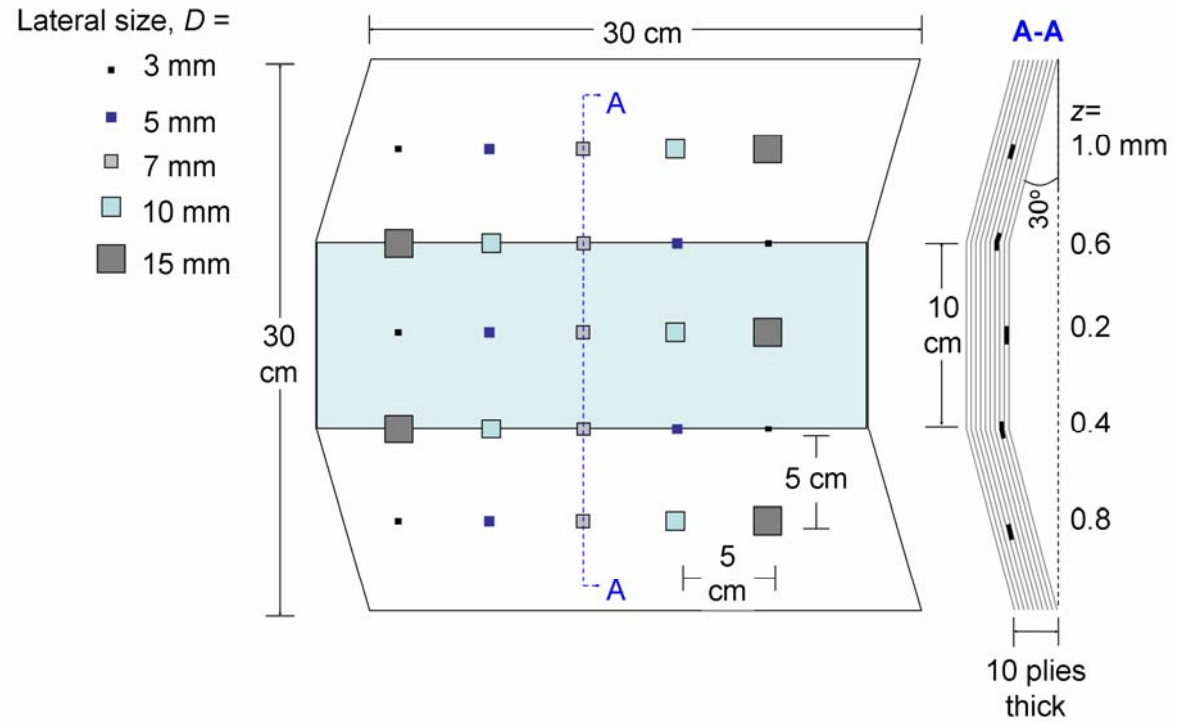

Appendix G. Available Equipment at the CVSL

G.1 Cameras IR

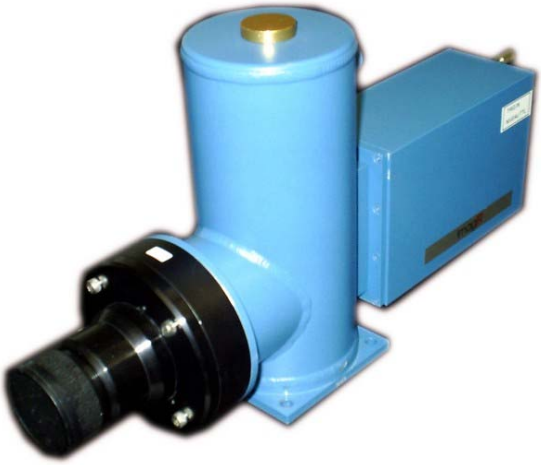

Santa Barbara Focal Plane SBF125

CCD detector matrix
InSb (Indium Antimony)
Dynamic window range: from 128x8 to 320x256.
Frequency/(resolution) :
8 kHz/(128x8), 1 kHz/(128x128), and 400 Hz/(320x256).
14 bits (16,384 levels)
Liquid nitrogen cooling (77 K)
Spectral band: 3 to 5 μm.
45 badpixels

Cincinnati Electronics

FPA array
InSb (Indium Antimony)
160x120 matrix detector;
54 images/s
34 badpixels
NETD 20 mK at 20°C
20° opening
14 bits (16,384 levels)
Liquid nitrogen cooling (77 K)
Spectral band: 3 to 5 μm

G.2 Heating sources

2 flashes Balcar FX 60

Pulse duration: 5 ms
Energy: 6,4 kJ x 2 flashes.

Heating lamp

6 infrared tubes 1.2 kW each
Shutter-solenoid configuration
Minimum pulse duration: 300 ms

G.3 Blackbody

Mikron M340

Temperature Range: –20.0° to 150.0°C
Accuracy: ±0.3°C
Temperature Resolution: 0.1 degree
Emissivity (effective): +0.99
Temperature Sensor: Precision platinum RTD: 1/3 DIN
Digital self-tuning PID controller
6 minutes from ambient to –15°C or 100°C
Operating Ambient Temperature: 5 to 40°C (40 to 104°F)